



# Study of protein in the respiratory chain by IR spectroscopy and electrochemistry

Yashvin Neehaul

## ► To cite this version:

Yashvin Neehaul. Study of protein in the respiratory chain by IR spectroscopy and electrochemistry. Agricultural sciences. Université de Strasbourg, 2012. English. NNT : 2012STRAF042 . tel-00827526

**HAL Id: tel-00827526**

**<https://theses.hal.science/tel-00827526>**

Submitted on 29 May 2013

**HAL** is a multi-disciplinary open access archive for the deposit and dissemination of scientific research documents, whether they are published or not. The documents may come from teaching and research institutions in France or abroad, or from public or private research centers.

L'archive ouverte pluridisciplinaire **HAL**, est destinée au dépôt et à la diffusion de documents scientifiques de niveau recherche, publiés ou non, émanant des établissements d'enseignement et de recherche français ou étrangers, des laboratoires publics ou privés.



**ÉCOLE DOCTORALE DES SCIENCES CHIMIQUES**

**Institut de Chimie UMR 7177**

## **THÈSE**

présentée par

**Yashvin NEEHAUL**

soutenance le : **13 septembre 2012**

pour obtenir le grade de

**Docteur de l'Université de Strasbourg**

Discipline / Spécialité : Chimie

**Etude des interactions des protéines dans  
la chaîne respiratoire par spectroscopie IR  
et par électrochimie**

**Study of protein interactions in the respiratory chain  
by IR spectroscopy and electrochemistry**

**THÈSE dirigée par :**

**Prof. Dr. HELLWIG Petra**

Université de Strasbourg

**Membres du jury**

**Dr. BACIOU PARTISETI Laura**

Université Paris Sud

**Prof. Dr. MÂNTELE Werner**

Johann Wolfgang Goethe-Universität

**Dr. LEIZE-WAGNER Emmanuelle**

Université de Strasbourg

*The woods are lovely, dark, and deep,  
But I have promises to keep,  
And miles to go before I sleep,  
And miles to go before I sleep...*

Robert Frost (1874–1963)

# Table of contents

<i>Résumé</i>	I
<i>Acknowledgments</i>	VI
<i>Abbreviations and Nomenclature</i>	VII
<i>List of figures</i>	IX
<i>List of tables</i>	XIV
<i>Publications</i>	XVI
 <b>Chapter I : Introduction</b>	 1
<b>1.0 Abstract</b>	2
<b>1.1 Ion transport across membranes</b>	3
<b>1.2 Cellular respiration</b>	6
1.2.1 The respiratory chain	7
1.2.1.1 NADH dehydrogenase superfamily	8
1.2.1.2 Succinate:ubiquinone oxidoreductase	10
1.2.1.3 Quinone pool	10
1.2.1.4 Cytochrome <i>bc</i> <sub>1</sub> complex	11
1.2.1.5 Cytochrome <i>c</i>	12
1.2.1.6 Cytochrome <i>c</i> oxidase	12
1.2.1.7 ATP synthase	13
<b>1.3 The Na<sup>+</sup>-translocation NADH:quinone oxidoreductase from <i>Vibrio cholerae</i></b>	14
1.3.1 <i>Vibrio cholerae</i> and the sodium cycle	14
1.3.2 The Na <sup>+</sup> -NQR	16
1.3.3 Sub-units composition	16
1.3.4 Chemical versatility of flavins	19
1.3.5 Electron pathway	21
1.3.6 Ion dependence	22
1.3.7 Na <sup>+</sup> binding to the Na <sup>+</sup> -NQR	23
<b>1.4 Protein-protein interaction</b>	25
1.4.1 Thermophiles and thermozymes	26
1.4.2 Protein-protein interaction and oxygen reduction in <i>Thermus thermophilus</i>	27
1.4.3 The <i>ba</i> <sub>3</sub> oxidase	28
1.4.4 The Cu <sub>A</sub> fragment	29

1.4.5	Cytochrome <i>c</i> <sub>552</sub>	30
1.4.6	[Cytochrome <i>c</i> <sub>552</sub> -Cu <sub>A</sub> fragment] complex	31
<b>1.5</b>	<b>Cytochrome <i>bc</i><sub>1</sub>-<i>aa</i><sub>3</sub> supercomplex from <i>Corynebacterium glutamicum</i></b>	<b>33</b>
1.5.1	The <i>Corynebacterium glutamicum</i>	33
1.5.2	Respiration based on menaquinone	34
1.5.3	Cytochrome <i>bc</i> <sub>1</sub> - <i>aa</i> <sub>3</sub> oxidase	34
<b>1.6</b>	<b>Aim of work</b>	<b>36</b>
 <b>Chapter II : Experimental Techniques</b>		<b>37</b>
<b>2.0</b>	<b>Spectroscopy</b>	<b>28</b>
<b>2.1</b>	UV-visible: electronic spectroscopy	39
<b>2.2</b>	Infrared: vibrational spectroscopy	40
2.2.1	IR spectrometer	41
2.2.3	Fourier-Transformation	43
2.2.4	Study of proteins: why IR spectroscopy?	43
2.2.5	Hydrogen/deuterium exchange kinetics	46
2.2.6	Electrochemistry	48
2.2.7	Difference spectroscopy	49
 <b>Chapter III : Materials and methods</b>		<b>51</b>
<b>3.1</b>	<b>Sample preparation</b>	<b>52</b>
3.1.1	The Na <sup>+</sup> pumping NADH:quinone oxidoreductase from <i>Vibrio cholerae</i>	52
3.1.1.1	Wild type enzyme	52
3.1.1.2	Mutant enzymes	53
3.1.2	Cytochrome <i>c</i> <sub>552</sub> and the Cu <sub>A</sub> fragment of the <i>ba</i> <sub>3</sub> oxidase from <i>Thermus thermophilus</i>	53
3.1.3	The <i>bc</i> <sub>1</sub> - <i>aa</i> <sub>3</sub> supercomplex from <i>Corynebacterium glutamicum</i>	54
<b>3.2</b>	<b>The thin layer electrochemical cell</b>	<b>54</b>
<b>3.3</b>	<b>Redox titration monitored in the UV-visible</b>	<b>55</b>
<b>3.4</b>	<b>FTIR measurements</b>	<b>59</b>
3.4.1	Redox induced mid-IR difference spectroscopy	59
3.4.2	Hydrogen-deuterium exchange kinetics monitored in mid-IR	60
3.4.2.1	HDX data analysis	61
3.4.2.2	Determination of the coefficient of H <sub>2</sub> O in the recorded spectra	62
3.4.2.3	Normalisation with respect to the amide I band	63
3.4.2.4	Monitoring the rate of amide II decrease	63

3.4.2.5	Determination of exchange fractions and rate constants	65
<b>3.6</b>	<b>Estimation of secondary structure</b>	66
3.6.1	Amide I band separation in the mid-IR	66
3.6.2	Circular dichroism spectroscopy	67
<b>Chapter IV</b>	<b>Results and discussions</b>	68
<b>4.1</b>	<b>The Na<sup>+</sup>-pumping NADH:quinone oxidoreductase</b>	69
4.1.1	Redox titration monitored in the UV-visible	69
4.1.2	Redox induced FTIR difference spectra of model compounds: FAD, FMN and riboflavin	77
4.1.3	Redox induced FTIR difference spectra of Na <sup>+</sup> -NQR	78
4.1.4	Redox induced difference spectra obtained in the presence of different	81
4.1.5	Double difference spectra in the presence of the different ions	83
4.1.6	H/D exchange kinetics measurements of the Na <sup>+</sup> -NQR	88
4.1.7	Analysis of the secondary structure of the Na <sup>+</sup> -NQR	93
4.1.8	Mechanism of Na <sup>+</sup> -pumping	95
<b>4.2</b>	<b>Study of mutant enzymes involved in Na<sup>+</sup> binding</b>	97
4.2.1	Redox titration of the cofactors present in the NqrB D397E mutant enzyme	97
4.2.2	Redox induced mid-IR difference spectroscopic studies of the NqrB D397E mutant enzyme	99
4.2.3	Double difference spectra of the NqrB D397E mutant enzyme studied in the present of different ions.	101
4.2.4	Comparison with the wild type enzyme	104
4.2.5	H/D exchange kinetics measurements of the NqrB D397E mutant enzyme	106
4.2.6	Study of the NqrE E95Q mutant enzyme	108
4.2.7	Study of other mutations of the NqrB D397 and NqrE E95 residues	110
4.2.8	The role of NqrB D397 and NqrE E95 residues in Na <sup>+</sup> binding	111
<b>4.3</b>	<b>Study of the quinone binding site of the Na<sup>+</sup>-NQR</b>	113
4.3.1	Redox titration of the NqrB G140A mutant enzyme	113
4.3.2	Redox induced difference spectroscopic studies	114
4.3.3	Redox induced difference spectroscopic studies for the critical potential step including riboflavin cofactor and quinone.	116
4.3.4	Double difference spectra for the critical potential step including the riboflavin cofactor and quinone.	119
4.3.5	Effects HQNO inhibition	121

4.3.6	Secondary structure analysis of the NqrB G140A mutant enzyme	122
4.3.7	Involvement of the NqrB G140 residue in quinone binding	122
<b>4.4</b>	<b>The [cytochrome <i>c</i><sub>552</sub>-Cu<sub>A</sub> fragment] complex from <i>Thermus thermophilus</i></b>	<b>124</b>
4.4.1	Redox titration	124
4.4.2	Redox induced mid-IR difference spectroscopy	128
4.4.3	Electron transfer complex	132
<b>4.5</b>	<b>Characterisation of the mid-point potentials of the hemes in the <i>bc</i><sub>1</sub>-<i>aa</i><sub>3</sub> supercomplex from <i>Corynebacterium glutamicum</i></b>	<b>135</b>
4.5.1	Redox potentials of the <i>a</i> and <i>a</i> <sub>3</sub> hemes	137
4.5.2	Redox potentials of the <i>c</i> and <i>c</i> <sub>1</sub> hemes	138
4.5.3	Redox potential of the <i>b</i> <sub>L</sub> and <i>b</i> <sub>H</sub> hemes	139
4.5.4	Comparison with analogues from <i>Paracoccus denitrificans</i>	140
	<b>Chapter V : Conclusion and perspectives</b>	<b>141</b>
	<b>References</b>	<b>145</b>
	<b>Appendix</b>	<b>160</b>

## Résumé (for the doctoral school)

### Introduction

Le catabolisme d'aliments nutritionnels résulte dans la formation de coenzymes réduites tel que le NADH (nicotinamide adénine dinucléotide). Ces coenzymes sont oxydées par le premier complexe de la chaîne respiratoire, la NADH:quinone oxydoréductase aussi appelée le complexe I. Il catalyse le transfert d'électron vers des quinones qui sont réduites en quinols. Ce transfert d'électron est couplé à un transfert de protons à travers la membrane plasmique et contribue à mettre en place un gradient de protons. Les quinols sont oxydés par le complexe  $bc_1$  qui transfère aussi des protons à travers la membrane. Le cytochrome  $c$  transfère des électrons entre du complexe  $bc_1$  à la cytochrome  $c$  oxydase. La cytochrome  $c$  oxydase catalyse la réduction de l'oxygène en molécules d'eau tout en participant aussi à un transfert de protons à travers la membrane. Le gradient de proton est finalement utilisé par l'ATP synthase pour synthétiser de l'ATP (adénosine triphosphate) qui est utilisée comme source d'énergie métabolique.

### La $\text{Na}^+$ -NADH:quinone réductase de l'organisme *Vibrio cholerae*

Dans le cadre de ce travail, un analogue du complexe I est étudié, la  $\text{Na}^+$ -NADH:quinone réductase ( $\text{Na}^+$ -NQR) de l'organisme *Vibrio cholerae*. Analogue par sa fonction d'entrée d'électrons dans la chaîne respiratoire, mais contrairement au complexe I, cette protéine transfère des cations  $\text{Na}^+$  à travers la membrane. L'activité catalytique de cet enzyme est stimulée 8 fois en présence de  $\text{Na}^+$ , 3 fois en présence de  $\text{Li}^+$ , insensible en présence de  $\text{K}^+$  et inhibée par les ions  $\text{Rb}^+$ . En se basant sur ces mesures d'activité, un dosage redox des cofacteurs en UV-visible a permis de mettre en évidence une augmentation du potentiel redox d'un des cofacteurs le  $\text{FMN}_C$  (Flavine mono nucléotide présent dans la sous-unité NqrC) de 100 mV en présence d'ions  $\text{Na}^+$  et  $\text{Li}^+$  par rapport aux échantillons contenant des ions  $\text{K}^+$  and  $\text{Rb}^+$ . La dépendance d'ions était aussi étudiée en moyen IR (Figure I). Les résultats ont mis en évidence les modes d'élongation symétrique des liaisons de type  $\text{COO}^-\text{Na}^+$  et  $\text{COO}^-\text{Li}^+$  dans la forme oxydée ainsi que dans la forme réduite de l'enzyme. Ces types de liaisons peuvent être de type mono ou bi dentate. Pour définir le type de liaison, ces mêmes expériences ont été faites dans  $\text{D}_2\text{O}$ . En connaissant la différence de nombre d'onde entre le mode symétrique et asymétrique de cette



élongation, on peut connaître la coordination de ces ions. Par ailleurs, une bande observée dans la forme réduite uniquement en présence d'ion  $\text{Rb}^+$  suggère que cet inhibiteur se lie à la protéine dans sa forme réduite. Le changement conformationnel qui se fait entre les deux états redox, est similaire en présence de  $\text{Na}^+$  et  $\text{Li}^+$ . Ce changement est bloqué en présence de  $\text{Rb}^+$ .

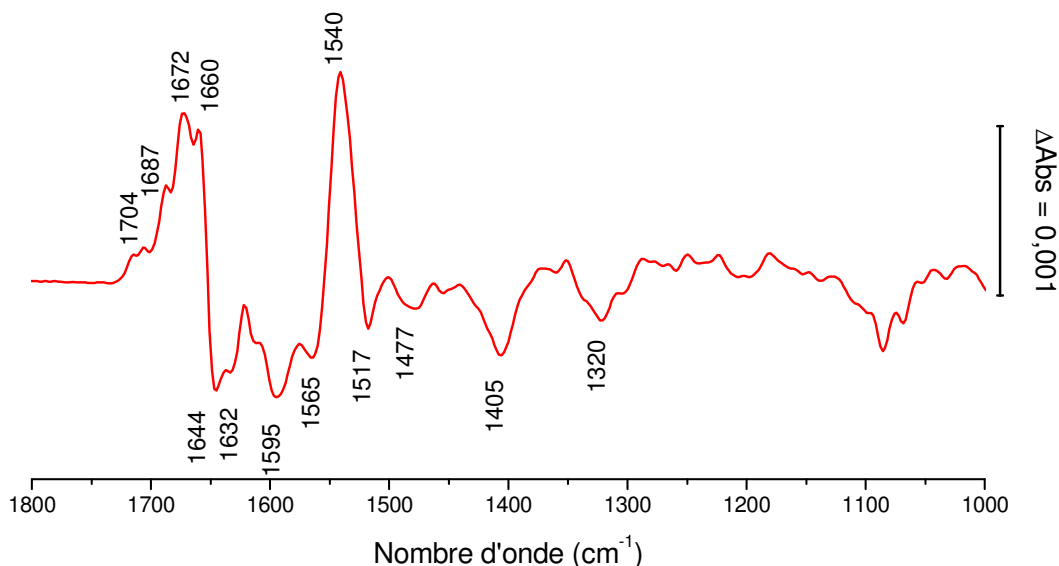


**Figure I: Spectre différentiel de la  $\text{Na}^+$ -NQR, les signaux observés montrent les changements de conformation, des cofacteurs ainsi que l'implication de certains résidus dans la réaction redox.**

La spectroscopie IR différentielle couplée à l'électrochimie donne des informations sur le changement conformationnel local et les états de protonation des résidus après l'application d'un potentiel. Les changements de structure tertiaire par contre ne sont pas observés. Pour les visualiser, la cinétique d'échange hydrogène/deutérium en moyen IR est utilisée. Cette technique permet aussi de mettre en évidence des canaux de transfert transmembranaire. Les résultats montrent que la cinétique d'échange H/D est similaire en présence de  $\text{Na}^+$  et  $\text{Li}^+$ , alors qu'en présence d'ions  $\text{K}^+$  et  $\text{Rb}^+$  la cinétique d'échange est plus lente et 4% des liaisons amides ne sont plus accessibles. Ces résultats suggèrent la présence d'un canal de transfert qui n'est accessible qu'en présence d'ions  $\text{Na}^+$  et  $\text{Li}^+$ .

Des résidus acides (Figures II) ont été identifiés qui peuvent être les sites d'entrée et de sortie d'ions. L'acide aspartique en position 397 de la sous-unité NqrB a été remplacé par l'acide glutamique par mutagenèse dirigée. Les mesures d'activité enzymatique de cette protéine mutée montrent que la réduction de la quinone est stimulée par la présence de  $\text{Na}^+$  mais pas en présence de  $\text{Li}^+$  et de  $\text{K}^+$ . Comme pour la protéine sauvage, un dosage redox des cofacteurs montre qu'il n'y a plus de dépendance des potentiels de demi-vague des cofacteurs en fonction du type d'ions présents. La spectroscopie différentielle montre que le changement de conformation observé pour la protéine sauvage en présence de  $\text{Na}^+$  n'est plus observé par le mutant. Par ailleurs, les spectres différentiels obtenus en présence de  $\text{Li}^+$  et de  $\text{K}^+$  sont identiques. Ces résultats corroborent les analyses d'activité qui sont identiques en présence de  $\text{Li}^+$  et  $\text{K}^+$ . La cinétique d'échange H/D montre que cette enzyme est moins accessible au solvant en comparaison avec la protéine sauvage. Par ailleurs les cinétiques d'échange sont similaires en présence de  $\text{Li}^+$ ,  $\text{K}^+$  et  $\text{Rb}^+$ . De ces résultats l'importance de l'acide aspartique 397 est mise en évidence. Le rôle de ce résidu dans le transfert de  $\text{Na}^+$  est souligné. Une publication incluant la spectroscopie différentielle de la protéine sauvage et le mutant, ainsi que la cinétique d'échange H/D est en préparation.

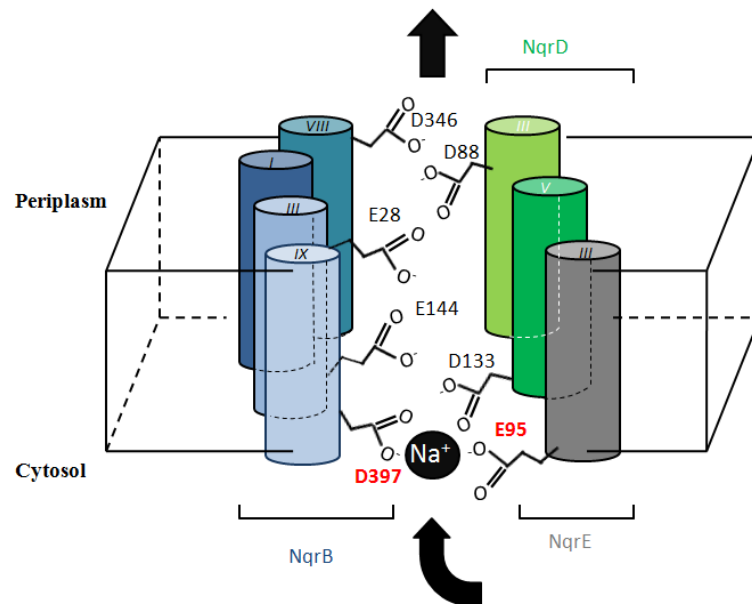


**Figure II: Représentation schématique des résidus acides qui forment le site d'attache des ions  $\text{Na}^+$ .**

La  $\text{Na}^+$ -NQR catalyse aussi la réduction à deux électrons de la quinone en quinol. Le site d'ancrage de la quinone est la cible d'inhibiteurs tels que le HQNO ou la korormicin. Les protéines résistant à ces inhibiteurs ont comme unique mutation la glycine 140 de la sous-unité NqrB. Pour l'étude du site d'ancrage de la quinone, le mutant G140A a été étudié où la glycine est remplacée par l'alanine. Un dosage redox des cofacteurs a mis en évidence la dépendance du  $\text{FMN}_C$  au type d'ions présents, comme pour la protéine sauvage. La spectroscopie IR différentielle du dernier cofacteur du chemin de transfert d'électron (la riboflavine) a été faite pour le mutant et pour la protéine sauvage. Ces analyses montrent clairement que la quinone n'est plus présente dans le mutant et confirme l'identification du site d'attache de la quinone. L'analyse du site quinone est encore en progression, notamment la spectroscopie différentielle en présence de l'inhibiteur HQNO.

### **Le complexe [cytochrome $c_{552}$ -fragment $\text{Cu}_A$ ] du *Thermus thermophilus***

Le cytochrome *c* transfère des électrons entre le complexe  $bc_1$  et la cytochrome *c* oxydase dans la mitochondrie. L'interaction entre ces molécules se fait par une reconnaissance à longue distance par des forces électrostatiques et un ajustement à courte distance par des interactions hydrophobes. Dans l'organisme *Thermus thermophilus*, l'interaction entre ces protéines se fait uniquement par des forces hydrophobes entre le cytochrome  $c_{552}$  et l'oxydase de type  $ba_3$ . Cette adaptation est une conséquence de l'environnement thermophilique de l'organisme car à température élevée les interactions électrostatiques sont fragilisées tandis que les interactions hydrophobes deviennent plus conséquentes. D'un point de vue expérimentale ce phénomène nous donne la possibilité de réaliser des mesures électrochimiques sans perturber la formation du complexe. Par ailleurs, pour simplifier les expériences seulement la partie soluble de l'oxydase de type  $ba_3$ , le fragment  $\text{Cu}_A$  a été étudié.

Le potentiel redox de l'hème du cytochrome  $c_{552}$  et du centre bi nucléaire de cuivre du fragment  $\text{Cu}_A$  ont été déterminés à pH 7 et 9. Dans la forme complexée, une chute de 90 mV du potentiel de l'hème de type *c* est observée. La spectroscopie différentielle en IR a permis de mettre en évidence que l'environnement des propionates de l'hème est perturbé dans la forme complexée. Précédemment la structure de ce complexe a été résolue par la spectroscopie RMN couplée à des techniques de modélisation moléculaire.

Ces analyses ont montré que les résidus qui sont les plus touchés par la formation du complexe sont ceux situés sur la surface d'interaction mais aussi Ala<sub>34</sub> et His<sub>32</sub> qui recouvre le groupement propionate A de l'hème à l'opposé de la surface de contact. Ces perturbations peuvent être à l'origine de cette différence de potentiel redox. Par ailleurs des analyses similaires réalisées sur le cytochrome *c* et le fragment Cu<sub>A</sub> de l'organisme *Parraccocus denitrificans*, où l'interaction est de type électrostatique, ont aussi montré que des résidus situés à proximité du propionate A sont perturbés lors de la formation du complexe. Mais dans ce cas l'ajout de sel perturbera la formation de ce complexe.

### **Le complexe *bc*<sub>1</sub>-*aa*<sub>3</sub> de l'organisme *Corynebacterium glutamicum***

Les éléments de la chaîne respiratoire forment des complexes intermoléculaires notamment pour faciliter le transfert d'électrons. Dans l'organisme *Corynebacterium glutamicum* un supercomplexe le *bc*<sub>1</sub>-*aa*<sub>3</sub> existe naturellement. Au lieu d'avoir deux complexes séparés, le complexe *bc*<sub>1</sub> et l'oxidase, il y a un super complexe où la navette cytochrome *c* est fusionnée directement dans le complexe. La caractérisation des potentiels redox des cofacteurs observables en UV-visible a été faite.

## Acknowledgements

I am indebted to Prof. Petra Hellwig who accepted me as a trainee in her laboratory during my master's degree five years ago. I am grateful for her patience, her kindness, her impeccable supervision and helpful advice.

I am grateful to my colleagues for their support; Sébastien Kriegel for being the perfect office neighbor, Michelle Yegres and Batoul Srour for their kindness, Thomas Meyer for his friendship, Julien Gross for his presence. I am also thankful to Aurélien Trivella for his help and training sessions for laser and cryogenic experiments. Laurent Fresmond is acknowledged for giving me an introduction to laboratory software and his support. I am thankful to Youssef El Khoury for his friendship. Ruth Hielscher, Nesrine Oueslati, Mariana Voicesu are warmly acknowledged for their support. I am thankful to Najat Chahboun and Arnaud Petrovich for their help. Lea Gisquet and Mireille Khalil are also acknowledged for their friendship. I am thankful to Martine Heinrich for an introduction to fluorescence spectroscopy and circular dichroism spectroscopy. Finally, I am indebted to Frédéric Melin for his words; most of the time full of wisdom, sometimes rich in fantasy.

I am thankful to Prof. Blanca Barquera and Oscar Juárez for providing samples, for their support, their kindness and most important of all for their friendship.

I would like to acknowledge thank Prof. Carola Hunte for accepting in her laboratory on a short training course. Thomas Kleinschroth and Christophe Wirth are thanked for their support, advice and friendship. I am grateful to Prof. Bernd Ludwig and Prof. James Fee for providing samples and valuable discussions. Unfortunately, Prof. James Fee left us after a long fight against disease.

I would like to thank the University of Strasbourg.

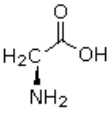
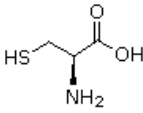
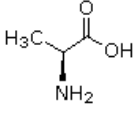
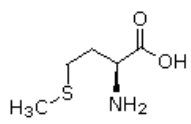
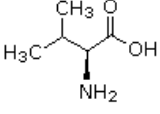
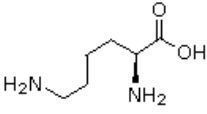
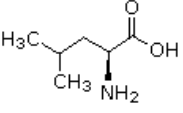
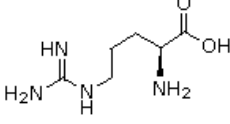
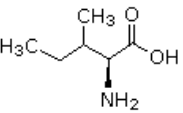
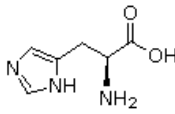
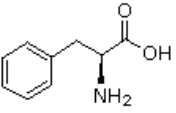
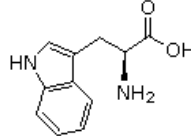
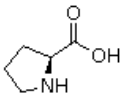
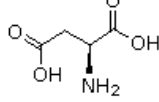
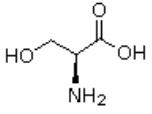
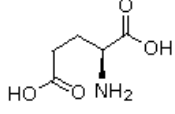
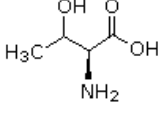
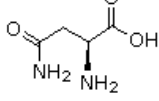
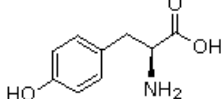
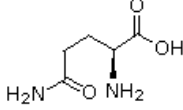
I am also indebted to my beloved wife Preeyam for her unconditional support each time I needed help. I am also thankful to my parents.

## Abbreviations and Nomenclature

$\nu_{as}$	Asymmetric stretching vibrational mode
$\nu_s$	Symmetric stretching vibrational mode
$\delta$	Bending vibrational mode
ABC	ATP binding cassette
Abs	Absorbance
ADP	Adenosine diphosphate
ATP	Adenosine triphosphate
ATR	Attenuated total reflection
Da	Dalton
DDM	n-dodecyl- $\beta$ -D-maltoside
EDTA	Ethylenediamine tetra-acetic acid
EPR	Electron paramagnetic resonance
FAD	Flavin adenine dinucleotide
2Fe-2S	Iron-sulfur center
FMN	Flavin mononucleotide
Fl	Oxidized flavin
$Fl^{\bullet-}$	Anionic flavosemiquinone
$FlH^-$	Anionic form of reduced flavin
$FlH^{\bullet}$	Neutral flavosemiquinone
$FlH_2$	Neutral form of reduced flavin
FT	Fourier transform
Glut	Glucose transporter
$H^+$ -NQR	$H^+$ translocating NADH:ubiquinone oxidoreductase, complex I
HDX	Hydrogen-Deuterium exchange
IR	Infrared
$K_M$	Michaelis constant
MCT	Mercury Cadmium Telluride
$Na^+$ -NQR	$Na^+$ -pumping NADH:ubiquinone oxidoreductase
$NAD^+$	Oxidized nicotinamide adenine dinucleotide
NADH	Reduced nicotinamide adenine dinucleotide
NDH-2	Type 2 NADH dehydrogenase
NMR	Nuclear magnetic resonance
Pi	Inorganic phosphate
PDB	Protein database
RNF	Rhodobacter nitrogen fixation proteins
Rf	Riboflavin
SHE	Standard hydrogen electrode
$T_m$	mid-point temperature

Tris	Tris(hydroxymethyl)aminomethane
UV	Ultraviolet
$\epsilon$	Molar extinction coefficient
$\lambda$	Wavelength

## The 20 common amino acids

Name	Formula	Abbreviations	Name	Formula	Abbreviations
Glycine		Gly G	Cysteine		Cys C
Alanine		Ala A	Methionine		Met M
Valine		Val V	Lysine		Lys K
Leucine		Leu L	Arginine		Arg R
Isoleucine		Ile I	Histidine		His H
Phenylalanine		Phe F	Tryptophan		Trp W
Proline		Pro P	Aspartic Acid		Asp D
Serine		Ser S	Glutamic Acid		Glu E
Threonine		Thr T	Asparagine		Asn N
Tyrosine		Tyr Y	Glutamine		Gln Q

## List of figures

Figure 1.1	Passive transport involves channel proteins and carrier proteins that translocate chemicals across the membrane following a concentration gradient. No energy is used for this mode of transport.	4
Figure 1.2	Active transport involves proteins that transport chemicals against a concentration gradient. The energy required for this mode of transport is obtained by either ATP or free energy released from electron transfer.	5
Figure 1.3	Schematic representation of a eukaryotic cell.	7
Figure 1.4	Brief representation of a prokaryotic cell.	7
Figure 1.5	Model of the respiratory chain	8
Figure 1.6	Proposed model for proton pumping in the respiratory complex I reproduced from (14).	9
Figure 1.7	$2e^- 2H^+$ reduction of $CoQ_8$	11
Figure 1.8	<i>Vibrio cholerae</i> possesses a single flagellum which is used for movement of the bacterium	14
Figure 1.9	The four main proteins involved in $Na^+$ transport across the membrane. $Na^+$ -NQR and $Na^+/H^+$ antiporter eject $Na^+$ from the cytoplasm resulting in a $Na^+$ gradient across the membrane. The $Na^+$ gradient is used by symporters for intake of amino acids. The rotational movement of the flagellum is also powered by the $Na^+$ gradient.	15
Figure 1.10	Schematic representation of the 6 sub-units (NqrA-F), the cofactors and the electron pathway in the $Na^+$ -NQR. $Na^+$ uptake occurs when electrons move from the 2Fe-2S center to the $FMN_C$ while $Na^+$ is released when electrons move from the riboflavin to ubiquinone.	18
Figure 1.11	The three types of flavins and atomic numbering.	19
Figure 1.12	The different redox transitions of flavins, reproduced from (108)	20
Figure 1.13	The redox transition of the flavins cofactors in the $Na^+$ -NQR with the pH dependence of the transitions	21
Figure 1.14	The electron pathway of the $Na^+$ -NQR	22
Figure 1.15	Quinone reduction activity measurements of the $Na^+$ -NQR in the presence of $Na^+$ , $Li^+$ , $K^+$ and $Rb^+$ at different ionic concentration, figure reproduced from (112)	23
Figure 1.16	Schematic representation of acidic residues on the cytosolic and periplasmic side of the membrane, and also spanning across the membrane. These residues are suggested to play an important role in $Na^+$ transfer across the membrane, figure reproduced from (89)	24
Figure 1.17	Suggested supercomplex from bovine respiratory chain including complex I (yellow), the dimeric complex III (red), cytochrome <i>c</i> (yellow) and complex IV (green), figure reproduced from (118).	25
Figure 1.18	Depending on oxygen availability, <i>Thermus thermophilus</i> can express two different terminal oxidases providing two alternatives for oxygen reduction	27
Figure 1.19	Structure of the $ba_3$ oxidase depicting the cofactors present (PDB 1EHK) (18)	28



Figure 1.20	Crystallographic structure of the Cu <sub>A</sub> fragment, the polypeptide consists mainly of anti-parallel $\beta$ -sheets and random structures (PDB 2CUA). The binuclear Cu center is represented in blue (136).	29
Figure 1.21	Schematic representation of the coordination of the binuclear Cu <sub>A</sub> center, reproduced from (136).	30
Figure 1.22	Structure of cytochrome <i>c</i> <sub>552</sub> centered by the c type heme (PDB 1C52) (17)	30
Figure 1.23	Structure of the complex [cytochrome <i>c</i> <sub>552</sub> -Cu <sub>A</sub> fragment] obtained by a combined NMR spectroscopic computational method (PDB 2FWL) (120)	32
Figure 1.24	The rod-shaped <i>Corynebacterium glutamicum</i> (145)	33
Figure 1.25	Schematic representation of the subunits and cofactors present in the <i>bc</i> <sub>1</sub> -aa <sub>3</sub> supercomplex, reproduced from (144).	35
Figure 2.1	Electromagnetic spectrum represented in terms of wavelength, frequency and energy. The changes induced at the molecular or atomic level. The expanded region is of interest in this work (154)	38
Figure 2.2	Representation of UV-visible interaction with a sample of a given concentration (C) and a molar absorption coefficient $\epsilon$ . $I_0$ is the incident radiation, and $I$ is the radiation that is not absorbed by the sample.	39
Figure 2.3	Simplified spring ball model to represent the harmonic oscillator.	40
Figure 2.4	Different uncoupled normal vibrational modes	41
Figure 2.5	Schematic representation of a Michelson interferometer (left). The interferogram of a monochromatic source (right) is a simple cosine curve (158).	42
Figure 2.6	The interferogram (left) is Fourier-transformed to obtain an absorption spectrum in terms of wavenumber (right).	43
Figure 2.7	Representation of the cytochrome <i>c</i> in an aqueous environment. In IR spectroscopy, contributions from the cofactor, the polypeptide backbone, the side chains and the buffer/solvent can be observed.	44
Figure 2.8	Absorption spectrum of a protein in solution in the mid-IR region depicting contributions of the amide bands and contribution from water.	45
Figure 2.9	Left panel depict a sample in H <sub>2</sub> O, with the water molecules in grey. Upon HDX, H on the surface of the molecule is exchanged to D (stick model cyan); whereas H located in the hydrophobic core are not exchanged (stick model blue).	47
Figure 2.10	Representation of a 3 electrode setup	49
Figure 2.11	The absorption spectra of the oxidized and reduced form are similar. The difference spectrum is obtained by subtraction the spectrum of the reduced form of the enzyme from the spectrum of the oxidized enzyme.	50
Figure 3.1	Schematic representation of the electrochemical cell. The blue arrow shows the optical axis.	54
Figure 3.2	Schematic representation of the gold surface modified by cysteamine and mercaptopropionic acid	55

Figure 3.3	On the left panel, the difference spectra of cytochrome $c_{552}$ from -400 mV to +200 mV for a reductive titration. On the right panel, the plot of $\Delta$ absorbance recorded at 552 nm against the applied potential, a Nernst equation is fitted (black curve).	57
Figure 3.4	Schematic representation of the Bruker Bio ATR 2 dialysis system	60
Figure 3.5	Integration of signals arising from the $\nu(\text{O-H})$ 3800-2750 $\text{cm}^{-1}$ , the $\nu(\text{O-D})$ 2750-2000 $\text{cm}^{-1}$ and the $\nu(\text{C-H})$ 3000-2750 $\text{cm}^{-1}$ with baseline correction.	62
Figure 3.6	Fraction of $\text{H}_2\text{O}$ , $\text{D}_2\text{O}$ and HOD present in the sample at a given time $t$ .	63
Figure 3.7	Buffer subtraction from the recorded data, and the normalization step with respect to the amide I band.	64
Figure 3.8	Integration of the amide I and amide II band.	64
Figure 3.9	3D plot of the amide I and amide II band after buffer subtraction and normalization	65
Figure 3.10	Baseline correction is performed by subtracting a straight line between 1710 and 1595 $\text{cm}^{-1}$	66
Figure 3.11	The second derivative of the amide I band gives minima that correspond to the components present. Band separation is performed on the amide I signature by fitting multi Gaussian curves. The relative area of each component correspond to the % of a secondary structure in the protein.	67
Figure 4.1.1	Evolution of the spectral contribution of the cofactors from the $\text{Na}^+$ -NQR upon reduction	69
Figure 4.1.2	Absorbance change upon reduction monitored at 460 nm (left). Plot of the first derivative of $\Delta$ Abs vs. applied potential for each 5 nm from 350-650 nm (right).	70
Figure 4.1.3	Redox titration of the $\text{Na}^+$ -NQR monitored at 560, 460 and 380 nm. Samples were studied in the presence of $\text{Li}^+$ , $\text{Na}^+$ , $\text{K}^+$ , $\text{Rb}^+$ and $\text{NH}_4^+$ (from top to bottom).	72
Figure 4.1.4	The plot of the first derivative of the difference in absorbance vs. applied potential from 350 to 650 nm for each 5 nm in the presence of $\text{Na}^+$ ions (red) and in the presence of $\text{K}^+$ ions (blue).	74
Figure 4.1.5	The difference spectra for the potential range -275 mV to -50 mV, -400 mV to -275 mV and -620 mV to -400 mV, in the presence of $\text{Na}^+$ ions (red) and $\text{K}^+$ ions (blue)	74
Figure 4.1.6	Redox mid-point potential of the cofactors involved in electron transfer in the $\text{Na}^+$ -NQR	75
Figure 4.1.7	Oxidized-reduced difference spectra of FAD, FMN and riboflavin.	78
Figure 4.1.8	Oxidized-reduced difference spectrum for the potential range -620 to +200 mV of the $\text{Na}^+$ -NQR (red) in the presence of $\text{Na}^+$ ions and FAD (black) in $\text{H}_2\text{O}$ buffer.	79
Figure 4.1.9	Oxidized-reduced difference spectrum for the potential range -620 to +200 mV of the $\text{Na}^+$ -NQR (blue) in the presence of $\text{Na}^+$ ions and FAD (black) in $\text{D}_2\text{O}$ buffer	79
Figure 4.1.10	Oxidized-reduced difference spectra for the potential range -620 to +200 mV of the $\text{Na}^+$ -NQR in $\text{H}_2\text{O}$ buffer in the presence of $\text{Li}^+$ (red), $\text{K}^+$ (blue) and $\text{Rb}^+$ (green) ions. The overlaid spectrum was obtained in the presence of $\text{Na}^+$ ions.	82
Figure 4.1.11	Oxidized-reduced difference spectra for the potential range -620 to +200 mV of the $\text{Na}^+$ -NQR in $\text{D}_2\text{O}$ buffer in the presence of $\text{Li}^+$ (red), $\text{K}^+$ (blue) and $\text{Rb}^+$ (green) ions. The	82

overlaid spectrum was obtained in the presence of  $\text{Na}^+$  ions.

Figure 4.1.12	Double difference spectra in $\text{H}_2\text{O}$ buffer obtained by interactive subtraction.	84
Figure 4.1.13	Double difference spectra in $\text{D}_2\text{O}$ buffer obtained by interactive subtraction	84
Figure 4.1.14	Double difference spectra $\text{Li}^+\text{-K}^+$ and $\text{Na}^+\text{-K}^+$ in the spectral region between 1500 and 1300 $\text{cm}^{-1}$ for samples in $\text{H}_2\text{O}$ and $\text{D}_2\text{O}$ buffer depicting the ion dependency of signals attributed to $\nu_s(\text{COO}^-\text{M}^+)$ .	86
Figure 4.1.15	HDX of the $\text{Na}^+\text{-NQR}$ in the presence of $\text{Na}^+$ and phospholipids monitored by probing the decrease of the amide II contribution.	89
Figure 4.1.16	: HDX of the $\text{Na}^+\text{-NQR}$ in the presence of $\text{Na}^+$ ions, phospholipids and either 1mM NADH (red) or 1 mM $\text{Na}_2\text{SO}_4$ (blue).	90
Figure 4.1.17	Figure 4.1.17 : HDX of the $\text{Na}^+\text{-NQR}$ in the presence of phospholipids and either $\text{Li}^+$ (red), $\text{Na}^+$ (blue), $\text{K}^+$ (black) and $\text{Rb}^+$ (green) ions.	92
Figure 4.1.18	Band deconvolution of the amide I signature in the presence of $\text{Na}^+$ and $\text{K}^+$ , and after addition of phospholipids to the sample	93
Figure 4.1.19	CD spectra of the $\text{Na}^+\text{-NQR}$ in the presence of $\text{Na}^+$ and $\text{K}^+$ ions and with/without phospholipids.	94
Figure 4.2.1	Redox titration of the NqrB D397E mutant protein monitored at 560, 460 and 380 nm. Samples were studied in the presence of $\text{Na}^+$ , $\text{Li}^+$ , $\text{K}^+$ and $\text{Rb}^+$ ions (from top to bottom).	98
Figure 4.2.2	Redox induced FTIR difference spectra of the NqrB D397E mutant enzyme in the presence of $\text{Na}^+$ ions (red) and FAD (black) for the potential range between -620 mV to +200 mV	100
Figure 4.2.3	Redox induced FTIR difference spectra of the NqrB D397E mutant enzyme in the presence of $\text{Li}^+$ ions (red), $\text{K}^+$ ions (blue), $\text{Rb}^+$ ions (green) and in the presence of $\text{Na}^+$ ions (black) for the potential range between -620 mV to +200 mV.	100
Figure 4.2.4	Double difference spectra of the NqrB D397E mutant enzyme prepared with the different salts.	102
Figure 4.2.5	Double difference spectra $\text{Li}^+\text{-K}^+$ and $\text{Na}^+\text{-K}^+$ in the spectral region between 1500 and 1300 $\text{cm}^{-1}$ of the NqrB D397E mutant enzyme and the wild type protein	103
Figure 4.2.6	NqrB D397E mutant – wild type double difference spectra of samples prepared in the presence of $\text{Na}^+$ , $\text{Li}^+$ , $\text{K}^+$ and $\text{Rb}^+$ ions	105
Figure 4.2.7	HDX kinetics of the NqrB D397E mutant enzyme in the presence of $\text{Li}^+$ , $\text{Na}^+$ , $\text{K}^+$ and $\text{Rb}^+$ ions.	107
Figure 4.2.8	Redox titration of the NqrE E95Q mutant enzyme monitored at 560, 460 and 380 nm in the presence of $\text{Li}^+$ , $\text{Na}^+$ and $\text{K}^+$ ions	109
Figure 4.2.9	Reduced minus oxidized difference spectra of the D397S mutant enzyme after 2 washes and 3 washes through centrifugal membranes.	110

Figure 4.2.10	Absorption spectra of the air oxidized form (blue) and the Na <sub>2</sub> SO <sub>4</sub> reduced state of the wild type enzyme, and the oxidized minus reduced difference spectrum (black).	111
Figure 4.2.11	Absorption spectra of the air oxidized form (blue) and the Na <sub>2</sub> SO <sub>4</sub> reduced state of the NqrE E95A enzyme, and the oxidized minus reduced difference spectrum (black).	111
Figure 4.3.1	Redox titration of the NqrB G140A mutant enzyme monitored at 560, 460 and 380 nm in the presence of Na <sup>+</sup> and K <sup>+</sup> ions	113
Figure 4.3.2	Redox induced difference spectra of the NqrB G140A mutant enzyme (red) and the wild type (blue) for the potential range from -620 to +200 mV in the presence of Na <sup>+</sup> ions	115
Figure 4.3.3	Wild type – G140A double difference spectrum for the potential range between -620 mV to +200 mV	115
Figure 4.3.4	Redox induced difference spectra of the wild type protein (red) and the NqrB G140A mutant enzyme (blue) for the potential step between -280 mV to +200 mV in H <sub>2</sub> O buffer	117
Figure 4.3.5	Redox induced difference spectra of the wild type protein (red) and the NqrB G140A mutant enzyme (blue) for the potential step between -280 mV to +200 mV in D <sub>2</sub> O buffer	117
Figure 4.3.6	Wild type – NqrB G140A double difference spectra for the potential step between -280 mV to +200 mV in H <sub>2</sub> O (red) and D <sub>2</sub> O (blue).	120
Figure 4.3.7	Redox induced difference spectra of the wild type enzyme (red) and the NqrB G140A mutant (blue) in the presence of HQNO for the potential range between -280 mV to +200 mV	121
Figure 4.3.8	Amide I deconvolution of the wild type protein and the NqrB G140A mutant enzyme	122
Figure 4.4.1	Titration of cytochrome <i>c</i> <sub>552</sub> from -250 mV to +300mV (left). The difference in absorbance observed at 552 nm is plotted against the applied potential (right).	124
Figure 4.4.2	Crystallographic structure of cytochrome <i>c</i> <sub>552</sub> from <i>Thermus thermophilus</i> (PDB 1C52) depicts the absence of water molecules in the inner core compared to horse heart cytochrome <i>c</i> , PDB 1HRC (18, 48)	125
Figure 4.4.3	Redox titration monitored from +200 mV to -150 mV for the Cu <sub>A</sub> fragment (left). The difference in absorbance at 530 nm was plotted against the applied potential to determine the mid-point potential	126
Figure 4.4.4	Reduced minus oxidized difference spectra (bold) in the UV-visible spectral domain for the potential range between -300 mV to +300 mV of the Cu <sub>A</sub> fragment (black), cytochrome <i>c</i> <sub>552</sub> (blue) and the complex [cyt. <i>c</i> <sub>552</sub> -Cu <sub>A</sub> fragment] (red).	127
Figure 4.4.5	A -90 mV shift is observed in the mid-point potential of cytochrome <i>c</i> <sub>552</sub> in the complex.	127
Figure 4.4.6	Oxidized minus reduced difference spectra of cytochrome <i>c</i> <sub>552</sub> at pH 7 (bleu) and pH 9 (red) for the potential step between -300 mV to +300 mV	128
Figure 4.4.7	Oxidized minus reduced difference spectra of the Cu <sub>A</sub> fragment at pH 7 (blue) and 9 (red) for the potential range between -300 mV to +300 mV	129

Figure 4.4.8	Oxidized minus reduced difference spectra of the complex [cytochrome $c_{552}$ -Cu <sub>A</sub> fragment] at pH 7 (blue) and pH 9 (red) for the potential range between -300 mV to +300 mV	131
Figure 4.4.9	Double difference spectra obtained by interactive subtraction of the spectrum of the Cu <sub>A</sub> fragment from the spectrum of the complex, at pH 7 (blue) and pH 9 (red). Data in black are the corresponding difference spectra of cytochrome $c_{552}$ .	131
Figure 4.4.10	3-dimensional structure of the complex (PDB 2FWL) depicting His <sup>32</sup> and Arg <sup>125</sup> which are suggested to form a hydrogen bonding network with the propionate A (69).	133
Figure 4.5.1	Redox induced difference spectrum of the $bc_1$ - $aa_3$ supercomplex in the UV-visible domain for the potential range between -650 mV to +250 mV	135
Figure 4.5.2	Reductive titration of the $bc_1$ - $aa_3$ supercomplex from +250 mV to -650 mV	136
Figure 4.5.3	Evolution of the difference spectrum in the UV-visible depicting the appearance of signals attributed to the $a$ (600 nm), $b$ (565 nm) and $c$ (550 nm) type hemes	136
Figure 4.5.4	Reductive (left) and oxidative (right) titration of the $a$ hemes in the $bc_1$ - $aa_3$ supercomplex monitored at 600 nm.	137
Figure 4.5.5	Reductive (left) and oxidative (right) titration of the $c$ hemes in the $bc_1$ - $aa_3$ supercomplex monitored at 550 nm	138
Figure 4.5.6	Reductive (left) and oxidative (right) titration of the $b$ hemes in the $bc_1$ - $aa_3$ supercomplex monitored at 565 nm.	139

## List of tables

Table 1.1	Summary of the redox cofactors present in the Na <sup>+</sup> -NQR	21
Table 2.1	Amide contribution of the polypeptide backbone in the mid-IR region	44
Table 2.2	Protein secondary structure is probed by band separation of the amide I band. Each element can be observed at specific wavenumbers.	45
Table 2.3	Band shift observed upon hydrogen/deuterium exchange.	48
Table 3.1	19 mediators used for electrochemical measurements and their corresponding mid-point potential (60)	56
Table 3.2	The potential range, the potential step and equilibration time used for each sample studied.	57
Table 3.3	The potential applied for oxidation and reduction, and equilibration time for each sample studied	59
Table 4.1.1	Molar extinction coefficients of all the cofactors of the Na <sup>+</sup> -NQR at 380, 460 and 560 nm (130)	71

Table 4.1.2	Summary of the redox mid-point potentials of the cofactors present in the Na <sup>+</sup> -NQR in the presence of Li <sup>+</sup> , Na <sup>+</sup> , K <sup>+</sup> , Rb <sup>+</sup> and NH <sub>4</sub> <sup>+</sup> ions.	73
Table 4.1.3	HDX kinetics of the Na <sup>+</sup> -NQR with and without phospholipids	88
Table 4.1.4	HDX kinetics of the Na <sup>+</sup> -NQR in the air oxidized state, the Na <sub>2</sub> SO <sub>4</sub> reduced state and the NADH reduced state	90
Table 4.1.5	HDX constants of the Na <sup>+</sup> -NQR obtained in the presence of Li <sup>+</sup> , Na <sup>+</sup> , K <sup>+</sup> and Rb <sup>+</sup> ions.	92
Table 4.1.6	Secondary structure composition of the Na <sup>+</sup> -NQR in the presence of Na <sup>+</sup> and K <sup>+</sup> ions and the effect of phospholipids.	93
Table 4.1.7	Band deconvolution of the CD data gives an estimation of the secondary structure of the Na <sup>+</sup> -NQR	94
Table 4.2.1	Midpoint potential of the cofactors present in the D397E mutant enzyme in the presence of Li <sup>+</sup> , Na <sup>+</sup> , K <sup>+</sup> and Rb <sup>+</sup> ions.	97
Table 4.2.2	HDX constants of the NqrB D397E mutant enzyme and the wild type protein obtained in the presence of Li <sup>+</sup> , Na <sup>+</sup> , K <sup>+</sup> and Rb <sup>+</sup> ions.	107
Table 4.2.3	Midpoint potentials of the cofactors in the NqrE E95Q mutant enzyme in the presence of Li <sup>+</sup> , Na <sup>+</sup> and K <sup>+</sup> ions.	108
Table 4.3.1	Mid-point potentials of the redox cofactors present in the NqrB G140A mutant enzyme in the presence of Na <sup>+</sup> and K <sup>+</sup> ions.	114
Table 4.3.2	Secondary structure of the wild type protein and the NqrB G140A mutant enzyme determined by deconvolution of the amide I band.	122
Table 4.5.1	The mid-point potentials of the hemes present in the <i>bc</i> <sub>1</sub> - <i>aa</i> <sub>3</sub> supercomplex from <i>Corynebacterium glutamicum</i> .	139
Table 4.5.2	Comparison of the redox potential of the hemes from the <i>bc</i> <sub>1</sub> - <i>aa</i> <sub>3</sub> supercomplex from <i>Corynebacterium glutamicum</i> with analogues from <i>Paracoccus denitrificans</i>	140

## **Publications**

### Published Articles

1. Thermodynamic contribution to the regulation of electron transfer in the Na<sup>+</sup>-pumping NADH:quinone oxidoreductase from *Vibrio cholerae*, *Biochemistry* (2012) 51, 4072-4077  
Yashvin Neehaul, Oscar Juárez, Blanca Barquera and Petra Hellwig
  
2. Electrochemical and infrared spectroscopic analysis of the interaction of the Cu<sub>A</sub> domain and cytochrome *c*<sub>552</sub> from *Thermus thermophilus*, *Biochimica et Biophysica Acta (BBA) Bioenergetics* (2012)  
<http://dx.doi.org/10.1016/j.bbabo.2012.02.027>  
Yashvin Neehaul, Ying Chen, Carolin Werner, James A. Fee, Bernd Ludwig, Petra Hellwig
  
3. The role of glycine residues 140 and 141 of subunit B in the functional ubiquinone binding site of the Na<sup>+</sup>-pumping NADH:quinone oxidoreductase from *Vibrio cholerae*, *Journal of Biological Chemistry* (2012) 287, 25678-25685.  
Oscar Juárez, Yashvin Neehaul, Erin Turk, Najat Chaboun, Petra Hellwig, Blanca Barquera

Articles in preparation:

1. “IR spectroscopic evidence on the role of D397 in the ion pumping in the Na<sup>+</sup> pumping NADH:quinone oxidoreductase from *V. cholerae*”  
Yashvin Neehaul Oscar Juárez, Blanca Barquera, Petra Hellwig
  
2. “Purification and characterization of the *bc*<sub>1</sub>-*aa*<sub>3</sub> super complex from *Corynebacterium glutamicum*”

# **Chapter I: Introduction**



## 1.0 Abstract

The field of molecular bioenergetics deals with the energy transduction in biological cells. Biochemical, spectroscopic and crystallographic studies gave insight into enzymes structure and mechanism. Important questions are open on the interaction of these enzymes, their diversity and their role in metabolism.

In this project, respiration and more specifically proton and sodium pumping enzymes have been in focus. Three main axes can be distinguished in this thesis report.

First we have been interested in the  $\text{Na}^+$ -pumping NADH:quinone reductase which is the entry site of electrons in the respiratory chain of several pathogens. The role of specific flavin cofactors and amino acids involved in  $\text{Na}^+$  transfer has been shown.

Then the interaction between proteins, namely the cytochrome  $c_{552}$  and the  $\text{Cu}_A$  fragment from the terminal  $ba_3$  oxidase from the organism *Thermus thermophilus* was investigated. Structural reorganization during electron transfer was revealed.

Finally, in the third part of the project the interaction within the  $bc_1$ - $aa_3$  supercomplex from the respiratory chain from *Corynebacterium glutamicum* was analyzed.

All these enzymes are membrane proteins and part of the large family of transport systems that rule life.

## **1.1 Ion transport across membranes**

The cell is the basic unit structure in living organisms. A simplified representation of a cell is a compartment of chemicals capable of surviving and of replicating itself. Without a barrier separating the inner compartment from the outer environment, vital molecules will diffuse freely, life will not exist. The barrier, known as the cell membrane, is a phospholipid bilayer, with hydrophilic phosphate head groups on both aqueous sides of the membrane and hydrophobic tails in the middle of the membrane. Proteins are also present as integral membrane proteins or partially embedded in the membrane. The general model accepted for the phospholipid membrane is the ‘fluid mosaic model’ proposed by Singer and Nicolson in 1972 (1). In this model, the proteins freely float in the membrane. Recent studies suggested that the phospholipid membrane is more mosaic than fluid; with certain areas rich in proteins, others rich in glycolipids and with variable thickness (2). All these properties are related to the function of the cell.

The membrane is impermeable to polar molecules such as glucose, ions and water. However, transport across the membrane is important to obtain nutrients, to excrete wastes, to maintain a suitable pH for the cell and also to secrete useful substances. Bulk transport, such as endocytosis and exocytosis involving formation of phospholipid vacuoles, participate in chemical communication with the outside of the cell. Other transport mechanisms involving transmembrane proteins also control the entry and exit of polar chemicals.

Transport across the membrane involving proteins is classified into two categories, passive transport and active transport. In the former mechanism, transport is based on diffusion (and facilitated diffusion) that is the movement of molecules and ions from a region of high concentration to a region of lower concentration ([figure 1.1](#)). The higher the difference in concentration, the faster is the process. Two different groups of proteins are involved in passive transport; channel proteins and carrier proteins. Channel proteins are considered as gates with free entrance and/or exit of molecules and ions. Nevertheless, these channel proteins are selective for specific chemicals. For example the  $K^+$  channel from *Streptomyces lividans* is 10,000 times less permeable for small cations such as  $Li^+$  and  $Na^+$  as compared to  $K^+$  ions (3). The structure of the  $K^+$  channel also revealed that the  $K^+$  ions are aligned in the protein across the membrane and up to 3 ions can be present at the same time. Channel proteins are classified according to the stoichiometry of transport

(4, 5). Uniport involves the transfer of one molecule at a time whereas symport involves the simultaneous transfer of two different molecules across the membrane in the same direction. The last group of channel proteins involves transporters which transfer two molecules in the opposite direction of the membrane. They are called antiport channel proteins and are also known as exchangers. The most studied are the  $\text{Na}^+/\text{H}^+$  antiporter and the  $\text{K}^+/\text{H}^+$  antiporter from the mitochondrion. During function,  $\text{H}^+$  is removed from the inner compartment as  $\text{K}^+$  and  $\text{Na}^+$  enter (6).

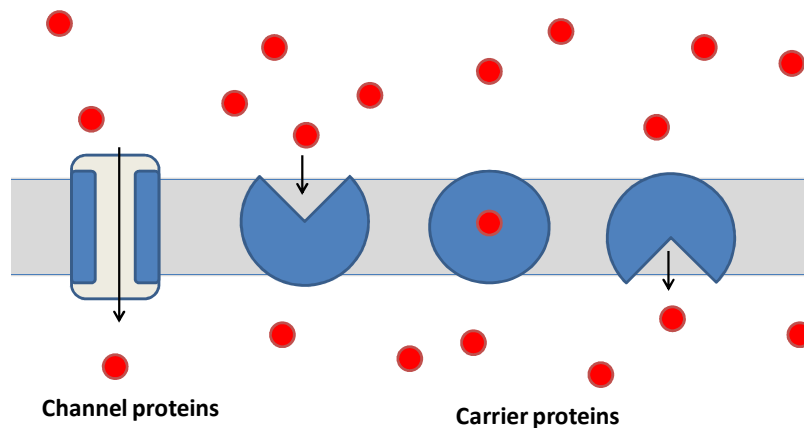


**Figure 1.1: Passive transport involves channel proteins and carrier proteins that translocate chemicals across the membrane following a concentration gradient. No energy is used for this mode of transport.**

Channel proteins remain in a unique conformation whereas the other proteins involved in transport like carrier proteins undergo conformational changes in order to translocate molecules across the membrane. The most studied carrier protein studied is the glucose transporter (Glut) (7). Glut is present in multicellular organisms and at a lesser level in unicellular organisms. This integral membrane protein is of great interest as insulin stimulates the production and excretion by exocytosis of Glut which increases the rate of glucose entry in muscle cells and adipocytes (8).

Active transport is another possibility by which polar molecules move across biological membranes. Here, the molecules or ions are transported against a concentration gradient and energy is required (figure 1.2). Several proteins use active transport, for example the ATP Binding Cassette (ABC) transporter family that includes more than 50 proteins. ABC transporters are involved both in import and export of molecules across the membrane, and the energy required is obtained from dephosphorylation of adenosine triphosphate (ATP) (9). Present in eukaryotes and prokaryotes, these proteins are specific to the molecule transported, which can be ions such as  $\text{Fe}^{3+}$  and  $\text{Cl}^-$ , polysaccharides,

peptides, vitamins and a wide variety of toxins (10). 5% of the genetic material from *Escherichia coli* codes for such transporters, reflecting the importance of ABC transporters (11). Proteins involved in transport across membrane are encoded by almost 20% of the genes from *Escherichia coli* (11).

Free energy released by electron transfer is also used for translocation. For example in the respiratory complex I, electrons are funneled from reduced nicotinamide adenine dinucleotide (NADH) to quinone. The free energy released in the process is used to transfer  $H^+$  ions across the membrane and to form a proton gradient which is the primary event in energy conservation of the cell. This pH gradient is used for a variety of processes, the most important being the synthesis of ATP.

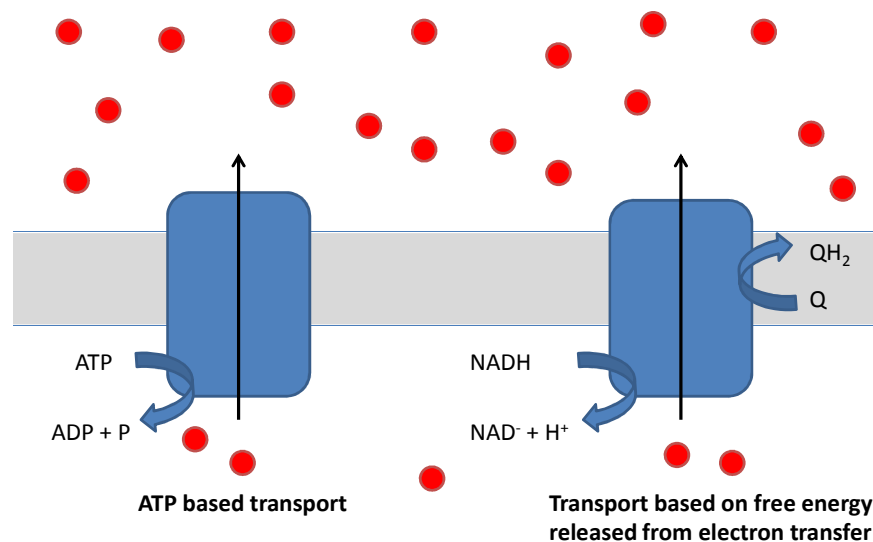


**Figure 1.2: Active transport involves proteins that transport chemicals against a concentration gradient. The energy required for this mode of transport is obtained by either ATP or free energy released from electron transfer.**

The proton gradient is part of the bioenergetics studies that made a turning point in 1961 when Mitchell proposed the chemiosmotic hypothesis of energy conservation (12). In 1978, he was awarded the Nobel prize for his work which was later summarized in 4 postulates (13):

1/ ATPase systems are hydro-dehydration proteins specific to water and ATP that couple the reversible flow of  $H^+$  across the membrane to the synthesis of ATP from ADP and  $P_i$ .

2/ The respiratory chain located in the membrane couples electron-flow between substrates of different redox potentials to  $H^+$ -translocation across the membrane. These membrane bound enzymes contribute to the  $H^+$ -gradient across the membrane that is then used by the ATP synthase.

3/ Exchange proteins transport anions against an  $OH^-$  gradient and cations against a  $H^+$  gradient in order to maintain the osmotic difference across the membrane. These proteins also allow the entrance of metabolites without collapsing the membrane potential.

4/ The enzymes involved in postulates 1, 2 and 3 are located in membranes with low permeability to ions and  $H^+$ .

In this work, enzymes from the respiratory chain of different organisms are studied. Notably we focus on  $Na^+$  and  $H^+$  pumps.

## **1.2 Cellular respiration**

Eukaryotic cells have different cytoplasmic compartments, such as the nucleus, endoplasmic reticulum, the golgi apparatus and the mitochondrion ([Figure 1.3](#)). All these compartments are separated from the cytosol by phospholipids membranes. Prior to the respiratory chain, nutrients are catabolised through the glycolysis process that occurs in the cytoplasm. For example glucose is broken down to pyruvate molecules. The latter enter the matrix of the mitochondrion and are transformed into acetyl coenzyme A molecules. These small molecules enter the Krebs cycle. This cycle was described by Hans Krebs who was awarded the Nobel Prize in 1953 for his discovery. This step occurs in the matrix of the mitochondrion. From this cycle, small reduced coenzymes such as the NADH are formed. The small molecules are the electron source for the respiratory chain located on the inner membrane of the mitochondrion. The respiratory chain is formed by a group of membrane proteins that couples electron transfer from reduced coenzymes to the last electron acceptor, oxygen to proton transfer across the membrane.

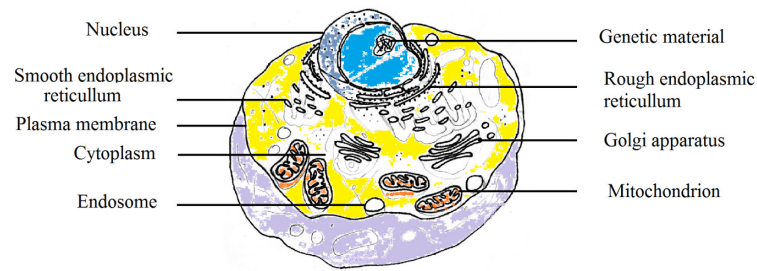


**Figure 1.3: Schematic representation of a eukaryotic cell.**

Prokaryotic cells are simpler and smaller compared to eukaryotes ([Figure 1.4](#)). Although the same processes are involved in energy production, glycolysis and the Krebs cycle occur in the cytoplasm. The respiratory chain is located on the cytoplasmic membrane.

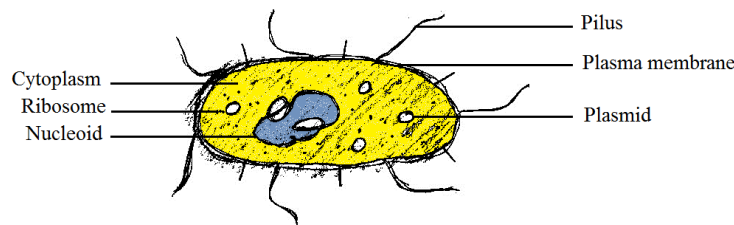


**Figure 1.4: Brief representation of a prokaryotic cell.**

### 1.2.1 The respiratory chain

The respiratory chain consists of membrane proteins that funnel electron transfer to oxygen; the free energy released is used to pump protons across the membrane hence participating in setting up the proton gradient. Enzymes are proteins with specific catalytic activity. The cofactors found in the respiratory complexes are iron sulfur clusters, flavins, hemes, copper centers and quinones.

[Figure 1.5](#) shows a schematic representation of a model bacterial respiratory chain. The reduced coenzyme NADH is the electron donor to the respiratory chain. These electrons are transferred to the different enzymes in the respiratory chain as the potential of the redox active cofactors increase. The final electron acceptor is oxygen which is reduced to water. The electron transfer is coupled to proton transfer across the membrane, setting up a proton gradient. Finally ATP synthase uses this proton gradient to synthesize ATP from ADP and inorganic phosphate.

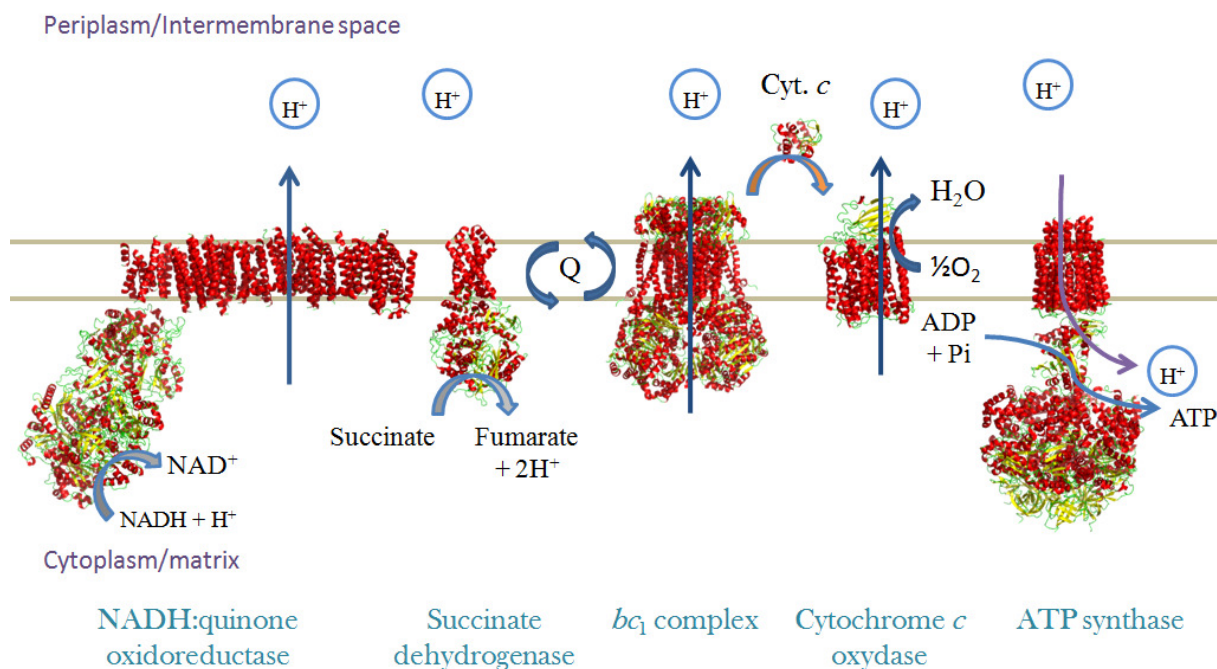


Figure 1.5: Model of the respiratory chain. From left to right: NADH:quinone oxidoreductase from *T. thermophilus* (pdb 3M9S) (14), succinate dehydrogenase from *E. coli* (pdb 1NEK) (15),  $bc_1$  complex from chicken (pdb 1BCC) (16), cytochrome  $c_{552}$  from *T. thermophilus* (pdb 1C52) (17),  $ba_3$  oxidase from *T. thermophilus* (pdb 1EHK) (18), ATP synthase from yeast mitochondrion (pdb 1QO1) (19).

### 1.2.1.1 NADH dehydrogenase superfamily

NADH dehydrogenase enzymes form a superfamily consisting of three groups (20). These enzymes form one of the major entry sites of electrons in the respiratory chain. The  $H^+$  translocating NADH:ubiquinone oxidoreductase ( $H^+$ -NQR) also termed as the respiratory complex I, links the oxidation of NADH ( $E_m = -320$  mV) to the reduction of ubiquinone ( $E_m = +90$  mV). The free energy released couples translocation of  $4H^+$  across the membrane (21, 22).

The  $H^+$ -NQR remains the largest enzymatic complex of the respiratory chain. The mitochondrial  $H^+$ -NQR has an approximate mass of 1MDa for 41 subunits. The prokaryotic analogue is much smaller with only 14 subunits and a mass around 530 kDa (23). These 14 subunits are considered as the minimal structure of the complex I. The protein has an L-shaped structure, with a hydrophobic membrane bound part and a hydrophilic cytosolic domain. The latter contains all known redox active cofactors.

The hydrophilic domain of the complex I from the bacterial organism *Thermus thermophilus* (pdb 319V) shows that the cofactors involved are 9 iron sulphur clusters and





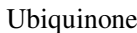
of 50-60 kDa and consists of a single chain(26). Another particularity of the NDH-2 is that it does not pump protons across the membrane, nevertheless the enzyme catalyses the oxidation of NADH and the reduction of ubiquinone (27). The isoprenoid tail of ubiquinone is hydrophobic, however the head group can diffuse freely in the phosphodiester surface of the membrane and interact with the NDH-2. Usually a unique cofactor is present in the NDH-2 which can either be FAD or FMN (26, 28). The third group of NADH dehydrogenases is the  $\text{Na}^+$ -pumping NADH:ubiquinone oxidoreductase ( $\text{Na}^+$ -NQR). A detailed description of this enzyme is given in [section 1.3](#).

#### 1.2.1.2 Succinate:ubiquinone oxidoreductase

Also known as the complex II, succinate:ubiquinone oxidoreductase catalyses electron transfer from succinate which is reduced to pyruvate, to ubiquinone (29, 30). Complex II is the second entry site of electrons in the respiratory chain and also participates to the Krebs cycle. Typically, it includes iron-sulfur clusters, FAD and a *b*-type heme (30). However the exact composition varies in function of the organism. This protein is the only respiratory complex that does not pump  $\text{H}^+$  across the membrane. Ubiquinone is reduced to ubiquinol and is delivered in the membrane quinone pool. In anaerobic respiration, a homologous enzyme fumarate reductase accepts electrons from the quinone pool and catalyses the reduction of fumarate which is the last electron acceptor into succinate (31, 32).

#### 1.2.1.3 Quinone pool

Ubiquinone is reduced to ubiquinol by the respiratory complexes I, II and IV. In some organisms, complex IV can also reduced ubiquinone. Also known as the coenzyme Q (CoQ), ubiquinone consists of a 2,3-dimethoxy-5-methylpara-benzoquinone ring (33, 34). On the 6<sup>th</sup> position of the ring, a long isoprenoid tail is present. If there are ten isoprenoid group present, the coenzyme is denominated  $\text{CoQ}_{10}$ . The longer the isoprenoid tail, the more hydrophobic is the molecule. Due to its high hydrophobicity, quinones are mainly found in the membrane. Generally, the head group of ubiquinone is attached by hydrogen bonding interactions of the  $\text{C}=\text{O}$ . The long isoprenoid tail interacts with the hydrophobic domain of proteins that are generally transmembrane helices.



In an aqueous environment, reduction of ubiquinone leads to ubiquinol. In the absence of  $H^+$ , the unstable semiquinoid radical form can also be produced (35). These semiquinones can be stabilized when anchored to specific binding-sites of respiratory enzymes. Quinones bind to proteins mainly by hydrophobic interaction of the isoprenoid tail and by hydrogen bonds of the oxygen atoms present on the head group. A wide variety of quinone binding sites with little similarity are reported (36-38). Reduced and released by the respiratory complex I and II, ubiquinol transfers electrons to the  $bc_1$  complex (34).

The  $bc_1$  complex is the third complex of the respiratory chain. The first structure resolved for this enzyme was from chicken and consists of 11 sub-units, 3 of which contain the redox active cofactors (16). The Rieske protein contains a 2Fe-2S cluster. Cytochrome  $b$  contains two  $b$  types hemes, heme  $b_L$  and heme  $b_H$ , and cytochrome  $c_1$  contains a  $c$  type heme. Biochemical, spectroscopic and crystallographic studies contributed to the comprehension of the mechanism of electron transfer in this enzyme (39-45).

11

cytoplasm, 2  $H^+$  are translocated across the membrane and two are used for reduction of ubiquinone, while two electrons are donated one at a time to cytochrome *c* (47-49).

#### 1.2.1.5 Cytochrome *c*

Cytochrome *c* is a small soluble protein centered by a *c*-type heme. The crystal structure of this protein is available from a wide variety of organism and show that the protein consists mainly of  $\alpha$ -helices and random structures (50, 51). The function of the cytochrome *c* is to transport electrons one from the  $bc_1$  complex to the cytochrome *c* oxidase. The interaction between cytochrome *c* and its redox partners is governed by long range electrostatic forces. Short range hydrophobic refinements help in maintaining a proper conformation of the redox partners for electron transfer. Cytochrome *c* also plays a crucial role in cellular death, the so called apoptosis (52, 53).

#### 1.2.1.6 Cytochrome *c* oxidase

Cytochrome *c* oxidase is the fourth complex of the respiratory chain. It catalyses the oxidation of cytochrome *c* and the reduction of oxygen to water (54). The mechanism couples electron transfer and proton transfer across the membrane with an  $e^-/H^+$  transfer ratio of 1. Originally, the structures of the cytochrome *c* oxidase from *Paraccocus denitrificans* and bovine heart were resolved (55, 56). Since then structures from various organisms have been described (18, 57, 58). Electrons enter the enzyme via the periplasmic soluble  $Cu_A$  fragment containing the binuclear copper center. The electron is then delivered to heme *a*, and to the binuclear site formed by heme  $a_3$  and the  $Cu_B$  center. This bimetallic site is the oxygen binding site and catalyses the reduction of oxygen to water. Oxygen enters the enzyme via the membrane. The protons required for the reduction of oxygen enters the oxidase via the two conserved D and K channel (59). The free energy released is used to pump  $H^+$  across the membrane. The structure of the enzyme from various species has been resolved and studies of site-directed mutants as well as studies of inhibitors contributed to the understanding of the mechanism (58, 60, 61). Redox induced FT-IR difference spectroscopy also contributed to the understanding of the enzyme in the identification of acidic residues involved in proton transfer (62-64).

#### **1.2.1.7 ATP synthase**

Complexes I, II and IV contribute to the proton gradient across the membrane which is used by the ATP synthase (complex V) to synthesize ATP from ADP and Pi. The multisubunit enzyme consists of a membrane bound part ( $F_0$ ) and a large soluble cytoplasmic part ( $F_1$ ) (65).  $H^+$  enters the protein via channels to a central ring system made up of  $c$  subunits. Subsequent protonation of aspartate residues lead to a rotational movement of a part of the membrane bound enzyme (66-68). This process is coupled with the formation of ATP from ADP and inorganic phosphate.

### **1.3 The Na<sup>+</sup>-translocating NADH:quinone oxidoreductase from *Vibrio cholerae***

In marine and pathogenic organisms, Na<sup>+</sup> is used together with H<sup>+</sup> in chemiosmotic regulation. The Na<sup>+</sup>-translocating NADH:quinone oxidoreductase is analogue to the complex I in its function, but instead of H<sup>+</sup>, Na<sup>+</sup> ions are pumped across the membrane. The Na<sup>+</sup>-NQR is present in many pathogenic organisms including *Vibrio cholerae*, *Yersinia pestis* and *Vibrio harveyi* (69). This membrane protein is also found in air-borne pathogens such as *Haemophilus influenzae* and *Klebsiella pneumonia*.

#### **1.3.1 *Vibrio cholerae* and the sodium cycle**

*Vibrio cholerae* is suggested to cause the potentially lethal disease cholera (Figure 1.8). The symptom of the disease is acute diarrhea accompanied by severe fever. Without treatment, the infection may lead to dehydration and death follows. The first identification of the agent responsible for cholera was done in 1854 by Pacini who observed comma-shaped organisms in the intestine of cholera victims, which he named *Vibrio cholerae* (70). This halotolerant organism thrives in polluted rivers and coastal waters and is nowadays found in developing countries. Transmission occurs by ingestion of contaminated water or food, the bacterium anchors itself in the small intestine and produces the toxin responsible for the diarrheal symptoms. The bacteria are then released back in the environment through stool (71).

All strains of *Vibrio cholerae* are not considered as dangerous. Indeed only organisms belonging to the O1 and O139 serogroup produce the cholera enterotoxin, and are responsible for the epidemic spread. It is important to point out that other strains are more resistant to environmental change (71). The conditions necessary for the growth of this organism and pandemic spread is high salinity and high temperature. The epidemic end usually coincides with monsoon season, where the salinity of water decreases.

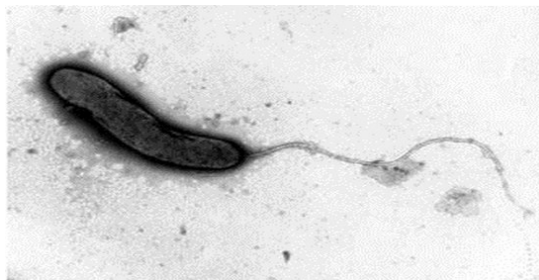
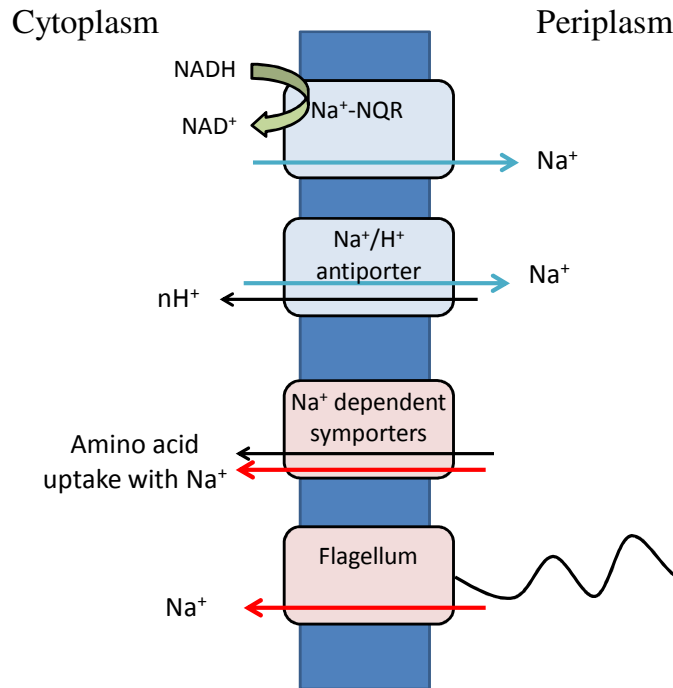


Figure 1.8: *Vibrio cholerae* possesses a single flagellum which is used for movement of the bacterium.

The thriving of this eu-bacterium is closely related to the salinity of its habitat, and more precisely the presence of  $\text{Na}^+$  ions. On a metabolic level, the organism is highly dependent on the  $\text{Na}^+$  cycle (72). The two major molecules involved in  $\text{Na}^+$  ejection from the organism are  $\text{Na}^+/\text{H}^+$  antiporters and the  $\text{Na}^+$ -translocating NADH:quinone oxidoreductase ( $\text{Na}^+$ -NQR) (Figure 1.9).



**Figure 1.9:** The four main proteins involved in  $\text{Na}^+$  transport across the membrane.  $\text{Na}^+$ -NQR and  $\text{Na}^+/\text{H}^+$  antiporter eject  $\text{Na}^+$  from the cytoplasm resulting in a  $\text{Na}^+$  gradient across the membrane. The  $\text{Na}^+$  gradient is used by symporters for intake of amino acids. The rotational movement of the flagellum is also powered by the  $\text{Na}^+$  gradient.

The  $\text{Na}^+$ -gradient set up across the plasmic membrane, known as the 'sodium motive force' is used for various vital processes, for example amino acid uptake through symporters by co-transport of  $\text{Na}^+$  and amino acids (5). The rotational movement of the single flagellum is also dependent on the sodium motive force (73). This  $\text{Na}^+$ -gradient also participates in energy conservation and directly involved in  $\text{Na}^+$  dependent ATP synthesis (74). The main proteins involved in the  $\text{Na}^+$  cycle are shown in figure 1.9.

### 1.3.2 The Na<sup>+</sup>-NQR

The Na<sup>+</sup>-NQR is a 200 kDa membrane protein analogous to the complex I. Discovered initially in the 1980's by the groups of Unemoto and Dimroth in *Vibrio alginolyticus*, the Na<sup>+</sup>-NQR is more widespread than expected (75, 76). It was found to be present in many pathogenic water-borne organisms (69). This membrane protein is also found in air-borne pathogens such as *Haemophilus influenzae* and *Klebsiella pneumonia* (76, 77). Preliminary studies on membrane extracts from *Vibrio alginolyticus* showed that the activation of NADH oxidase is dependent on the presence of Na<sup>+</sup> ions (78). Later it was found that Na<sup>+</sup> is translocated across the membrane of Na<sup>+</sup>-NQR reconstituted in vesicles (79). The genes coding for the Na<sup>+</sup>-NQR are found in a single operon (*nqr*) and produce six sub-units NqrA-F (80, 81).

### 1.3.3 Subunit composition

The **NqrA** subunit is the most hydrophilic domain and does not present any transmembrane helix. Furthermore, no redox active cofactors were observed in this 48 kDa large subunit. Although it is the largest subunit, the role of this subunit is still unknown. Membrane topology mapping of the protein showed that this domain is located in the cytosolic part of the protein (82).

On the contrary, the so-called **NqrB** subunit is very hydrophobic with 8 transmembrane helices. SDS-PAGE gel studies were performed on the Na<sup>+</sup>-NQR. In this technique the protein is in an unfolded state and since the FMN identified under UV illumination comigrate with the subunit, it could be deduced that the FMN was covalently attached (80). Conserved threonine (serine) residues were identified for covalent phosphoester linkage of FMN (83). It was the first time such an attachment for a FMN molecule was observed. When expressed in *Escherichia coli*, the Na<sup>+</sup>-NQR lacked the covalently attached FMN suggesting that the anchoring requires another enzymatic reaction (84, 85). The phosphoester linkage of the FMN is the only mode of attachment of an FMN molecule that does not involve the perturbation of the isoalloxazine moiety (86). Furthermore, studies of individual subunit composition suggested that riboflavin is attached to the NqrB (87). In mutant enzymes lacking the FMN<sub>B</sub>, the EPR signal attributed to the riboflavin is also detected (88). Acidic residues both in the cytosolic and

periplasmic side were observed and are suggested to play a critical role in Na<sup>+</sup> transfer (89).

Korormicin and HQNO (2-n-Heptyl-4-hydroxyquinoline N-oxide) are two inhibitors that mimic the binding of ubiquinone to the Na<sup>+</sup>-NQR. Korormicin is an antibiotic that works at subnanomolar concentrations ( $K_i=82$  pM), while HQNO inhibits the Na<sup>+</sup>-NQR at micromolar range ( $K_i=300$  nM) (90, 91). Hayashi et al. isolated mutants resistant to these inhibitors and observed a single mutation of G140 on the NqrB subunit in the Na<sup>+</sup>-NQR from *Vibrio alginolyticus* (92). Interestingly, two contiguous glycine residues G139 and G140 (G140 and G141 in *Vibrio cholerae*) are suggested to be part of the quinone binding site.

More recently, biotinylated quinone derivatives were used to identify the binding site of the quinone by photo cross linking. The results showed that the quinone binds to the NqrA subunit (93). It is not excluded that the quinone binding site is located at the interface of the hydrophilic NqrA and the hydrophobic NqrB domain.

**NqrC** is a smaller subunit and has a molecular weight of approximately 27 kD. Two transmembrane helices are present and similarly to NqrB, a conservative threonine (serine) residue involved in covalent FMN binding to the protein (83). Mutants where the threonine residue is replaced by tyrosine lack the covalently bound FMN (94).

NqrB and NqrC are homologous to the subunits RnfD and RnfG from RNFs proteins (Rhodobacter nitrogen fixation proteins) with covalent attachment of FMN (95). Nevertheless, membrane topology mapping showed that those FMN molecules are located in the cytosolic side in the Na<sup>+</sup>-NQR and in the periplasmic side of the membrane in RNF proteins. Furthermore, NqrB and NqrC have opposite orientation in the membrane and is suggested to play an important role in Na<sup>+</sup> transfer (96).

**NqrD** and **NqrE** subunits have molecular mass of 23 kD and 22 kD respectively. Both have 6 transmembrane helices and do not contain redox active cofactors. These subunits are homologous to sub-units from the so-called Rnf complex (95). Furthermore, NqrD and NqrE have an opposite orientation in the membrane, and it was suggested that the resulting topology is an almost symmetric transmembrane structure with a specific functional role; ion transfer (96). These subunits also have acidic residues in the cytosolic



and periplasmic ends of the helices. Mutation of these residues induces a large decrease in activity (89).

**NqrF** has one transmembrane helix and a large cytosolic soluble domain. This subunit has a molecular weight of 45 kD and contains the first electron acceptors in the  $\text{Na}^+$ -NQR. Binding motifs for NADH, FAD and [2Fe-2S] center were determined by homology compared to other proteins (97). Sequence alignment of this subunit with other organisms identified cysteine residues 70, 76, 79 and 111 as the iron-sulphur cluster binding site at the N-terminal half (97). Arginine 210, tyrosine 212 and serine 246 form the binding motif for FAD. Mutagenesis studies confirmed the role of these residues, as substitution resulted in mutant enzymes lacking either the FAD or the [2Fe-2S] (98). Although the crystallization of this subunit was successful, the structure is so far not available for *Vibrio cholerae* (99). The PDB file of a crystal structure obtained from X-ray diffraction of an homologue from *Porphyromonas gingivalis* was deposited in 2007 by Kim et al, but the results are not yet published. Structural prediction of the NqrF performed on the basis of high-resolution crystallographic structure of the benzoate 1,2-dioxygenase reductase from *Acinetobacter* sp. strain ADP1 gave a rough model of this sub-unit however with only 23% sequence identity between the two polypeptides (100).

A schematic representation of the 6 subunits (NqrA-F), the cofactors and the electron pathway in the  $\text{Na}^+$ -NQR is given in [figure 1.10](#).

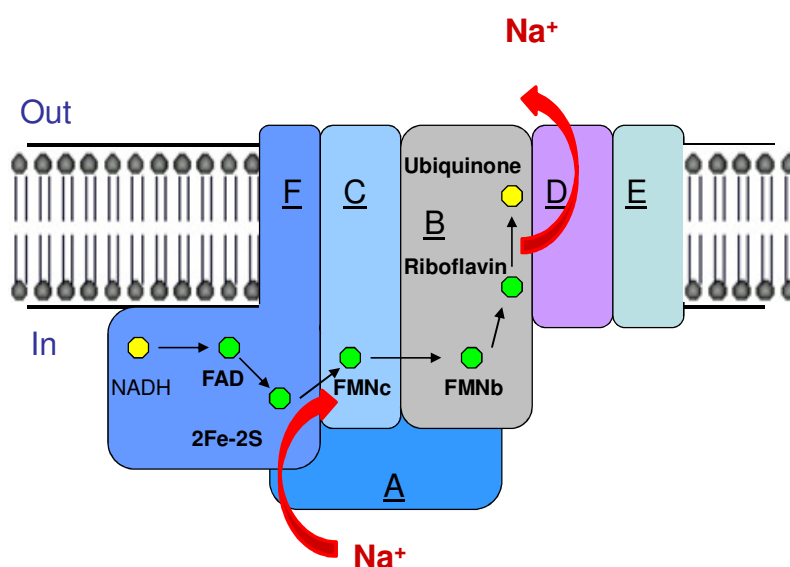


Figure 1.10: Schematic representation of the  $\text{Na}^+$ -NQR.

### 1.3.4 Chemical versatility of flavins

The cofactors present in the  $\text{Na}^+$ -NQR are one FAD, two covalently bound FMN, one riboflavin and one [2Fe-2S] center. Compared to the cofactors involved in the electron pathway of the complex I where mainly iron-sulphur centers are involved, the  $\text{Na}^+$ -NQR presents a unique mechanism involving four flavins and several radical intermediaries. Flavins are known for their chemical and biological versatility.

Riboflavin, vitamin B<sub>2</sub>, is a tri-cycle aromatic molecule with a ribityl side chain. Phosphorylation of the side chain leads to the formation of FMN, a further adenylation results in the FAD (Figure 1.11). FAD and FMN are well known redox cofactors involved in electron transfer and present in a wide variety of proteins. For long, riboflavin was considered as a precursor for the insertion and biosynthesis of FMN and FAD in flavoproteins (101). But riboflavin is also an integral cofactor.

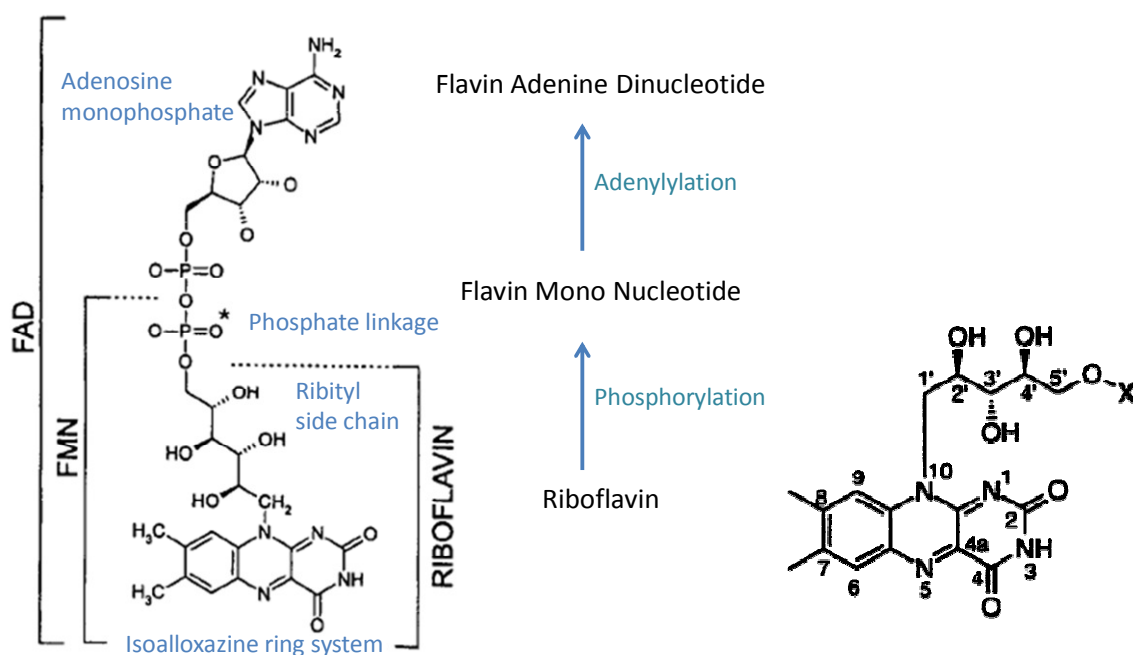


Figure 1.11: The three types of flavins and atomic numbering.

Flavins exhibit a wide range of redox forms (Figure 1.12) and are capable of transferring either one or two electrons.

The first macroscopic observation of a reaction involving flavins found in literature can be found in the accounts of the HMS Challenger expedition in 1874 (102). Sir Charles

Wyville Thompson reported luminescence of the sea surface when mechanically perturbed. It was later found that this reaction involves FAD bound to bacterial luciferase. Light is emitted when FMN C4a peroxide (an intermediate) reacts with oxygen and aldehyde long chains, the resulting products are FMN and the corresponding fatty acid together with light emission (103).

In 1879, A.W. Blyth observed a bright yellow pigment as component of cow milk, which he named lactochrome (104). Afterwards in the early 1930's, the similar bright yellow pigments were isolated from different sources and different names such as lactoflavin or ovoflavin were given to the pigment (105). In 1935, the groups of R. Kuhn and P. Karrer both determined the structure of the yellow pigment and the name riboflavin was given (106, 107). Since then, riboflavin, FMN and FAD have been discovered in a variety of sources.

The versatility of flavin in redox reaction is described in [Figure 1.12](#) and shows the different forms present in aqueous solution, although the radical forms are not stable (108). In proteins and in aprotic solvents these radical forms or ionic forms are stabilized.

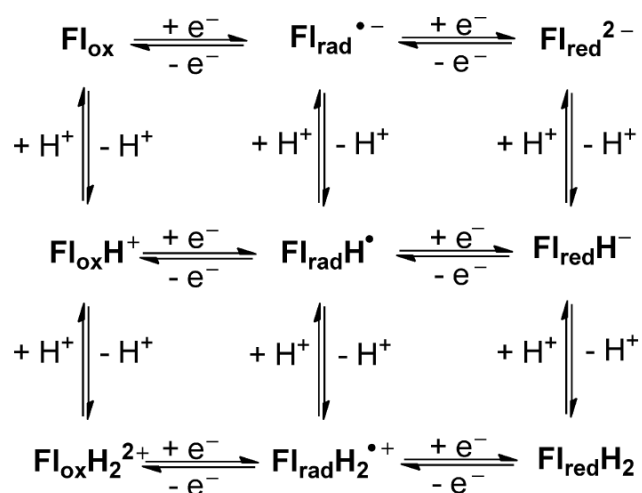
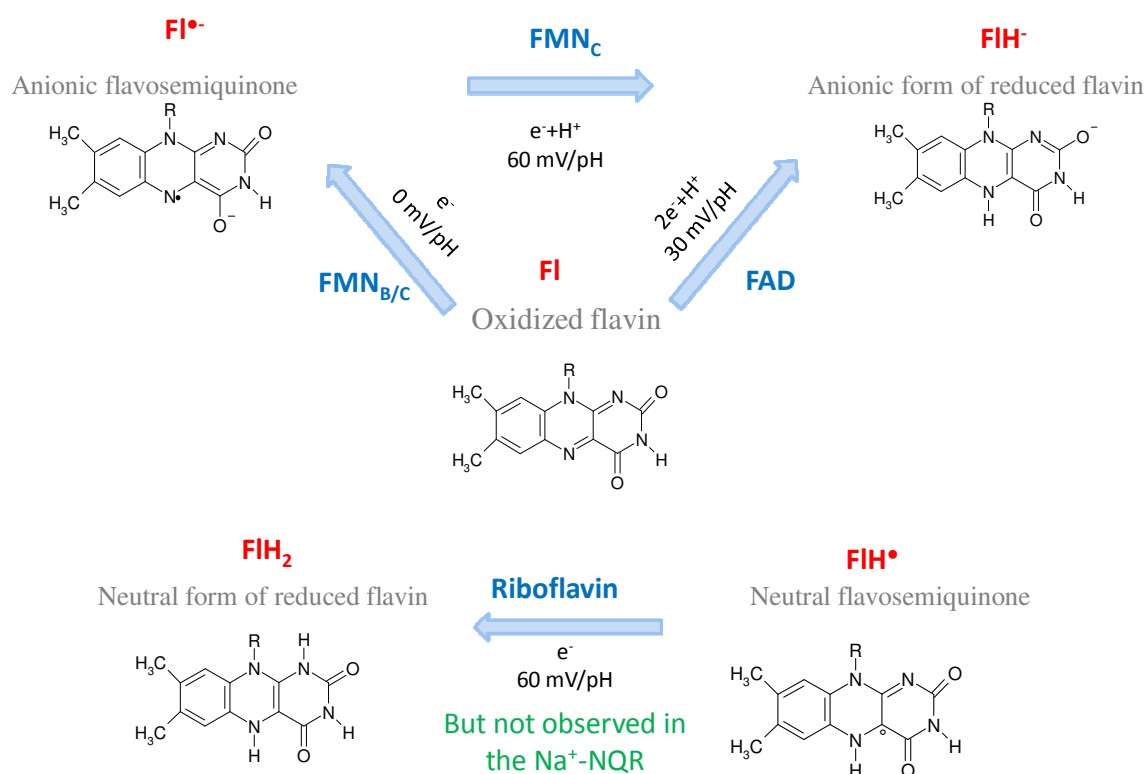


Figure 1.12: The different redox transitions of flavins, reproduced from (108).

In the  $\text{Na}^+$ -NQR, all three naturally occurring flavins are present: riboflavin, FMN and FAD. They all participate in the electron transfer from NADH to quinone. The redox transition of the cofactors and the number of electrons involved are presented in [table 1.1](#) and [figure 1.13](#).

Cofactor	Localisation	Redox transition	Number of electrons
FAD	NqrF	$\text{FIH}^- \leftrightarrow \text{FI}$	2
$[2\text{Fe-2S}]$	NqrF	$[2\text{Fe-2S}]^+ \leftrightarrow [2\text{Fe-2S}]^{2+}$	1
$\text{FMN}_{\text{C/B}}$	NqrC/B	$\text{FI}^{\bullet-} \leftrightarrow \text{FI}$	1
$\text{FMN}_{\text{C}}$	NqrC	$\text{FIH}^- \leftrightarrow \text{FI}^{\bullet-}$	1
Riboflavin	NqrB	$\text{FIH}^{\bullet} \leftrightarrow \text{FIH}_2$	1

Table 1.1: Summary of the redox cofactors present in the  $\text{Na}^+$ -NQRFigure 1.13: The redox transition of the flavins cofactors in the  $\text{Na}^+$ -NQR with the pH dependence of the transitions.

### 1.3.5 Electron pathway in the $\text{Na}^+$ -NQR

The electron pathway was determined on the basis of studies where the enzyme lacked specific cofactors (94). Initially two electrons are donated to the non-covalently bound oxidized FAD in NqrF. The latter is reduced to the anionic form of the reduced flavin. This step has a pH dependence of 30mV. The  $[2\text{Fe}2\text{S}]^{2+}$  accepts one electron to

form reduced  $[2\text{Fe}2\text{S}]^+$ . Simultaneously, FAD is oxidized to the unstable flavosemiquinone form that has been observed by ultra-fast freeze-quench experiments only (109). The next step is the reduction of fully oxidized  $\text{FMN}_\text{C}$  to form the anionic flavosemiquinone form. Afterwards, the  $\text{FMN}_\text{B}$  accepts the electron and also forms the flavosemiquinone. The neutral flavosemiquinone form of riboflavin accepts the electron and is reduced to the neutral form of reduced flavin (110). Redox titration showed that the redox transition involved is pH independent. The conclusion was that the neutral flavosemiquinone form was reduced to the anionic form of reduced flavin. EPR measurements later showed that this transition results in the formation of the neutral form of reduced flavin which is supposed to be pH dependent (88). But due to the stabilization of the neutral flavosemiquinone in the oxidized form of the enzyme, it was suggested that pH independence observed is mainly due to the fact that this flavin is well protected and encapsulated in the hydrophobic part of the protein. And may well explain the pH independence observed as protons are not accessible. The last electron acceptor, ubiquinone<sub>8</sub> is reduced to form the ubiquinol. The electron pathway is summarized in Figure 1.23.

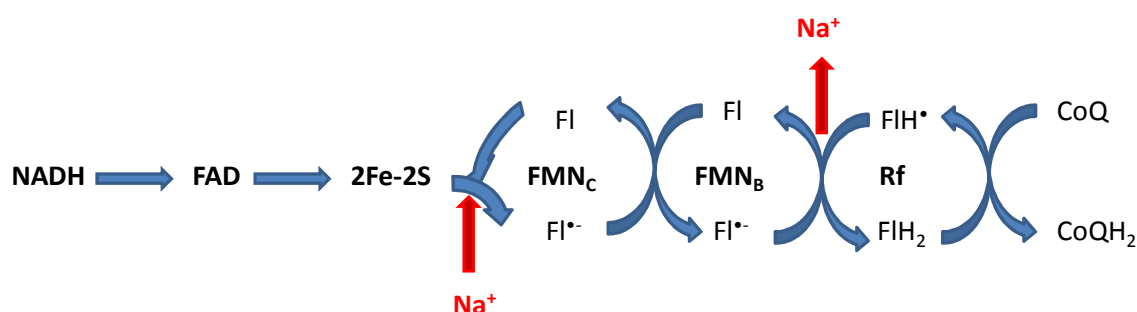


Figure 1.14: The electron pathway of the Na<sup>+</sup>-NQR.

Na<sup>+</sup> uptake occurs when electrons move from the 2Fe-2S center to the FMN<sub>C</sub>, whereas Na<sup>+</sup> release occurs when electrons move from FMN<sub>B</sub> to riboflavin. Interestingly no single cofactor cofactor is involved in uptake/release of Na<sup>+</sup> (111).

### 1.3.6 Ion dependence

In 1977, membrane extracts from both *Vibrio alginolyticus* and *Vibrio costicola* showed NADH reduction were stimulated by Na<sup>+</sup> (75). Addition of CCCP protonophore, did not perturb the NADH reduction, and subsequently led to the finding that the Na<sup>+</sup>-NQR is in fact a Na<sup>+</sup> pump.

The quinone reduction activity measurements of the wild type enzyme, expressed in turnover rate is  $65.4 \text{ s}^{-1}$  without  $\text{Na}^+$  ions and  $521.4 \text{ s}^{-1}$  with  $\text{Na}^+$  ions (89). These measurements clearly show the  $\text{Na}^+$  dependence. Activity was also stimulated by  $\text{Li}^+$  ions as shown in Figure 1.15 (112) and is found to be only 30% as efficient as in the presence of  $\text{Na}^+$  ions. Although  $\text{K}^+$  ions do not stimulate enzymatic activity, in the presence of  $\text{Na}^+$  ions, the activity is slightly increased.  $\text{K}^+$  is described as a nonessential activator for the  $\text{Na}^+$ -NQR. Furthermore  $\text{K}^+$  ions also increase the apparent affinity of the enzyme for  $\text{Na}^+$  ions. On the contrary,  $\text{Rb}^+$  ions act as an inhibitor for the enzyme and decrease its apparent affinity for  $\text{Na}^+$  ions. Furthermore  $\text{Rb}^+$  ions are suggested to have the same binding site as  $\text{K}^+$  ions. Interestingly reactivation of the enzyme is observed when  $\text{K}^+$  ions are added to samples in the presence of  $\text{Rb}^+$  ions. These results strongly suggest that both  $\text{K}^+$  and  $\text{Rb}^+$  have the same binding site (112).

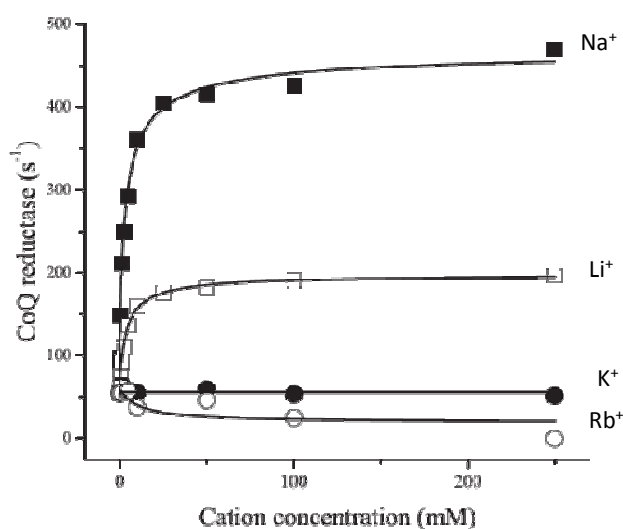


Figure 1.15 : Quinone reduction activity measurements of the  $\text{Na}^+$ -NQR in the presence of  $\text{Na}^+$ ,  $\text{Li}^+$ ,  $\text{K}^+$  and  $\text{Rb}^+$  at different ionic concentration, figure reproduced from (112).

### 1.3.7 $\text{Na}^+$ -binding to the $\text{Na}^+$ -NQR

Residues involved in  $\text{Na}^+$  binding are often carboxylic side chains from aspartic acid or glutamic acid residues. Nevertheless,  $\text{C=O}$  from the polypeptide backbone can also participate in  $\text{Na}^+$ -binding.  $\text{Na}^+$ -binding motifs are difficult to identify, mainly because the residues involved are separated in the primary structure by segments of variable length. Furthermore, in protein crystallographic structures, water molecules and  $\text{Na}^+$  ions have a

similar electron density.  $\text{Na}^+$ -binding site include six oxygen atoms from carboxylic groups which are organized in an octahedral geometry (113).

In the  $\text{Na}^+$ -NQR, topology mapping has identified acidic residues spanning across the membrane helices (89). Usually in transmembrane proteins, charged residues are located in segments on either side of the membrane. To integrate charged residues in the hydrophobic membrane requires high energy. Those located in the membrane have specific functions such as protein-protein interaction in formation of dimeric protein. Acidic residues are also found in channels present in proton pump proteins such as the cytochrome *c* oxidase (55).

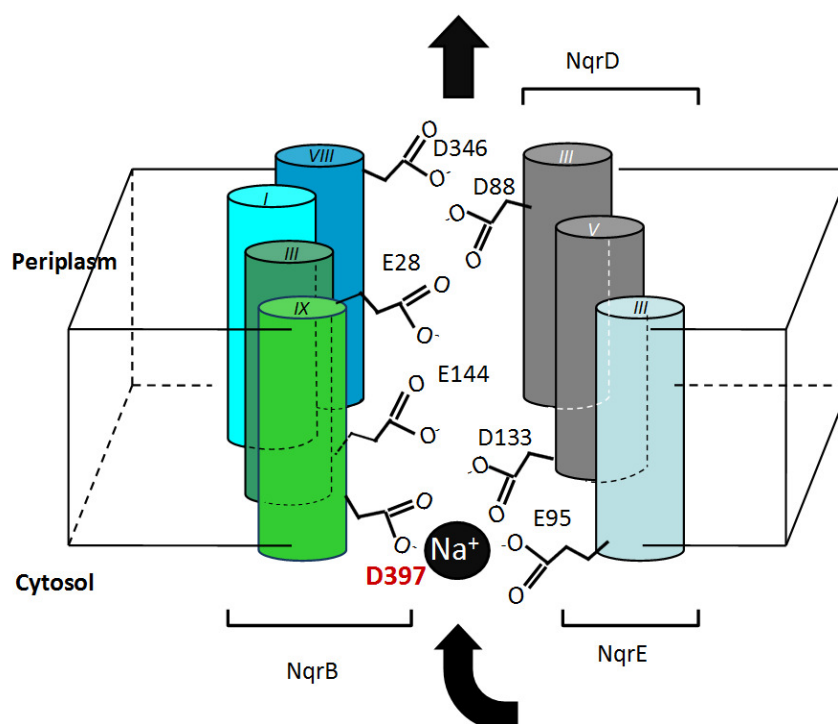


**Figure 1.16:** Schematic representation of acidic residues on the cytosolic and periplasmic side of the membrane, and also spanning across the membrane. These residues are suggested to play an important role in  $\text{Na}^+$  transfer across the membrane, figure reproduced from (89).

In the cytosolic side of the  $\text{Na}^+$ -NQR, acidic residues D397, E95 and D133 from NqrB, NqrE and NqrD sub-units were identified as the first  $\text{Na}^+$  binding site (Figure 1.16). In mutant enzymes where these acidic residues were replaced by alanine, the  $\text{Na}^+$  affinity of the protein decreased considerably and when reconstituted in proteoliposomes, these mutant enzymes lost  $\text{Na}^+$  pumping activity.

## 1.4 Protein-protein interaction

Protein-protein interaction in the respiratory chain is governed by long range electrostatic recognition between acidic side chains. At a shorter distance, hydrophobic refinements rearrange the conformation of both redox partners for an optimal electron transfer (*114*).

Moreover, although the fluid mosaic model suggests that the membrane bound enzymes move freely in the phospholipid bilayer, there are areas of the membrane where the proteins are in higher concentration and organized in supramolecular structures (*1*). These molecular organizations consequently optimize electron transfer between the different components of the respiratory chain (*115*). In 1978, it was shown that electron transfer rates in respiratory complexes are optimized if different components were present at specific stoichiometry (*116*). A 3D model of the organization of respiratory complexes show that the interaction surfaces on complex I and III for quinone face each other. Instead of going through a pool like system, quinol is channeled to the dimeric  $bc_1$  complex ([Figure 1.17](#)) (*115*). Similarly, the interaction surfaces for cytochrome  $c$  both in the complex III and complex IV face each other in this model, thus optimizing electron transfer.

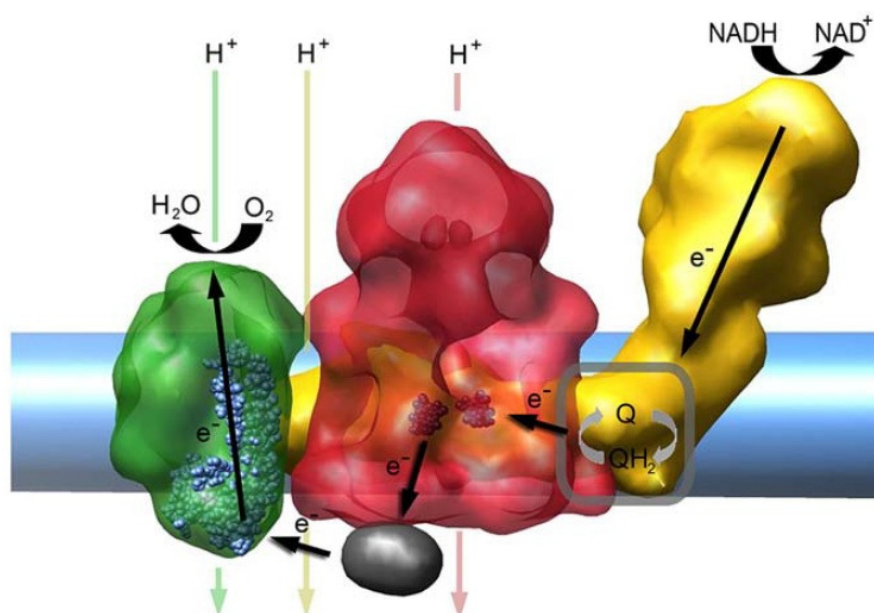


Figure 1.17: Suggested supercomplex from bovine respiratory chain including complex I (yellow), the dimeric complex III (red), cytochrome  $c$  (yellow) and complex IV (green), figure reproduced from (*115*).



Protein-protein interaction is governed by long range electrostatic recognition and at a shorter distance by hydrophobic refinements. In the organism *Thermus thermophilus*, the interaction is mainly hydrophobic between the cytochrome *c*<sub>552</sub> and the Cu<sub>A</sub> fragment from the *ba*<sub>3</sub> oxidase (117). This property provides a unique window of opportunity to study the complex formed by the two partner proteins by electrochemistry.

#### 1.4.1 Thermophiles and thermozymes

Organisms that thrive in extreme conditions are known as extremophiles. Temperature is used to classify organisms into three groups. Mesophiles live and grow at normal temperature. Psychrophile organisms are those who have an optimal growth below 15°C and thermophiles are those who grow and live at 50°C and above. *Thermus thermophilus*, as its name suggests, is a thermophile organism that has for habitat hot water springs or the surroundings of submarine thermal chimneys.

In order to increase the  $T_m$  (mid-point temperature between the denatured form and the functional form of proteins), thermophiles have adopted different strategies which are reflected in the structure of the thermozymes. Starting with the primary structure, an increase in non-polar and hydrophobic residues is observed in the inner core compared to mesophilic analogous proteins. Moreover, an increase in arginine and glutamine residues on the surface which contribute to better ionic interactions is also observed (118). On the opposite a net decrease of uncharged polar amino acids is observed (119).

A study of 16 protein families from thermophiles and their analogues in mesophiles showed a recurrent pattern of increasing length of the main chain and also an increase in hydrogen bonding in the main chain. As for secondary structure analysis, the relative percentage of  $\alpha$ -helices,  $3_{10}$ -helices and  $\beta$ -strand structures increases in thermophiles while the relative contribution of  $\beta$ -turn and random coils decreases. The increase in  $\alpha$ -helical structures in thermozymes is usually accompanied by an increase in the interaction of intra-helices. (120). All these adaptations result in an increased hydrophobicity and a better packing of the inner core of the proteins (121).

### 1.4.2 Protein-protein interaction and oxygen reduction in *Thermus thermophilus*

Depending on the availability of oxygen in the growth environment, *Thermus thermophilus* can express two different terminal oxidases (122). At high oxygen concentration, the *caa<sub>3</sub>* oxidase is preferably expressed. On the contrary, at low oxygen concentration, the *ba<sub>3</sub>* oxidase is expressed (123). Electrons from the complex III are donated to the terminal oxidase. Electron transfer to the *caa<sub>3</sub>* oxidase is suggested to occur with complex formation between the two enzymes, with an equilibrium constant of 250-300 (124). For the *ba<sub>3</sub>* terminal oxidase, electrons are transported via the cytochrome *c<sub>552</sub>*. The equilibrium constant for the formation of the complex between the *bc<sub>1</sub>* complex and the cytochrome *c<sub>552</sub>* is 1.1, but the equilibrium constant for the formation of the cytochrome *c<sub>552</sub>* to the *ba<sub>3</sub>* oxidase is 4.8 (124). Nevertheless, cytochrome *c<sub>552</sub>* was also found to be a very efficient electron donor to the *caa<sub>3</sub>* oxidase. This step is not clear as contradictory results have been reported (125, 126). The general scheme of electron transfer is summarized in [figure 1.18](#).

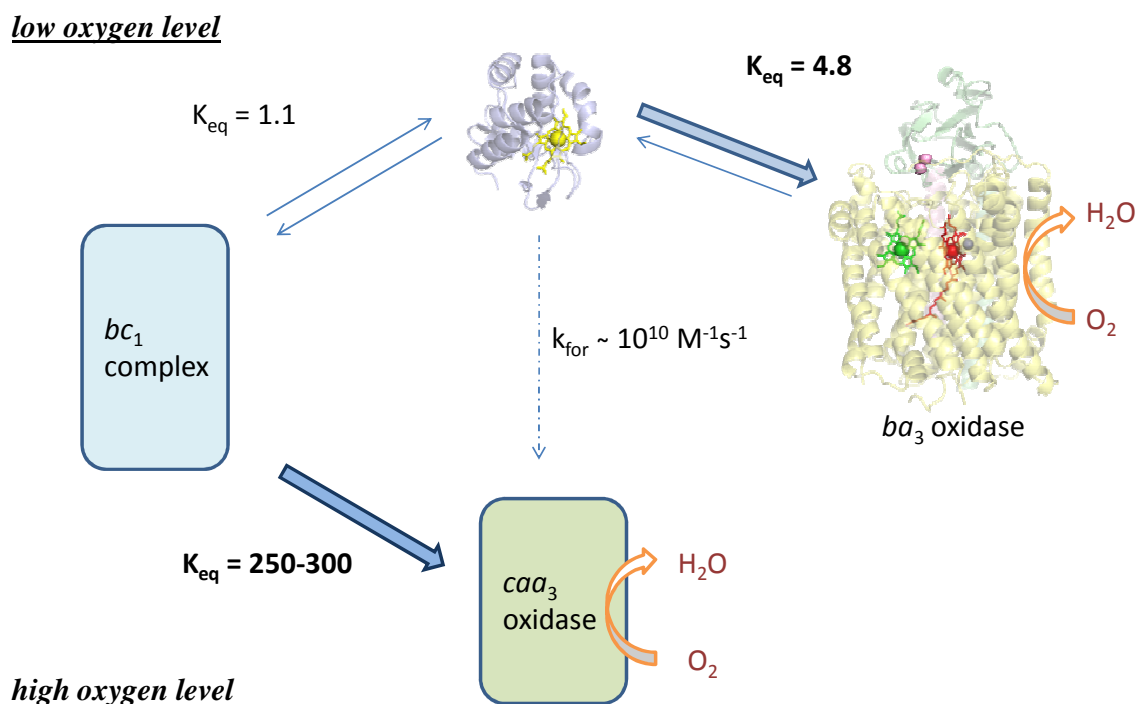


Figure 1.18: Depending on oxygen availability, *Thermus thermophilus* can express two different terminal oxidases providing two alternatives for oxygen reduction.

The use of subunit fragments for biophysical studies of electron transfer instead of the whole protein was shown to be successful (114, 127, 128). Experimental setups are simple in the absence of detergents. In this work, the complex formed by the cytochrome  $c_{552}$  and the soluble  $\text{Cu}_A$  fragment of the  $ba_3$  oxidase has been studied.

### 1.4.3 The $ba_3$ oxidase

The  $ba_3$  oxidase couples the reduction of oxygen to water with proton pumping across the membrane similar to the cytochrome  $c$  oxidase described in [section 1.2.1.6](#) (129). This enzyme is the smallest known terminal oxidase and has 3 subunits, subunit I is the largest and consists of 13 transmembrane helices (18). Three cofactors are present in this subunit and are located in the middle of the membrane, one  $b$ -type heme, one  $a_3$ -type heme and a mononuclear  $\text{Cu}_B$  center. Oxygen enters the enzyme through a y-shaped canal parallel to the membrane on the level of the  $\text{Cu}_B$  center (130). Oxygen fixation and reduction occurs on the bimetallic center formed by the  $\text{Cu}_B$  and the  $a_3$  heme. Electrons enter the enzyme via the periplasmic subunit II, which contains a binuclear  $\text{Cu}_A$  center. This subunit is anchored to the membrane and the subunit I by a transmembrane helix. The structure of the enzyme showing the cofactors is presented in [figure 1.19](#).

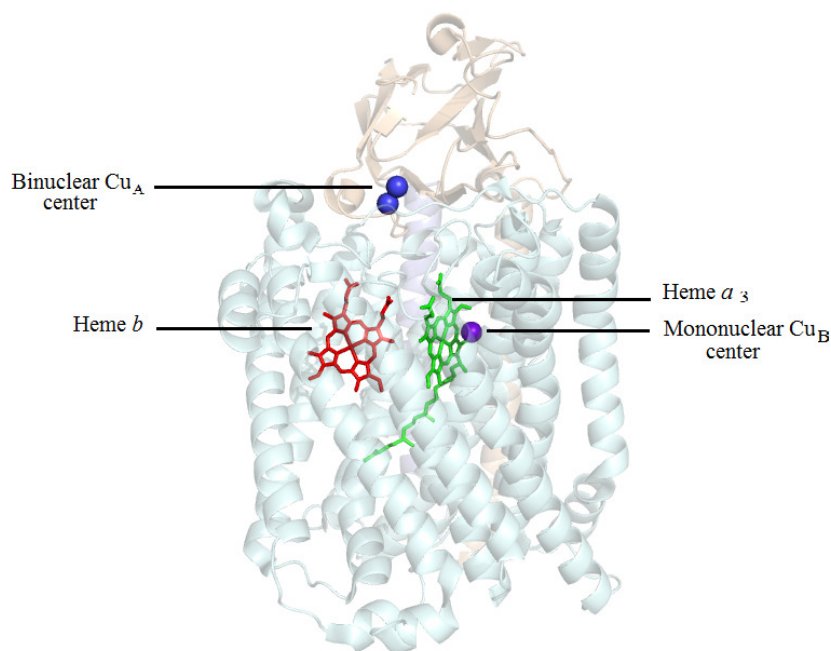


Figure 1.19: Structure of the  $ba_3$  oxidase depicting the cofactors present (PDB 1EHK) (18).

The  $ba_3$  oxidase has a molecular mass of 85 kDa. The structure was resolved in 2000 by Soulimane et al. and refined since then (18, 130, 131). The results show the arrangement of intramolecular water molecules forming a cluster on the propionates of the  $a_3$  heme.

#### 1.4.4 The $Cu_A$ fragment

Electrons are donated by the cytochrome  $c_{552}$  and enter the  $ba_3$  oxidase through the first electron acceptor, the binuclear  $Cu_A$  center in the periplasmic subunit 2. This fragment consists mainly of antiparallel  $\beta$ -sheets and random structures. A transmembrane  $\alpha$ -helix is also present which keeps the subunit anchored to the membrane domain. To solubilise a fragment and abolish from the constraints of working with detergents, the helix is typically removed from the  $Cu_A$  fragment (132). The crystallographic structure of the fragment was determined by Williams et al. in 1999 (Figure 1.20) (133).

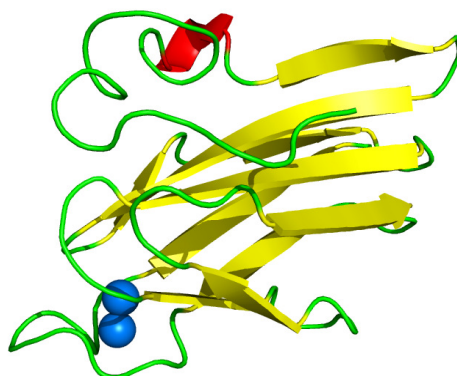


Figure 1.20: Crystallographic structure of the  $Cu_A$  fragment, the polypeptide consists mainly of anti-parallel  $\beta$ -sheets and random structures (PDB 2CUA). The binuclear Cu center is represented in blue (133).

Figure 1.3.4 depicts the asymmetric binuclear  $Cu_A$  center with the  $Cu_1$  coordinated by His<sup>114</sup>, Met<sup>160</sup>, Cys<sup>153</sup> and Cys<sup>149</sup> while the  $Cu_2$  center is coordinated by Gln<sup>151</sup>, His<sup>157</sup>, Cys<sup>153</sup> and Cys<sup>149</sup> (Figure 1.21). EPR measurements showed that one Cu atom has a charge of + 1 while the other has a charge of + 2. These charges are delocalized on the two atoms resulting in an apparent charge of + 1.5 (134). This Cu site gives the protein fragment the typical purple color by metal-ligand charge transfer. Electrochemical analysis of the  $Cu_A$  fragment by immobilizing the protein on a modified gold electrode yielded a mid-point potential of 240 mV vs SHE' (135).

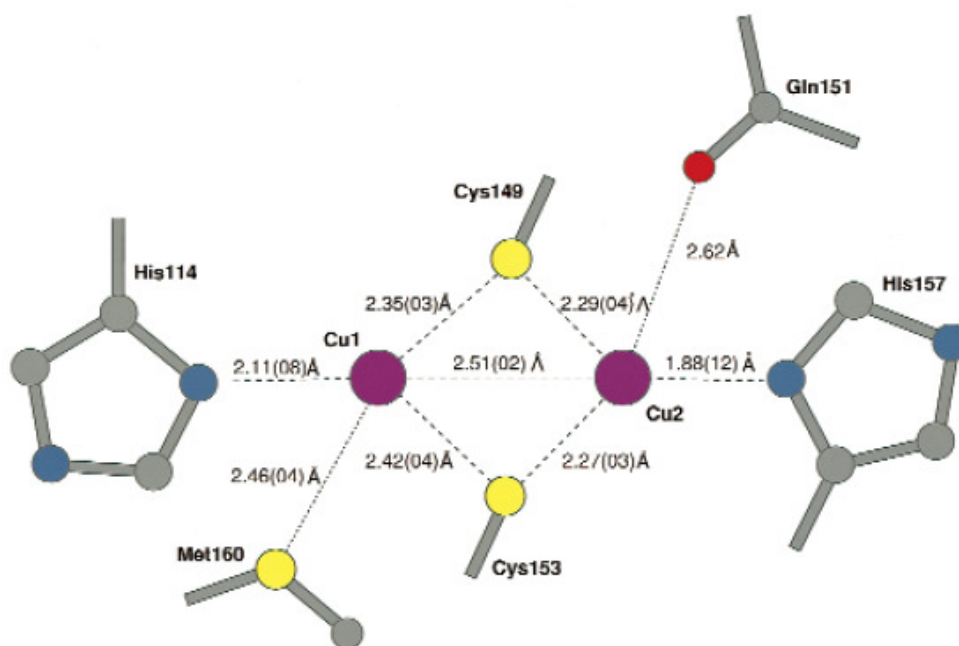


Figure 1.21: Schematic representation of the coordination of the binuclear  $\text{Cu}_A$  center, reproduced from (133).

#### 1.4.5 Cytochrome $c_{552}$

Cytochrome  $c_{552}$  accepts electron from the  $bc_1$  complex and delivers it to the  $\text{Cu}_A$  fragment. This periplasmic soluble molecule is made up of 131 residues for a molecular weight of 14158 Da (126, 136). The enzyme is centered by a  $c$  type heme and the appellation of cytochrome  $c_{552}$  results from the  $\alpha$  band observed in the reduced form of the enzyme at 552 nm. Comparing the cytochrome  $c_{552}$  from *Thermus thermophilus* to cytochrome  $c$  from mesophiles, the first striking observation is the presence of  $\beta$ -strands in the secondary structure of cytochrome  $c_{552}$  (Figure 1.22) (17).

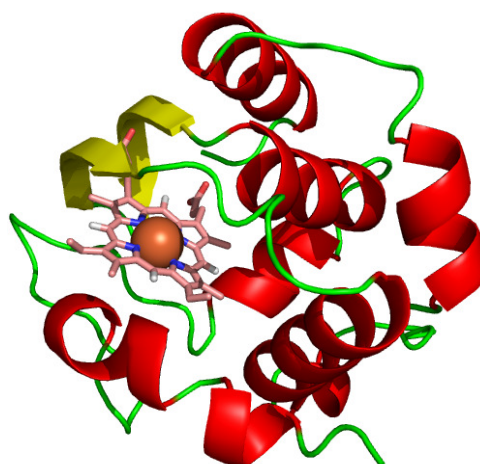


Figure 1.22: Structure of cytochrome  $c_{552}$  centered by the  $c$  type heme (PDB 1C52) (17).

Furthermore, no water molecules have been observed in the inner core of the protein. Indeed, a more hydrophobic core increases thermal stability. Electrochemical analysis of the cytochrome  $c_{552}$  on a modified gold electrode previously reported a mid-point potential of 200 mV vs SHE' (137).

#### 1.4.6 [Cytochrome $c_{552}$ -Cu<sub>A</sub> fragment] complex

The interaction between cytochrome  $c$  and the cytochrome  $c$  oxidase is described in a two step model (114, 128, 138). The interaction surface in the  $aa_3$  terminal oxidase in *Paracoccus denitrificans* and in *Rhodobacter sphaeroides* is surrounded by acidic residues that play an essential role in the protein docking dynamics. Cytochrome  $c$  itself has positively charged residues surrounding the heme cleft. The first step consists of the recognition and the pre-orientation of the redox partners by long range electrostatic forces. For  $aa_3$  oxidase from *Paracoccus denitrificans*, the plot turnover numbers ( $s^{-1}$ ) against ionic strength is described by a bell shape curve with a maximum at 56 mM, increasing the ionic strength progressively shields the interaction surface (139). Mutation of these acidic residues resulted in a shift to lower ionic strength dependency to lower values and an increase in the  $K_M$  values. The second step consists of the fine tuning of the interaction where the two redox partners are placed in an optimal conformation for electron transfer. Mutation of these residues exposed on the surface of the of the  $aa_3$  oxidase from *Paracoccus denitrificans* does not affect the values of  $K_M$ , but  $k_{cat}$  values are decreased (139).

In the respiratory chain of *Thermus thermophilus*, there is a completely different scenario; the interaction between the proteins is mainly hydrophobic with less than one charged residue present on the interaction surface (117). In a Brønsted plot, the logarithm of bimolecular rate constants is presented against the square root of the ionic strength of the medium. For the interaction between the cytochrome  $c_{552}$  and the Cu<sub>A</sub> fragment from *Thermus thermophilus*, the plot shows a very low dependency with a slope of less 0.57. Less than one charged residue is involved on the interaction surface (114). This is suggested to favor complex formation in thermophiles; as at high temperatures electrostatic interactions are weakened and hydrophobic interactions become stronger.

The structure of the complex formed by the cytochrome  $c_{552}$  and the  $\text{Cu}_A$  fragment from *Thermus thermophilus* has been obtained by a combined NMR spectroscopic and computational method (figure 1.14, PDB 2FWL). Both proteins were studied in the oxidized and reduced form.  $^{15}\text{N}$  enriched samples were analyzed, thus defining the residues that play an important role in inter-protein interaction and as well as electron transfer. In the complex form, residues in cytochrome  $c_{552}$  that have the highest chemical shift perturbation are those located directly on the surface of interaction that is the region surrounding the heme cleft. Furthermore Ala<sup>34</sup> and His<sup>32</sup> located at the back of the heme cleft also exhibit high chemical shift perturbation (117).

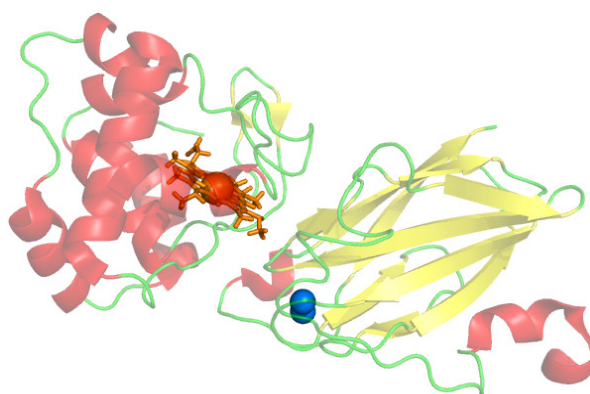


**Figure 1.23: Structure of the complex [cytochrome  $c_{552}$ - $\text{Cu}_A$  fragment] obtained by a combined NMR spectroscopic computational method (PDB 2FWL) (117).**

Studies on same proteins from *Paracoccus denitrificans* revealed that together with the residues on the interaction surface, Gly<sup>54</sup>, Gly<sup>55</sup> and Asp<sup>56</sup> located on the back of the heme, show the largest chemical shift perturbation in cytochrome  $c_{552}$  (128).

## **1.5 Cytochrome $bc_1$ - $aa_3$ supercomplex from *C. glutamicum***

Another type of interaction can be observed in supercomplexes. The respiratory chain of *Corynebacterium glutamicum* includes a supercomplex formed by the dimeric  $bc_1$  complex, cytochrome  $c$  and the  $aa_3$  oxidase.

### **1.5.1 The *Corynebacterium glutamicum***

The rod-shaped *Corynebacterium glutamicum* is very resistant to mechanical stress and is adapted to varying environmental conditions (figure 1.24). First isolated in 1957, this gram-positive bacterium has since then been of great interest (140). *Corynebacterium glutamicum* is a biotin-auxotrophic bacterium that utilizes glucose as carbon source to synthesise L-glutamate under aerobic conditions and biotin limitation. Optimal production strains of the organism have been used industrially for the production of L-glutamate at a scale of one million tons per year. The latter is used as a flavor enhancer in industrial food production (141, 142). Other genetically modified and metabolic engineered strains have also been used for the industrial production of L-lysine, which is used as food additive. Nevertheless, 0.5 million tons are produced annually (141).



**Figure 1.24: The rod-shaped *Corynebacterium glutamicum* (142).**

For long the study of this organism was limited and related to amino acid synthesis. These mainly included metabolic engineering for optimization of industrial production. But it soon became evident to have an optimal strain for amino acid production, it was important to have a better knowledge of the metabolism of the bacterium as a whole. On a medical level, *Corynebacterium glutamicum* is also used as a non-pathogenic model to study related pathogens such as *Corynebacterium diphtheria* and



*Mycobacterium tuberculosis*. More recently, the organism has been of interest in the treatment of phenol-contaminated soil. More than 94% degradation of phenol within 3 days was observed reflecting the effectiveness of this organism in biodegradation (143).

### 1.5.2 Respiration based on menaquinone

Although the quinone pool involved in the electron transfer mainly consists of ubiquinone, some organisms have adopted other forms of quinone as membrane electron shuttle. In *Escherichia coli* for example, cells grown under anoxic conditions shifted the quinone pool from ubiquinone to menaquinone (144). Other organisms including the *Corynebacterium glutamicum* exclusively use menaquinone. One particularity of menaquinone is the redox potential that is much lower than the ubiquinone. Ubiquinone and menaquinone have a midpoint potential of 102 mV and -61 mV (vs SHE') respectively, in other words approximately 150 mV lower for menaquinone (145-148).

The second group includes of enzymes that oxidize menaquinol to menaquinone. Reduced minus oxidized UV-visible difference spectra membrane extracts from *Corynebacterium glutamicum* exhibit bands at 600, 562 and 552 nm which are typical of *a*, *b* and *c* type hemes. When cells are grown in a copper limited medium or a cyanide enriched medium, there is less *a*-type and *c*-type hemes whereas a new signal attributed to *d*-type hemes were observed (149, 150). These results demonstrate that there are two different type of terminal oxidase present (151).

### 1.4.3 Cytochrome *bc*<sub>1</sub>-*aa*<sub>3</sub> oxidase supercomplex.

The enzyme of interest in this project is the naturally occurring *bc*<sub>1</sub>-*aa*<sub>3</sub> supercomplex from *Corynebacterium glutamicum*. The *bc*<sub>1</sub> unit of the super complex shows some notable differences when compared to analogues from other organisms although three subunits are present. In the N-terminus of the Rieske protein, three putative transmembrane helices are observed instead of one. In the C-terminal region of cytochrome *b*, a 120 amino acid extension is observed. Another particularity in the cytochrome *c*<sub>1</sub> is the presence of two motifs for covalent heme binding, indicating that the enzyme has two *c* type hemes (141).

The  $aa_3$  oxidase part also shows some differences when compared to analogues. Although sub-unit I is similar to other  $aa_3$  terminal oxidases, the main difference is in the sub-unit II where an extension of 30 residues is observed. It was proposed that this extension plays an important role in attachment to the  $bc_1$  unit (152). Figure 1.25 shows a schematic simplified model of the  $bc_1$ - $aa_3$  supercomplex.

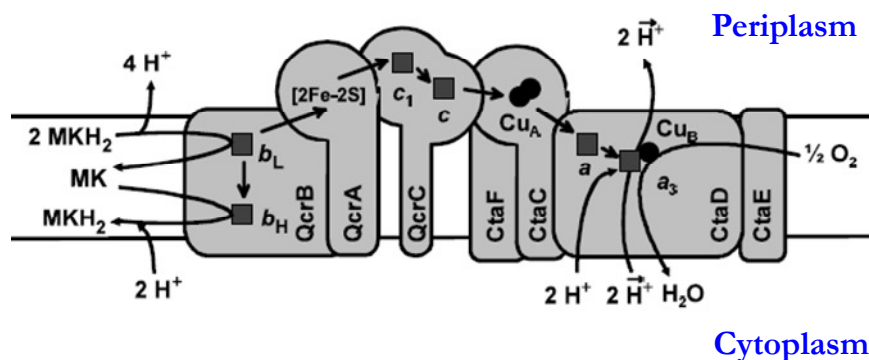


Figure 1.25: Schematic representation of the subunits and cofactors present in the  $bc_1$ - $aa_3$  supercomplex, reproduced from (141).

The cofactors present are two  $b$ -type hemes in the QcrB subunit, one heme  $b_L$  and one heme  $b_H$ . QcrA, the Rieske protein sub-unit contains one  $[2Fe-2S]$  center. The QcrC contains two  $c$ -type hemes. In the terminal oxidase part, a binuclear  $Cu_A$  center is present in CtaC. Finally, the CtaD sub-unit contains one  $a$  type heme, one  $a_3$ -type heme and a mononuclear  $Cu_B$  center are present.

## **1.6 Aim of work**

One of the important questions in the field of molecular bioenergetics is on the interaction of the enzymes with ions and ligands, with lipids and with other proteins. Within these lines the following systems will be studied.

1. Role of the ions for Na<sup>+</sup>-NQR transport and interaction with the cofactors. Determination of the redox mid-point potential of the cofactors present in the Na<sup>+</sup>-NQR wild type in the presence of Li<sup>+</sup>, Na<sup>+</sup>, K<sup>+</sup>, Rb<sup>+</sup> and NH<sub>4</sub><sup>+</sup> ions. Redox induced FT-IR spectroscopic studies will show this interaction on a molecular level. HDX kinetics measurements monitor the solvent accessibility of the protein in the presence of the different salts.

The same experiments will also apply to the study on the role of specific residues involved in Na<sup>+</sup>-transport. Mutant enzymes NqrB D397E and NqrE E95Q forming the first Na<sup>+</sup> binding site of the protein will be studied.

The interaction of Na<sup>+</sup>-NQR with quinone and inhibitors will be analyzed with the help of NqrB G140A mutant enzyme.

2. The interaction between complexes from the respiratory chain of *Thermus thermophilus* are studied as a model for protein-protein interaction during electron transfer as well as the supercomplex from *Corynebacterium glutamicum*. In both cases, the influences of electrochemical and spectroscopic properties are analyzed.

## **Chapter II: Experimental Techniques**

## 2.0 Spectroscopy

Spectroscopy deals with the interaction of atoms and molecules with electromagnetic radiation. These interactions can be absorption, emission or scattering. Electromagnetic radiation is described by Maxwell's law consists of two oscillating fields perpendicular to each other on a unique plane. These components are represented by simple sinusoidal functions at a constant velocity ( $c$ ), the speed of light. The energy ( $E$ ) and the frequency ( $\nu$ ) associated to the radiation is give by the following equations where  $h$  is the Planck's constant:

$$E = \frac{h \cdot c}{\lambda} \quad \nu = \frac{c}{\lambda} \quad \text{Equation 1}$$

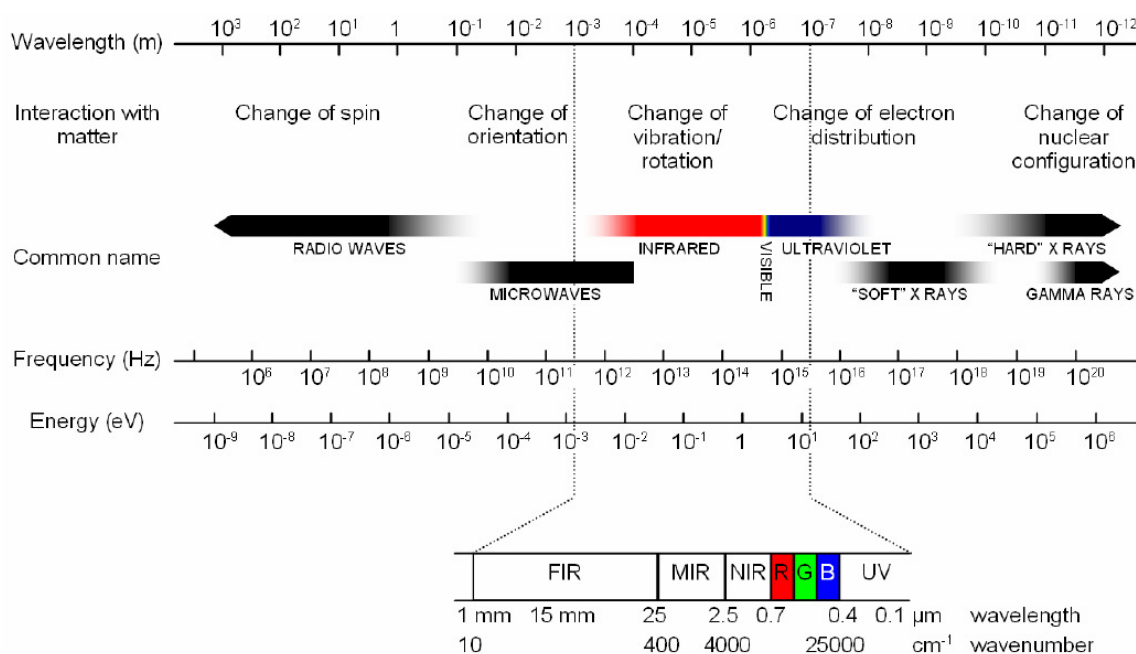


Figure 2.1: The electromagnetic spectrum represented in terms of wavelength, frequency and energy. The changes induced at the molecular or atomic level. The expanded region is of interest in this work (153).

The interaction of electromagnetic radiation with matter can induce different phenomena depending on the energy of the radiation. Low energy radio waves will only change the spin orientation, whereas at the opposite extreme gamma rays will change the nuclear configuration of matter. [Figure 2.1](#) summarizes the different types of radiation, their energy levels and their interaction with matter. Probing the interaction of matter with a specific radiation summarizes the principle of spectroscopy.

In the present study, two spectral regions are of interest and are represented in the expanded region of figure 2.1: the infrared domain and the UV-visible region.

## 2.1 UV-visible: electronic spectroscopy

The absorption of UV-visible radiation corresponds to the energy required for electronic transition; the electrons get to a more energetic orbital, the excited state. The plot of absorbance against the wavelength gives the absorbance spectrum. Absorbance is the difference between the logarithm of the incident beam and the transmitted beam (Figure 2.2). Lambert-Beer's law also defines absorbance as a being proportional to molar extinction coefficient ( $\epsilon$ ) given in  $\text{mol}^{-1}.\text{cm}^{-1}.\text{L}$ , the concentration of the sample ( $C$ ) in  $\text{mol}.\text{L}^{-1}$  and the path length of the sample ( $l$ ) in cm. The equations defining absorbance are given as follows:

$$A = \log_{10} \frac{I_0}{I} = \epsilon \cdot l \cdot C \quad \text{Equation 2}$$

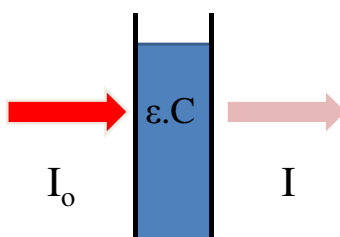


**Figure 2.2: Representation of UV-visible interaction with a sample of a given concentration ( $C$ ) and a molar absorption coefficient  $\epsilon$ .  $I_0$  is the incident radiation, and  $I$  is the radiation that is not absorbed by the sample.**

In the study of proteins of the respiratory chain, UV-visible spectroscopy has been very useful in studying proteins containing hemes. The typical spectrum of a heme includes a large signal in the region around 400 nm, the so-called Soret band ( $\gamma$ -band) that induces the electronic transition of the porphyrin aromatic system. At higher wavelength, smaller signals, the q-bands are observed. These bands are sensible to the redox state, spin state and ligation of the heme. Coupled to an electrochemical setup, the evolution of these signals is used to determine the redox potential of heme cofactors in proteins (154). The oxidation of NADH and reduction of quinone can also be monitored in UV, and have been used to measure the activity of complex I and the  $\text{Na}^+$ -NQR (81, 155). Similar measurements were performed to measure the activity of the  $bc_1$  complex and the

cytochrome *c* oxidase (156, 157). UV-visible spectroscopy has also been used to probe the kinetic of reduction or oxidation of these molecules. Stop-flow techniques have also been used to characterize formation or dissociation constants in the study of protein-protein interaction (124).

## 2.2 Infrared: vibrational spectroscopy

Absorption of less energetic ( $10^{-3}$ -1 eV) IR radiation results in changes in vibrational and rotational modes of atomic bonds. The absorption of IR radiation is dictated by a selection rule that requests a change in the dipole moment of the molecule during vibration (158). For non-linear molecules of *N* atoms, the number of vibrational modes is  $3N-6$ . In classical mechanics, the simplest description of the chemical bond formed between two atoms, A and B with corresponding masses in vibration is the harmonic oscillator (Figure 2.3). For the stretching mode, *d* represents the displacement of the spring (cm), *k* is the force constant ( $\text{N}\cdot\text{cm}^{-1}$ ) and *F* is the force required for the spring to get back in its initial state (N). The reduced mass  $\mu$  of the two atoms is used.

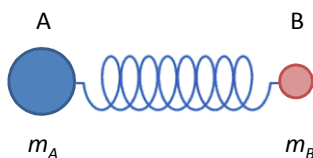


Figure 2.3: Simplified spring ball model to represent the harmonic oscillator.

$$F = k \cdot d \qquad \mu = \frac{m_A \cdot m_B}{m_A + m_B} \qquad \text{Equation 3}$$

The system possesses both kinetic and potential energies ( $E_k$  and  $E_p$  respectively).

$$E_k = \frac{1}{2} (m_1 \dot{d}_1^2 + m_2 \dot{d}_2^2) \qquad \text{Equation 4}$$

$$E_p = \frac{1}{2} (k d_1 - k d_2)^2 \qquad \text{Equation 5}$$

Using the Lagrange's set of equations to solve the energy of this vibration, a simple equation relating the frequency to the reduced mass and the force constant of the spring is obtained.

$$\nu = \frac{1}{2\pi} \sqrt{\frac{k}{\mu}}$$

Equation 6

In IR spectroscopy, the wavenumber ( $\text{cm}^{-1}$ ) obtained by dividing the  $\nu$  by  $c$  the speed of light, is commonly used instead of the frequency. From this equation, we can see that molecules with a higher reduced mass will absorb at lower frequencies.

This equation gives a good description of the stretching mode vibration. Other modes represented in [figure 2.4](#), are defined by more complicated equations as the system is placed in a Cartesian reference with 3 dimensions.

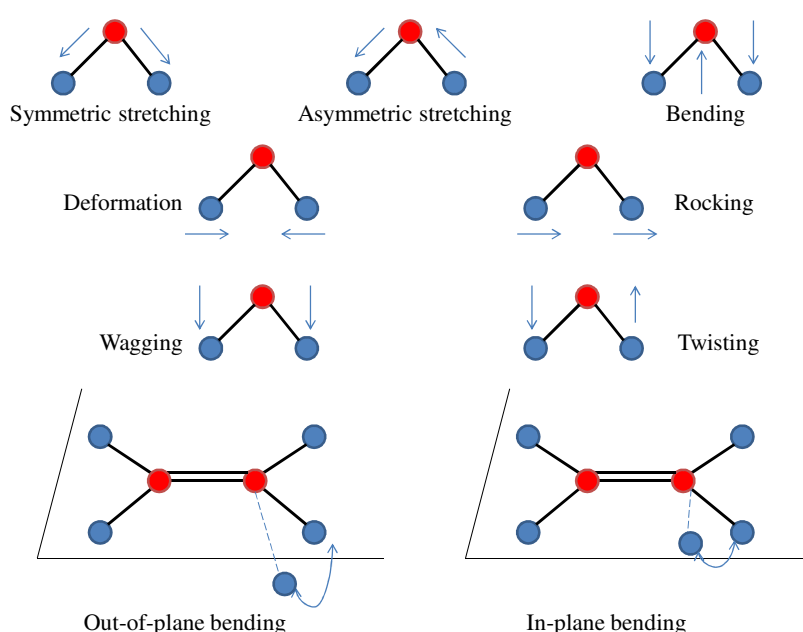


Figure 2.4: Different uncoupled normal vibrational modes.

### 2.2.1 IR spectrometer

In an IR spectrometer, the radiation source for the mid-IR region is most of the time a globar. For far IR measurements, although a globar can also be used, best signals are obtained with a high pressure mercury source. Synchrotron light source is another alternative. The IR radiation goes through the interferometer, the main instrument of all FT-IR spectrometers.



The most important component of a FT-IR spectrometer is the Michelson interferometer. The setup consists of two mirrors perpendicular to each other with respect to the plane, one is fixed and one has a controlled back and forth movement (Figure 2.5). IR radiation from the source strikes a beamsplitter resulting in 50% of reflection on the movable mirror (ray 1) and 50% transmission on the fixed mirror (ray 2). Both ray 1 and 2 are reflected back to the beamsplitter. At this point the two rays go through different paths and interfere. For example for a monochromatic source, the resulting interference can either be constructive or destructive (when the two paths are equivalent) depending on the movement of the mirror. The velocity of the mirror movement is measured by a He-Ne laser using a reference interferometer. For a monochromatic measurement, the signal detected is a simple cosine with the intensity varying in function of the displacement of the mirror, more precisely the retardation  $\delta$  of ray 1 with respect to ray 2. Usually, a polychromatic source is used with a wide range of wavenumbers. Fourier transformation is then required to obtain a spectrum of absorbance against wavenumber.

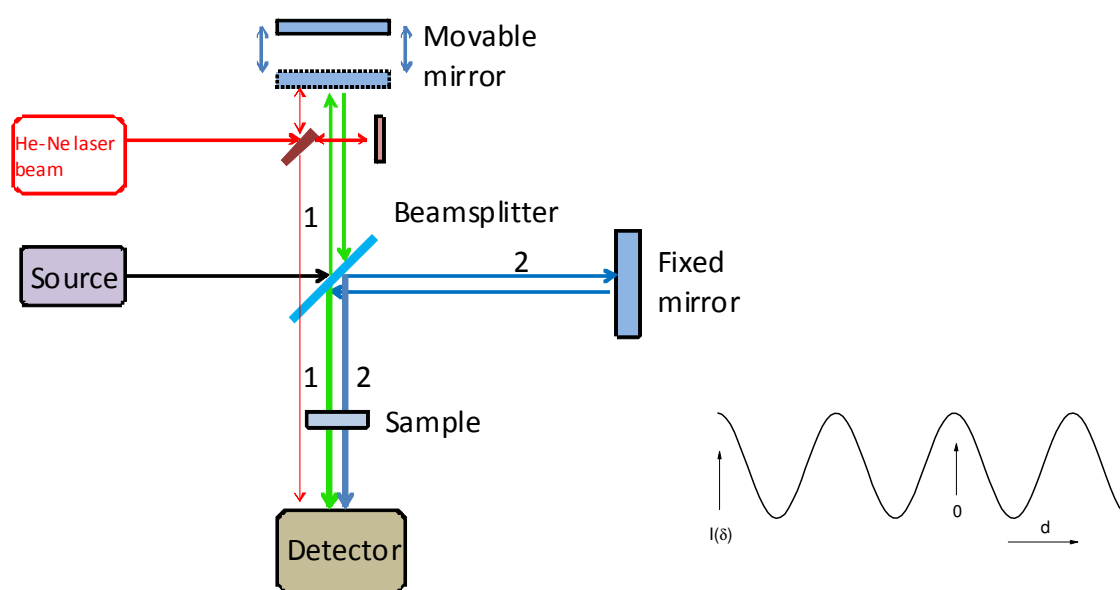


Figure 2.5: Schematic representation of a Michelson interferometer (left). The interferogram of a monochromatic source (right) is a simple cosine curve (158).

### 2.2.3 Fourier-Transformation

For a polychromatic source radiation, the interferogram is complicated. The intensity of the interferogram is given by

$$I(\delta) = \int_0^{\infty} S(\tilde{\nu}) \cos(2\pi\tilde{\nu}\delta) d\tilde{\nu} \quad \text{Equation 7}$$

Where  $S$  is the source intensity,  $\tilde{\nu}$  is the wavenumber of the radiation, and  $\delta$  is the mirror displacement. To have a readable spectrum in terms of wavenumbers (Figure 2.6), we need to perform a Fourier transformation according to the equation:

$$S(\tilde{\nu}) = \int_0^{\infty} I(\delta) \cos(2\pi\tilde{\nu}\delta) d\delta \quad \text{Equation 8}$$

The two equations are interconvertible. It is important to note that the resolution of an IR spectrometer is inversely proportional to difference in pathlength due to the displacement of the mirror.

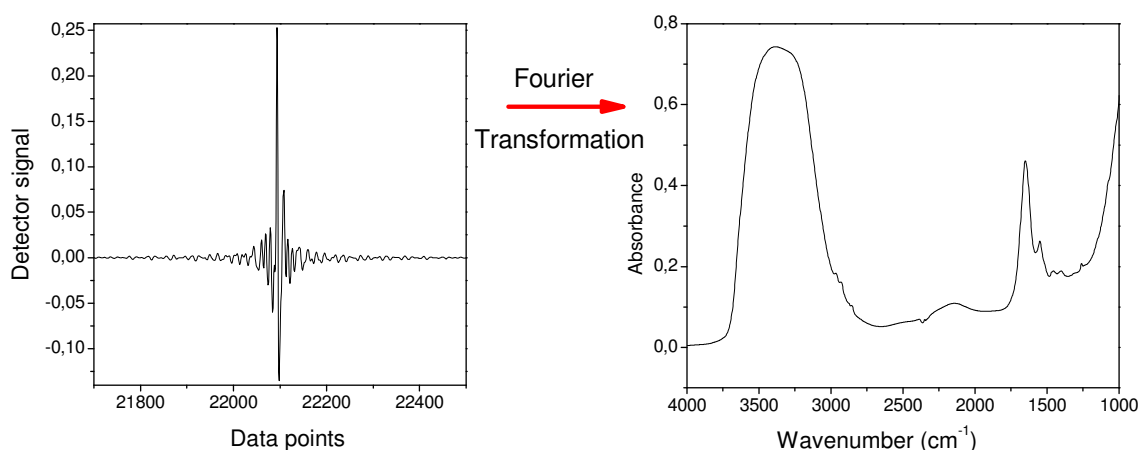
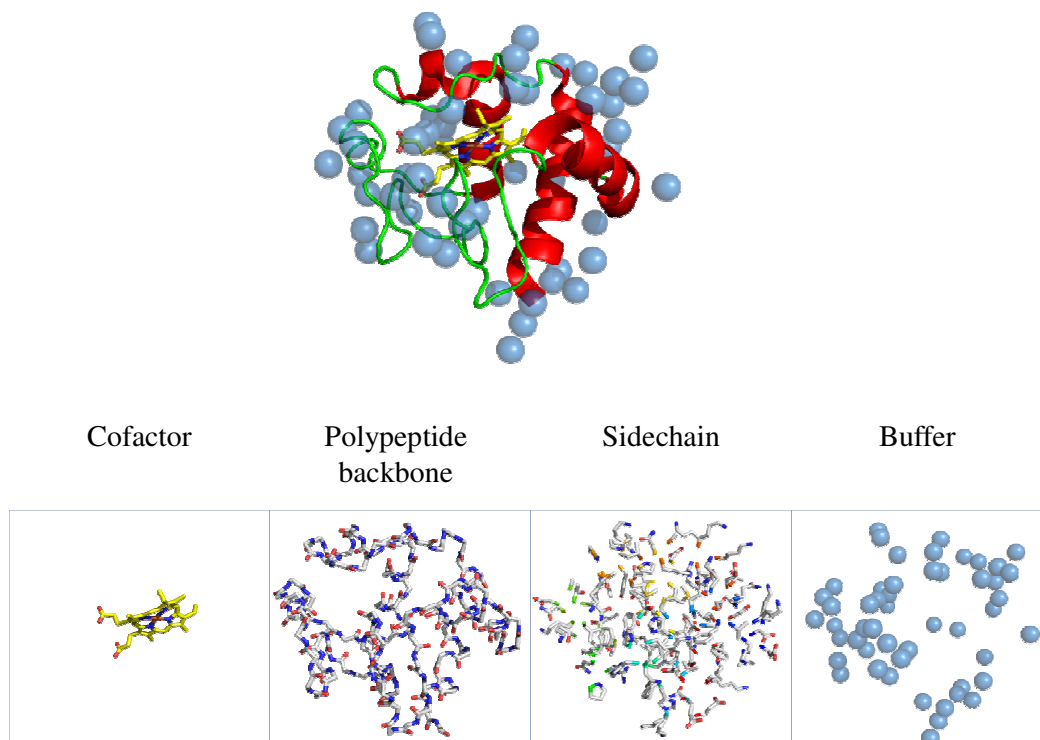


Figure 2.6: The interferogram (left) is Fourier-transformed to obtain an absorption spectrum in terms of wavenumber (right).

### 2.2.4 Study of proteins: why IR spectroscopy?

Proteins are macromolecular structures consisting of arrangement of amino acid residues linked by the peptide bond, cofactors may also be present. For example taking the cytochrome  $c$  represented in figure 2.7 as a model, the different components that are observed in IR are the  $c$  type heme as cofactor, the polypeptide back bone of the protein, amino acid side chain and the solvent/buffer of the medium.



**Figure 2.7: Representation of the cytochrome c in an aqueous environment. In IR spectroscopy, contributions from the cofactor, the polypeptide backbone, the side chains and the buffer/solvent can be observed.**

The contributions of all the components usually overlap. The polypeptide backbone contribution gives rise to large signals as seen in [figure 2.8](#). In the mid-IR region, the most energetic vibrations observed are the stretching mode of N-H designated the amide A ([Table 2.1](#)). At lower frequencies, the amide B arises from the  $\nu(\text{C-H})$  vibrational modes.

Designation	Wavenumber ( $\text{cm}^{-1}$ )	Assignment
Amide A	3500-3000	$\nu(\text{N-H})$
Amide B	3000-2800	$\nu(\text{C-H})$
Amide I	1700-1600	80% $\nu(\text{C=O})$ , 10% $\nu(\text{C-N})$ , 10% $\delta(\text{N-H})$
Amide II	1575-1480	coupled mode, 60% $\delta(\text{N-H})$ , 40% $\nu(\text{C-N})$
Amide III	1320-1220	coupled mode, 30% $\delta(\text{C-N})$ , 30% $\delta(\text{N-H})$ , 10% $\nu(\text{C=O})$ , 10% $\delta(\text{O=C-N})$

**Table 2.1: Amide contribution of the polypeptide backbone in the mid-IR region**

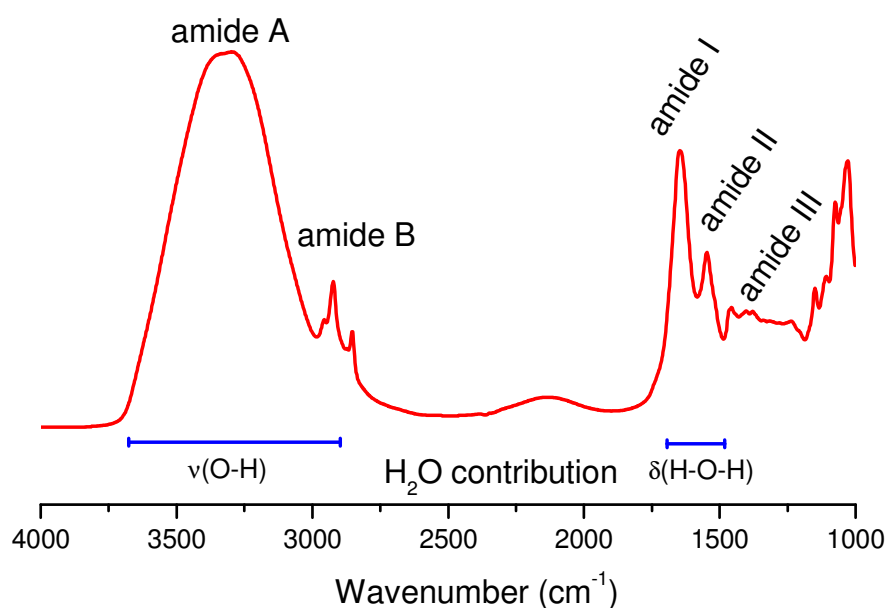


**Figure 2.8:** Absorption spectrum of a protein in solution in the mid-IR region depicting contributions of the amide bands and contribution from water.

The amide I region is the most studied spectral region and mainly include  $\nu(\text{C}=\text{O})$  of the polypeptide backbone. This signal is very sensible to secondary structure of proteins. Band separation is used to probe secondary structure of proteins (159-161). Indeed depending on the hydrogen bonding environment of the backbone, the polypeptide adopts a specific secondary structure. Each secondary structural elements is represented by the  $\nu(\text{C}=\text{O})$  mode of the polypeptide backbone and is summarized in [table 2.2](#).

Wavenumber ( $\text{cm}^{-1}$ )	Secondary structure assignment
1624-1642	$\beta$ -sheet
1648	Random coil
1656	$\alpha$ -helix
1663	$3_{10}$ -helix
1667-1685	$\beta$ -turns
1691-1696	$\beta$ -sheet

**Table 2.2:** Protein secondary structure is probed by band separation of the amide I band. Each element can be observed at specific wavenumbers.

Unless performed correctly, the study of the amide I band in the determination of protein secondary structure can be error prone. Indeed, the  $\delta(\text{H-O-H})$  mode from water also contributes in this spectral region, furthermore most buffers also give signals in this region (162). Dried samples are studied to limit the contribution of water. But for unstable

samples, removing the solvent can lead to change in conformation or even denaturing. Measurements in D<sub>2</sub>O can also be performed to increase the precision of the technique, and works correctly for small soluble proteins. But for large membrane proteins, not all the H bound to the N on the polypeptide backbone are exchanged, and giving rise to more complex spectral data. The experimental setup consists of an ATR (attenuated total reflexion) crystal on which a deposition of the sample is made. Depending on the nature of the crystal, the protein may find a conformation more favorable than another. The ATR setup in itself has a polarizing effect and has long been neglected in these experiments (163). Nevertheless this technique gives a good estimation of the protein secondary structure. It can also be used for example to check the integrity of a mutant enzyme compared to the wild type.

The amide II and amide III signatures involve coupled modes which are less specific to the secondary structure of the protein. Although the study of the amide III mode has been restricted due to contributions of amino acid side chain in the same region, the study of the amide II band has been of interest in the study of protein dynamics. At lower frequencies, between 800-500 cm<sup>-1</sup>, less energetic modes of the polypeptide backbone are observed. Individual amino acid contribution can hardly be observed in the absorption spectrum of a protein except for the intense  $\nu(\text{CC})$  ring,  $\delta(\text{CH})$  modes of tyrosine at 1516-1518 cm<sup>-1</sup> that overlaps the amide II band. Contribution from the buffer and the solvent are also observed. The  $\nu(\text{O-H})$  vibrational mode overlaps the amide A band whereas  $\delta(\text{H-O-H})$  has a high absorption in the amide I region.

### **2.2.5 Hydrogen/deuterium exchange kinetics**

Hydrogen/deuterium exchange (HDX) kinetics is a technique used to measure accessibility of a protein sample to the solvent. Accessibility of specific transport channels as well as allosteric changes can be observed. HDX is monitored by different experimental setup including mass spectrometry, NMR spectroscopy and IR spectroscopy (164-166). It is also used to monitor flexibility, hydrogen bonding as well as conformational changes of proteins. The protons involved in HDX are those bound to nitrogen on the polypeptide backbone. Since all the peptides excluding proline do possess an amide proton, the rate of exchange of amide H is used to monitor HDX experiments (167). Side chain hydrogen atoms which are bound to S, O, N and aromatic residues are also exchangeable. Hydrogen

toms that are bound to carbon atoms require high energy usually obtained from a chemical reaction to be exchanged (167). In mass spectrometry, the protein is mixed with the D<sub>2</sub>O buffer, a sample is taken after each minute and the HDX is stopped either by quick-freezing the sample or reducing the pH. The mass spectra are recorded and data is plotted against time to monitor HDX (164).

In IR spectroscopy, the experimental setup is simpler and the exchange is studied directly in the experimental setup. Upon HDX, the most important changes observed, arise from modes involving the N-H bond on the backbone. The  $\nu(\text{N-H})$  is downshifted to 3300  $\text{cm}^{-1}$  to 2400  $\text{cm}^{-1}$ . This band cannot be used to monitor HDX because  $\nu(\text{O-D})$  also contribute in this region. The  $\delta(\text{N-H})$  mode in the region between 1575 and 1545  $\text{cm}^{-1}$ , known as the amide II band also shifts to lower frequencies. Upon HDX, the amide II band is decoupled and  $\delta(\text{N-D})$  mode shifts to 1035  $\text{cm}^{-1}$  whereas the  $\nu(\text{C-N})$  mode shifts to 1455  $\text{cm}^{-1}$ . Spectral changes upon HDX is summarised in [table 2.3](#).

HDX kinetics can be monitored by integrating the amide II band as its decrease reflects the % of exchanged protons of the backbone. The area of the amide I band which arises mainly from  $\nu(\text{C=O})$  of the polypeptide backbone should not vary upon HDX although a 10  $\text{cm}^{-1}$  downshift is observed. This shift arises by a small change in the coupled N-D vibration upon HDX. Since the amount of protein observed may vary during the HDX experiment, the % of amide protons is always given with respect to the amide I and amide II band (160, 168).

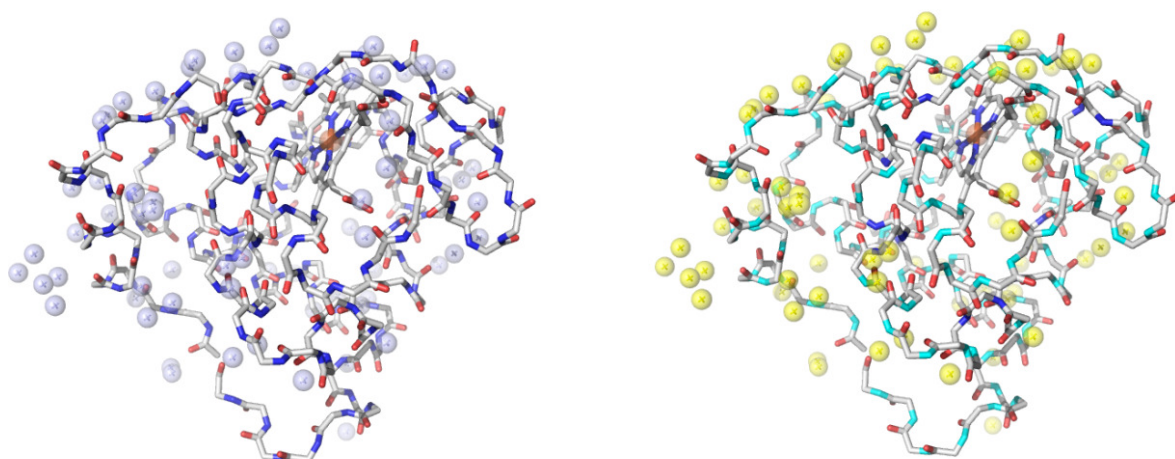


Figure 2.9: Left panel depict a sample in H<sub>2</sub>O, with the water molecules in grey. Upon HDX, H on the surface of the molecule is exchanged to D (stick model cyan); whereas H located in the hydrophobic core are not exchanged (stick model blue).

Monitoring the rate of HDX, different categories of amide H can be observed and distinguished. Amide H just on the surface of the protein will be exchange rapidly (169). Amide H just beneath the surface of the protein will follow a slower exchange kinetic. Amide H located in channels that is accessible to the solvent will exchange slower than the former two groups. The last group consists of amide H that are not accessible to the solvent and that are not exchanged (170). The latter group involves mainly amide H of residues forming membrane bound helices (Figure 2.9). The rate of HDX of the different groups is also a parameter to monitor conformational changes.

Vibrational mode		Wavenumber (cm <sup>-1</sup> )	
H <sub>2</sub> O	D <sub>2</sub> O	H <sub>2</sub> O	D <sub>2</sub> O
$\nu(\text{O-H}), \nu(\text{N-H})$	$\nu(\text{O-D}), \nu(\text{N-D})$	3500-3100	2600-2350
$\nu(\text{C=O})$	$\nu(\text{C=O})$	1646	1641
$\delta(\text{N-H})/\nu(\text{C=N})$	$\delta(\text{N-D})$	1543	1035
	$\nu(\text{C=N})$		1455

Table 2.3: Band shift observed upon hydrogen/deuterium exchange.

### 2.2.6 Electrochemistry

The proteins studied in this work are involved in electron transfer. A spectroelectrochemical cell may be used to study electrochemical reactions by spectroscopy. A setup consisting of two electrodes cannot control precisely an applied potential mainly since the current would pass through the reference electrode. A three electrode setup is required consisting of a working electrode, a reference electrode and a counter electrode (figure 2.10).

The working electrode is the site where the redox reaction takes place. The reference electrode has a specific and constant potential. It allows the application of precise potential at the working electrode. Finally the counter electrode allows the passage of current from the working electrode without going through the reference electrode.

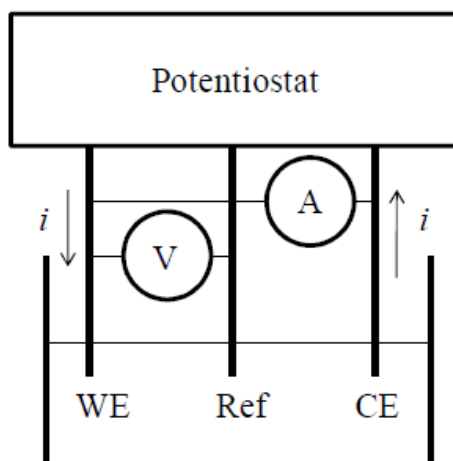


Figure 2.10: Representation of a 3 electrode setup for electrochemistry.

With the thin layer electrochemical cell, we can study a redox active sample in its oxidized state or reduced state. Since the UV-visible spectral properties of redox cofactors are dependent on the redox state of the molecule, redox titration can be monitored in the UV-visible. A detailed description of the thin layer electrochemical cell is given in the material and methods section 3.2. The thin layer electrochemical cell is also used in IR spectroscopy. The description of the redox potential can be made by the Nernst equation that includes the information of the redox potential in function of the concentration of the reduced and oxidized state. In spectroelectrochemistry, the concentration is indirectly obtained from UV-visible or IR spectra. Details on methods are given in [section 3.3](#).

### 2.2.7 Difference spectroscopy

In IR spectroscopy, contributions from the protein sample, the buffer and water are observed. Small changes induced by a reaction are difficult to depict. Difference spectroscopy has been developed as an answer to this problem as only changes induced by the reaction are highlighted. The difficulty of this technique is that the reaction must be induced in the analysis cell. The reaction can be for example light induced, substrate induced or redox induced (154, 168, 171-173). For redox active proteins difference spectra can be obtained in transmission with the optically transparent thin layer electrochemical cell (154).



As mentioned before, the intense absorption of water in the amide I region makes analysis difficult. In the spectroelectrochemical cell, the pathlength is at most 10  $\mu\text{m}$  thick which decreases the contribution of  $\text{H}_2\text{O}$  provided the sample is concentrated enough. The potential of the sample is controlled by a three electrode setup connected to a potentiostat.

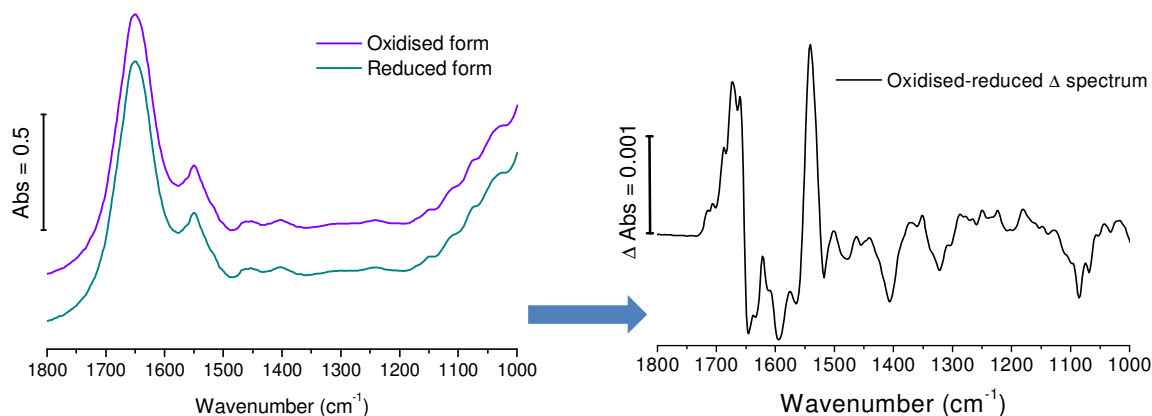


**Figure 2.11:** The absorption spectra of the oxidized and reduced form are similar. The difference spectrum is obtained by subtraction the spectrum of the reduced form of the enzyme from the spectrum of the oxidized enzyme.

Either the oxidized form or the reduced form of the protein is studied. The absorbance unit of a difference spectrum is approximately 500 times smaller than that of an absorbance spectrum. To have highly defined spectral data, the oxidized form and the reduced form are cycled several times and the data is averaged. This step reduces the signal to noise ratio.

Different strategies have been used to assign difference spectra. For the attribution of signals arising from the cofactor, model compounds like heme for hemes have been studied (174-176). FMN, FAD as well as quinone have been studied (177). Coupled to computational methods, the attribution of FAD signals for example is well documented (178, 179). For contribution side chain residues, individual amino acids have been studied and the extinction coefficient of each mode is also well documented. Furthermore, solvent  $\text{H}_2\text{O}/\text{D}_2\text{O}$  exchange can also help in signal attribution (180, 181). Conformational changes in a protein sample are also detected in difference spectroscopy as signals in the amide I region are characteristic of the secondary structure involved in the reaction (180, 182).

## **Chapter III: Materials and methods**

### **3.1 Sample preparation**

#### **3.1.1 The Na<sup>+</sup> pumping NADH:quinone oxidoreductase from *Vibrio cholerae***

The Na<sup>+</sup>-NQR wild type and mutant enzyme samples were prepared in the laboratory of Prof. Blanca Barquera, Department of Biology, Center for Biotechnology and Interdisciplinary Studies, Rensselaer Polytechnic Institute, Troy, New York by Dr. Oscar Juarez and Dr. Michael E. Shea.

##### **3.1.1.1 Wild type enzyme**

As reported before, recombinant Na<sup>+</sup>-NQR was cloned in a pBAD vector and over expressed in *Vibrio cholerae* cells (81). Purification was performed on a Ni-NTA affinity column, followed by a fast flow in DEAE sepharose column for cation exchange (112). At this level, the samples are in 50 mM TRIS-HCl pH 8.0, 1mM EDTA, 0.05%  $\beta$ -D dodecyl maltoside (weight/volume) and 5% glycerol (volume/volume). Prior to studies, the sample was washed with 50 mM Tris-HCl at pH 8.0, 0.05%  $\beta$ -D dodecyl maltoside and 150 mM of either LiCl, NaCl, KCl, RbCl or NH<sub>4</sub>Cl. This step consisted of 3 washes with 400  $\mu$ L buffer on AMICON centrifugal membranes with a cut off of 100 kDa at 6000 rpm on the Eppendorf Centrifuge 5804R. EDTA and glycerol are omitted. EDTA can form metal-ligand complexes with the salts added and the mediators. Glycerol helps maintaining the integrity of the enzyme upon freezing. But for electrochemical measurements, glycerol slows the rate of electron transfer. Fresh samples were prepared before each experiment without EDTA and glycerol. The resulting sample was approximately at 0.75 mM estimated using  $\epsilon_{460\text{nm}} = 34.6 \text{ mM}^{-1}\text{cm}^{-1}$  for the oxidized minus reduced form of the enzyme (111). As a control of the integrity of the cofactors of the sample,  $\epsilon_{560\text{nm}} = 6.7 \text{ mM}^{-1}\text{cm}^{-1}$  for the oxidized minus reduced form of the enzyme has also been used (111).

For IR spectroscopy, the buffer was exchanged to phosphate to avoid contributions of Tris that overlaps signals in the amide I region. The most intense contribution of phosphate buffer are located between 1100-1050  $\text{cm}^{-1}$ , a region where the phosphate groups from FMN and FAD are also expected. For mid-IR studies, the sample was washed with 50 mM phosphate buffer at pH 8.0, 0.05%  $\beta$ -D dodecyl maltoside (DDM) and 150 mM of either NaCl, LiCl, KCl or RbCl. For experiments with Na<sup>+</sup> and Li<sup>+</sup> ions, sodium phosphate and lithium phosphate buffers were used respectively. Arguably, there are still

K<sup>+</sup> ions present in samples with Rb<sup>+</sup>. But the redox dependence observed are similar may it be in Tris buffer or phosphate buffer.

### 3.1.1.2 Mutant enzymes

Quickchange site-directed mutagenesis kit (Stratagene) was used to build the mutant enzyme from templates of the Na<sup>+</sup>-NQR wild-type operon. In the NqrB, aspartic acid 397 is replaced by glutamic acid (89). This mutant was made to study the role of ions. Mutant enzyme for the study of the quinone binding has also been constructed. Glycine 140 in the NqrB has been replaced by alanine. Samples were concentrated on Amicon centrifugal device with a cut-off of 100 kDa in buffer solution as described for the wild type.

### 3.1.2 Cytochrome *c*<sub>552</sub> and the Cu<sub>A</sub> fragment of the *ba*<sub>3</sub> oxidase from *Thermus thermophilus*

Cytochrome *c*<sub>552</sub> was prepared in Prof. Bernd Ludwig laboratory, Molekulare Genetik, Institut für Biochemie, Johann Wolfgang Goethe-Universität, Max-von-Laue-Str. 9. 60438 Frankfurt am Main, Germany, by Carolin Werner.

The cytochrome *c*<sub>552</sub> gene was cloned in a pET22b vector which guides the protein in the periplasm. Co-transforming of the *E.coli* cells with heme maturation plasmid helps in heme incorporation in the apoprotein (138). Purification was done according to Fee et al (137). The samples were prepared in two different buffer solutions prior to studies, either 30 mM KPi at pH 9.0 or 30 mM Tris at pH 7.0. Both buffer solutions also contained 100 mM KCl. Sample concentration was determined by  $\epsilon_{\text{red-ox } 552 \text{ nm}} = 21.0 \text{ mM}^{-1} \cdot \text{cm}^{-1}$  (138).

The Cu<sub>A</sub> fragment sample was prepared in Prof. James Fee laboratory, Department of Molecular Biology, The Scripps Research Institute, La Jolla, CA, 92037, USA, by Ying Chen.

The Cu<sub>A</sub> domain was expressed in *E.coli* cells and purified as described before (132). This domain also contains a hydrophobic helix which helps in anchoring the fragment to the membrane. The latter has been removed. As for the cyt.*c*<sub>552</sub>, the protein was concentrated in either KPi or Tris buffer at pH 9 and 7 respectively.  $\epsilon_{530\text{nm}} = 3.1 \text{ mM}^{-1} \cdot \text{cm}^{-1}$  was used to determine the concentration of the samples.

### 3.1.3 The $bc_1$ - $aa_3$ supercomplex from *Corynebacterium glutamicum*

The  $bc_1$ - $aa_3$  supercomplex was been prepared in the laboratory of Prof. Carola Hunte, Freiburg, by Dr. Thomas Kleinsroth.

The protein was overexpressed from plasmid in *Corynebacterium glutamicum* cells. The purification step is not published yet. The protein was purified on a streptavidin column and concentrated on a glucose gradient. Due to the presence of 3 types of hemes, the concentration can be determined by  $\epsilon_{\text{red-ox } 600 \text{ nm}} = 23.2 \text{ mM}^{-1} \cdot \text{cm}^{-1}$  for the  $a$ -hemes,  $\epsilon_{\text{red-ox } 565 \text{ nm}} = 44 \text{ mM}^{-1} \cdot \text{cm}^{-1}$  for the  $b$ -hemes and  $\epsilon_{\text{red-ox } 550 \text{ nm}} = 38.2 \text{ mM}^{-1} \cdot \text{cm}^{-1}$  for the  $c$ -hemes (141).

## 3.2 The thin layer electrochemical cell

The optically transparent thin layer electrochemical cell was used to monitor spectroelectrochemical changes (154). In the UV-visible, redox titration of cofactors was performed with this cell. In the mid-IR, the contribution of the cofactors, local conformation changes, sidechain of specific residues are observed.

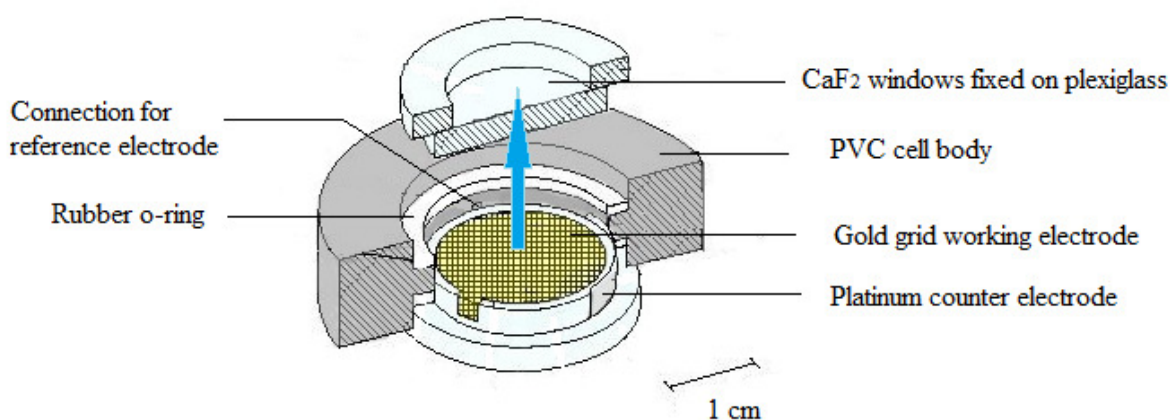


Figure 3.1: Schematic representation of the electrochemical cell. The blue arrow shows the optical axis.

The cell consists of a three electrode setup; a gold grid as working electrode, a platinum counter electrode and a Ag/AgCl 3 M KCl reference electrode (add 208 mV for SHE') (Figure 3.1). Both the platinum counter electrode and the gold grid are in contact to platinum threads for connection with a home-made potentiostat. The PVC body has four inlets, three of which are for screwing the two platinum threads for the working and counter electrode, and also the reference electrode. The fourth inlet is for addition of buffer to the experimental medium to complete the volume of the electrochemical cell.

Undesired air bubbles are also eliminated when the buffer is added. To prevent protein adsorption to the gold surface which can lead to denaturation, the gold grid has been modified by dipping in a solution of 2 mM cysteamine and 2 mM mercaptopropionic acid for at least one hour. These thiol based organic compounds are self-assembled on the gold surface forming a network of  $-\text{COOH}$  and  $-\text{NH}_2$  groups to which the protein interact (Figure 3.2).

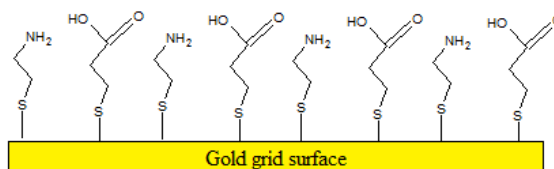


Figure 3.2: Schematic representation of the gold surface modified by cysteamine and mercaptopropionic acid.

Two  $\text{CaF}_2$  windows (fixed on plexiglass support) were mainly used due to the transparency of  $\text{CaF}_2$  in both UV-visible and mid-IR. The sample is placed on the modified gold grid working electrode and squeezed between the two windows. Path-length did not exceed 15  $\mu\text{m}$ . Two rubber o-rings were used while mounting the cell to prevent leaking of sample and thus providing a constant environment during the experiments. The cell is placed between two steel plates which are cooled to 10  $^\circ\text{C}$  for redox titrations and to 5 $^\circ\text{C}$  for mid-IR studies.

### **3.3 Redox titration monitored in the UV-visible**

The mid-point potential of several cofactors can be determined by combining electrochemistry to the UV-visible provided a change in the redox state results in a change of spectral properties. Prior to the titration, the protein sample is mixed with several mediators (Table 3.1) (63). The role of these mediators is to facilitate electron transfer from the working electrode to the protein cofactors as the mid-point potential of the mediators covers a wide range of potential. The final concentration of each compound is approximately 25  $\mu\text{M}$ . If used at a higher concentration, the spectral contributions of these mediators will be observed and will have to be subtracted from the contribution of the protein.

The redox state of the protein sample is controlled by a home-made potentiostat. For example in the titration of the  $\text{Na}^+\text{-NQR}$ , an oxidative potential of +200 mV is applied and taken as background after 15 mins of equilibration. A potential sweep is performed

with 10 mins of equilibration for each 50 mV step to -600 mV. This first titration gives an approximate potential of the cofactors for a given sample. The next titration will consist of shorter steps and longer equilibration. The mid-point potential of all the enzymes studied have been established. Information regarding the potential range studied, the potential step and equilibration time is presented in (Table 3.2).

Mediator	$E_m(\text{mV})$ vs. Ag/AgCl
Ferrocenylmethyltrimethylammoniumiodid	607
1,1'-Ferrocenedicarboxylic acid	436
Potassiumhexacyano-ferrate(II) trihydrate	212
1,1'-Dimethylferrocene	133
Quinhydrone	70
Tetrachloro-1,4-benzoquinone (p-Chloranil)	72
N,N,N',N'-Tetramethyl-p-phenylenediamine dihydrochloride	62
2,6-Dichloroindophenolsodium salt hydrate	9
Hexaminruthenium(III)chlorid	-8
Anthraquinone-2-sulfonic acid sodium salt	-23
1,4 Naphthoquinone	-63
Trimethylhydroquinone	-108
Anthraquinone	-108
5-Hydroxy-1,4-naphthoquinone	-158
Duroquinone	-198
Menadione	-220
2-Hydroxyl-1,4-naphthoquinone	-333
9,10-Antraquinone-2,6-disulfonic acid disodium salt	-433
Neutral red	-515
1,1'-Dimethyl-4,4'-bipyridium dichloride hydrate	-628

**Table 3.1: 19 mediators used for electrochemical measurements and their corresponding mid-point potential (63).**

Sample	Potential range studied	Potential step	Equilibration time (mins)
Na <sup>+</sup> -NQR	-625 to +100	25 or 20	40
Cu <sub>A</sub>	-300 to +300	50	30
Cyt. <i>c</i> <sub>552</sub>	-300 to +300	50	30
Cu <sub>A</sub> -cyt. <i>c</i> <sub>552</sub> complex	-300 to +300	50	30
<i>bc</i> <sub>1</sub> - <i>aa</i> <sub>3</sub> supercomplex	-650 to +250	50 or 25	60

**Table 3.2:** The potential range, the potential step and equilibration time used for each sample studied.

When an overpotential is applied, equilibration time is shorter, typically 10 mins. But in the proximity to the expected redox mid-point potential ( $\pm 150$  mV) equilibration time is longer and the potential step applied needs to be shorter. This optimization of the redox titration gives highly reproducible results. At the end of titration, the integrity of the sample is checked by performing full oxidized-reduced and reduced-oxidized difference spectra. All the titrations done were reproduced at least twice. The expected error is  $\pm 10$  mV.

Data exploitation starts with the normalization of all the difference spectra at a wavelength where no contributions of the cofactors are observed. This step is crucial, because the baseline is taken at the very start of the experiment, and with time a thermal drift of the baseline is observed. The difference in absorbance ( $\Delta$ Abs) observed is then plotted against the applied potential.

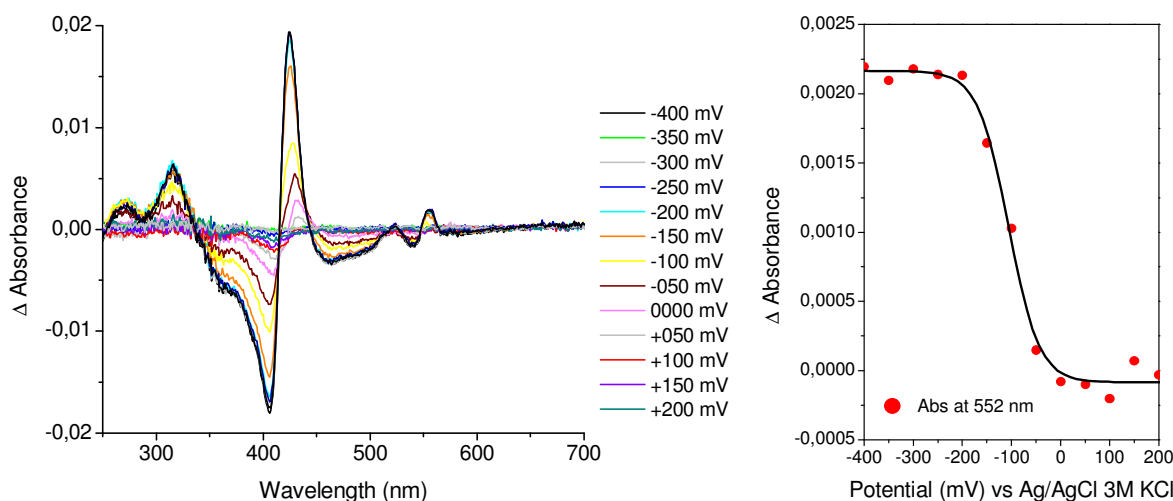


**Figure 3.3:** On the left panel, the difference spectra of cytochrome *c*<sub>552</sub> from -400 mV to +200 mV for a reductive titration. On the right panel, the plot of  $\Delta$ absorbance recorded at 552 nm against the applied potential, a Nernst equation is fitted (black curve).

Using the Origin software, a Nernst equation is fitted to the plot at different wavelength. For example in the case of cytochrome *c*<sub>552</sub>, either the Soret band or smaller *q*



bands at 552 nm can be used to determine the potential (Figure 2.3). The general Nernst equation is as follows:

$$E_M = E^0 + \frac{RT}{nF} \ln \frac{a_{ox}}{a_{red}} \quad \text{Equation 9}$$

With  $E_M$ : mid-point potential,  $E^0$ : standard potential,  $R$ : universal gas constant of  $8.314 \text{ J.K}^{-1}.\text{mol}^{-1}$ ,  $T$ : temperature in K,  $n$ : number of electrons transferred,  $F$ : Faraday constant of  $9.648.10^4 \text{ C.mol}^{-1}$ ,  $a_{ox}$  and  $a_{red}$ : the chemical activity of the oxidized and reduced species respectively. Assuming that the chemical activity is proportional to the spectral changes observed, the equation can be written:

$$E_M = E^0 + \frac{RT}{nF} \ln \frac{A_{ox} - \Delta A}{\Delta A - A_{red}} \quad \text{Equation 10}$$

With  $\Delta A$ : the difference in absorbance observed,  $A_{ox}$ : the absorbance for the fully oxidized state,  $A_{red}$ : the absorbance for the fully reduced state. The final equation used for the fitting is

$$\Delta A = A_{red} + \frac{(A_{ox} - A_{red})}{1 + \exp\left(\frac{x - b_1}{24.4}\right)} \quad \text{Equation 11}$$

With  $x$ : the applied potential,  $b_1$ : the mid-point potential, 24.4: is an estimate of the constants for  $n = 1$ , and  $T = 283 \text{ K}$  ( $10^\circ \text{C}$ ). This method works with one or two components at a specific wavelength. But, when three or more components are involved at the same wavelength, this equation is error prone in terms of fitting. Furthermore, if two redox transitions have close mid-point potentials, it is also difficult to distinguish between them. This is the case for the  $\text{Na}^+$ -NQR, where the flavins have broad signals spread in the visible domain.

The strategy used to determine the redox potential in such cases is to plot the first derivative of the difference in absorbance observed ( $\delta\Delta\text{Abs}$ ) against the applied potential (183). The resulting plot can easily be fitted by simple Gaussian equations. The half-width of the Gaussian is dependent on the number of electrons transferred, 90 mV for a two electron transfer and 45 mV for a one electron transfer. The amplitude of the Gaussian is proportional to the molar extinction coefficient of the component at the specific wavelength. With this method, multiple components contributing at a specific wavelength can be separated; the error observed by this method is  $\pm 15 \text{ mV}$  estimated from an experiment reproduced four times (184).

### 3.4 FTIR measurements

#### 3.4.1 Redox induced mid-IR difference spectroscopy

Difference spectra are obtained between two different states of the enzyme. In this work, the proteins were studied with respect to their redox state. The electrochemical cell is mounted in a Bruker Vertex 70 (Germany) spectrometer equipped with a liquid nitrogen cooled MCT detector for the 4000-1000 $\text{cm}^{-1}$  range. The scan velocity used was 20 kHz and typically 2 \* 256 interferograms were recorded at 4  $\text{cm}^{-1}$  resolution for the oxidized and the reduced form of the enzyme. This step was cycled at least 50 times. Difference spectra have low absorbance intensities when compared to transmission spectra. Averaging the data recorded for the oxidized-reduced and reduced-oxidized difference spectra helps in improving signal to noise. The contribution of water vapor in the spectrometer is also observed. The strategy used here is to have a constant pumping of dry air in the sample compartment of the spectrometer. Although we cannot abolish completely the presence of humidity, it is kept constant throughout the experiment.

The potential applied for the oxidized and the reduced form of the enzyme, as well as equilibration time are presented in [Table 3.3](#). The choice of potential range was done with respect of the values obtained by redox titration. Prior to each experiment, the difference spectra were done in UV-visible to determine the equilibration time for oxidation and reduction. For sample stability, temperature was maintained at 5°C throughout the experiment.

Sample	Potential (mV)		Equilibration time (sec)	
	Ox	Red	Ox	Red
Na <sup>+</sup> -NQR wild type	200	-625	120	240
Na <sup>+</sup> -NQR D397E	200	-625	120	240
Na <sup>+</sup> -NQR G140A	200	-625	120	240
Na <sup>+</sup> -NQR wild type, step	200	-280	120	300
Cyt. <i>C</i> <sub>552</sub>	300	-300	90	180
Cu <sub>A</sub> fragment	300	-300	90	180
Complex cyt. <i>C</i> <sub>552</sub> -Cu <sub>A</sub>	300	-300	90	180

**Table 3.3:** The potential applied for oxidation and reduction, and equilibration time for each sample studied.

At the end of the experiment, a redox induced difference spectrum in the UV-visible spectral range was performed again to verify the stability of the sample. Since the overall time of the experiment is about 20 hours, it is important that the internal medium of the electrochemical cell is kept constant. Any leak will result in unwanted drop in signal intensity and lost in reversibility of the oxidized-reduced and reduced-oxidised difference spectra.

### 3.4.2 Hydrogen-deuterium exchange kinetics monitored in mid-IR

HDX kinetics was monitored on a Bruker IFS28 spectrometer equipped with a DTGS detector. The experimental setup, the Bruker BioATR 2 (Figure 2.7), consists of a two compartment dialysis cell mounted on a ATR crystal. In total reflection mode the evanescence wave on the surface of the crystal penetrates only 6-8  $\mu\text{m}$ . The latter is in fact made of two crystals, the zinc selenide crystal is protected by a silicium crystal. The silicium crystal is hydrophobic and measurements with hydrophobic membrane proteins are better suited than for example with a diamond crystal.

The body of the cell is made of stainless steel. The two compartments are separated with a semi permeable cellulose membrane with a cutoff of 3 kDa. The advantage of using this two compartment system is that the mechanical perturbation of the sample in the lower is minimized. Furthermore, the sample in the lower compartment remains at a constant concentration. The upper compartment is connected to a circuit of tubing, with an input and an output. Buffer is pumped in the tubing system by an eternal pump with a constant flux of 0.12 ml/min. When closed the cell is air tight by different rubber o-ring. The temperature of the whole system was fixed at 5°C.

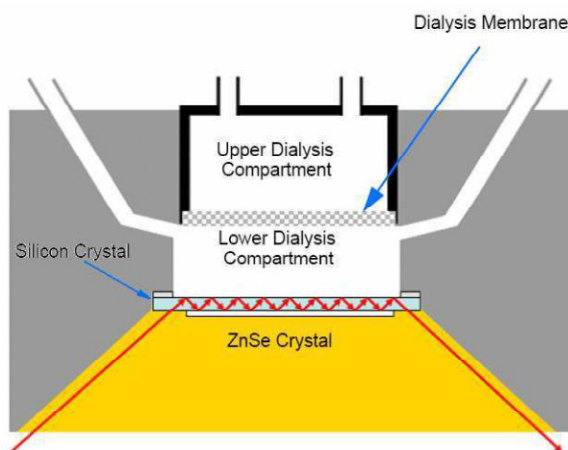


Figure 3.4: Schematic representation of the Bruker Bio ATR 2 dialysis system.

The HDX kinetics of the Na<sup>+</sup>-NQR wild type and the D397E mutant enzyme were measured with the four different ions, Li<sup>+</sup>, Na<sup>+</sup>, K<sup>+</sup> and Rb<sup>+</sup>. Prior to the measurements, the sample was mixed with *E.coli* membrane extract (Avanti 100500C) in an approximate molar ratio of 1:30 for four hours at 5°C on a thermomixer. The sample is placed on the crystal in the lower compartment and air-dried. The cell is closed and the sample is rehydrated by H<sub>2</sub>O buffer solution. Drying and then rehydrating the sample on the crystal surface, increases the amount of sample in direct contact with the crystal surface. The exchange starts when the rehydration step is over and the sample is stabilized that is when consecutive spectra are identical.

D<sub>2</sub>O buffer is flushed in the upper compartment with a flow rate of 0.95 ml/min and data is recorded. Blocks of 16 spectra are taken with 1 sec between each spectrum. The first block consists of spectra with 16 scans, mainly because the first few minutes the exchange is fast. Then blocks of 16 spectra are recorded with 32 and 64 scans. The flow rate is decreased to 0.2 ml/min and 16 spectra with 128 scans followed by 8 spectra with 256 scans are recorded. Finally 80 spectra are recorded with 256 scans with 20 mins between each spectrum. The first 12 mL of the D<sub>2</sub>O buffer solution are evacuated before a closed circuit is set in the upper compartment. The most complicated part is data analysis that is monitoring the rate of decrease of the amide II signature.

#### **3.4.2.1 HDX data analysis**

Data analysis starts with subtraction of H<sub>2</sub>O contribution since the H<sub>2</sub>O buffer also contributes to the recorded spectra but with different coefficient at a given measurement time. The first step is to calculate the coefficient of H<sub>2</sub>O present in all the recorded data. Then using this coefficient, the H<sub>2</sub>O contribution is removed from each spectrum. Furthermore although the concentration of the sample in the lower compartment is constant, the amount of sample in the vicinity of the evanescence wave does vary slightly. In order to limit, this all the spectra must be normalized with respect of an internal standard, the amide I band. The most intense band observed is the amide I signature which is less than 50 cm<sup>-1</sup> distant from the amide II band. The choice of the amide I signal as internal standard is also promoted by the fact that the intensity of this signal does not change upon HDX, although a 10 cm<sup>-1</sup> downshift is observed. The area of the amide I and amide II band are calculated by interactive integration (170, 185). Stepwise data processing is detailed as follows.

### 3.4.2.2 Determination of the coefficient of H<sub>2</sub>O in the recorded spectra

To determine the coefficient of H<sub>2</sub>O in the sample at a given time, the area of the large signal between 3800-2750 cm<sup>-1</sup> representative of both  $\nu(\text{O-H})$  and  $\nu(\text{N-H})$ , is calculated for each spectrum. The area of  $\nu(\text{C-H})$  stretching mode between 3000-2750 cm<sup>-1</sup> is also calculated. Simultaneously, the area of the band representative of the  $\nu(\text{O-D})$  mode is also calculated by interactive integration. Each integration is calculated with the Bruker OPUS software with a baseline correction as shown in [Figure 3.5](#).

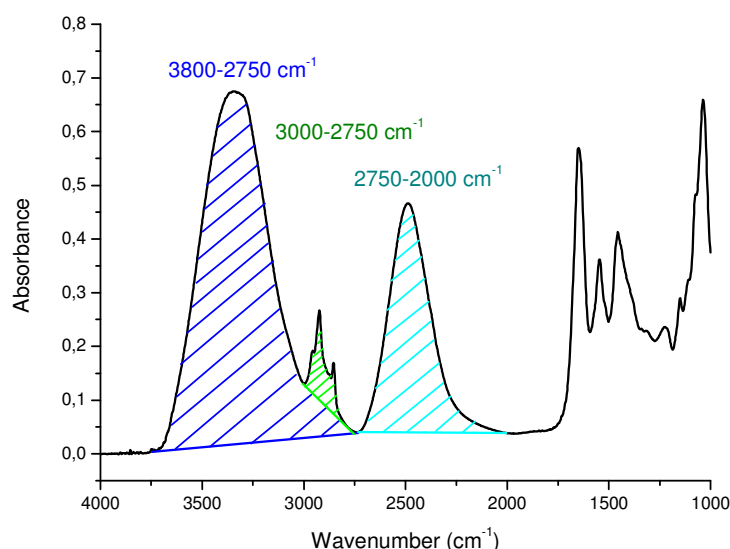


Figure 3.5: Integration of signals arising from the  $\nu(\text{O-H})$  3800-2750 cm<sup>-1</sup>, the  $\nu(\text{O-D})$  2750-2000 cm<sup>-1</sup> and the  $\nu(\text{C-H})$  3000-2750 cm<sup>-1</sup> with baseline correction.

The coefficient of H<sub>2</sub>O and D<sub>2</sub>O at a given time is then obtained from the following equations:

$$a_{\text{H}_2\text{O}} + b_{\text{D}_2\text{O}} + c_{\text{HOD}} = 1 \quad \text{Equation 12}$$

$$\text{With } a = \frac{\int_{2750}^{3800} S - \int_{2750}^{3800} D}{\int_{2750}^{3800} H - \int_{2750}^{3800} D}, \quad b = \frac{\int_{2000}^{2750} S - \int_{2000}^{2750} H}{\int_{2000}^{2750} D - \int_{2000}^{2750} H}, \quad c = 1 - a - b$$

$a$ ,  $b$  and  $c$  are the fraction of H<sub>2</sub>O, D<sub>2</sub>O and HOD respectively in a spectrum at a given time. For example in a sample with only H<sub>2</sub>O solvent,  $a = 1$ , both  $b$  and  $c$  are nil.  $H$  and  $D$  are the spectrum with only H<sub>2</sub>O and D<sub>2</sub>O (last spectrum obtained for the experiment) respectively.  $S$  is the spectrum at a given time  $t$ . To check the method to calculate the coefficients,  $a$ ,  $b$  and  $c$  are plotted against time ([Figure 3.6](#)). We can observe the fraction of D<sub>2</sub>O increases with time while the fraction of H<sub>2</sub>O decreases. The amount of HOD present also increases at the start of the experiment and decreases gradually.

Finally the spectrum of  $\text{H}_2\text{O}$  multiplied by the coefficient  $a$  is subtracted from each spectrum.

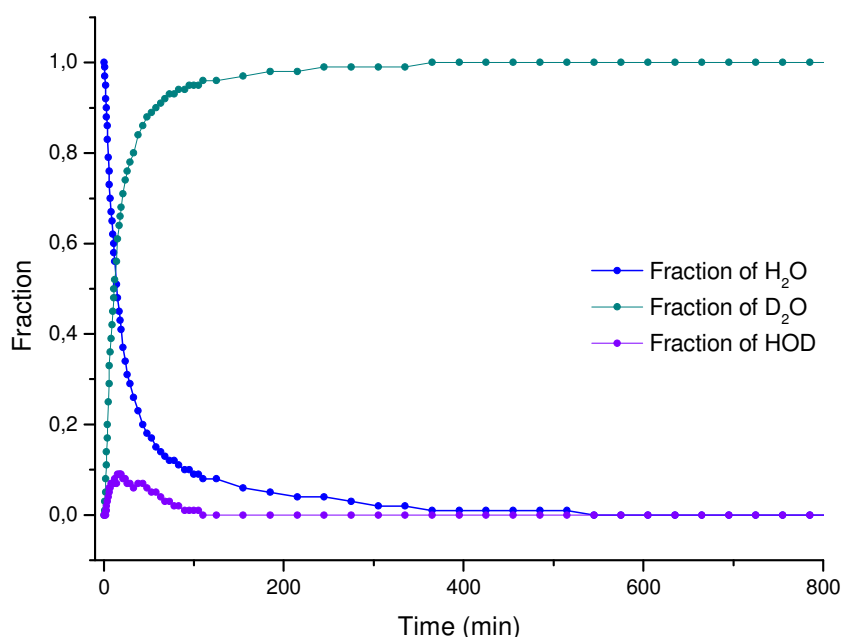


Figure 3.6: Fraction of  $\text{H}_2\text{O}$ ,  $\text{D}_2\text{O}$  and  $\text{HOD}$  present in the sample at a given time  $t$ .

### 3.4.2.3 Normalization with respect to the amide I band.

After subtracting the buffer, all the spectra are normalized with respect to the amide I band for the region between  $1710\text{--}1590\text{ cm}^{-1}$ . In other words, the area of the amide I band is taken as a constant internal standard although a  $10\text{ cm}^{-1}$  downshift is observed (Figure 3.7).

### 3.4.2.4 Monitoring the rate of amide II decrease.

The amide I and amide II bands are integrated for the region between  $1710\text{--}1600\text{ cm}^{-1}$  and  $1575\text{--}1525\text{ cm}^{-1}$  respectively (Figure 3.8). The range selected for integration was determined at  $1710$ ,  $1600$  and  $1575\text{ cm}^{-1}$ . The lower limit for the amide II contribution was selected at  $1525\text{ cm}^{-1}$  as at lower frequencies strong contributions from tyrosines are expected.

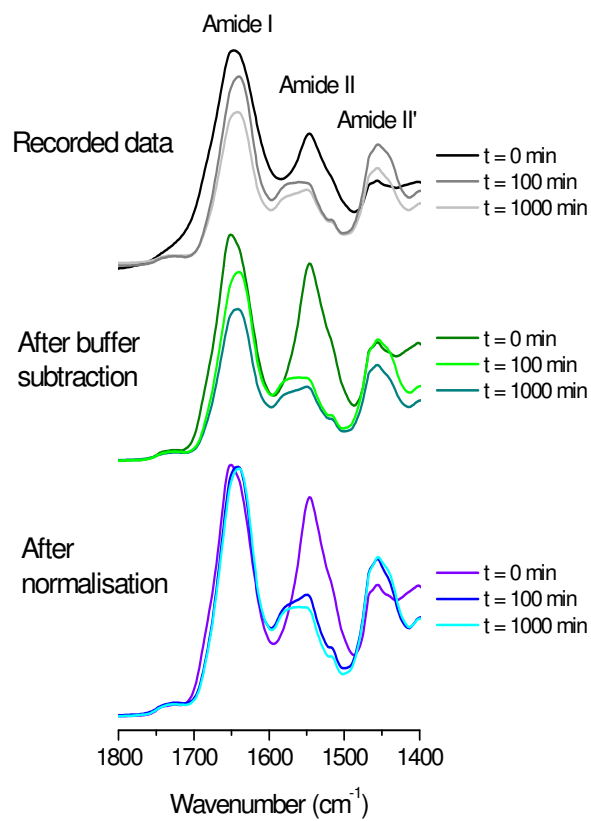


Figure 3.7: Buffer subtraction from the recorded data, and the normalization step with respect to the amide I band.

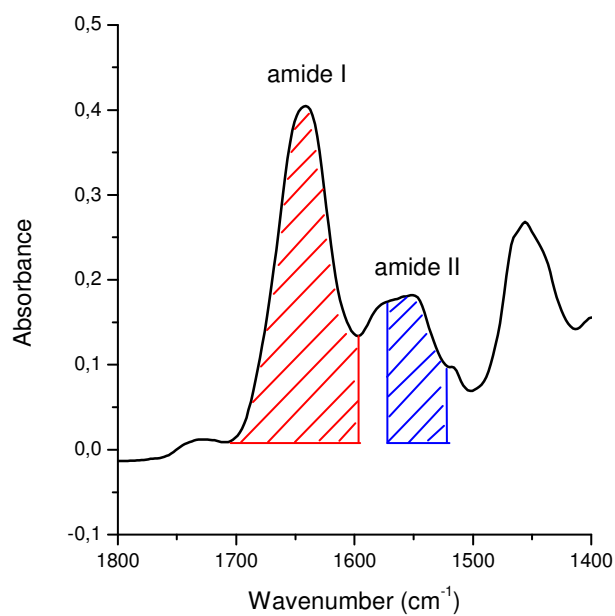
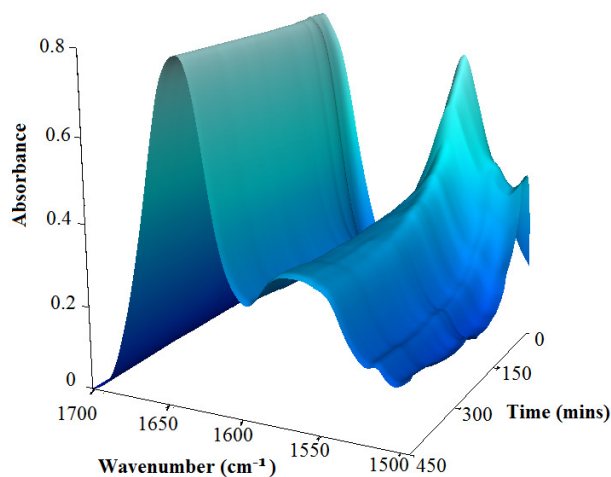


Figure 3.8: Integration of the amide I and amide II band.

The 3-D plot of the spectra against experimental time is given in [Figure 3.9](#) depicting the rate of decrease of the amide II contribution. Finally the fraction of amide H left in the sample is calculated using the following equation:

$$\frac{\left(\frac{\int_{1525}^{1575} \text{amide II}}{\int_{1710}^{1710} \text{amide I}}\right)_t}{\left(\frac{\int_{1525}^{1575} \text{amide II}}{\int_{1710}^{1710} \text{amide I}}\right)_0} = \text{Fraction of amide H} \quad \text{Equation 13}$$



**Figure 3.9:** 3D plot of the amide I and amide II band after buffer subtraction and normalization.

### 3.4.2.5 Determination of exchange fractions and rate constants.

The last step is to plot the fraction of amide H against experimental time. Different strategies have been used to represent the different groups of H/D exchange. In the case of the  $\text{Na}^+$ -NQR, the best fit was obtained with 2 exponential equations and one constant. The first exponential is representative of the fast exchanging amide H located on the surface of the protein. This group is defined with the variable  $C_f$  and rate constant  $\tau_f$ . The second group is representative of amide H located just beneath the surface and in specific channels and is described by the variable  $C_s$  and rate constant  $\tau_s$ . The last group defined by  $C_c$  refers to the amide H that are not accessible to the solvent and that are not exchanged. Usually this group is representative of membrane bound hydrophobic  $\alpha$ -helices. The fit is obtained by the following equation:

$$\text{Fraction of amide H} = C_f \cdot \exp\left(-t/\tau_f\right) + C_s \cdot \exp\left(-t/\tau_s\right) + C_c \quad \text{Equation 14}$$



### 3.6 Estimation of the secondary structure of proteins

Determination of the secondary structure was done by two methods; mid-IR absorption spectroscopy and circular dichroism. These complementary methods give important information about the structural integrity, for example of a mutant sample compared to the wild type. It is important to note that comparing the secondary structure obtained by these methods results in errors of  $\pm 5\%$  (162).

#### 3.6.1 Amide I band separation in the mid-IR

Mid-IR absorbance spectra were recorded on a Bruker 70 spectrometer (Germany) equipped with a liquid nitrogen cooled MCT detector. 1  $\mu\text{L}$  of the sample is dried on a ZnSe ATR crystal coated with silicium with a flux of argon, 256 scans were accumulated for each spectrum. Due to the contribution of Tris buffer in the amide I region, all the sample studied by this method were in phosphate buffer.

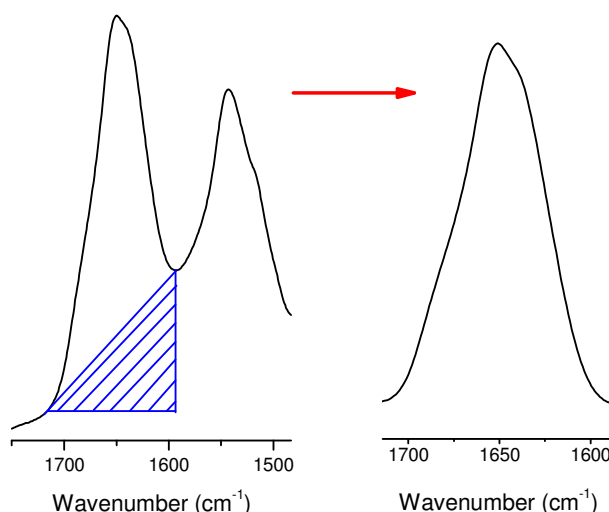
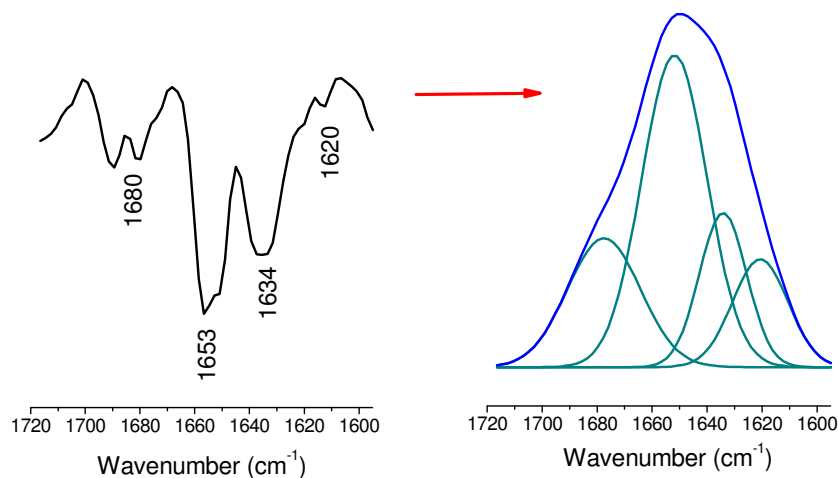


Figure 3.10: Baseline correction is performed by subtracting a straight line between 1710 and 1595  $\text{cm}^{-1}$ .

Data analysis was performed using the Origin software. Baseline correction on the amide I band (1710-1595  $\text{cm}^{-1}$ ) is performed by subtracting a straight line (Figure 3.10) (161). This process is important for band separation, but also contributes to the error of this method as a certain area of the amide I band is removed (162). The second derivative of the amide I dataset is performed to identify points of inflection that gives an approximation of where each component is localized in the spectrum (186, 187). Band separation was done by fitting multi Gaussian components on the amide I signal. The area of each component relative to the area of the whole band gives the % contribution of a

specific secondary structure (Figure 3.11). The typical positions for the secondary structural elements are summarized in [table 2.2](#).



**Figure 3.11:** The second derivative of the amide I band gives minima that correspond to the components present. Band separation is performed on the amide I signature by fitting multi Gaussian curves. The relative area of each component corresponds to the % of a secondary structure in the protein.

### 3.6.2 Circular dichroism spectroscopy

Circular dichroism (CD) is another technique that is complementary to FTIR spectroscopy in the analysis of protein secondary structure (*188*). The principle of circular dichroism spectroscopy is based on the ability of an optically active sample to polarized linearly polarized light, the sample is said to possess circular dichroism. CD spectral contribution separation usually yields in an accuracy of up to 97 % for  $\alpha$ -helical and distorted  $\alpha$ -helical structures provided that the correct reference dataset is used for band separation (*188, 189*). Furthermore different algorithm have been developed for the data deconvolution; depending on the algorithm used for data analysis, the results may differ (*190*). Although the analysis of secondary structures in soluble proteins is very successful, it has not been the case for membrane proteins (*191*). Subsequently, it is difficult to compare results from different membrane protein samples. Nevertheless, CD measurements can give an estimation of the secondary structures present in the  $\text{Na}^+$ -NQR, and structural changes in the presence of different ions can also be probed.

Measurements were performed on a JascoJ-810 spectropolarimeter equipped with an air-cooled xenon lamp as source and a head-on photomultiplier tube detector. Data analysis was performed on the DICHROWEB website (*192, 193*).

## **Chapter IV: Results and discussions**

## 4.1 The wild type Na<sup>+</sup>-pumping NADH:quinone oxidoreductase

To have a better understanding of the mechanism of ion transfer, the Na<sup>+</sup>-NQR has been studied in the presence of Li<sup>+</sup>, Na<sup>+</sup>, K<sup>+</sup>, Rb<sup>+</sup> and NH<sub>4</sub><sup>+</sup>. Redox titration has been monitored in UV-visible spectral domain to determine the mid-point potentials of the cofactors.

### 4.1.1 Redox titration monitored in the UV-visible

Flavins have broad contribution expanding over a large domain in the UV-visible. In the Na<sup>+</sup>-NQR, signals arising from the four flavins (FAD, FMN<sub>C</sub>, FMN<sub>B</sub> and riboflavin) overlap each other ([figure 4.1.1](#)). The [2Fe-2S] center also contributes in this region. All these cofactors have different absorption coefficients at specific wavelength.

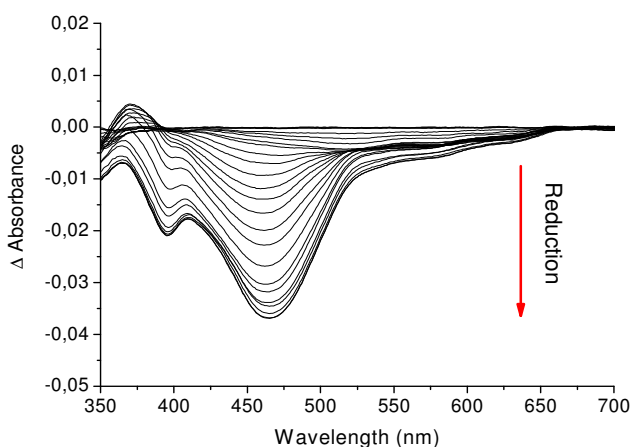
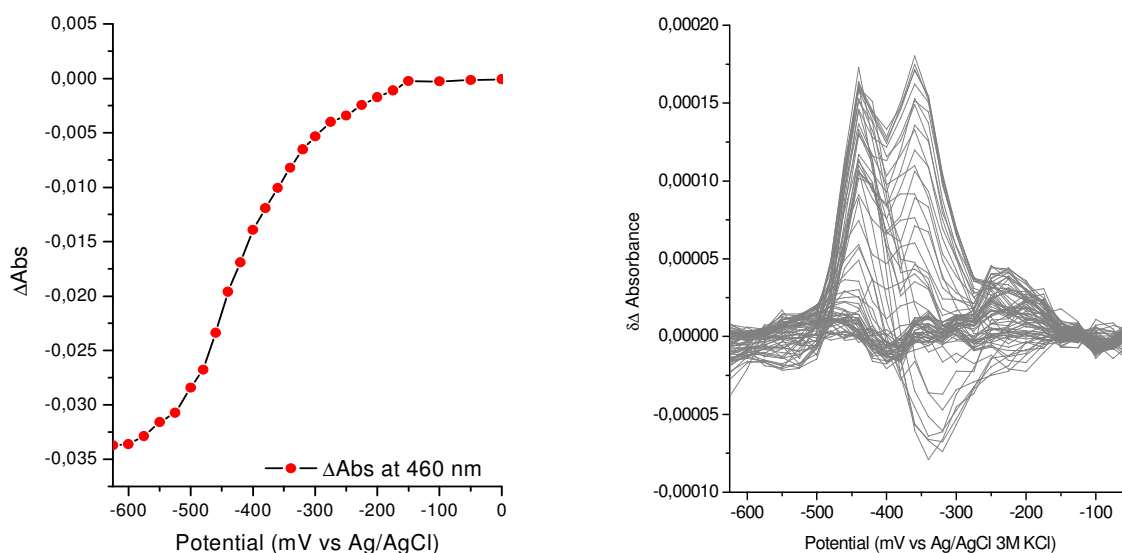


Figure 4.1.1: Evolution of the spectral contribution of the cofactors from the Na<sup>+</sup>-NQR upon reduction.

A fit of the Nernst equation directly on the plot of  $\Delta\text{Abs}/\text{applied potential}$  can identify at most 2 cofactors in our case ([figure 4.1.2](#)). This method although very successful in the study of hemes is less adapted for the Na<sup>+</sup>-NQR due to the overlapping of signals from the cofactors (154). A new strategy has been developed for the study of Na<sup>+</sup>-NQR based on the spectral properties of the cofactors (183, 194). The first derivative of  $\Delta\text{absorbance}$  against the applied potential was performed. The peaks observed correspond to the redox mid-point potential of the cofactors. The plot of the first derivative of  $\Delta\text{absorbance}$  against the applied potential for each 5 nm from 350-650 nm is presented in [figure 4.1.2](#).



**Figure 4.1.2: Absorbance change upon reduction monitored at 460 nm (left). Plot of the first derivative of  $\Delta\text{Abs}$  vs. applied potential for each 5 nm from 350-650 nm (right).**

The flavins go through different redox transitions with different spectral properties and at specific wavelengths the molar extinction coefficients of some flavins are negligible while others have a large contribution. The absorption coefficients of each cofactor have been determined previously ([table 4.1.1](#)) by the study of mutants each lacking one cofactor (94). These data are essential to identify the cofactors as the molar extinction coefficients are directly proportional to the amplitude of the peaks observed in the plot of  $\Delta\Delta\text{Abs}$ /applied potential. Three wavelengths have been selected to distinguish the cofactors, 380, 460 and 560 nm (183). Furthermore, apart from the FAD that performs a two electron transition, the other cofactors make one electron transitions. This redox property is also evident in the plot as peaks for one electron transition have a half-width of 90 mV and peaks for two electron transition have a half-width of 45 mV, according to Nernst equation. With these parameters, the plot of  $\Delta\Delta\text{Abs}$ /applied potential is fitted with [equation 4.1](#). Instead of using the derivative of the Nernst equation, a multi-gaussian fit has been used to simplify the model.

$$y = A_i \cdot \exp\left(\frac{(x-E_i)^2}{-w_i^2}\right) \quad \text{Equation 4.1}$$

where  $y$  is the first derivative of  $\Delta\text{absorbance}$ ,  $A_i$  is the amplitude for the component  $i$ ,  $x$  is the applied potential in mV,  $E_i$  is mid-point potential and  $w$  is the half-width of the peak. Depending on the wavelength at which the absorbance is studied, the fit may contain 1, 2 or 3 components.

Cofactor	Redox transition	Red-ox molar extinction coefficients ( $\text{mM}^{-1}\text{cm}^{-1}$ )		
		380 nm	460 nm	560 nm
<b>FAD</b>	$\text{FlH}^- \leftrightarrow \text{Fl}$	-4,25	-11,17	1,07
<b>[2Fe-2S]</b>	$[\text{2Fe-2S}]^+ \leftrightarrow [\text{2Fe-2S}]^{2+}$	-1,9	-3,12	-1,54
<b>FMN<sub>C</sub></b>	$\text{Fl}^{\bullet-} \leftrightarrow \text{Fl}$	3,81	-8,81	-0,5
<b>FMN<sub>C</sub></b>	$\text{FlH}^- \leftrightarrow \text{Fl}^{\bullet-}$	-6,95	-3,46	-1,4
<b>FMN<sub>B</sub></b>	$\text{Fl}^{\bullet-} \leftrightarrow \text{Fl}$	3,81	-8,81	-0,5
<b>Riboflavin</b>	$\text{FlH}^\bullet \leftrightarrow \text{FlH}_2$	-2,26	-0,66	-3,84

**Table 4.1.1: Molar extinction coefficients of all the cofactors of the  $\text{Na}^+$ -NQR at 380, 460 and 560 nm (94).**

**At 560 nm**, contributions from the riboflavin  $\text{FlH}^\bullet \leftrightarrow \text{FlH}_2$  transition and the [2Fe-2S] center ( $[\text{2Fe-2S}]^+ \leftrightarrow [\text{2Fe-2S}]^{2+}$ ) have the largest contributions ([figure 4.1.3](#)). FAD also has an important contribution at this wavelength. Nevertheless only two peaks are observed in the plot suggesting that the negative contribution of the FAD is cancelled out by the contribution of the FMNs which are smaller but positive. Based on the amplitude of the signals, the transition observed at -500 mV corresponds to the [2Fe-2S] center whereas riboflavin is observed at -210 mV. These redox mid-point potentials are independent of the type ions present.

**At 460 nm**, FAD ( $\text{FlH}^- \leftrightarrow \text{Fl}$ ) has the most important contribution and a half-width of 45 mV. Both FMN<sub>B</sub> and FMN<sub>C</sub> perform the same one electron transition,  $\text{Fl}^{\bullet-} \leftrightarrow \text{Fl}$ . The spectral contributions of the two FMN are identical with a half-width of 90 mV. The absorbance from the riboflavin at this wavelength is negligible. Contributions from the [2Fe-2S] center and the riboflavin  $\text{FlH}^- \leftrightarrow \text{Fl}^{\bullet-}$  transition are three times smaller than that of the FMN  $\text{Fl}^{\bullet-} \leftrightarrow \text{Fl}$  transition and four times smaller than the contributions of the FAD. Therefore these contributions are neglected in the fitting of the Gaussian components. A mid-point potential of -445 mV is obtained for the FAD independent on the types of ions present ([figure 3.1.3](#)). Previous analysis identified this redox transition as being pH dependent (183). For FMN<sub>B</sub> and FMN<sub>C</sub>, in the presence of  $\text{Li}^+$  and  $\text{Na}^+$  ions, two components are depicted at -350 and -360 mV. In the presence of  $\text{K}^+$ ,  $\text{Rb}^+$  and  $\text{NH}_4^+$  ions, one of the FMN has an unchanged potential at -350 mV whereas the contribution from the other FMN is observed at a lower potential, namely -450 mV. Due to the identical spectral contribution of these cofactors, it is not possible to discriminate the FMN<sub>B/C</sub>.

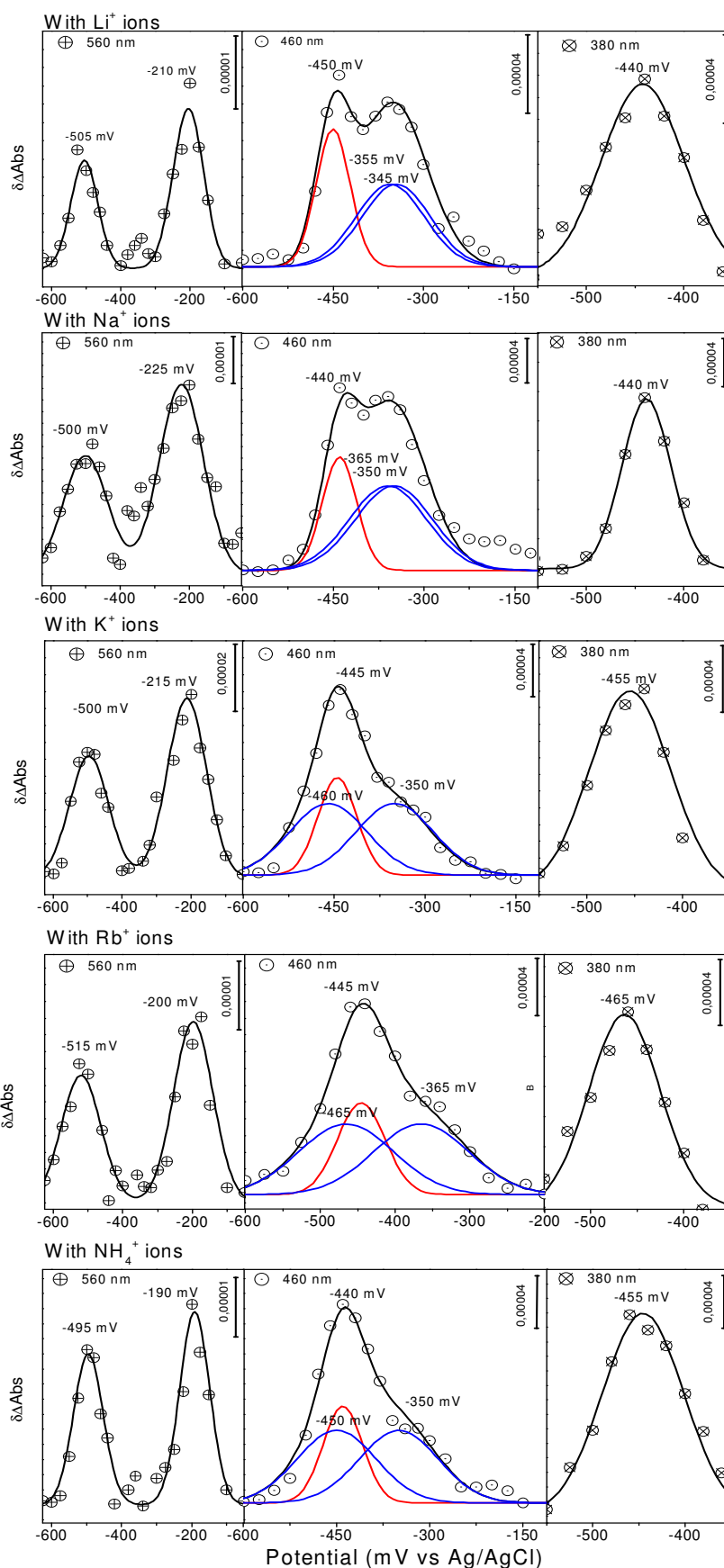


Figure 4.1.3: Redox titration of the Na<sup>+</sup>-NQR monitored at 560, 460 and 380 nm. Samples were studied in the presence of Li<sup>+</sup>, Na<sup>+</sup>, K<sup>+</sup>, Rb<sup>+</sup> and NH<sub>4</sub><sup>+</sup> (from top to bottom).

At 380 nm, the contribution of the cofactor FAD for the  $\text{FlH}^- \leftrightarrow \text{Fl}$  transition and the  $\text{FMN}_\text{C}$   $\text{FlH}^- \leftrightarrow \text{Fl}^{\bullet-}$  transition are expected to have the most intense signals (figure 3.1.3). But the  $\text{Fl}^{\bullet-} \leftrightarrow \text{Fl}$  transition from both FMN cofactors also contribute to this wavelength with a negative intensity. Band separation was not successful at this wavelength and only one signal was identified. Since the molar extinction coefficient of the  $\text{FMN}_\text{C}$   $\text{FlH}^- \leftrightarrow \text{Fl}^{\bullet-}$  transition is almost double the FAD  $\text{FlH}^- \leftrightarrow \text{Fl}$  transition, the observed component is attributed to  $\text{FMN}_\text{C}$  cofactor. A potential of -440 mV is observed in the presence of  $\text{Na}^+$  and  $\text{Li}^+$  ions that is lowered to -465 mV in the presence of  $\text{K}^+$ ,  $\text{Rb}^+$  and  $\text{NH}_4^+$  ions. The results are summarized in table 4.1.2.

Cofactor	Redox transition	Number of electrons	$E_m$ (mV vs Ag/AgCl)				
			$\text{Li}^+$	$\text{Na}^+$	$\text{K}^+$	$\text{Rb}^+$	$\text{NH}_4^+$
FAD	$\text{FlH}^- \leftrightarrow \text{Fl}$	2	-445	-440	-450	-445	-440
[2Fe-2S]	$[\text{2Fe-2S}]^+ \leftrightarrow [\text{2Fe-2S}]^{2+}$	1	-510	-500	-500	-510	-500
$\text{FMN}_{\text{C/B}}$	$\text{Fl}^{\bullet-} \leftrightarrow \text{Fl}$	1	-350/-360	-345/-360	-450/-360	-460/-340	-450/-340
$\text{FMN}_\text{C}$	$\text{FlH}^- \leftrightarrow \text{Fl}^{\bullet-}$	1	-440	-440	-465	-465	-460
Riboflavin	$\text{FlH}^\bullet \leftrightarrow \text{FlH}_2$	1	-210	-215	-220	-210	-200

**Table 4.1.2: Summary of the redox mid-point potentials of the cofactors present in the  $\text{Na}^+$ -NQR in the presence of  $\text{Li}^+$ ,  $\text{Na}^+$ ,  $\text{K}^+$ ,  $\text{Rb}^+$  and  $\text{NH}_4^+$  ions.**

The plot of the first derivative of the difference in absorbance vs. applied potential was also performed from 350 to 650 nm for each 5nm step. The observed differences include a decrease of the component at -360 mV in the presence of  $\text{K}^+$  ions while the component at -450 mV increases in intensity and becomes broader. Similar plots were made for experiments performed in the presence of  $\text{Li}^+$ ,  $\text{Rb}^+$  and  $\text{NH}_4^+$  ions (seen in Appendix figure 7.1).



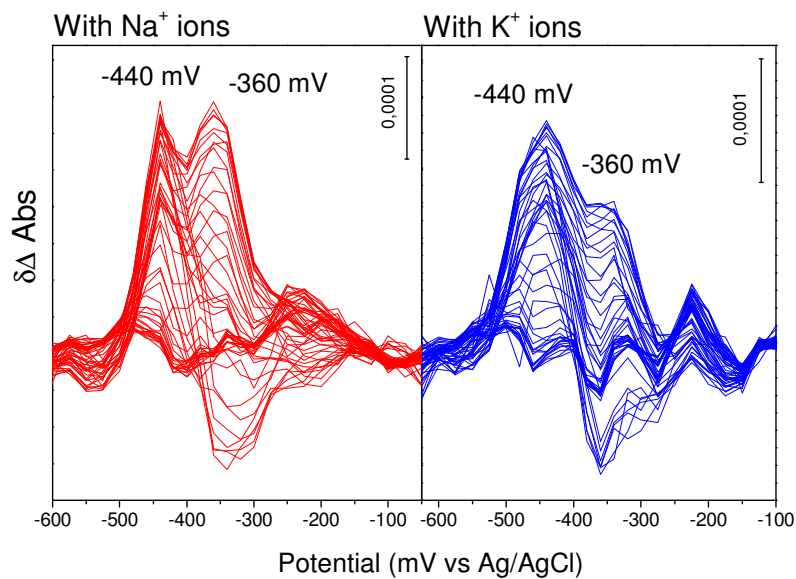


Figure 4.1.4: The plot of the first derivative of the difference in absorbance vs. applied potential from 350 to 650 nm for each 5 nm in the presence of  $\text{Na}^+$  ions (red) and in the presence of  $\text{K}^+$  ions (blue).

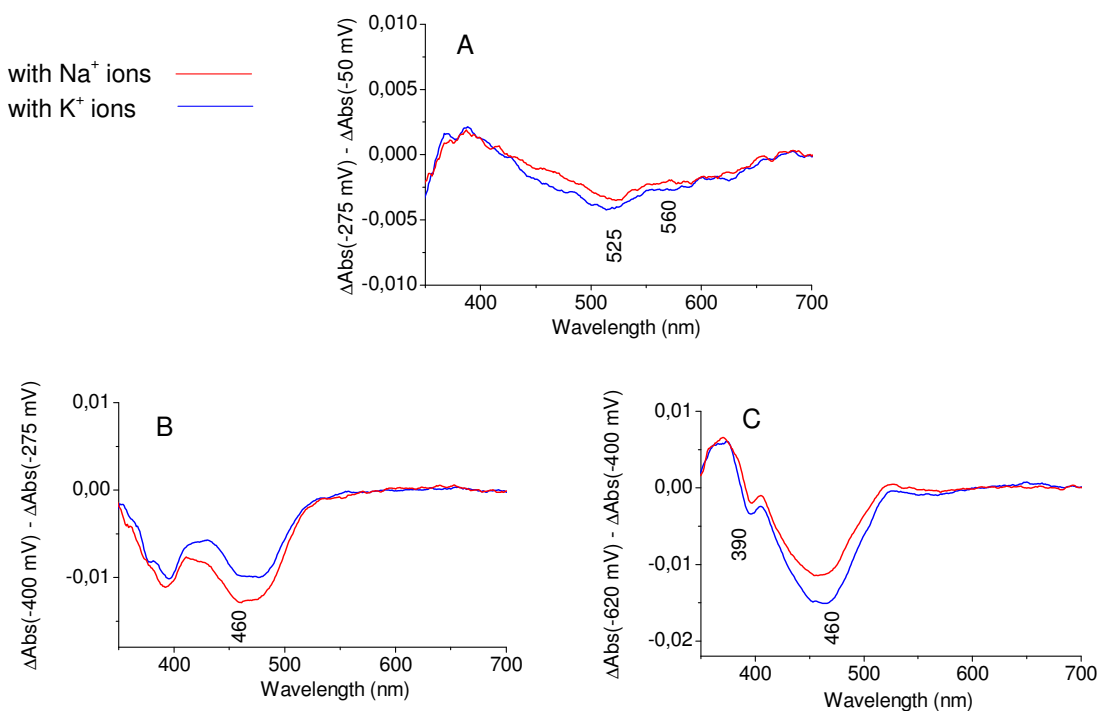


Figure 4.1.5: The difference spectra for the potential range -275 mV to -50 mV (A), -400 mV to -275 mV (B) and -620 mV to -400 mV (C), in the presence of  $\text{Na}^+$  ions (red) and  $\text{K}^+$  ions (blue)

To further investigate and corroborate the results, the UV-visible difference spectra at specific potentials were plotted (figure 4.1.5) (184). Since the redox potential of the riboflavin cofactor is not independent of the type of ions present, the difference spectra for the potential range -275 mV to -50 mV was taken as internal standard to calculate the difference spectra for the potential -400 mV to -275 mV and -620 mV to -400 mV.

Between -275 and -50 mV, only the contributions of riboflavin ( $\text{FlH}^\bullet \leftrightarrow \text{FlH}_2$ ) is observed in the presence of both  $\text{Na}^+$  and  $\text{K}^+$  ions with characteristic signals at 525 and 560 nm. The spectra obtained in the presence of  $\text{Na}^+$  ions between -400 mV and -275 mV shows an intense signal at 460 nm corresponding to the  $\text{Fl}^{\bullet-} \leftrightarrow \text{Fl}$  transition of FMN. The intensity of this signal decreases in the presence of  $\text{K}^+$  ions. Moreover the signal for the  $\text{Fl}^{\bullet-} \leftrightarrow \text{Fl}$  transition of the FMN cofactor at 460 nm is observed in the UV-visible difference spectrum obtained in the presence of  $\text{K}^+$  ions between -480 mV and -400 mV.

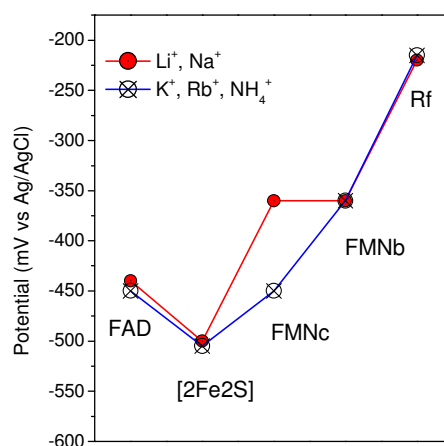


Figure 4.1.6: Redox mid-point potential of the cofactors involved in electron transfer in the  $\text{Na}^+$ -NQR.

Previously, it was shown that  $\text{Na}^+$ -uptake is coupled to electron transfer from the  $[2\text{Fe}2\text{S}]$  center to  $\text{FMN}_\text{C}$  (111). On this basis, the FMN which is affected by the presence of  $\text{Na}^+/\text{Li}^+$  tentatively attributed to  $\text{FMN}_\text{C}$ . The plot of the potential level clearly shows the difference in the thermodynamic properties of the  $\text{FMN}_\text{C}$  dependent on the ions present (figure 4.1.6).  $\text{Na}^+$  uptake and release occur during electron transfer from the  $[2\text{Fe}2\text{S}]$  center to  $\text{FMN}_\text{C}$  and  $\text{FMN}_\text{B}$  to riboflavin respectively. It is interesting to note that in our study a single cofactor is dependent on the type of ions present even though uptake and release of  $\text{Na}^+$  involves two cofactors. Interestingly, the activity of the enzyme is stimulated by the presence of  $\text{Na}^+$  and  $\text{Li}^+$  ions (112). Saturating concentrations of  $\text{Na}^+$  and

$\text{Li}^+$  stimulate the activity 8-fold and 3-fold respectively even though the redox potential are similar in the presence of both  $\text{Li}^+$  and  $\text{Na}^+$ .

The affinity of the enzyme for  $\text{Na}^+$  ions is not dependent on the redox state (112). These results show that while  $\text{Na}^+/\text{Li}^+$  regulates the mid-point potential of  $\text{FMN}_\text{C}$ , the redox state does not affect the affinity of the enzyme for  $\text{Na}^+/\text{Li}^+$ , showing that the cofactor does not follow the redox Bohr effect (195, 196). The  $\text{Na}^+$  binding site is therefore physically separated from the  $\text{FMN}_\text{C}$  and may account for the absence of reciprocal effect between the affinity of  $\text{Na}^+$  binding and thermodynamic properties of the cofactors.

Although, there is an ion dependence of the thermodynamic properties in the mechanism of the enzyme, the kinetic control has also been demonstrated (111). The unique machinery of the  $\text{Na}^+$ -NQR may have both a thermodynamic regulation and a kinetic control (184). The shift in potential (-350 mV in the presence of  $\text{Na}^+$  ions, -450 mV in the presence of  $\text{K}^+$  ions) observed may be the result of conformational changes. In the flavodoxin from *Clostridium beijerinckii*, which also possess a FMN cofactor, the redox potential is controlled by conformational changes which affect the environment of the isoalloxazine ring system (197). It is not excluded that in the  $\text{Na}^+$ -NQR,  $\text{Na}^+$ -binding induces conformational change that perturbs the environment of the isoalloxazine system of  $\text{FMN}_\text{C}$ .

In 2006, Bogachev et al. reported the titration of the  $\text{Na}^+$ -NQR from *Vibrio harveyi* (198). The analysis omitted the presence of the riboflavin. No ion dependent redox potential was observed. A few years later, the same authors reported the titration monitored by both optical and EPR spectroscopy (183, 199). Midpoint potentials of -410 mV and -340 mV were reported for  $\text{FMN}_\text{C}$  and  $\text{FMN}_\text{B}$  respectively independent from the type of ions present. It is difficult to account for the differences noted for the ion dependence of the FMN cofactor to our study (183). Nevertheless, the sample studied in this work has the largest  $\text{Na}^+$  dependent activity reported this far, a higher purity (>95%) and pumping activity of  $\text{Li}^+$  and  $\text{Na}^+$  when reconstituted in liposomes (111, 112). Bogachev et al. also reported the pH dependence of the  $\text{FAD FIH}^- \leftrightarrow \text{FI}$  transition and the  $\text{FMN}_\text{C} \text{FIH}^- \leftrightarrow \text{FI}^{\bullet-}$  transition respectively by -30 mV/pH and -60 mV/pH (183). Since no pH dependence was observed for riboflavin, the authors concluded that only the transition from  $\text{FIH}^-$  to  $\text{FIH}^{\bullet}$  is found. It was later demonstrated by EPR spectroscopy that the

transition for this cofactor is the pH dependent  $\text{FlH}^\bullet \leftrightarrow \text{FlH}_2$  transition (88). The pH independence observed may be the result of the cofactor being caged in a hydrophobic pocket inaccessible to the solvent. This hypothesis may well explain the stabilization of the neutral flavosemiquinone ( $\text{FlH}^\bullet$ ) form in the oxidized state of the enzyme.

All these measurements were performed at equilibrium and in real time the redox mid-point potentials of the cofactors may differ.

#### 4.1.2 Redox induced FTIR difference spectra of model compounds: FAD, FMN and riboflavin

Before studying the enzyme, redox induced difference spectroscopic studies of FAD, FMN and riboflavin were performed for the potential range between -620 mV to +200 mV. For the full potential step, only the difference spectra for the  $\text{Fl} \leftrightarrow \text{FlH}_2$  redox transition can be observed.

The difference spectrum of FAD presented in [figure 4.1.7](#) is dominated by an intense positive signal at  $1548\text{ cm}^{-1}$  attributed to the  $\nu(\text{C}=\text{C})$  of neutral flavins (180, 200). The signals observed at 1711, 1673 and  $1632\text{ cm}^{-1}$  include the  $\nu(\text{C}=\text{O})$  mode (179). Negative peaks at 1599 and  $1567\text{ cm}^{-1}$  are attributed to the  $\nu(\text{C}=\text{N})$  modes. The negative signal at  $1517\text{ cm}^{-1}$  include the  $\delta(\text{C-H})^{\text{in plane}}/\delta(\text{N-H})^{\text{in plane}}$  modes (201). In  $\text{D}_2\text{O}$ , no shift is observed but a decrease in intensity which may be the result of decoupling (179). Indeed in deuterated lumiflavin, frequency calculations showed that the  $\delta(\text{N-D})^{\text{in plane}}$  mode gives rise to a band at  $1055\text{ cm}^{-1}$  (179). In the study of FAD in solution, this shift upon H/D exchange may be lower than the spectral range studied. The negative signal at  $1410\text{ cm}^{-1}$  is tentatively attributed to the  $\delta(\text{N-H})^{\text{in plane}}$  modes. This signal shifts to higher frequencies in  $\text{D}_2\text{O}$  and may be the result of decoupling of the  $\delta(\text{N-D})^{\text{in plane}}$  modes (179). Isoalloxazine ring reorganization modes also contribute to smaller signals observed below  $1400\text{ cm}^{-1}$ . The signals observed in this spectral region are difficult to identify mainly because the bands observed correspond to highly coupled modes involving different parts of the isoalloxazine ring system (179). Modes arising from the phosphate groups are expected around  $1100\text{ cm}^{-1}$  (180).

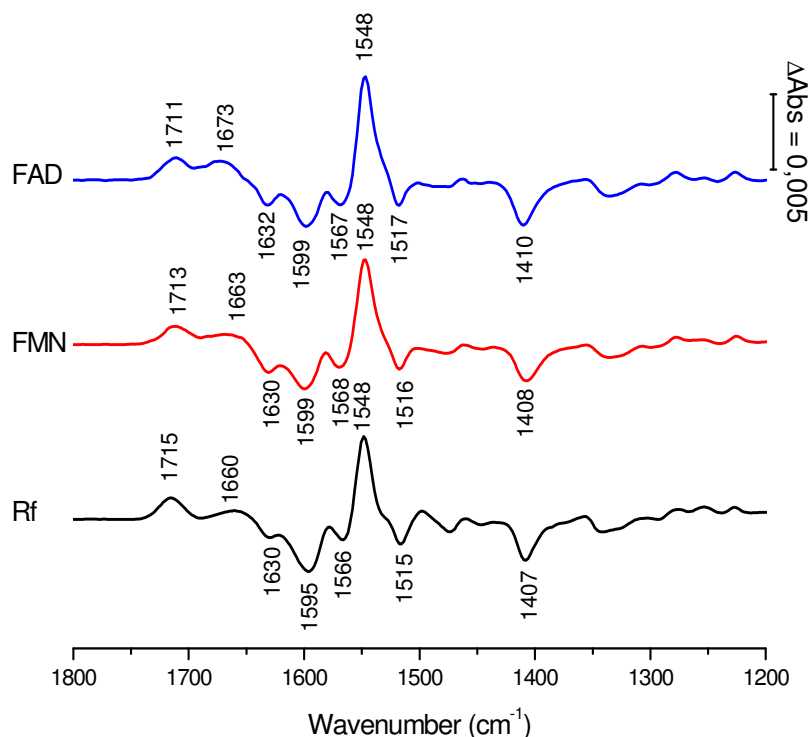


Figure 4.1.7: Oxidized-reduced FTIR difference spectra of FAD, FMN and riboflavin.

Directly comparing the redox induced difference spectra of FMN and riboflavin to that of FAD, small shifts are observed for the  $\nu(\text{C=O})$  and  $\nu(\text{C=N})$  modes. These shifts may arise from perturbation of the isoalloxazine system by the additional phosphate group and the nucleotide. (The assignments are summarized in [Appendix table 7.1](#))

#### 4.1.3 Redox induced FTIR difference spectra of $\text{Na}^+$ -NQR

The oxidized-reduced mid-IR difference spectrum of the  $\text{Na}^+$ -NQR in the presence of  $\text{Na}^+$  ions in  $\text{H}_2\text{O}$  buffer is presented in [figure 4.1.8](#) and the difference spectrum in the presence of  $\text{D}_2\text{O}$  is presented in [figure 4.1.9](#). We expect contributions from the flavin cofactors, individual amino acids and the polypeptide backbone upon redox reaction. The results show that the mid-IR difference spectrum of the  $\text{Na}^+$ -NQR is dominated by contributions arising mainly from the flavin cofactors. The first region from 1750 to 1620  $\text{cm}^{-1}$  include contributions from the  $\nu(\text{C=O})$  modes.

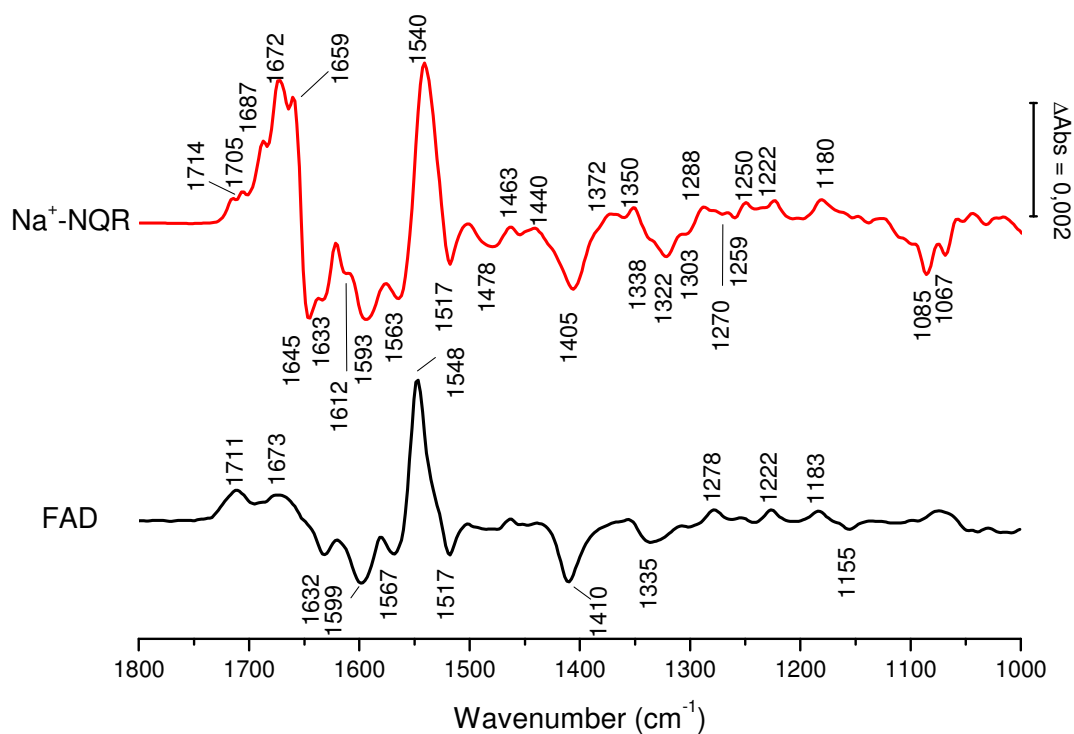


Figure 4.1.8: Oxidized-reduced difference spectrum for the potential range -620 to +200 mV of the Na<sup>+</sup>-NQR (red) in the presence of Na<sup>+</sup> ions and FAD (black) in H<sub>2</sub>O buffer.

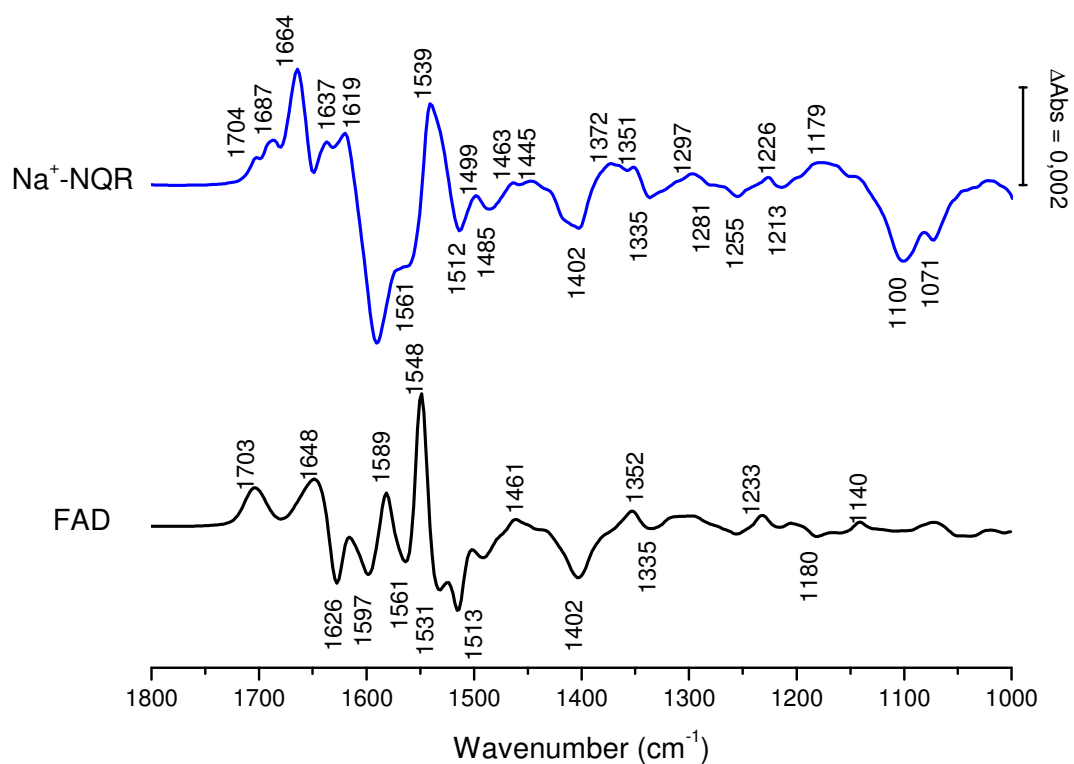


Figure 4.1.9: Oxidized-reduced difference spectrum for the potential range -620 to +200 mV of the Na<sup>+</sup>-NQR (blue) in the presence of Na<sup>+</sup> ions and FAD (black) in D<sub>2</sub>O buffer.

Positive signals at 1714, 1705, 1687, 1672 and 1659  $\text{cm}^{-1}$  may include the  $\nu(\text{C=O})$  modes of flavins (179, 202). Positive signals at 1687, 1672, 1659  $\text{cm}^{-1}$  and negative signals at 1645, 1633 and 1612  $\text{cm}^{-1}$  are attributed to the  $\nu(\text{C=O})$  mode of the polypeptide backbone, the so-called amide I region (181). These signals depict the conformational changes between the oxidized and the reduced state of the enzyme. In more detail, the signals at 1687, 1659, 1645 and 1633  $\text{cm}^{-1}$  show contributions from  $\beta$ -turns,  $\alpha$ -helix, random coil and  $\beta$ -sheet respectively (160). Contributions from the  $\nu(\text{C=O})$  from protonated acidic sidechains of Asp/Glu residues are also expected at 1714 and 1705  $\text{cm}^{-1}$  (63). In this spectral region contributions from the  $\nu(\text{C=O})$  modes of oxidized quinone are also expected (177).

The difference spectrum of the  $\text{Na}^+$ -NQR in  $\text{D}_2\text{O}$  buffer is presented in [figure 4.1.9](#). The signal seen in  $\text{H}_2\text{O}$  at 1715  $\text{cm}^{-1}$  is not observed in  $\text{D}_2\text{O}$  buffer. In the amide I region signals are observed at 1687, 1664, 1637 and 1618  $\text{cm}^{-1}$ .

The second spectral region is from 1620 to 1520  $\text{cm}^{-1}$ . The  $\nu(\text{C=N})$  modes from flavins are expected to have a negative contributions at 1593 and 1563  $\text{cm}^{-1}$  (179, 180). This region also include the coupled  $\delta(\text{N-H})/\nu(\text{C=N})$  mode of the polypeptide backbone, the amide II band from 1575 to 1525  $\text{cm}^{-1}$ . At 1540  $\text{cm}^{-1}$ , the intense signal is typical of the  $\nu(\text{C=C})$  mode of neutral flavins (180). The FAD and both FMN exist in the neutral oxidized form and may explain the large intensity of this signal. Amide II contribution to this peak cannot be excluded. Furthermore, the  $\nu(\text{COO}^-)^{\text{as}}$  modes of acidic residues are also expected in this spectral region (203). In  $\text{D}_2\text{O}$  buffer, a strong negative band is observed at 1589  $\text{cm}^{-1}$  representative of the  $\nu(\text{C=N})$  vibrational mode from flavins. This mode also contributes to the signal at 1561  $\text{cm}^{-1}$ . The strong positive signal observed at 1540  $\text{cm}^{-1}$  in  $\text{H}_2\text{O}$  attributed to the  $\nu(\text{C=C})$  mode from neutral flavins is shifted by 1  $\text{cm}^{-1}$  to lower frequencies in  $\text{D}_2\text{O}$  buffer. Moreover the intensity of the signal is decreased upon H/D exchange suggesting amide II contributions are also observed in  $\text{H}_2\text{O}$  in this region. The negative signals at 1517  $\text{cm}^{-1}$  in  $\text{H}_2\text{O}$  and 1512  $\text{cm}^{-1}$  in  $\text{D}_2\text{O}$  are typical of the  $\delta(\text{C-H})^{\text{in plane}}/\delta(\text{N-H})^{\text{in plane}}$  mode of flavins.

In the third spectral region from 1500 to 1100  $\text{cm}^{-1}$ , the so-called finger print area, several signals overlap. The signals observed at 1478 and 1463  $\text{cm}^{-1}$  are attributed to the  $\delta_{\text{as}}(\text{C-H}_3)$  of amino acid side chain. At lower wavenumbers, the  $\delta(\text{C-H}_2)$  modes are observed at 1440  $\text{cm}^{-1}$  (203, 204). Between 1400-1200  $\text{cm}^{-1}$ , contributions from the

isoalloxazine ring rearrangement are expected (179). The strong negative signals at 1405  $\text{cm}^{-1}$  in  $\text{H}_2\text{O}$  and at 1402  $\text{cm}^{-1}$  in  $\text{D}_2\text{O}$  are attributed to the  $\delta(\text{N-H})/\text{ring}$  mode from the flavins (179). The  $\nu_s(\text{COO}^-)$  mode from Asp/Glu side chain is also expected in this region and may also give rise to signals at 1372 and 1350  $\text{cm}^{-1}$ . Three negative signals at 1338, 1322 and 1303  $\text{cm}^{-1}$  are representative of the  $\delta(\text{C-H})$  modes and the ring reorganization of flavins. The spectral region between 1400 and 1200  $\text{cm}^{-1}$  also includes amide III contributions.

The last spectral region includes contribution from the phosphate buffer. Two negative bands at 1085 and 1067  $\text{cm}^{-1}$  in  $\text{H}_2\text{O}$  arise from the phosphate vibrations. In  $\text{D}_2\text{O}$  buffer, the signals are observed at 1100 and 1071  $\text{cm}^{-1}$ . The tentative assignments are given in [table 7.2](#) and [table 7.3](#) in the Appendix section.

#### 4.1.4 Redox induced FTIR difference spectra obtained in the presence of different ions

Redox induced FTIR difference spectroscopic measurements were also performed in the presence of  $\text{Li}^+$ ,  $\text{K}^+$  and  $\text{Rb}^+$  ions. The general shape of the spectra is similar ([Figure 4.1.10](#)). The only significant signal shift observed is at 1405  $\text{cm}^{-1}$  attributed to the  $\delta(\text{N-H})/\text{ring}$  mode from the flavins and the  $\nu(\text{COO}^-)^s$  mode from Asp/Glu side chain (179). A downshift of 2  $\text{cm}^{-1}$  is observed in the presence of  $\text{Li}^+$  ions, an upshift of 3  $\text{cm}^{-1}$  is observed in the presence of  $\text{Rb}^+$  and no shift is observed with  $\text{K}^+$  ions. Furthermore changes in signal intensity are also observed in the amide I and amide II region. To further investigate the data, double difference spectra were calculated by interactive subtraction.

In  $\text{D}_2\text{O}$  buffer, the general shape of the redox induced difference spectra are similar in the presence of  $\text{Li}^+$  (red),  $\text{Na}^+$  (black) and  $\text{K}^+$  (blue) ions as seen in [figure 4.1.11](#). The main changes are observed around 1400  $\text{cm}^{-1}$ . Negative signals are observed at 1410, 1402 and 1400  $\text{cm}^{-1}$  in the presence of  $\text{Li}^+$ ,  $\text{Na}^+$  and  $\text{K}^+$  ions respectively. The positive signal is also ion dependent as bands observed at 1375, 1370 and 1373  $\text{cm}^{-1}$  arise in the presence of  $\text{Li}^+$ ,  $\text{Na}^+$  and  $\text{K}^+$  ions respectively. In the amide I and amide II region, the alterations observed mainly involve changes in intensity. In the presence of  $\text{Rb}^+$  ions, the difference spectrum shows larger changes in the amide regions. Furthermore in the region where the  $\nu^s(\text{COO}^-)$  modes are expected only a negative signal is depicted at 1397  $\text{cm}^{-1}$ . To further investigate the spectral changes, double difference spectra were calculated by interactive subtraction.



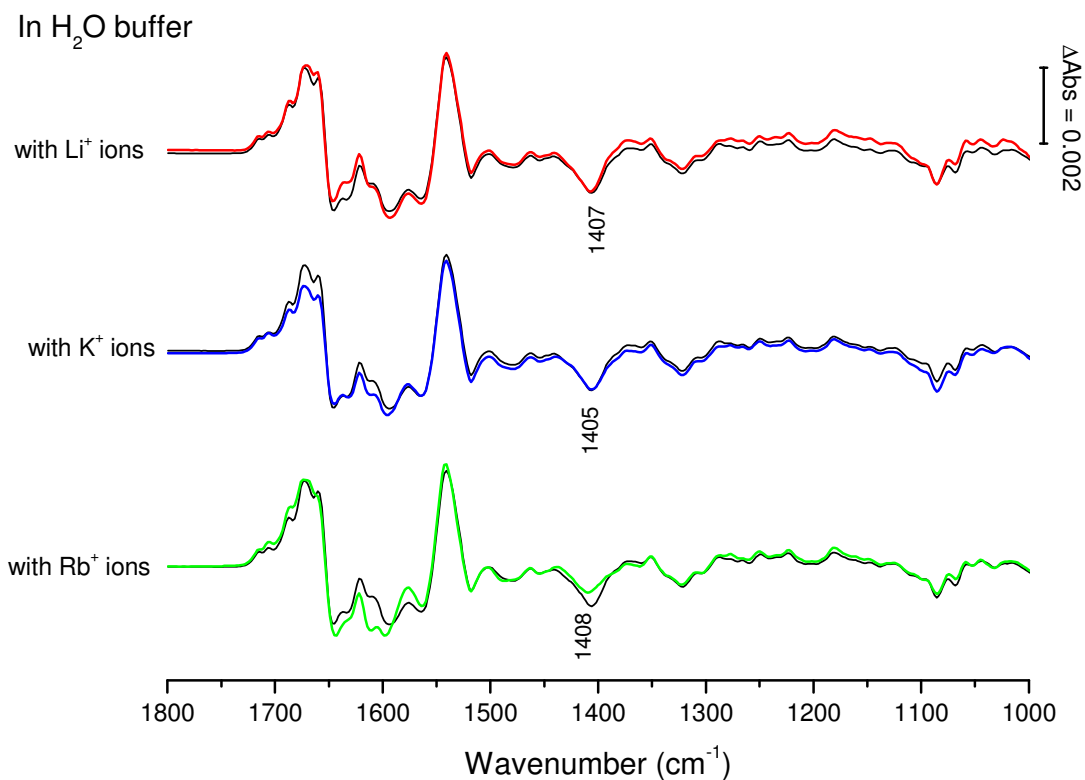


**Figure 4.1.10:** Oxidized-reduced difference spectra for the potential range -620 to +200 mV of the  $\text{Na}^+$ -NQR in  $\text{H}_2\text{O}$  buffer in the presence of  $\text{Li}^+$  (red),  $\text{K}^+$  (blue) and  $\text{Rb}^+$  (green) ions. The overlaid spectrum was obtained in the presence of  $\text{Na}^+$  ions.

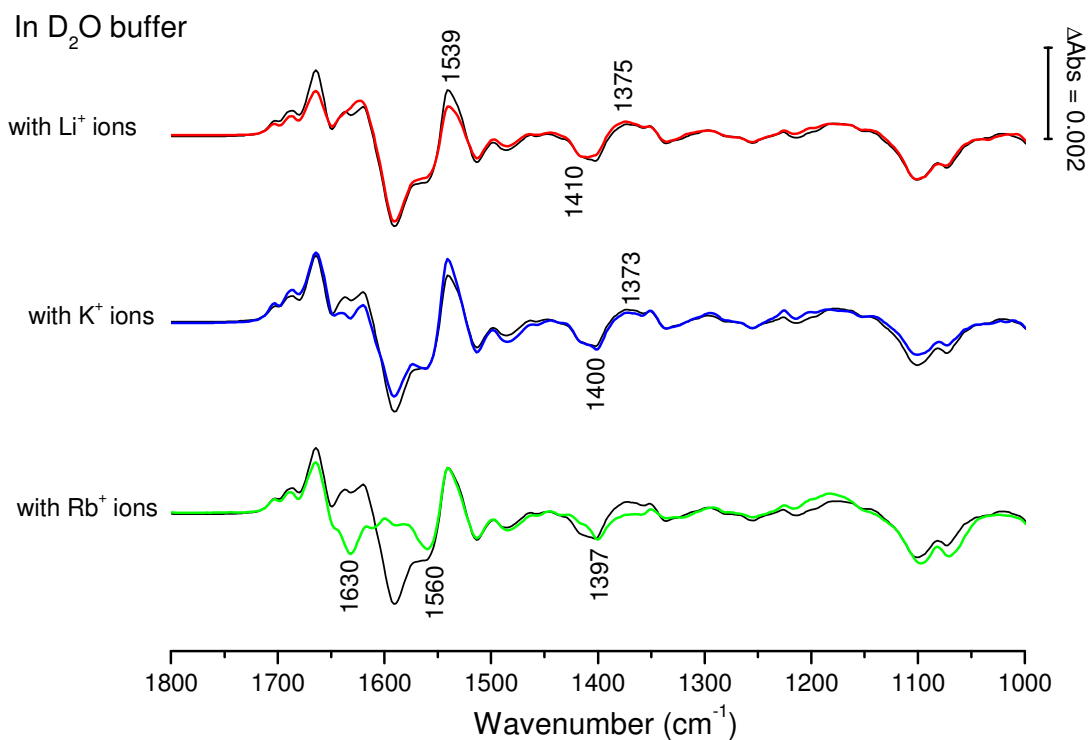


**Figure 4.1.11:** Oxidized-reduced difference spectra for the potential range -620 to +200 mV of the  $\text{Na}^+$ -NQR in  $\text{D}_2\text{O}$  buffer in the presence of  $\text{Li}^+$  (red),  $\text{K}^+$  (blue) and  $\text{Rb}^+$  (green) ions. The overlaid spectrum was obtained in the presence of  $\text{Na}^+$  ions.

#### 4.1.5 Double difference spectra in the presence of the different ions

Double difference spectra were obtained by interactive subtraction of the redox induced difference spectra obtained, for example in the presence of  $\text{Li}^+$  ions from the difference spectrum obtained in the presence of  $\text{Na}^+$  ions. The intensity of the signals observed in the double difference spectra is approximately 40 times smaller than in the simple FTIR difference spectrum ([figure 4.1.12](#)).

The  $\text{Na}^+$ - $\text{Li}^+$  double difference spectrum in  $\text{H}_2\text{O}$ , shows positive signals in the presence of  $\text{Na}^+$  whereas negative signals arise in the presence of  $\text{Li}^+$  ions. Although both  $\text{Na}^+$  and  $\text{Li}^+$  ions are translocated changes are observed in the amide I region at 1675, 1663, 1654 and 1634  $\text{cm}^{-1}$ . The signals observed at 1675 and 1634  $\text{cm}^{-1}$  are attributed to conformational changes assigned to  $\beta$ -turn and  $\beta$ -sheet structures (*161*). The signal at 1663  $\text{cm}^{-1}$  is typical of  $3_{10}$ -helical structures and is observed in the presence of  $\text{Li}^+$  (*205*). Finally the signal at 1654  $\text{cm}^{-1}$  observed in the presence of  $\text{Na}^+$  ions is attributed to  $\alpha$ -helical structures, random structures may also be included. Smaller changes in the amide II region can be seen at 1549  $\text{cm}^{-1}$ . A positive signal at 1406  $\text{cm}^{-1}$  and a negative signal at 1376  $\text{cm}^{-1}$  are tentatively assigned to the  $\nu_s(\text{COO}^-)$  modes of acidic side chains of Asp/Glu (*63*). The respective asymmetric mode is expected between 1590 and 1520  $\text{cm}^{-1}$ . In this spectral region two positive bands are depicted at 1592 and 1549  $\text{cm}^{-1}$ . This region is also crowded by the amide II.

Comparing the spectrum obtained in the presence of  $\text{Na}^+$  ions and in the presence of  $\text{Li}^+$  ions in  $\text{D}_2\text{O}$  buffer ([figure 4.1.13](#)), the main changes observed involve the amide I region. In the region around 1400  $\text{cm}^{-1}$ , similar to studies in the presence of  $\text{H}_2\text{O}$ , a positive signal is observed at 1416  $\text{cm}^{-1}$  and a negative signal is observed at 1383  $\text{cm}^{-1}$ .

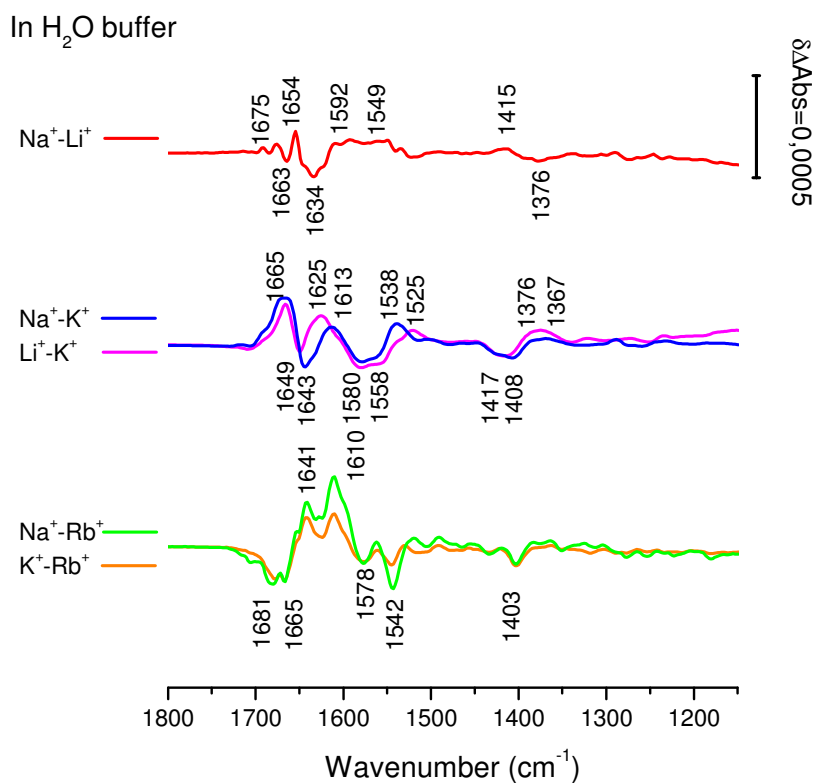


Figure 4.1.12: Double difference spectra in H<sub>2</sub>O buffer obtained by interactive subtraction.

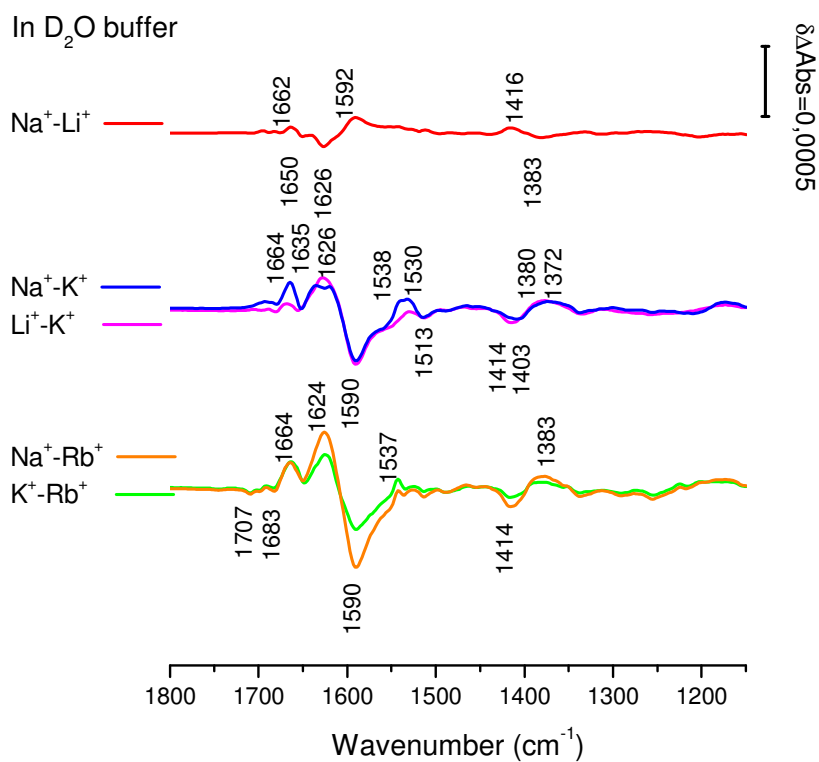


Figure 4.1.13: Double difference spectra in D<sub>2</sub>O buffer obtained by interactive subtraction.

The difference spectra obtained in the presence of  $\text{Na}^+$  and  $\text{Li}^+$  (the two ions that are translocated by the  $\text{Na}^+$ -NQR) were compared to the difference spectrum obtained in the presence of  $\text{K}^+$  ions. The general shape of the two double difference spectra is similar. A positive signal at  $1665\text{ cm}^{-1}$  is observed in both spectra but with different intensities indicating changes of  $\beta$ -turn structures. Negative signals at  $1649\text{ cm}^{-1}$  in the presence of  $\text{Li}^+$  and  $1643\text{ cm}^{-1}$  in the presence of  $\text{Na}^+$  are attributed to changes random coil structures. Finally at  $1625\text{ cm}^{-1}$  and  $1613\text{ cm}^{-1}$  in the presence of  $\text{Li}^+$  and  $\text{Na}^+$  respectively, signals involving  $\beta$ -sheet are observed. Interestingly, the signals observed around  $1400\text{ cm}^{-1}$  are dependent on the type of ions present. This spectral region is typical of  $\nu_s(\text{COO}^-)$  modes of Asp/Glu residues side chains. Negative bands at  $1417$  and  $1408\text{ cm}^{-1}$  in the presence of  $\text{Li}^+$  and  $\text{Na}^+$  ions respectively arise in the reduced state of the enzyme ([figure 4.1.1.12](#)). These results suggest that the signals are representative of  $\nu_s(\text{COO}^-\text{Li}^+)$  and  $\nu_s(\text{COO}^-\text{Na}^+)$  modes (206-208). At lower wavenumbers, similar signals dependent on the type of ion present are observed at  $1376$  and  $1367\text{ cm}^{-1}$ . Since the signals are positive, it can be deduced that they arise only in the oxidized form of the enzyme. These can also be attributed to  $\nu_s(\text{COO}^-\text{Li}^+)$  and  $\nu_s(\text{COO}^-\text{Na}^+)$  modes respectively. The metal ions studied in this work bind to carboxylic groups by two types of coordination: monodentate or bidentate. Bidentate coordination typically give rise to signals for the  $\nu_s(\text{COO}^-\text{M}^+)$  mode at  $1410\text{ cm}^{-1}$ . Signals arising from monodentate binding are observed at lower frequencies around  $1370\text{ cm}^{-1}$  (206, 208).

The results obtained suggest that  $\text{Na}^+$  and  $\text{Li}^+$  are bound by bidentate coordination in the reduced form of the enzyme and by monodentate coordination in the oxidized state. To further investigate the coordination of the metal ions, it is important to determine the wavenumbers at which the asymmetric modes are observed. The difference in wavenumbers between the symmetric and the asymmetric mode can be used to determine the type of coordination involved (206). The asymmetric modes are expected between  $1600\text{-}1500\text{ cm}^{-1}$ . This spectral region also includes contributions from the amide II. Upon H/D exchange amide II contributions are shifted to lower frequencies. The  $\nu(\text{C}=\text{N})$  mode is seen around  $1490\text{-}1460\text{ cm}^{-1}$  whereas the  $\delta(\text{N-D})$  mode is observed around  $1070\text{-}900\text{ cm}^{-1}$  where it mixes with other modes (181).

In the double difference spectra of  $\text{Li}^+\text{-K}^+$  and  $\text{Na}^+\text{-K}^+$  in  $\text{D}_2\text{O}$  buffer, signals observed in the amide I region at  $1664$ ,  $1635$  and  $1626\text{ cm}^{-1}$  reveal changes in conformation that are only observed in the presence of  $\text{Na}^+$  and  $\text{Li}^+$ . Negative

contributions from either the amide II or the  $\nu_{\text{as}}(\text{COO}^-)$  mode is observed at  $1590\text{ cm}^{-1}$ . The symmetric modes are observed at  $1416$  and  $1383\text{ cm}^{-1}$ . Comparing the double difference spectra of  $\text{Na}^+\text{-K}^+$  and  $\text{Li}^+\text{-K}^+$  show the same contribution as in  $\text{H}_2\text{O}$  at  $1414$  and  $1380\text{ cm}^{-1}$  for the  $\nu_{\text{s}}(\text{COO}^-\text{Li}^+)$ , and at  $1403$  and  $1372\text{ cm}^{-1}$  for the  $\nu_{\text{s}}(\text{COO}^-\text{Na}^+)$  mode (figure 4.1.13). The asymmetric mode is expected between  $1520$  and  $1590\text{ cm}^{-1}$ , upon H/D exchange the signal is expected to up shift by approximately  $10\text{ cm}^{-1}$ , but the relative intensity compared to the asymmetric mode in  $\text{H}_2\text{O}$  is doubled. Figure 4.1.1.14 shows the contributions of the  $\nu_{\text{s}}(\text{COO}^-\text{Na}^+)$  and the  $\nu_{\text{s}}(\text{COO}^-\text{Li}^+)$  for samples prepared both in  $\text{H}_2\text{O}$  and  $\text{D}_2\text{O}$  buffer for the spectral region between  $1500$  and  $1300\text{ cm}^{-1}$ .

The strong negative signal at  $1590\text{ cm}^{-1}$  seems to include contributions from both the  $\nu_{\text{as}}(\text{COO}^-\text{Na}^+)$  and the  $\nu_{\text{as}}(\text{COO}^-\text{Li}^+)$  modes (figure 4.1.13). Even though the spectra were recorded for samples prepared in  $\text{D}_2\text{O}$ , amide II contribution cannot be completely excluded from this region. Smaller peaks are observed at  $1538\text{ cm}^{-1}$  (in the presence of  $\text{Na}^+$  ions) and  $1530\text{ cm}^{-1}$  (in the presence of both  $\text{Na}^+$  ions and  $\text{Li}^+$  ions) can also arise from amide II contribution.

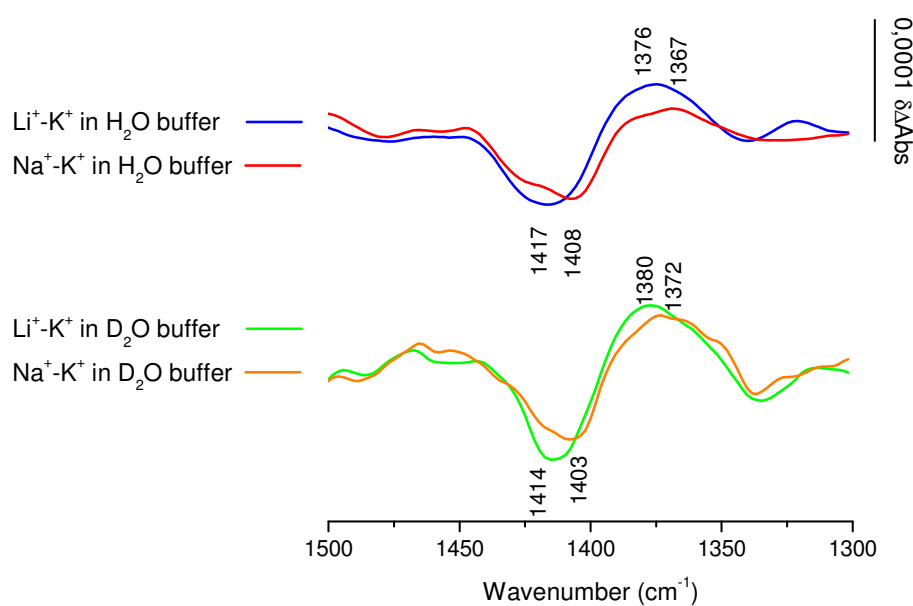


**Figure 4.1.14:** Double difference spectra  $\text{Li}^+\text{-K}^+$  and  $\text{Na}^+\text{-K}^+$  in the spectral region between  $1500$  and  $1300\text{ cm}^{-1}$  for samples in  $\text{H}_2\text{O}$  and  $\text{D}_2\text{O}$  buffer depicting the ion dependency of signals attributed to  $\nu_{\text{s}}(\text{COO}^-\text{M}^+)$ .

It has been shown that the Na<sup>+</sup>-NQR binds to Na<sup>+</sup> ions in the reaction step involving electron transfer from the [2Fe2S] center to the FMN<sub>C</sub>. Release of Na<sup>+</sup> across the membrane occurs when electrons are transferred from the FMN<sub>B</sub> to the riboflavin (*III*). In our experimental approach, the enzyme is studied in the two redox states, that is the fully oxidized and the fully reduced form. It is most likely that these positive signals tentatively attributed to  $\nu_s(\text{COO}^-\text{M}^+)$  are representative of the ion binding in the oxidized form of the enzyme.

Double difference spectra were also calculated to study the effects of Rb<sup>+</sup> ions which are known to inhibit the Na<sup>+</sup>-NQR ([figure 4.1.12](#)). For samples prepared in H<sub>2</sub>O buffer, in the amide I region, signals are observed at 1681, 1665, 1640 and 1610 cm<sup>-1</sup> in comparison to the difference spectra obtained for sample in the presence of Na<sup>+</sup> ions and K<sup>+</sup> ions. Interestingly in the region around 1400 cm<sup>-1</sup>, a negative signal is observed in both double difference spectra at 1403 cm<sup>-1</sup>. A tentative attribution suggest that this signal arises from  $\nu_s(\text{COO}^-\text{Rb}^+)$  mode and is observed only in the reduced state of the enzyme. The asymmetric mode is included in either of the signals observed at 1578 and 1542 cm<sup>-1</sup>.

The Na<sup>+</sup>-Rb<sup>+</sup> and K<sup>+</sup>-Rb<sup>+</sup> double difference spectra for samples prepared in D<sub>2</sub>O buffer show some similarities in the amide I region at 1683 and 1624 cm<sup>-1</sup> reflecting the absence of conformational change in the presence of Rb<sup>+</sup> ions ([figure 4.1.13](#)). The difference in intensity of the observed bands shows the change in conformation that does occur in the presence of Na<sup>+</sup> compare to K<sup>+</sup>. The signal observed previously at 1590 cm<sup>-1</sup> in both the Na<sup>+</sup>-K<sup>+</sup> and Li<sup>+</sup>-K<sup>+</sup> double difference spectra, is also observed here. At 1414 and 1383 cm<sup>-1</sup>, signal attributed to  $\nu_s(\text{COO}^-\text{Na}^+)$  modes are also seen. The signal attributed to  $\nu_s(\text{COO}^-\text{Rb}^+)$  mode seen at 1403 cm<sup>-1</sup> in H<sub>2</sub>O buffer, is not observed in D<sub>2</sub>O buffer. The tentative attributions are summarized in [table 7.4](#) and [table 7.5](#) in the Appendix section.

#### 4.1.6 H/D exchange kinetics measurements of the Na<sup>+</sup>-NQR

The solvent accessibility of the wild type enzyme was monitored in mi-IR to study conformational changes of the Na<sup>+</sup>-NQR. The rate of decrease of the amide II signature is taken as parameter to probe solvent accessibility of the protein. For experimental details, see materials and methods. In a first set of experiments, three groups of amide H were identified. The fast exchanging group consists of amide H on the surface of the protein which is easily accessible to HDX. This amide H group is usually exchanged with a rate constant of about 10 mins. The next group consists of amide H just beneath the surface or in channels, the exchange rate constant is usually around 200 mins. And finally the hydrophobic core consists of amide H which is not accessible to the solvent.

The experiments were performed three times for the wild type enzyme in the presence of Na<sup>+</sup> ions and showed high reproducibility for the percentage involved in each groups (Table 4.1.5). But the time constant for the slow exchanging group showed variations of more than 100 mins. For the fast exchanging group, a variation of 8 mins in the time constant was observed. It is difficult to account for these variations in the results. Since this technique is sensible to the concentration of the sample, small variation in the concentration may explain the differences observed (167, 209). Furthermore, the first experimental step consists of drying the sample on the crystal surface, and may affect the integrity of the enzyme.

	Exchange Kinetics	Exp 1		Exp 2		Exp 3	
		%	Time	%	Time	%	Time
Without lipids	Fast	40	10	41	10	40	10
	Slow	6	350	5	200	5	300
	Hydrophobic core	54	-	54	-	55	-
With lipids	Fast	40	10	40	10	40	10
	Slow	6	150	5	155	6	150
	Hydrophobic core	54	-	55	-	54	-

Table 4.1.3: HDX kinetics of the Na<sup>+</sup>-NQR with and without phospholipids.

In an attempt to improve the results, phospholipids extracts from *Escherichia coli* membrane were added to the sample in a 30:1 molar ratio before the measurements. The results are summarized in table 4.1.3. 40% of the amide H follow a fast exchange kinetic with a rate constant of 10 mins (figure 4.1.15). The slow exchange involves 6% of amide H with a time constant of 150 mins. The hydrophobic core consists of 54 % of amide

protons. The percentage involved in each exchange group and their respective rate constants were highly reproducible (table 4.1.3). It is difficult to account to such changes, but membrane proteins are known to gain in stability in phospholipids (210, 211). Furthermore, in the presence of phospholipids, an increase in protein flexibility has also been shown as there is less constraint surrounding the hydrophobic helices. On this basis, all the HDX experiments were performed in the presence of phospholipids. Nevertheless in our experimental conditions there is a mixture of lipids and detergents. Attempts to remove the detergent content from the sample using biobeads were not successful as the sample precipitated.

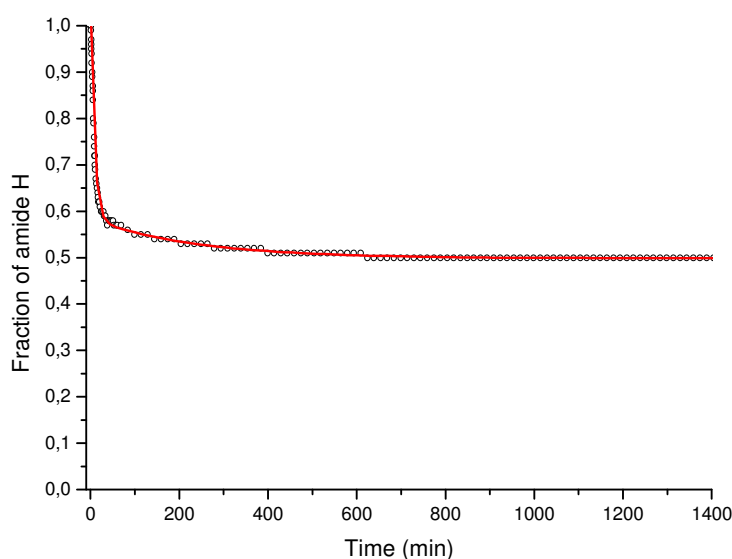


**Figure 4.1.15: HDX of the Na<sup>+</sup>-NQR in the presence of Na<sup>+</sup> and phospholipids monitored by probing the decrease of the amide II contribution.**

The stabilizing effect of phospholipids was investigated by secondary structure analysis by band deconvolution of the amide I signature in mid-IR and by circular dichroism spectroscopic analysis. See section 4.1.1.6: Analysis of the secondary structure of the Na<sup>+</sup>-NQR.

To investigate solvent accessibility of the reduced state of the enzyme, the same experiments were carried out with 1 mM of either NADH or Na<sub>2</sub>SO<sub>4</sub> added to the buffer.



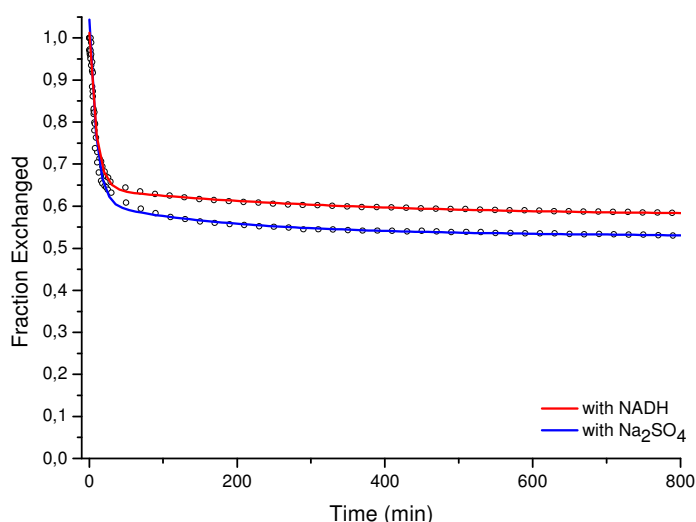


**Figure 4.1.16:** HDX of the  $\text{Na}^+$ -NQR in the presence of  $\text{Na}^+$  ions, phospholipids and either 1mM NADH (red) or 1 mM  $\text{Na}_2\text{SO}_4$  (blue).

For samples prepared in the presence of  $\text{Na}_2\text{SO}_4$  as seen in [figure 4.1.16](#), the results are similar to the analysis performed on the air oxidized enzyme with 40% of amide H following a fast exchange with a rate constant of 10 min. 5% follow a slow exchange, 1 % less than in the oxidized state. But considering the error expected for the slow exchange being  $\pm 2\%$ , the difference observed is not significant. The rate constant for the slow exchange is also increased to 10 mins. The hydrophobic core consists of 54% of the amide H. In the presence of NADH, only 37% of the amide H exchange with a fast kinetic. 6% follows a slow exchange with a time constant of 180 mins. 57% remains in the hydrophobic core. The results show important changes in the presence NADH. However NADH contributes in the amide I and amide II region. It is not excluded that the contribution of NADH is involved in the changes observed. To confirm this part, HDX kinetics should be monitored in the presence of different NADH concentrations.

Exchange Kinetics	Oxidized state		$\text{Na}_2\text{SO}_4$ reduced		NADH reduced	
	%	Time	%	Time	%	Time
Fast	40	10	40	10	37	10
Slow	6	150	5	160	6	180
Hydrophobic core	54	-	55	-	57	-

**Table 4.1.4:** HDX kinetics of the  $\text{Na}^+$ -NQR in the air oxidized state, the  $\text{Na}_2\text{SO}_4$  reduced state and the NADH reduced state.

To further investigate the solvent accessibility of the oxidized and reduced state of the enzyme, solvent accessibility of the air oxidized state of the enzyme was monitored for

800 mins after which  $\text{Na}_2\text{SO}_4$  was added to the buffer. No change was observed and suggested that the accessibility of the enzyme is not dependent on the redox state.

The effects of the different ions on the protein accessibility were also monitored ([figure 4.1.17](#)). Comparing the results obtained in the presence of  $\text{Na}^+$  and  $\text{Li}^+$  ions, the percentage involved in the three groups do not vary that is 40 % of the amide H follows a fast exchange kinetics, 6 % of the amide protons follows a slow exchange kinetic and 54 % remain in the hydrophobic core. The most important change observed is the time constant for the slow exchange which increases from 150 mins in the presence of  $\text{Na}^+$  to 400 mins in the presence of  $\text{Li}^+$  ions. These results suggest that in the presence of both  $\text{Na}^+$  and  $\text{Li}^+$  ions, the  $\text{Na}^+$ -NQR is in a similar conformation. The similar percentage exchange suggests that the slow exchange group attributed to amide H in channels or just beneath the surface have the same accessibility. Nevertheless, the difference in the rate constant suggests that in the presence of  $\text{Li}^+$  ions, the enzyme is less flexible. Furthermore quinone reduction activity measurements of the  $\text{Na}^+$ -NQR is stimulated 8 in the presence of  $\text{Na}^+$  ions and 3 times in the presence of  $\text{Li}^+$  ions. These results correlates with the slow exchange rate constant which is almost three times faster in the presence of  $\text{Na}^+$  ions (150 mins) compared to the rate constant in the presence of  $\text{Li}^+$  ions (400 mins).

In the presence of  $\text{K}^+$  ions, only 37% of the amide H follow a slow exchange kinetic with a rate constant of 10 mins. 5 % follow a slow exchange within 250 mins, 100 mins longer than in the presence of  $\text{Na}^+$  ions. The hydrophobic core is increased to 58%. These observations suggest that 4% of amide H is no more accessible in the presence of  $\text{K}^+$  ions. Interestingly, it is not the slow exchange group that decreases, but the fast exchanging group. It is difficult to interpret these results, but in the presence of the two ions that are translocated,  $\text{Na}^+$  and  $\text{Li}^+$ , 40 % of amide H are exchanged with a fast kinetics, and only 37 % in the presence of  $\text{K}^+$ ; an ion that is not translocated. These results also suggest that enzyme adopts a specific conformation in the presence of  $\text{Na}^+$  and  $\text{Li}^+$  ions (165). Similar measurements have been performed in the presence of  $\text{Rb}^+$  ions. The amide H group following a fast kinetic is similar to results obtained in the presence of  $\text{K}^+$  ions. For the slow exchange group, only 4% of amide H are found with a rate constant of 415 mins. The hydrophobic core involves of 59% of amide H. The results are summarized in [table 4.1.5](#).

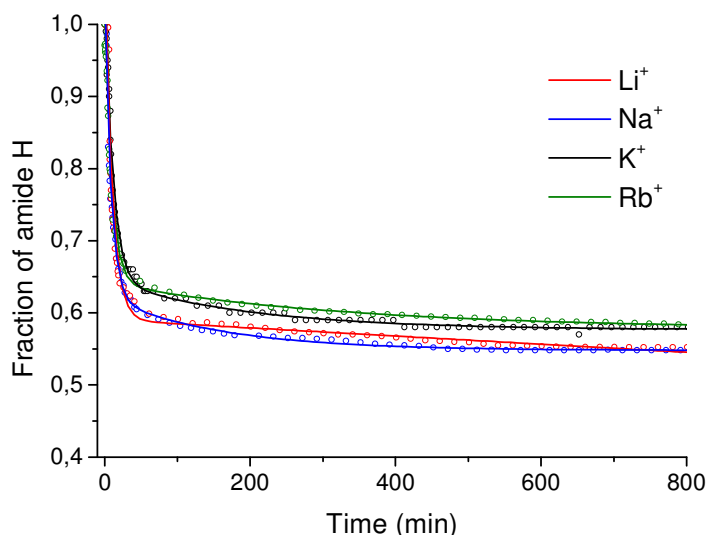


Figure 4.1.17 : HDX of the Na<sup>+</sup>-NQR in the presence of phospholipids and either Li<sup>+</sup> (red), Na<sup>+</sup> (blue) , K<sup>+</sup> (black) and Rb<sup>+</sup> (green) ions.

Exchange Kinetics	Li <sup>+</sup>		Na <sup>+</sup>		K <sup>+</sup>		Rb <sup>+</sup>	
	%	Time	%	Time	%	Time	%	Time
Fast	40	10	40	10	37	10	37	10
Slow	6	400	6	150	5	250	4	415
Hydrophobic core	54	-	54	-	58	-	59	-

Table 4.1.5: HDX constants of the Na<sup>+</sup>-NQR obtained in the presence of Li<sup>+</sup>, Na<sup>+</sup>, K<sup>+</sup> and Rb<sup>+</sup> ions.

The effects of the type of ions on the HDX kinetics measurements of the Na<sup>+</sup>-NQR can be divided into two distinct categories. The first one is in the presence of ions that are translocated by the Na<sup>+</sup>-NQR (Na<sup>+</sup> and Li<sup>+</sup> ions); the Na<sup>+</sup>-NQR is in a similar conformation state with the same percentage of amide H involved in each exchangeable group. The second one is in the presence of ions that are not translocated (K<sup>+</sup> and Rb<sup>+</sup> ions) with an increase in the percentage of amide H that are not exchanged up to 59%.

#### 4.1.7 Analysis of the secondary structure of the Na<sup>+</sup>-NQR

To investigate the influence of ions and phospholipids on the Na<sup>+</sup>-NQR, the secondary structure of the enzyme was determined in the mid-IR by deconvolution of the amide I component (161). For experimental details, see materials and methods [section 3.6.1](#). The results are presented in [figure 4.1.18](#), the amide I signature of the Na<sup>+</sup>-NQR in the presence of Na<sup>+</sup> ions include four bands at 1676, 1652, 1634 and 1620 cm<sup>-1</sup>. The component at 1676 cm<sup>-1</sup> is representative of the  $\nu(\text{C=O})$  mode from residues involved in

$\beta$ -turn structures and make up 23% of the amide I.  $\alpha$ -helical structures are typically observed at  $1656 \pm 2 \text{ cm}^{-1}$  whereas random structures are observed at  $1650 \pm 1 \text{ cm}^{-1}$ . In the  $\text{Na}^+$ -NQR a large component is observed at  $1652 \text{ cm}^{-1}$  and is attributed to the  $\alpha$ -helical structures (since the enzyme is membrane bound) making 44 % of the secondary structure. Random structures may also contribute to this component. At lower wavenumbers, components attributed to  $\beta$ -sheet structures are observed at 1634 (18%) and  $1620 \text{ cm}^{-1}$  (15%). Similar measurements were performed in the presence of  $\text{K}^+$  ions. The % of  $\beta$ -turn and  $\alpha$ -helical structures in the  $\text{Na}^+$ -NQR do not vary. Nevertheless only 6 % of  $\beta$ -sheet structures are observed at  $1634 \text{ cm}^{-1}$  while 27% are observed at  $1620 \text{ cm}^{-1}$ . In the presence of  $\text{Na}^+$  ions when phospholipids are added to the sample, a slight but reproducible decrease from 44% to 41% of  $\alpha$ -helical structures is observed. B-sheet components at  $1634 \text{ cm}^{-1}$  increases from 18% in the absence of phospholipids to 24% in the presence of phospholipids. In the presence of  $\text{K}^+$  ions and phospholipids, the main changes observe are the components that include the  $\beta$ -sheet structures. The component at  $1634 \text{ cm}^{-1}$  makes up only 6% of the amide I band in the absence of phospholipids and 14 % in the presence of phospholipids. The other component involving  $\beta$ -sheet structures at  $1620 \text{ cm}^{-1}$  decreases from 27% to 19% in the presence of phospholipids.

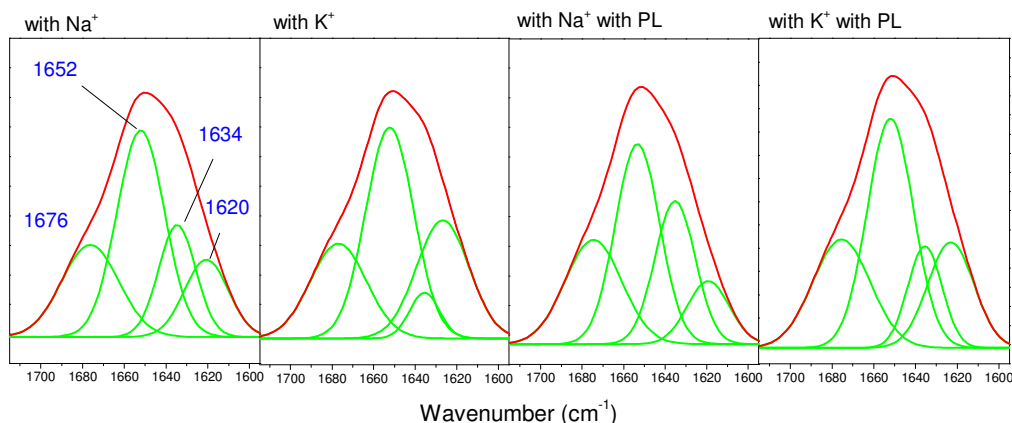


**Figure 4.1.18: Band deconvolution of the amide I signature in the presence of  $\text{Na}^+$  and  $\text{K}^+$ , and after addition of phospholipids to the sample.**

Wavenumbers $\text{cm}^{-1}$	Secondary structure	%			
		$\text{Na}^+$	$\text{K}^+$	$\text{Na}^+ + \text{PL}$	$\text{K}^+ + \text{PL}$
1676	$\beta$ -turn	23	23	24	25
1652	$\alpha$ -helix/unordered	44	44	41	42
1634	$\beta$ -sheet	18	6	24	14
1620	$\beta$ -sheet	15	27	11	19

**Table 4.1.6 : Secondary structure composition of the  $\text{Na}^+$ -NQR in the presence of  $\text{Na}^+$  and  $\text{K}^+$  ions and the effect of phospholipids.**

These results indicate that the secondary arrangement of the protein is dependent both on the type of ion present in the sample and the presence of phospholipids. Phospholipids are known to play a stabilizing role in proteins and are necessary for the functioning of integral membrane enzymes (41, 212).

Similar measurements were performed in circular dichroism to determine the secondary structure of the  $\text{Na}^+$ -NQR (figure 4.1.19). This method is complementary to mid-IR analysis of protein secondary structure (213). Nevertheless, band deconvolution of circular dichroism has been considered problematic for various reasons including the biasing effect of data sets and the complexity in obtaining CD spectra for membrane proteins (as the required concentration to avoid saturation is approximately 1  $\mu\text{M}$ ) (191). Secondary structure analysis was made from Dichroweb <http://dichroweb.cryst.bbk.ac.uk> using the CONTINLL algorithm (188, 189, 192, 214)

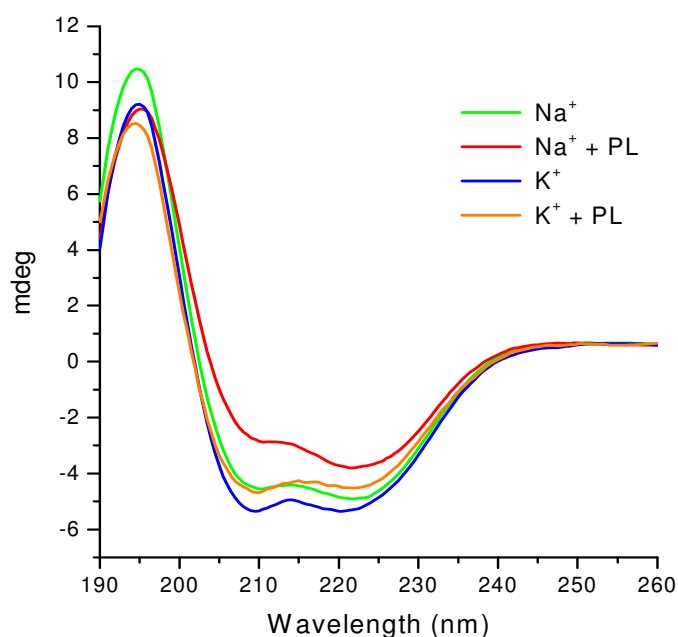


Figure 4.1.19: CD spectra of the  $\text{Na}^+$ -NQR in the presence of  $\text{Na}^+$  and  $\text{K}^+$  ions and with/without phospholipids.

Secondary structure	%			
	$\text{Na}^+$	$\text{K}^+$	$\text{Na}^+ + \text{PL}$	$\text{K}^+ + \text{PL}$
$\beta$ -turn	8	8	7	7
$\alpha$ -helix	74	63	76	74
$\beta$ -sheet	10	13	10	12
random	8	16	7	7

Table 4.1.7: Band deconvolution of the CD data gives an estimation of the secondary structure of the  $\text{Na}^+$ -NQR.

The results indicate that the Na<sup>+</sup>-NQR is made up mainly of  $\alpha$ -helical structures. The addition of phospholipids does not alter the secondary structure of the enzyme. In the presence of K<sup>+</sup> ions, the percentage of  $\alpha$ -helical structures decreases by almost 10 % whereas the % of unordered structures increases from 8 to 16 %. The % for the other secondary structures present does not vary significantly. This change in secondary structure is not observed in the presence of phospholipids.

Both FT-IR and circular dichroism spectroscopy showed structural differences of the Na<sup>+</sup>-NQR in the presence of Na<sup>+</sup> and K<sup>+</sup> ions. In CD spectroscopy, mainly  $\alpha$ -helical structures are perturbed, whereas in FT-IR spectroscopy the changes involved are mainly  $\beta$ -sheet structures. It is difficult to account for such differences but CD spectroscopy is known to overestimate  $\alpha$ -helical structures compared to FT-IR spectroscopy (191, 215). On the other side, in mid-IR analysis were performed on dried samples that can also affect the secondary structure of the sample (162). When phospholipids are added, analysis of secondary structure in the presence of both Na<sup>+</sup> and K<sup>+</sup> ions gave similar results, suggesting the Na<sup>+</sup>-NQR is stabilised in the presence of phospholipids. Similar observations is seen in mid-IR analysis, although the arrangement of  $\beta$ -sheet structures are still perturbed when phospholipids are added.

#### **4.1.8 Mechanism of Na<sup>+</sup>-pumping**

Different models have been proposed for the mechanism of Na<sup>+</sup>-transfer. Rich et al. suggested that to maintain electroneutrality of the [2Fe-2S] center, an uptake of Na<sup>+</sup> ions is necessary for charge counter balance in analogy to cytochrome *c* oxidase (97). Another model was proposed by Dimroth, with two quinone molecules attached to the Na<sup>+</sup>-NQR similar to the *bc*<sub>1</sub> complex and suggested that Na<sup>+</sup>-transfer occurs when the quinone is reduced to quinol (216). Bogachev et al. also proposed a model where the crucial cofactor involved in Na<sup>+</sup>-transfer is a flavin (217). All these models are developed from H<sup>+</sup>-pumping proteins where there is direct contact between the cofactors and the H<sup>+</sup>. Redox titration of the cofactors performed in this work showed that the redox mid-point potential of the FMN<sub>C</sub> is dependent on the type of ion present. A shift from -350 mV in the presence of Na<sup>+</sup> and Li<sup>+</sup> ions to -450 mV in the presence of K<sup>+</sup>, Rb<sup>+</sup> and NH<sub>4</sub><sup>+</sup> ions is observed. Although Na<sup>+</sup> and Li<sup>+</sup> ions induced the same increase in midpoint potential of the FMN<sub>C</sub>, in saturating conditions, Na<sup>+</sup> ions stimulate the quinone reduction activity 8–

fold whereas  $\text{Li}^+$  stimulates the activity 3-fold. These findings suggest that although there are thermodynamic parameters involved in  $\text{Na}^+$  transfer although the mechanism is based on kinetic parameters.

Prof. Barquera and Juárez proposed a coupling mechanism where  $\text{Na}^+$  transfer is regulated by kinetic controls involving a conformational change (218). In this model, the cofactors are not in direct contact with the coupling ions;  $\text{Na}^+$  and  $\text{Li}^+$  ions. In this thesis, no significant conformational change was detected by HDX measurements upon redox reaction, the amide H of the  $\text{Na}^+$ -NQR had similar exchange kinetics parameters. Nevertheless, HDX measurements showed that the conformation of the  $\text{Na}^+$ -NQR is dependent on the type of ions present. The  $\text{Na}^+$ -NQR is in two distinct conformation either in the presence of the coupling ions ( $\text{Li}^+$  and  $\text{Na}^+$  ions) or in the presence of ions that are not pumped ( $\text{K}^+$  and  $\text{Rb}^+$  ions).

Redox induced difference spectroscopy showed that the conformational change observed in the presence of  $\text{Na}^+$  and  $\text{Li}^+$  ions are similar, but different in the presence of  $\text{K}^+$  ions.  $\text{Rb}^+$  ions act as an inhibitor as seen in the amide I range in the FTIR difference spectra. Furthermore, redox induced difference data revealed that  $\text{Na}^+$  and  $\text{Li}^+$  ions are bound to the protein in both the oxidized and reduced state. On the basis of double difference spectra, signals were identified that can be attributed to the  $\nu_s(\text{COO}^-\text{Li}^+)$  and the  $\nu_s(\text{COO}^-\text{Na}^+)$  vibrational modes. The results also suggest that in the oxidised form, the ions have less energetic monodentate coordination and bidentate coordination in the reduced form. In conclusion, the mechanism seems to be sensibly more complex than previously suggested.

## 4.2 Study of mutant enzymes involved in Na<sup>+</sup> binding

A sodium binding site made up of NqrB D397, NqrE E95 and NqrD D133 in the cytoplasmic side of the membrane has previously been suggested (89). Mutant enzymes constructed by site-directed mutagenesis of these residues have a decreased quinone reduction activity when compared to the wild type Na<sup>+</sup>-NQR (89). Two mutant enzymes the NqrB D397E and the NqrE E95Q were investigated in this study.

### 4.2.1 Redox titration of the cofactors present in the NqrB D397E mutant enzyme

Similar to experiments performed on the wild type enzyme (section 4.1.1), redox titrations of the NqrB D397E mutant were monitored in the UV-visible. The NqrB D397E mutant was studied in the presence of Li<sup>+</sup>, Na<sup>+</sup>, K<sup>+</sup> and Rb<sup>+</sup> ions. As for the wild type enzyme, three wavelengths were selected for data analysis; 380, 460 and 560 nm ([figure 4.2.1](#)) (183, 184). Results averaged from at least two experiments are summarized in [table 4.2.1](#). No ion dependence is observed compared to the wild type enzyme where the redox potential of FMN<sub>C</sub> increases from -450 mV to -360 mV in the presence of Na<sup>+</sup> and Li<sup>+</sup> ions when compared to samples in the presence of K<sup>+</sup>, Rb<sup>+</sup> and NH<sub>4</sub><sup>+</sup> ions (184). These differences in the mid-point potential point out the crucial role of the D397 residue in the NqrB subunit in the mechanism of ion transfer.

Cofactor	Redox transition	Number of electrons	E <sub>m</sub> (mV vs Ag/AgCl)			
			Li <sup>+</sup>	Na <sup>+</sup>	K <sup>+</sup>	Rb <sup>+</sup>
FAD	FIH <sup>-</sup> ↔ FI	2	-435	-440	-445	-440
[2Fe-2S]	[2Fe-2S] <sup>+</sup> ↔ [2Fe-2S] <sup>2+</sup>	1	-510	-505	-500	-495
FMN <sub>C/B</sub>	FI <sup>•-</sup> ↔ FI	1	-460/-360	-460/-350	-455/-360	-460/-350
FMN <sub>C</sub>	FIH <sup>-</sup> ↔ FI <sup>•-</sup>	1	-435	-445	-455	-450
Riboflavin	FIH <sup>•</sup> ↔ FIH <sub>2</sub>	1	-215	-215	-220	-215

**Table 4.2.1: Midpoint potential of the cofactors present in the D397E mutant enzyme in the presence of Li<sup>+</sup>, Na<sup>+</sup>, K<sup>+</sup> and Rb<sup>+</sup> ions.**



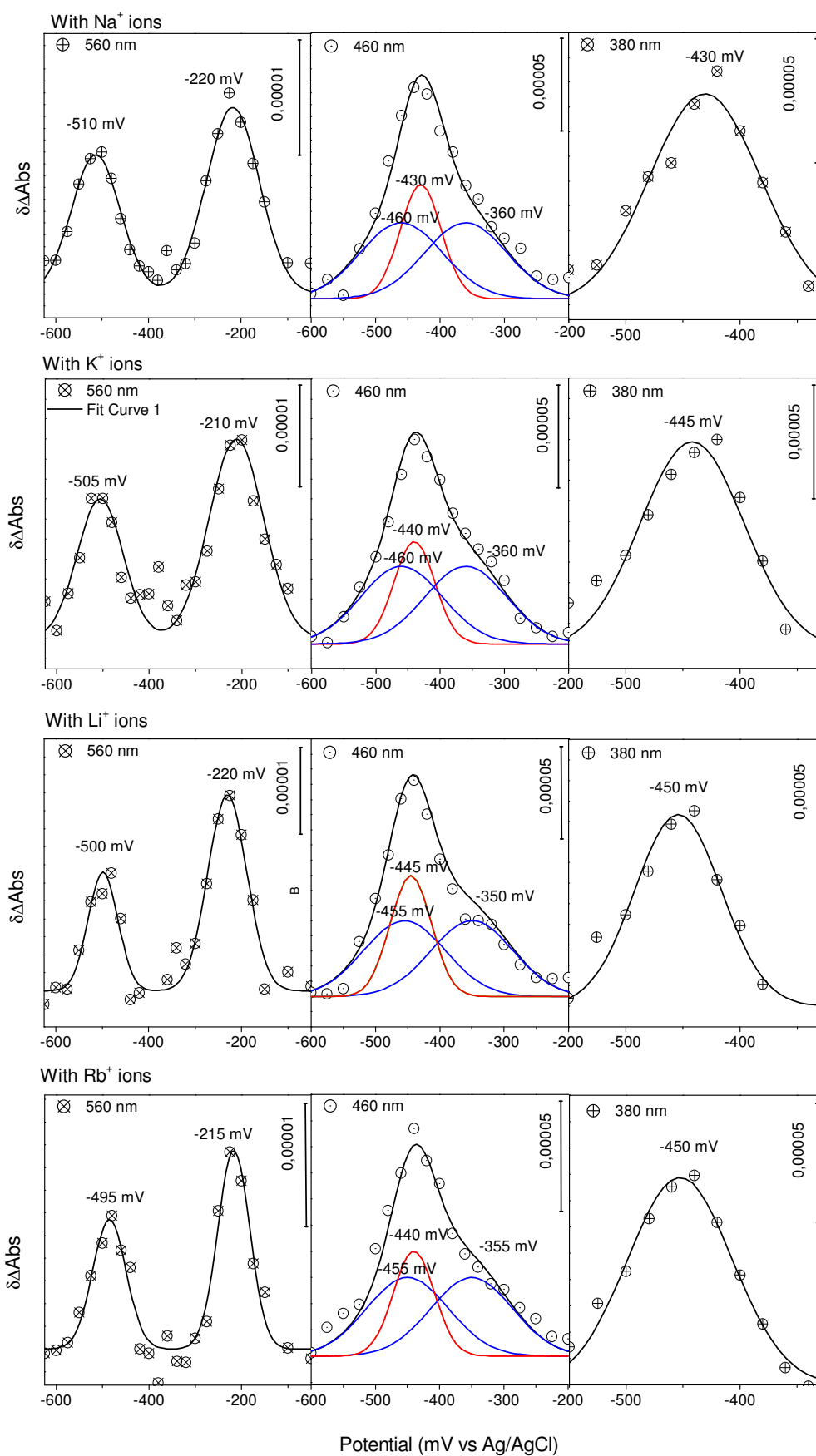


Figure 4.2.1: Redox titration of the NqrB D397E mutant protein monitored at 560, 460 and 380 nm. Samples were studied in the presence of Na<sup>+</sup>, Li<sup>+</sup>, K<sup>+</sup> and Rb<sup>+</sup> ions (from top to bottom).

#### 4.2.2 Redox induced mid-IR difference spectroscopic studies of the NqrB D397E mutant enzyme

The redox induced difference spectrum of the NqrB D397E mutant enzyme for the potential range between -620 to +200 mV is presented in [figure 4.2.2](#). Between 1720  $\text{cm}^{-1}$  and 1620  $\text{cm}^{-1}$  signals arising from the  $\nu(\text{C=O})$  modes are expected (215). The  $\nu(\text{C=O})$  vibrational modes from either Asp/Glu acid side chains or from flavins contribute to the signals at 1715 and 1705  $\text{cm}^{-1}$  (219). Amide I contributions are seen at 1687, 1675, 1659, 1647, and 1631  $\text{cm}^{-1}$  and are representative of the conformational change of the protein upon redox reaction. Signals arising from the flavin cofactors have strong contributions to the redox induced difference spectra as seen in [figure 4.2.2](#). The  $\nu(\text{C=O})$  vibrational modes from flavins may also contribute to the positive signals at 1705, 1687, 1675 and 1659  $\text{cm}^{-1}$  (180). The  $\nu(\text{C=N})$  modes of flavins are observed at 1595 and 1566  $\text{cm}^{-1}$ . An intense positive signal at 1541  $\text{cm}^{-1}$  is attributed to the  $\nu(\text{C=C})$  modes of neutral flavins (179, 180). More over amide II contributions are also expected in this spectral region. The negative signals at 1517  $\text{cm}^{-1}$  is typical for the  $\delta(\text{C-H})^{\text{in plane}}/\delta(\text{N-H})^{\text{in plane}}$  mode of flavins (179). The  $\nu(\text{COO}^-\text{Na}^+)$  modes of acid residues side chains are seen at 1405  $\text{cm}^{-1}$  (219). The negative signal also includes modes arising from the isoalloxazine ring reorganization upon redox reaction. Between 1400 and 1150  $\text{cm}^{-1}$ , modes arising from several amino acids side chains and ring reorganization of the flavins are expected. The phosphate buffer contributes to the two negative signals seen at 1085 and 1067  $\text{cm}^{-1}$ .

Redox induced FTIR difference spectroscopic studies were also performed for samples prepared with  $\text{Li}^+$ ,  $\text{K}^+$  and  $\text{Rb}^+$  ions ([figure 4.2.3](#)). The difference spectrum of samples prepared in the presence of  $\text{Li}^+$  ions has the same general shape as for the difference spectrum obtained in the presence of  $\text{Na}^+$  ions. The differences observed are a decrease in intensity of signals in the amide I region at 1687, 1675 and 1659  $\text{cm}^{-1}$ . These signals are representative of conformational change upon redox reaction involving  $\beta$ -turns and disordered structures (161). The negative signal observed at 1410  $\text{cm}^{-1}$  in the presence of  $\text{Na}^+$  ions is downshifted to 1404  $\text{cm}^{-1}$  in the presence of  $\text{Li}^+$  ions. In this spectral region the  $\nu_s(\text{COO}^-)$  modes from Asp/Glu acid side chains are expected as well as contributions from flavin ring reorganization (179, 219).

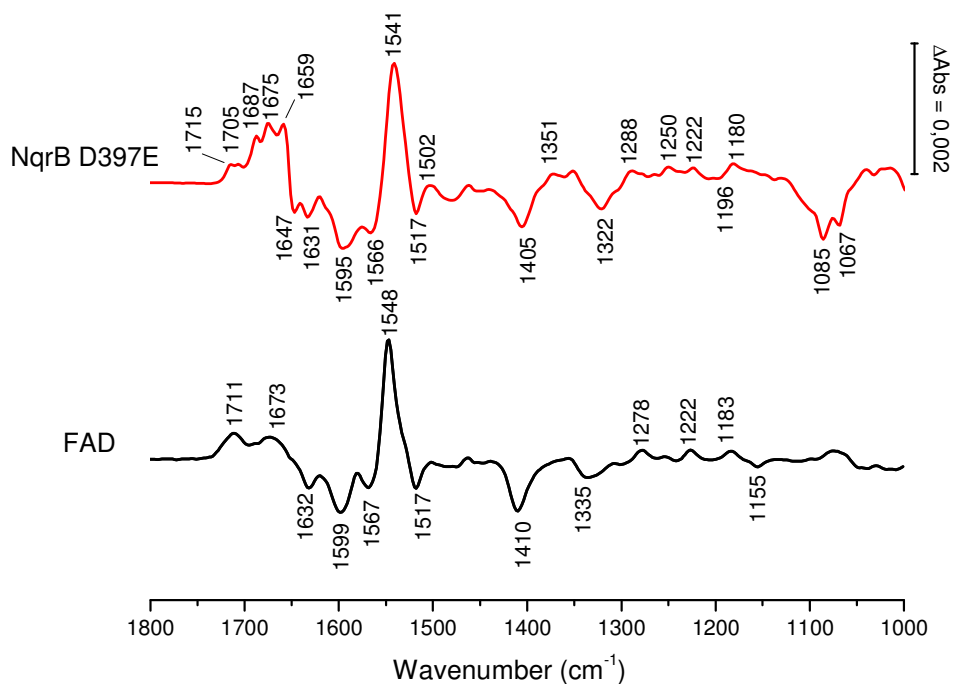


Figure 4.2.2: Redox induced FTIR difference spectra of the NqrB D397E mutant enzyme in the presence of  $\text{Na}^+$  ions (red) and FAD (black) for the potential range between -620 mV to +200 mV.

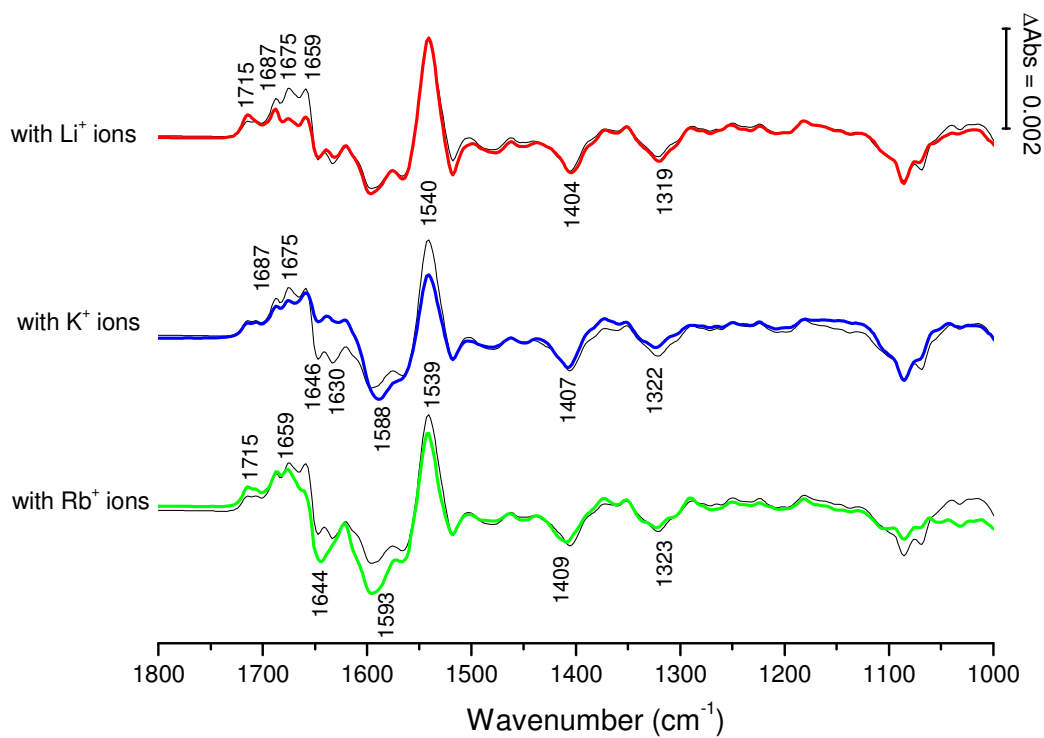


Figure 4.2.3: Redox induced FTIR difference spectra of the NqrB D397E mutant enzyme in the presence of  $\text{Li}^+$  ions (red),  $\text{K}^+$  ions (blue),  $\text{Rb}^+$  ions (green) and in the presence of  $\text{Na}^+$  ions (black) for the potential range between -620 mV to +200 mV.

Comparing the difference spectrum of the NqrB D397E mutant prepared with  $K^+$  ions with samples prepared with  $Na^+$  ions, The main differences involve a decrease in the intensity of signals in the amide I region. The positive signal at  $1540\text{ cm}^{-1}$  also decreases in intensity. This band include both contributions from the  $\nu(C=C)$  modes of neutral flavins and amide II contributions (180). The  $\nu_s(COO^-)$  mode of Asp/Glu acid side chains is seen at  $1407\text{ cm}^{-1}$ . For samples prepared in the presence of  $Rb^+$  ions, the difference spectrum shows large differences in the amide I and amide II regions. Furthermore the  $\nu_s(COO^-)$  mode of Asp/Glu acid side chains is also shifted to  $1409\text{ cm}^{-1}$  (203). The tentative assignments are presented in table 7.6 in the Appendix section. To depict these changes, double difference spectra were calculated by interactive subtraction.

#### 4.2.3 Double difference spectra of the NqrB D397E mutant enzyme studied in the present of different ions.

In the  $Na^+Li^+$  double difference spectrum seen in figure 4.2.4, large differences are observed in the amide I region at  $1675$ ,  $1660$ ,  $1643$  and  $1613\text{ cm}^{-1}$ . These signals reflect the perturbation of conformational change upon redox reaction in the presence of  $Li^+$  and  $Na^+$  ions, and are representative of  $\beta$ -turns and  $\beta$ -sheets (161). Signals observed at  $1547$  and  $1536\text{ cm}^{-1}$  can be attributed to amide II contributions and the  $\nu_{as}(COO^-)$  modes from Asp/Glu acid side chains. The signal at  $1402\text{ cm}^{-1}$  includes contribution from the  $\nu_s(COO^-)$  modes from Asp/Glu acid side chains may be included in the negative signal at  $1419\text{ cm}^{-1}$  and the positive signal at  $1400\text{ cm}^{-1}$  (219). Compared to the  $Na^+Li^+$  double difference spectrum of the wild type enzyme, these two signals are inverted, as a negative signal is observed at  $1415\text{ cm}^{-1}$  and a positive signal at  $1376\text{ cm}^{-1}$ .

The difference spectra obtained in the presence of  $Na^+$  and  $Li^+$  (the two ions that are pumped by the  $Na^+$ -NQR) were compared to the difference spectrum obtained in the presence of  $K^+$  ions. In the  $Na^+K^+$  double difference spectrum signals in the amide I region are observed at  $1672$ ,  $1648$  and  $1635\text{ cm}^{-1}$ . In the  $Li^+K^+$  double difference spectrum a positive signal is seen at  $1713\text{ cm}^{-1}$  and may include the  $\nu(C=O)$  mode of protonated Asp/Glu acid side chain. In the amide I region a broad negative band is observed from  $1676$  to  $1630\text{ cm}^{-1}$ . A positive signal is observed at  $1586\text{ cm}^{-1}$  may include amide II contributions. This spectral region may also include contributions from the  $\nu_{as}(COO^-)$  modes of Asp/Glu acid side chains.

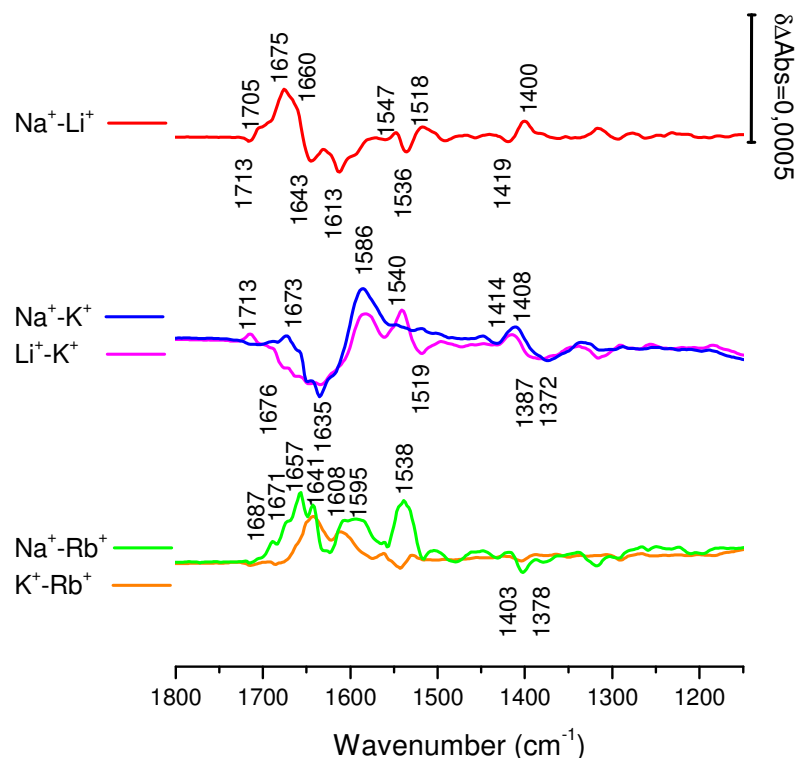
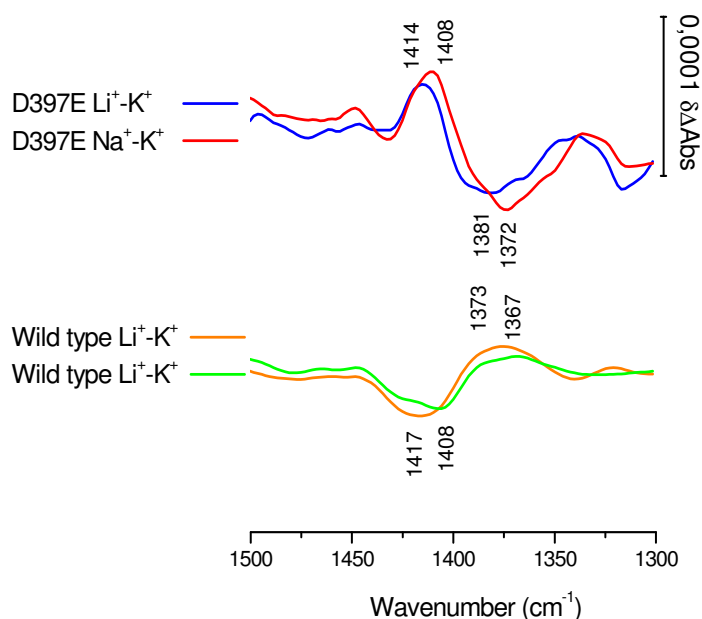


Figure 4.2.4: Double difference spectra of the NqrB D397E mutant enzyme prepared with the different salts.

The  $\nu_s(\text{COO}^-)$  modes of Asp/Glu acid side chains are observed at 1414 and 1381  $\text{cm}^{-1}$  in the  $\text{Li}^+ - \text{K}^+$  double difference spectra, and at 1408 and 1372  $\text{cm}^{-1}$  in the  $\text{Na}^+ - \text{K}^+$  double difference spectrum (figure 4.2.5) (206). Similar to the wild type enzyme, these signals are sensitive to the type of ions present in the sample. Interestingly, the positive signals observed in the double difference spectra of the wild type protein are negative in the NqrB D397E mutant. Typically, when replacing aspartic acid by glutamic acid, the  $\nu_s(\text{COO}^-)$  is up shifted by a few wavenumbers (203, 220). The inversion observed may result from a shift of signals observed at 1373 and 1367  $\text{cm}^{-1}$  in the difference spectra of the wild type enzyme to higher wavenumbers. Furthermore, since at least three carboxylic groups are required for  $\text{Na}^+$  binding, replacing one residue may affect the bond strength between  $\text{Na}^+$  ions with the other residues (206). The up shift observed suggest that  $\text{Na}^+$  and  $\text{Li}^+$  ion binding is weakened in the NqrB D397E mutant enzyme. Furthermore, since the asymmetric modes of these vibrations were not clearly identified, we cannot propose a coordination mode of the ions (207, 208).



**Figure 4.2.5:** Double difference spectra  $\text{Li}^+\text{-K}^+$  and  $\text{Na}^+\text{-K}^+$  in the spectral region between 1500 and 1300  $\text{cm}^{-1}$  of the NqrB D397E mutant enzyme and the wild type protein.

In the  $\text{Na}^+\text{-Rb}^+$  double difference spectrum depicted in [figure 4.2.4](#). The main changes observed are in the amide I region at 1687, 1671, 1657 and 1641  $\text{cm}^{-1}$ . These signals show the perturbation of conformation in the presence of  $\text{Rb}^+$  ions upon redox reaction. Amide II contributions can be seen at 1538  $\text{cm}^{-1}$ . In this spectral region  $\nu_{\text{as}}(\text{COO}^-)$  modes from Asp/Glu acid side chains are also expected. At lower wavenumbers, two negative signals at 1403 and 1378  $\text{cm}^{-1}$  show perturbations of the  $\nu_{\text{s}}(\text{COO}^-)$  modes from Asp/Glu acid side chains (219). Moreover compared to the  $\text{Na}^+\text{-Rb}^+$  double difference spectrum of the wild type enzyme where a similar component is observed at 1403  $\text{cm}^{-1}$ . These observations suggest that  $\text{Rb}^+$  binding does not involve the NqrB D397 residue.

Comparing the difference spectrum of the NqrB D397E mutant enzyme in the presence of  $\text{K}^+$  ions and in the presence of  $\text{Rb}^+$  ions, a broad signal is observed in the amide I region at 1541  $\text{cm}^{-1}$ . This signal depicts the difference in conformational changes upon redox reaction of the mutant enzyme in the presence of the two salts. Smaller changes are observed in the amide II region. As in the  $\text{Na}^+\text{-Rb}^+$  double difference spectrum, a negative signal is observed at 1403  $\text{cm}^{-1}$  and may include the  $\nu_{\text{s}}(\text{COO}^-\text{Rb}^+)$  vibrational modes. The tentative attributions are summarized in [table 7.7](#) in the appendix section.

#### 4.2.4 Comparison with the wild type enzyme.

To further investigate the redox induced difference spectra of the D397E mutant enzyme, the difference spectra were compared with that of the wild type enzyme. The difference spectra of the wild type protein with the different salts were subtracted from the difference spectra of the difference spectra of the NqrB D397E mutant enzyme.

The resulting double difference spectra for samples studied in the presence of Na<sup>+</sup> ions (seen in [figure 4.2.6](#)) show changes observed in the amide I region at 1670, 1644 and 1615 cm<sup>-1</sup> representative of conformational perturbation involving  $\beta$ -turns, random structures and  $\beta$ -sheets respectively. Interestingly, a positive band is observed at 1714 cm<sup>-1</sup>, a region typical of the  $\nu(\text{C=O})$  vibrational modes of protonated Asp/Glu acid side chains (64). A positive signal is observed at 1544 cm<sup>-1</sup> may include amide II modes and  $\nu_{\text{as}}(\text{COO}^-)$  modes from Asp/Glu acid side chains. The  $\nu_{\text{s}}(\text{COO}^-)$  modes from Asp/Glu acid side chains are observed at 1403 cm<sup>-1</sup> (203). While substituting aspartic acid to glutamic acid, the Na<sup>+</sup> binding network, involving several carboxylic groups, is modified and may explain the differences observed in the (COO<sup>-</sup>) vibrational modes.

For samples prepared in the presence of Li<sup>+</sup> ions, the double difference spectrum show changes in the amide I region at 1670 and 1644 cm<sup>-1</sup> as in the double difference spectrum of samples prepared with Na<sup>+</sup> ions. These signals are representative of changes in conformation involving  $\beta$ -turns and random structures (161, 205). A positive signal also in the amide region is observed at 1612 cm<sup>-1</sup> reflecting changes involving  $\beta$ -sheets. In the amide II region, a positive signal at 1554 cm<sup>-1</sup> and a negative signal at 1523 cm<sup>-1</sup> are seen. This region also includes the  $\nu_{\text{as}}(\text{COO}^-)$  modes from Asp/Glu acid side chains (203, 219). The differences in the (COO<sup>-</sup>) vibrational modes compared for samples prepared in the presence of Na<sup>+</sup> and Li<sup>+</sup> ions suggest that the NqrB D397 residue is involved in an ion binding motif. Nevertheless, the other residues involved may be different. Furthermore, the changes observed in the amide I region suggest that conformational perturbation between the wild type protein and the mutant enzyme in the presence of Li<sup>+</sup> and Na<sup>+</sup> ions is similar.

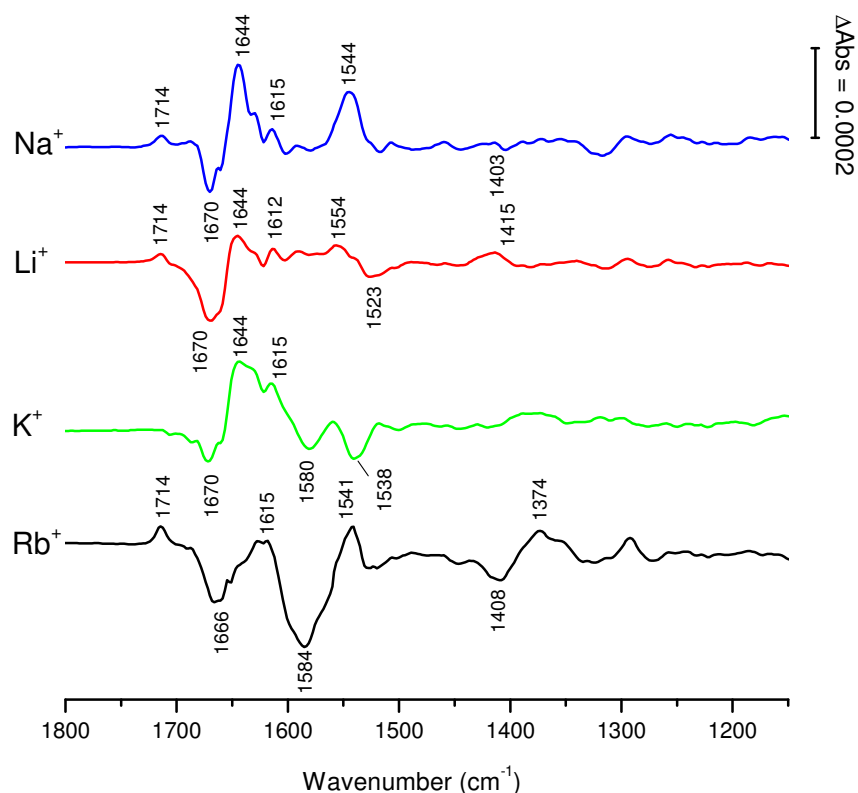


**Figure 4.2.6: NqrB D397E mutant – wild type double difference spectra of samples prepared in the presence of Na<sup>+</sup>, Li<sup>+</sup>, K<sup>+</sup> and Rb<sup>+</sup> ions.**

For samples studied in the presence of K<sup>+</sup> ions, an ion that is not translocated by the enzyme, the double difference spectrum also depicts changes in the amide I region at 1670, 1644 and 1615 cm<sup>-1</sup>. These signals show that independent of ion binding to the protein, a conformational perturbation is observed in the NqrB D397E mutant enzyme when compared to the wild type protein. At lower wavenumbers changes are also seen in the amide II region at 1580 and 1538 cm<sup>-1</sup>.

The double difference spectra of samples studied in the presence of Rb<sup>+</sup> ions show large perturbations in the whole range of the spectrum. In the amide I region a negative signal is seen at 1666 cm<sup>-1</sup> involving  $\beta$ -turn structures. An intense negative component is observed at 1584 cm<sup>-1</sup> and may involve both amide II contributions and the  $\nu_{as}(\text{COO}^-)$  modes of Asp/Glu acid side chains (219). These vibrational modes may also be included in the positive signal observed at 1541 cm<sup>-1</sup>. At lower wavenumbers, perturbation in the  $\nu_s(\text{COO}^-)$  modes are also seen. These results suggest that Rb<sup>+</sup> inhibitory binding to the enzyme involves the NqrB D397 residue. The tentative attributions of the signals observed are reported in [table 7.8](#) in the appendix section.



#### 4.2.5 H/D exchange kinetics measurements of the NqrB D397E mutant enzyme

Similar to the wild type enzyme, HDX kinetics was monitored in the mid-IR. The plot of the fraction of amide H against time is seen in [figure 4.2.7](#) and the HDX constants obtained after fitting are given in [table 4.2.2](#). In the presence of Na<sup>+</sup> ions, 39 % of amide H follows a fast exchange with a rate constant of 10 mins. 8 % of the amide H is exchange with a slow kinetic with a rate constant of 300 mins and 53% of amide H are not exchanged. Compared to HDX studies performed in the presence of the other ions, the fast exchange kinetics is almost the same in all cases with small variations not exceeding 2% of the amide H. The rate constant for the fast exchange kinetic is 10 mins in the presence of the different ions. Compared to measurements of the wild type enzyme, small variations in the percentage of amide H involved in each group are observed that do not exceed 2%. Although the rate constant for the fast exchange kinetic is not changed, the rate constant for the slow exchange in the NqrB D397E mutant enzyme is increased to 300 mins, twice the rate constant observed in the wild type enzyme. These results show that the mutant enzyme has less flexibility than the wild type protein, although the solvent accessibility is similar (169, 221).

In the presence of Li<sup>+</sup> ions, the fast exchange kinetic involves only 37% of amide H, with a rate constant of 10 mins. The percentage of amide H in the slow exchange is decreased by 5% in the presence of Li<sup>+</sup> ions with a rate constant of 200 mins, 100 mins less when compared with studies performed in the presence of Na<sup>+</sup> ions. These results suggest that in the presence of Li<sup>+</sup> ions, the flexibility of the enzyme increases (221). Nevertheless, 58% of amide H remains in the hydrophobic core that is 4% more than in the presence of Na<sup>+</sup> ions. These observations show that the NqrB D397E mutant enzyme is more accessible in the presence of Na<sup>+</sup> ions than in the presence of Li<sup>+</sup> ions. Compared to the wild type enzyme, the percentage of amide H involved in the fast exchange kinetic is decreased by 3%. The slow exchange kinetic involves the same percentage of amide H in both the NqrB D397E and the wild type enzyme. Nevertheless, the exchange rate for the slow exchange is surprisingly faster in the D397E mutant enzyme. Furthermore the hydrophobic domain that is not accessible to the solvent increases from 54% to 58% in the mutant enzyme when compared to the wild type protein.

HDX kinetics measurements were also performed for NqrB D397E in the presence of K<sup>+</sup> and Rb<sup>+</sup> ions. These ions are not pumped by the Na<sup>+</sup>-NQR and Rb<sup>+</sup> is also

an inhibitor. The fast exchange involves 37% and 39% of amide H in the presence of  $K^+$  and  $Rb^+$  ions respectively, with a time constant of 10 mins. The slow exchange involves 2% of amide H with a rate constant of 200 mins for samples studied in the presence of  $K^+$  ions. In the presence of  $Rb^+$  ions, the best fit was obtained with an equation including only one exponential equation representing the fast exchange group that involves 38% of amide H and a constant for the hydrophobic core which consists of 62% of amide H. These results show that the conformation of the NqrB D397E mutant enzyme is highly dependent on the type of ions present in the sample. The effect of  $Rb^+$  ions are enhanced in the D397E mutant enzyme when compared to the wild type protein as 62% of amide H are included in the hydrophobic core, the highest percentage obtained for the hydrophobic domain of the  $Na^+$ -NQR.

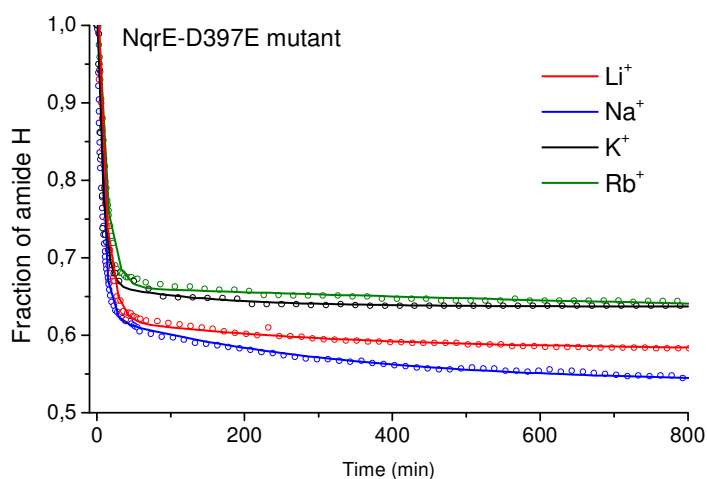


Figure 4.2.7: HDX kinetics of the NqrB D397E mutant enzyme in the presence of  $Li^+$ ,  $Na^+$ ,  $K^+$  and  $Rb^+$  ions.

	Exchange Kinetics	$Li^+$		$Na^+$		$K^+$		$Rb^+$	
		%	Time	%	Time	%	Time	%	Time
D397E mutant	Fast	37	10	39	10	37	10	38	10
	Slow	5	200	8	300	2	200	-	-
	Hydrophobic core	58	-	53	-	61	-	62	-
Wild type	Fast	40	10	40	10	37	10	37	10
	Slow	6	400	6	150	5	250	4	415
	Hydrophobic core	54	-	54	-	58	-	59	-

Table 4.2.2: HDX constants of the NqrB D397E mutant enzyme and the wild type protein obtained in the presence of  $Li^+$ ,  $Na^+$ ,  $K^+$  and  $Rb^+$  ions.

#### 4.2.6 Study of the NqrE E95Q mutant enzyme

Redox titration was monitored in the UV-visible spectral range in the presence of  $\text{Na}^+$ ,  $\text{Li}^+$  and  $\text{K}^+$  ions (figure 4.2.8). The first derivative of the difference in absorbance at 560, 460 and 380 nm was plotted against the applied potential as for the wild type enzyme. The mid-point potentials of the cofactors averaged from at least two experiments are summarized in table 4.2.3. Compared to the wild type enzyme, where the mid-point potential for the  $\text{FMN}_\text{C}$   $\text{Fl}^{\bullet-} \leftrightarrow \text{Fl}$  redox transition is -350 mV in the presence of  $\text{Li}^+$  and  $\text{Na}^+$  ions, and -450 mV in the presence of  $\text{K}^+$  and  $\text{Rb}^+$  ions, no ion dependence in the mid-point potential was observed. The only difference observed is the midpoint potential of  $\text{FMN}_\text{C}$   $\text{FlH}^- \leftrightarrow \text{Fl}^{\bullet-}$  transition. In the wild type enzyme a redox potential of -440 mV is observed in the presence of  $\text{Li}^+$  and  $\text{Na}^+$  ions whereas in the presence of  $\text{K}^+$  ions, the redox potential is decreased to -465 mV. In the E95Q, the redox potential observed for the  $\text{FMN}_\text{C}$   $\text{FlH}^- \leftrightarrow \text{Fl}^{\bullet-}$  transition is -480 mV in the presence of all  $\text{Li}^+$ ,  $\text{Na}^+$  and  $\text{K}^+$  ions.

Cofactor	Redox transition	Number of electrons	$E_m$ (mV vs Ag/AgCl)		
			$\text{Li}^+$	$\text{Na}^+$	$\text{K}^+$
<b>FAD</b>	$\text{FlH}^- \leftrightarrow \text{Fl}$	2	-445	-445	-440
<b>[2Fe-2S]</b>	$[\text{2Fe-2S}]^+ \leftrightarrow [\text{2Fe-2S}]^{2+}$	1	-495	-505	-505
<b><math>\text{FMN}_{\text{C/B}}</math></b>	$\text{Fl}^{\bullet-} \leftrightarrow \text{Fl}$	1	-460/-360	-460/-355	-470/-360
<b><math>\text{FMN}_\text{C}</math></b>	$\text{FlH}^- \leftrightarrow \text{Fl}^{\bullet-}$	1	-480	-480	-480
<b>Riboflavin</b>	$\text{FlH}^\bullet \leftrightarrow \text{FlH}_2$	1	-220	-225	-215

**Table 4.2.3: Midpoint potentials of the cofactors in the NqrE E95Q mutant enzyme in the presence of  $\text{Li}^+$ ,  $\text{Na}^+$  and  $\text{K}^+$  ions.**

Redox induced difference spectroscopic studies of the NqrE E95Q mutant enzyme must be performed to have a better understanding of the role of this residue in  $\text{Na}^+$  binding. Nevertheless, similar to the NqrB D397E mutant enzyme, the redox potentials of the cofactors are not affected by the type of ions present in the sample. This property together with activity measurements of the mutant enzyme suggest that this residue is involved in  $\text{Na}^+$  binding to the protein.

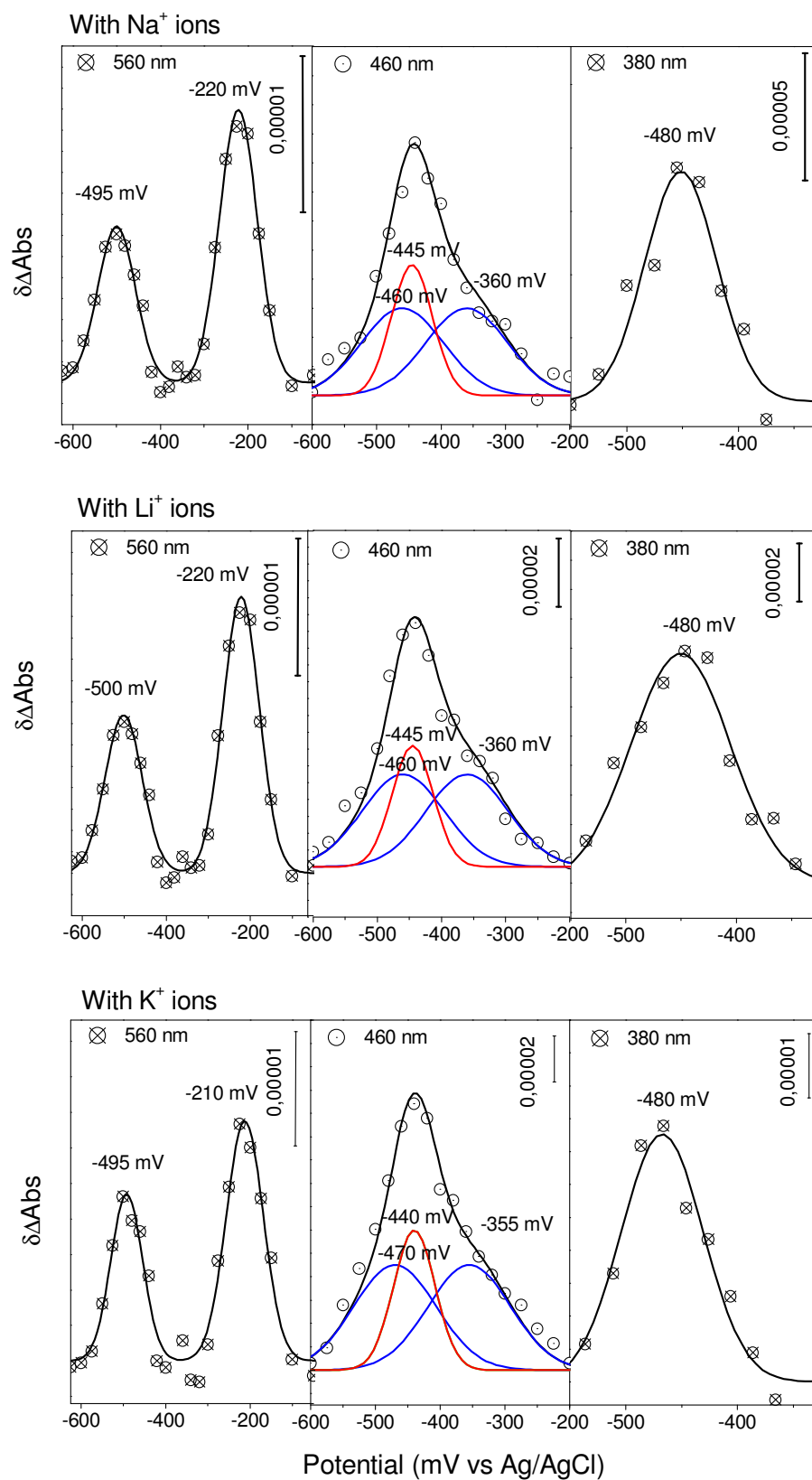
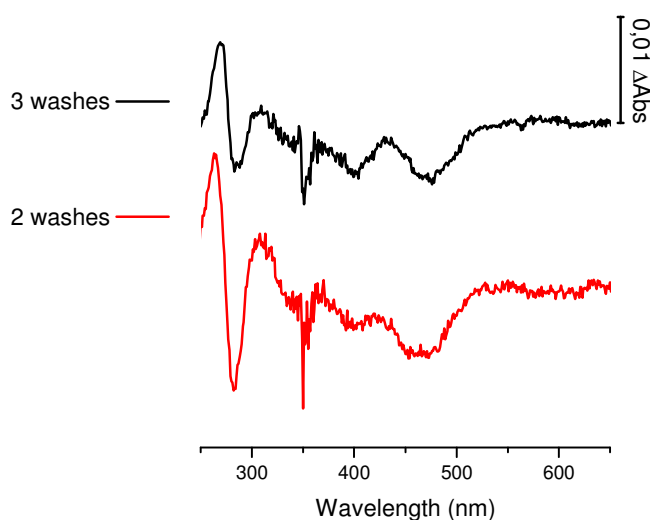


Figure 4.2.8: Redox titration of the NqrE E95Q mutant enzyme monitored at 560, 460 and 380 nm in the presence of Li<sup>+</sup>, Na<sup>+</sup> and K<sup>+</sup> ions.

#### 4.2.7 Study of other mutations of the NqrB D397 and NqrE E95 residues

Other mutations of the NqrB D397 and the NqrE E95 residues were studied, notably the NqrB D397A, the NqrB D397S, the NqrB D397N and the NqrE E95A. Unfortunately these mutant enzymes were unstable to centrifugal filtration. After 3 washes with 200  $\mu$ L of buffer, the samples lost crucial cofactors as seen in [figure 4.2.9](#). Furthermore, these mutant enzymes seem to have less riboflavin cofactor than the wild type enzyme.



**Figure 4.2.9: Reduced minus oxidized difference spectra of the D397S mutant enzyme after 2 washes and 3 washes through centrifugal membranes.**

Furthermore, these mutant enzymes seem to have less riboflavin cofactor than the wild type enzyme as seen in [figures 4.2.10 and 4.2.11](#). Redox titrations were performed on these mutant enzymes and no riboflavin could be detected. The difference spectra in the UV-visible taken before and after the experiments showed large differences that suggest that these mutants are not suitable for long lasting experiments. Redox induced FTIR difference spectra of these mutants were performed, but the results were not reproducible due to their instability. This confirms that these acidic residues are crucial for the stability of the enzyme.

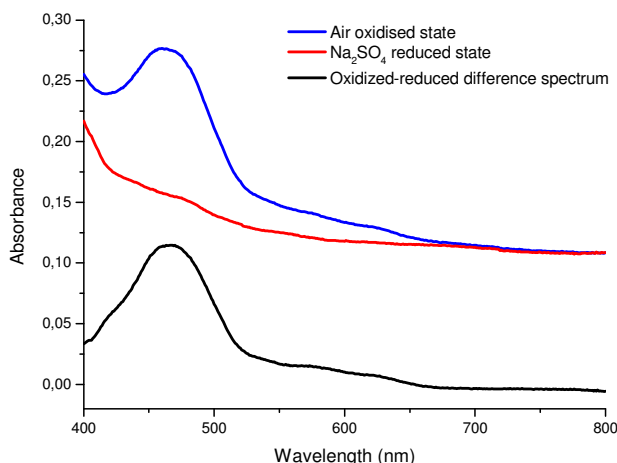


Figure 4.2.10: Absorption spectra of the air oxidized form (blue) and the  $\text{Na}_2\text{SO}_4$  reduced state of the wild type enzyme, and the oxidized minus reduced difference spectrum (black).

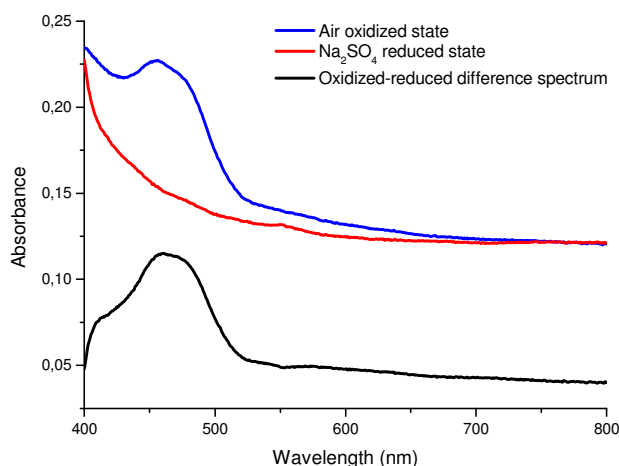


Figure 4.2.11: Absorption spectra of the air oxidized form (blue) and the  $\text{Na}_2\text{SO}_4$  reduced state of the NqrE E95A enzyme, and the oxidized minus reduced difference spectrum (black).

#### 4.2.8 The role of NqrB D397 and NqrE E95 residues in $\text{Na}^+$ binding.

Redox titrations of the cofactors present in the two stable mutant enzymes; the NqrB D397E and the NqrE E95Q, show that the redox mid-point potentials are not dependent on the type of ion present in the sample. In the wild type enzyme, a potential shift for the  $\text{FMN}_C \text{ Fl}^{\bullet-} \leftrightarrow \text{Fl}$  redox transition from -350 mV in the presence of  $\text{Na}^+$  and  $\text{Li}^+$  ions to -450 in the presence of  $\text{K}^+$  and  $\text{Rb}^+$  ions is observed. In the two mutant enzymes studied the mid-point potential for this redox transition is -460 mV independent of the type of ions present.

The redox mid-point potential of flavins anchored in proteins can be modulated by altering the environment of the isoalloxazine ring system. Redox induced difference spectroscopy showed that the conformational change upon redox reaction is perturbed

compared to the wild type enzyme. This perturbation may account for the insensibility of the redox potential of FMN<sub>C</sub> in the mutants to the different type of ions present.

The flavodoxin from *Desulfovibrio vulgaris* and *Clostridium beijerincki* possess an FMN molecule as cofactor. The mid-point potential of this FMN is highly influenced by conformational change involving loops that consists mainly of acidic residues (222). In our present study, signals in NqrB D397E-wild type double difference spectra for samples prepared in the presence of Na<sup>+</sup>, Li<sup>+</sup> and K<sup>+</sup> ions, indicate that the conformational change seen in the amide I region is the same. This structural change involves mainly random structures and  $\beta$ -turns. It is probable that this structural change in the NqrB D397E mutant enzyme is at the origin of the electrochemical properties of the redox cofactors present.

It was shown that signals tentatively attributed to the  $\nu_s(\text{COO}^-)$  modes of Asp/Glu acid side chains observed in the redox induced difference spectra of the NqrB D397E mutant enzyme are sensible to the presence of Na<sup>+</sup> and Li<sup>+</sup> ions. Compared to the wild type enzyme, these signals appear at higher wavenumbers, which indicates that in the NqrB D397E mutant enzyme, Na<sup>+</sup>-binding is weaker than in the wild type enzyme. These findings may encounter for the difference in quinone activity measurements of the enzyme where quinone reduction has a 8-fold stimulation in the presence of Na<sup>+</sup> ions (compared to measurements in the absence of Na<sup>+</sup> ions) and only a 2-fold stimulation for the NqrB D397E mutant protein.

In the Na<sup>+</sup>-Rb<sup>+</sup> and K<sup>+</sup>-Rb<sup>+</sup> double difference spectra, a negative signal was seen at 1403 cm<sup>-1</sup> and tentatively attributed to the  $\nu_s(\text{COO}^-\text{Rb}^+)$  modes. The same signal was also observed in the double difference spectra of the wild type enzyme. These findings suggest that the NqrB D397E residue is not involved in inhibitory Rb<sup>+</sup> binding to the enzyme.

HDX measurements showed that the enzyme is more accessible in the presence of Na<sup>+</sup> ions than in the presence of the other ions, indicating the conformational dependence of the protein to the type of ion present. In the presence of Rb<sup>+</sup> ions, the hydrophobic core consists of 62% of amide H and no slow exchange kinetic is observed. These results suggest that the protein is in a closed conformation in the presence of Rb<sup>+</sup> ions and in an open conformation in the presence of Na<sup>+</sup> ions.

### 4.3 Study of the quinone binding site of the Na<sup>+</sup>-NQR

Enzymes that are resistant to both HQNO and korormicin were found to have a single mutation in the NqrB subunit of the G140 residue (92). To investigate the quinone binding site, NqrB G140A mutant enzyme was studied.

#### 4.3.1 Redox titration of the NqrB G140A mutant enzyme

The mid-point potential of the cofactors present in the NqrB G140A mutant enzyme were determined by redox titration monitored in the UV-visible spectral range as described before for the wild type enzyme. The difference in absorbance was monitored at 560, 460 and 380 nm (184). The results are presented in [figure 4.3.1](#) and the mid-point potentials of the cofactors are summarized in [table 4.3.1](#).

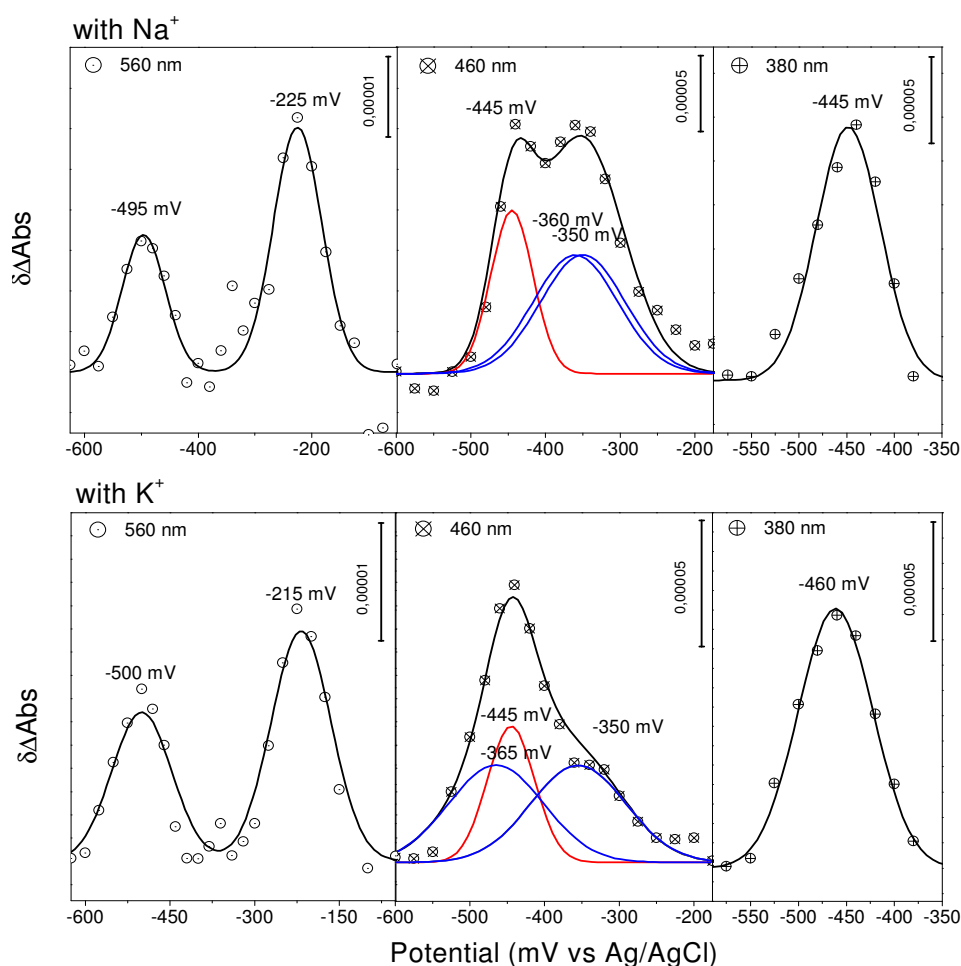


Figure 4.3.1: Redox titration of the NqrB G140A mutant enzyme monitored at 560, 460 and 380 nm in the presence of Na<sup>+</sup> and K<sup>+</sup> ions.



Cofactor	Redox transition	Number of electrons	E <sub>m</sub> (mV vs Ag/AgCl)	
			Na <sup>+</sup>	K <sup>+</sup>
<b>FAD</b>	FlH <sup>-</sup> ↔ Fl	2	-445	-445
<b>[2Fe-2S]</b>	[2Fe-2S] <sup>+</sup> ↔ [2Fe-2S] <sup>2+</sup>	1	-495	-505
<b>FMN<sub>C/B</sub></b>	Fl <sup>•-</sup> ↔ Fl	1	-360/-350	-460/-355
<b>FMN<sub>C</sub></b>	FlH <sup>-</sup> ↔ Fl <sup>•-</sup>	1	-440	-465
<b>Riboflavin</b>	FlH <sup>•</sup> ↔ FlH <sub>2</sub>	1	-220	-225

**Table 4.3.1: Mid-point potentials of the redox cofactors present in the NqrB G140A mutant enzyme in the presence of Na<sup>+</sup> and K<sup>+</sup> ions.**

Similar to the wild type enzyme, a mid-point potential shift is observed. A mid-point potential of -360 mV is obtained for the FMN<sub>C</sub> Fl<sup>•-</sup> ↔ Fl transition in the presence of Na<sup>+</sup> ions, a downshift of approximately 90 mV is observed in the presence of K<sup>+</sup> ions (184). These results demonstrate that the thermodynamic properties of the redox active cofactors are not altered in this mutant enzyme and are similar to the wild type enzyme. Furthermore in the wild type enzyme, ubiquinone 8 is present (93). So far the redox potential for the bound quinone has not been determined but is expected to be between 0 and 100 mV vs. Ag/AgCl (183).

#### 4.3.2 Redox induced difference spectroscopic studies

Figure 4.3.2 shows the redox induced difference spectrum for the potential range from -620 mV to +200 mV of mutant NqrB G140A protein. In the amide I region positive signals at 1687, 1672, 1660 cm<sup>-1</sup> and negative signals at 1644, 1632 cm<sup>-1</sup> are attributed to the  $\nu(\text{C=O})$  mode of the polypeptide backbone reflecting the redox induced conformational change (181). Signals at 1715, 1704 cm<sup>-1</sup> may be attributed to the  $\nu(\text{C=O})$  mode from the flavins or protonated side chain acidic groups from Asp/Glu (179, 180, 223).  $\nu(\text{C=O})$  mode from the flavins also contribute to the positive signals at 1687, 1672, 1660 cm<sup>-1</sup>. Signals at 1595, 1565 and 1540 cm<sup>-1</sup> are attributed to the amide II mode of the polypeptide backbone (181). In this region, the  $\nu(\text{C=N})$  stretching from the flavins are also expected (179, 180). The intense positive signal at 1540 cm<sup>-1</sup> also include the  $\nu(\text{C=C})$  mode of neutral flavins (179, 180). The negative signal at 1405 cm<sup>-1</sup> is attributed to the isoalloxazine ring mode vibration of the flavins and to the  $\nu_s(\text{COO}^-\text{Na}^+)$  modes from either Asp/Glu acid side chain (206, 208). At lower wavenumbers, signals arising from the isoalloxazine ring system reorganization are expected.

Comparing the difference spectra of the wild type to the G140A, the most important changes are observed in the region of amide I with a decrease in intensity of the signal at 1672 and 1658  $\text{cm}^{-1}$ . These spectral components are typical of protonated arginine side chains and can be attributed to the  $\nu_{\text{as}}(\text{CN}_3\text{H}_5^+)$  and the  $\nu_{\text{s}}(\text{CN}_3\text{H}_5^+)$  modes respectively (203, 220). Smaller changes are observed at 1450  $\text{cm}^{-1}$ . The  $\nu(\text{C}=\text{O})$  modes from glutamine side chains are also expected at 1672  $\text{cm}^{-1}$  (203, 219). The double difference spectrum of the wild type minus G140A mutant enzyme was obtained by interactive subtraction.

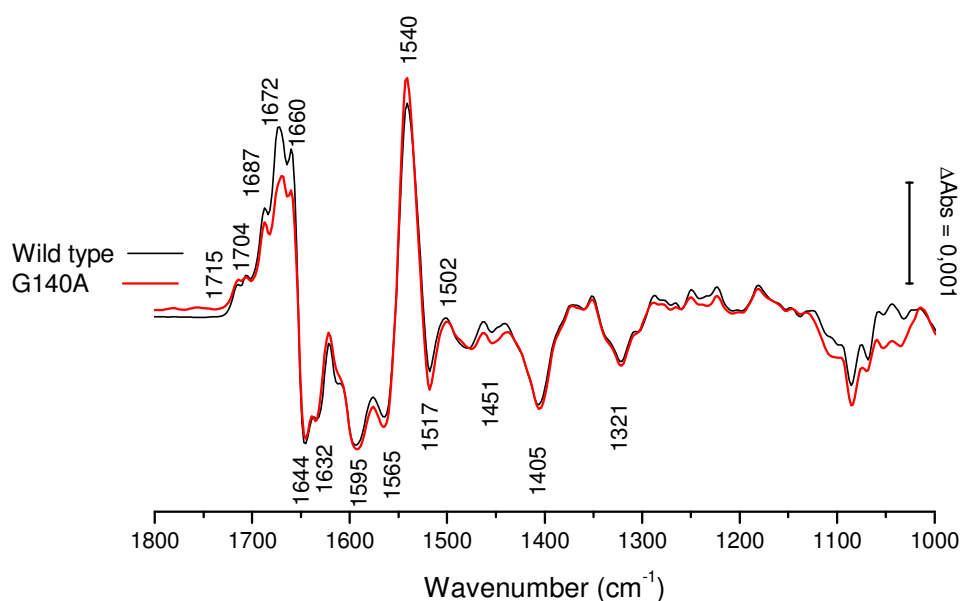


Figure 4.3.2 : Redox induced difference spectra of the NqrB G140A mutant enzyme (red) and the wild type (blue) for the potential range from -620 to +200 mV in the presence of  $\text{Na}^+$  ions.

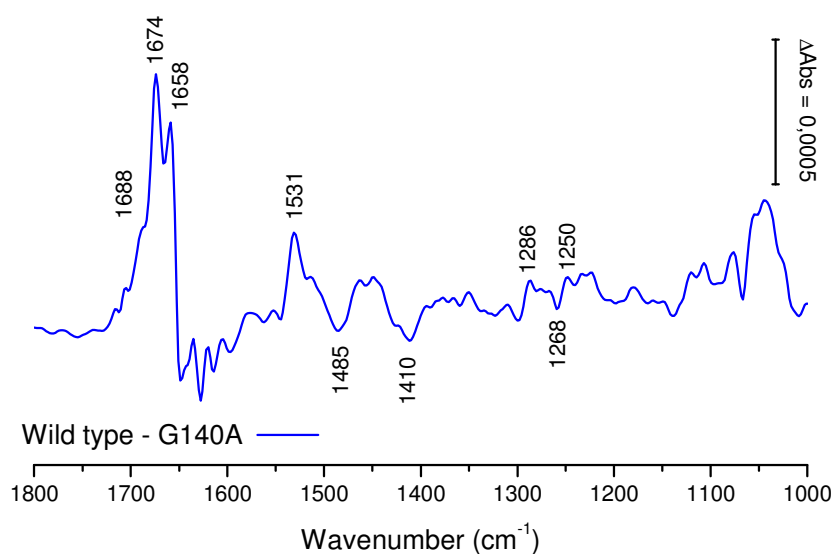


Figure 4.3.3: Wild type - G140A double difference spectrum for the potential range between -620 mV to +200 mV.

The  $\nu(\text{C=O})$  and the  $\nu(\text{C=C})$  vibrational modes from neutral quinone are seen at 1674 and 1658  $\text{cm}^{-1}$  respectively (figure 4.3.3) (223, 224). In this spectral region, amide I contributions are also expected. Smaller signals at 1485, 1410 and 1256  $\text{cm}^{-1}$  may be attributed to quinol ring rearrangement. Two positive signals observed at 1286 and 1250  $\text{cm}^{-1}$  are attributed to the  $\text{C-OCH}_3$  vibrations of the methoxy groups of quinone (224). A positive signal observed at 1530  $\text{cm}^{-1}$  may include contributions from amide II signature. The tentative assignments of the signals observed in the wild type-NqrB G140A double difference spectrum are reported in table 7.9 in the Appendix section.

#### 4.3.3 Redox induced difference spectroscopic studies for the critical potential step including riboflavin cofactor and quinone.

In order to depict the contribution of the ubiquinone and the nearby riboflavin, the FTIR difference spectrum for a selected step was obtained for the potential range between -280 mV to +200 mV (184).

For the wild type, positive signals in the amide I region are observed at 1688, 1670, 1660 and 1623  $\text{cm}^{-1}$  as seen in figure 4.3.4. The two positive signals at 1670 and 1623  $\text{cm}^{-1}$  are typical of the asymmetric and the symmetric  $\nu(\text{CN}_3\text{H}_5^+)$  modes of arginine side chains (203, 219). Furthermore, the  $\nu(\text{C=O})$  modes from glutamine side chains may contribute to the signal at 1688  $\text{cm}^{-1}$  (219). The positive signal at 1623  $\text{cm}^{-1}$  may also include contributions from the  $\delta_{\text{as}}(\text{NH}_3^+)$  of lysine side chains (203). The symmetric mode for this vibration may contribute to the signals at 1530  $\text{cm}^{-1}$  (204, 219). A strong negative signal at 1586  $\text{cm}^{-1}$  is tentatively attributed to either amide II contribution or the  $\nu(\text{C=N})$  mode of the riboflavin. The difference spectrum of flavins for the  $\text{Fl} \leftrightarrow \text{FlH}_2$  transition of flavins show an intense signal at 1548  $\text{cm}^{-1}$  attributed to the  $\nu(\text{C=C})$  mode which is not observed in the difference spectrum of the  $\text{Na}^+$ -NQR for the potential step between -280 mV to +200 mV (179). We cannot account for the absence of this signal although it can be hidden by negative contributions arising from the amide II band. Furthermore, in the  $\text{Na}^+$ -NQR, the redox transition of the riboflavin is  $\text{FlH}^\bullet \leftrightarrow \text{FlH}_2$ , this redox transition has not been studied before by FTIR difference spectroscopy. Although contributions from the flavins are expected in the spectral region between 1700-1500  $\text{cm}^{-1}$ , we cannot distinguish the signals from the amide contributions and the side chains vibrations. At lower wavenumbers, signals at 1413 and 1375  $\text{cm}^{-1}$  may be attributed to either the isoalloxazine ring mode of the riboflavin or the  $\nu_s(\text{COO}^-)$  modes of Asp/Glu side chains.

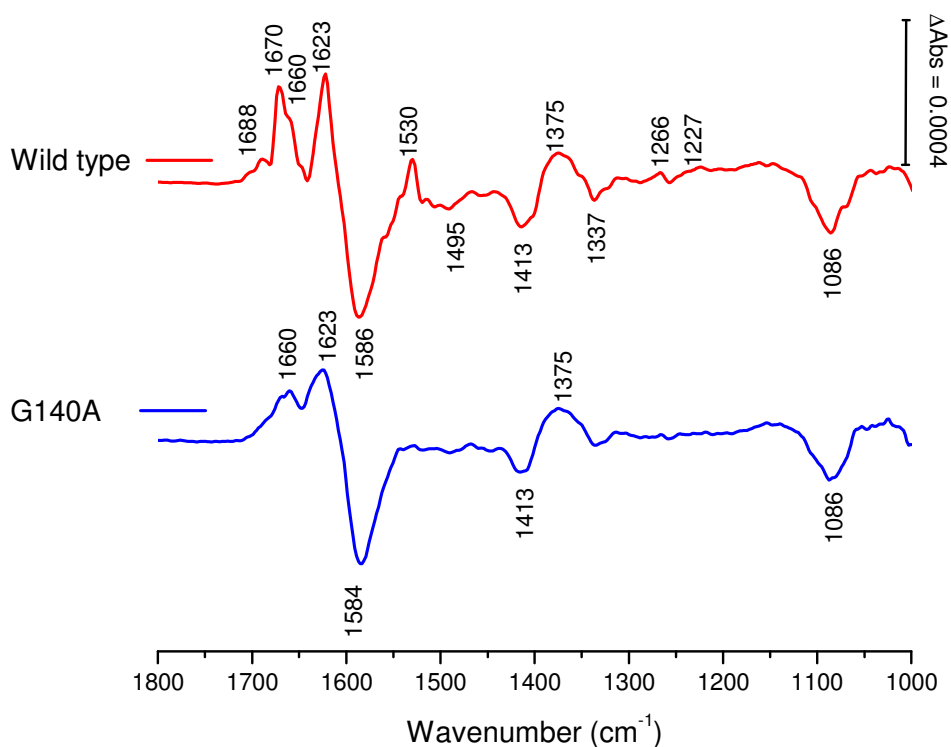


Figure 4.3.4: Redox induced difference spectra of the wild type protein (red) and the NqrB G140A mutant enzyme (blue) for the potential step between -280 mV to +200 mV in H<sub>2</sub>O buffer.

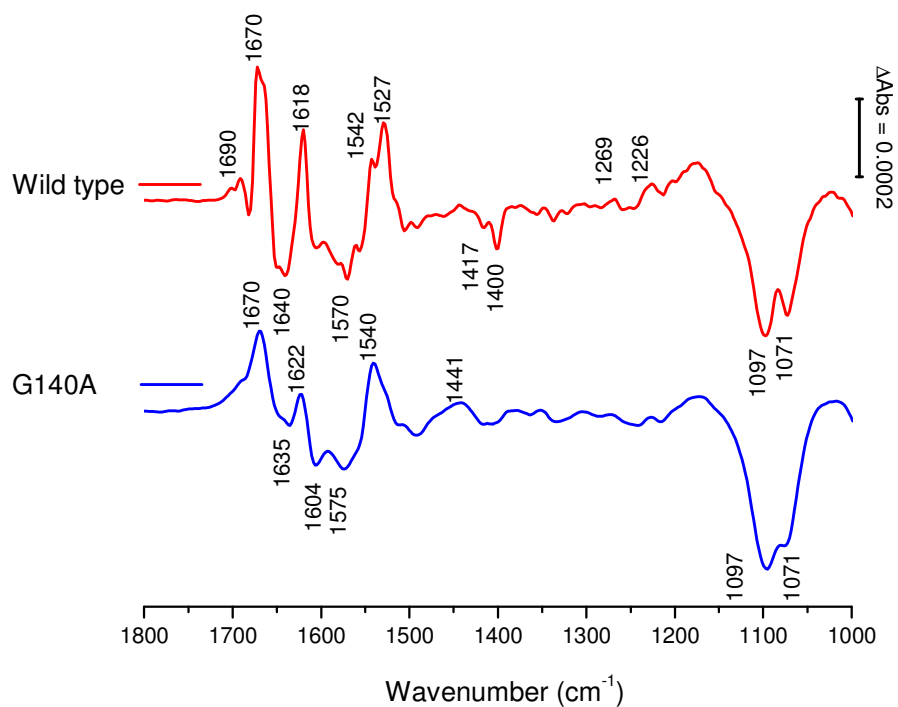


Figure 4.3.5: Redox induced difference spectra of the wild type protein (red) and the NqrB G140A mutant enzyme (blue) for the potential step between -280 mV to +200 mV in D<sub>2</sub>O buffer.

Signals arising from the quinone are also seen. The positive signals at 1670 and 1623  $\text{cm}^{-1}$  may include the  $\nu(\text{C}=\text{O})$  and the  $\nu(\text{C}=\text{C})$  vibrational modes from neutral quinone are seen at 1674 and 1658  $\text{cm}^{-1}$  respectively (223, 224). Typical  $\text{C}-\text{OCH}_3$  vibrational modes of the methoxy groups of quinone can be observed at 1266  $\text{cm}^{-1}$  (224).

In the redox induced difference spectrum of the G140A mutant (figure 4.3.4), only two positive signals are observed in the amide I region at 1660 and 1623  $\text{cm}^{-1}$  but with lower intensities when compared to the wild type enzyme. An intense negative signal is observed at 1584  $\text{cm}^{-1}$ , 2  $\text{cm}^{-1}$  lower than in the wild type enzyme. Positive and negative signals at 1413 and 1375  $\text{cm}^{-1}$  respectively are observed as for the wild type protein, although the signal at 1413  $\text{cm}^{-1}$  decreases in intensity.

Similar measurements were performed in  $\text{D}_2\text{O}$  buffer (figure 4.3.5). In the redox induced difference spectrum of the wild type enzyme, positive signals at 1690, 1670, 1618  $\text{cm}^{-1}$  and a negative signal at 1640  $\text{cm}^{-1}$  are observed in the amide I region.

In this spectral region, modes arising from the  $\nu(\text{C}=\text{O})$  and the  $\nu(\text{C}=\text{C})$  from neutral quinone are also expected (177). The positive signal at 1269  $\text{cm}^{-1}$  is typical of the  $\text{C}-\text{OCH}_3$  vibrational modes of the methoxy groups of quinone. Two negative signals are observed at 1417 and 1400  $\text{cm}^{-1}$  may be attributed to ring reorganization of quinone system.

Signals arising from flavins are usually shifted in  $\text{D}_2\text{O}$  buffer solutions. In the  $\text{Na}^+$ -NQR, riboflavin is stable in its neutral flavosemiquinone form ( $\text{FlH}^\bullet$ ) and undergoes a one electron reduction to form the neutral form of reduced flavins ( $\text{FlH}_2$ ) (88). This transition is usually pH dependent (60 mV / pH) but in the  $\text{Na}^+$ -NQR, no pH dependence is observed (184). These elements suggest that the riboflavin is protected from the outer environment in a pocket that can stabilize the  $\text{FlH}^\bullet$  form of the riboflavin in the oxidized form of the protein. Therefore, the signals arising from the riboflavin are not expected to shift in  $\text{D}_2\text{O}$  buffer. In the amide II region, negative signals are observed at 1570  $\text{cm}^{-1}$  less intense than the signal at 1586  $\text{cm}^{-1}$  in the difference spectrum obtained in  $\text{H}_2\text{O}$  buffer. This spectral region may also include modes from the flavins. A positive signal is observed at 1542  $\text{cm}^{-1}$  and may include the  $\nu(\text{C}=\text{C})$  mode of flavins. This signal is not seen in  $\text{H}_2\text{O}$  buffer due to the negative contribution of the amide II band in this spectral region.

Interestingly a positive signal is observed at 1527  $\text{cm}^{-1}$  (1530  $\text{cm}^{-1}$  in  $\text{H}_2\text{O}$  buffer) typical of  $\delta_s(\text{NH}_3^+)$  modes of lysine side chains. The  $\delta_{as}(\text{NH}_3^+)$  mode of this vibration is

expected to contribute to the signal at  $1618\text{ cm}^{-1}$ .  $\nu(\text{C=O})$  modes from glutamine side chains observed at  $1670\text{ cm}^{-1}$  in the difference spectrum obtained for samples prepared in  $\text{H}_2\text{O}$  buffer are expected to give rise to signals at lower frequencies. Nevertheless, since the signal is not shifted, it may suggest that this residue is not accessible to the solvent. Surprisingly the negative signal at  $1413\text{ cm}^{-1}$  and the positive signal at  $1375\text{ cm}^{-1}$  observed in the difference spectrum for samples prepared in  $\text{H}_2\text{O}$  buffer is not observed in the difference spectrum for samples in  $\text{D}_2\text{O}$  buffer. Contributions from the  $\nu_s(\text{COO}^-)$  modes of Asp/Glu side chains are not expected to have large shifts in  $\text{D}_2\text{O}$  buffer. We cannot account for these observations, although these signals may include contributions from the flavins.

In the FTIR difference spectrum of the NqrB G140A ([figure 4.3.5](#)), changes are observed in the full spectral range when compared to the difference spectrum of the wild type protein. Typical signals of the  $\text{C-OCH}_3$  vibrations of the methoxy groups of quinones are not observed any more in the mutant enzyme. The tentative assignments are summarized in [table 7.10](#) in the Appendix section.

#### **4.3.4 Double difference spectra for the critical potential step including the riboflavin cofactor and quinone.**

Interactive subtraction of the G140A mutant enzyme from the wild type was performed to obtain the double difference spectra ([figure 4.3.6](#)) and to highlight the changes described above. The intensity of the signals are weak since the data show the double difference spectra of a redox step involving only one cofactor of the  $\text{Na}^+\text{-NQR}$ . Nevertheless, in  $\text{H}_2\text{O}$  buffer, the signals of ubiquinone can be identified. Positive signals at  $1671$  and  $1621\text{ cm}^{-1}$  are attributed respectively to the so called  $\text{C=O}$  band and  $\nu(\text{C=C})$  mode of neutral quinone (*177*). The position of the  $\text{C=O}$  band reveals that the quinone is only weakly bound to the  $\text{Na}^+\text{-NQR}$  (*177*, 224-226). Smaller negative signals at  $1414$ ,  $1398$ ,  $1353$  and  $1336\text{ cm}^{-1}$  are attributed to rearrangements of the quinone ring upon reduction (*177*). The positive signal at  $1268\text{ cm}^{-1}$  is attributed to the  $\text{C-OCH}_3$  vibrations of the methoxy groups. These signals observed are also observed in the double difference spectrum of the wild type-G140A mutant enzyme. The results presented here suggest that compared to the wild type, the NqrB G140A mutant enzyme either has less quinone or does not bind it anymore.

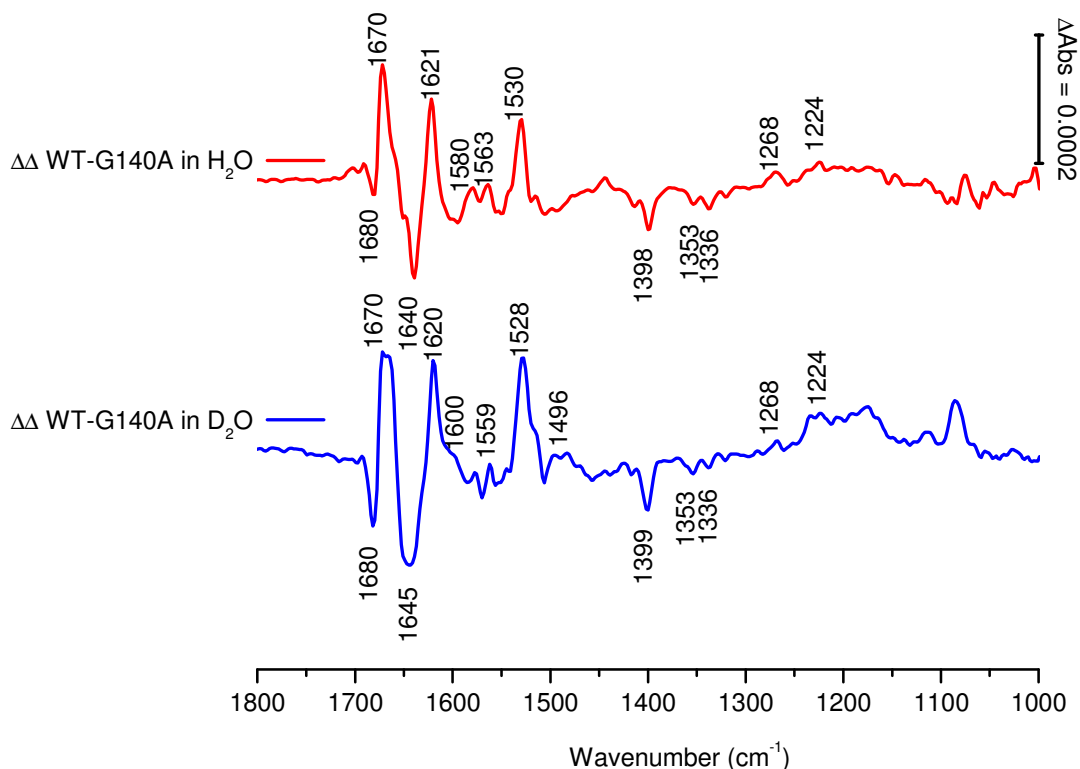


**Figure 4.3.6: Wild type – NqrB G140A double difference spectra for the potential step between -280 mV to +200 mV in H<sub>2</sub>O (red) and D<sub>2</sub>O (blue).**

The coupled  $\nu(\text{CN}_3\text{H}_5)$  asymmetric and symmetric modes of arginine may also contribute to the signals at 1671 and 1620 cm<sup>-1</sup> (1621 cm<sup>-1</sup> in D<sub>2</sub>O) respectively. The strong signal observed at 1530 cm<sup>-1</sup> may be attributed to the  $\delta_s(\text{NH}_3^+)$  of lysine. The asymmetric mode of this vibration may contribute to the signal at 1621 cm<sup>-1</sup> (181, 203, 219). The results suggest that a lysine residue is protonated in the oxidized form of the enzyme and may be deprotonated in the reduced form. Although these signals have typical positions for the lysine side chains vibrational modes, the high intensity of these bands are not characteristic of lysine residues. The tentative attributions are reported in [table 7.11](#) in the Appendix section.

The negative signal observed in the double difference spectra obtained for samples both in H<sub>2</sub>O and D<sub>2</sub>O buffer at 1680 cm<sup>-1</sup> can include contributions from  $\nu(\text{C=O})$  from glutamine side chain. The signals for lysine, arginine and glutamine described previously are usually shifted to lower wavenumbers in D<sub>2</sub>O buffer. Nevertheless when encapsulated in the hydrophobic core of the protein, these shifts may not be observed (227).

#### 4.3.5 Effects HQNO inhibition

HQNO is a non-competitive inhibitor for quinone binding and its binding site is suggested to be close to the quinone binding site. To further investigate the quinone binding site, the effect of HQNO on the wild type protein and the NqrB G140A mutant has been investigated. Redox induced difference spectroscopic studies have been performed for the potential range between -280 mV to +200 mV. In the difference spectrum of the wild type enzyme important changes are observed in the presence of HQNO mainly in the amide I and amide II region suggesting a perturbation of the conformational change that is found upon redox reaction (figure 4.3.7). Interestingly positive signals observed at 1622 and 1531  $\text{cm}^{-1}$  may include to the  $\delta(\text{NH}_3^+)$  symmetric and asymmetric modes of lysine residues. On the opposite, no significant change was observed on the G140A mutant enzyme except small changes in intensity in the amide I region. The tentative assignments are presented in [table 7.12](#) in the Appendix section.

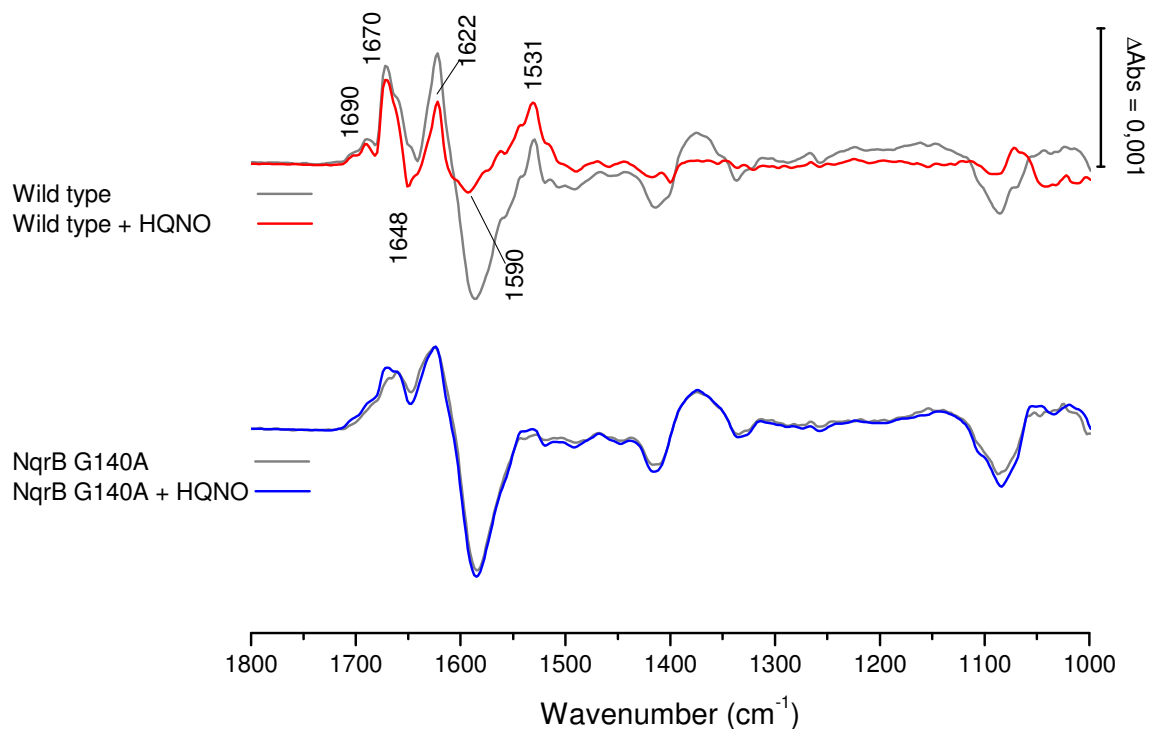


**Figure 4.3.7:** Redox induced difference spectra of the wild type enzyme (red) and the NqrB G140A mutant (blue) in the presence of HQNO for the potential range between -280 mV to +200 mV.



#### 4.3.6 Secondary structure analysis of the NqrB G140A mutant enzyme

In order to confirm the structural integrity of the mutant enzyme, the secondary structure of the NqrB G140A mutant enzyme was determined by amide I band deconvolution and compared with the secondary structure of the wild type enzyme (figure 4.3.8). The results show that the secondary structure is not perturbed in the mutant enzyme with 22% of  $\beta$ -turn, 45 % of  $\alpha$ -helical structures and 33 % of  $\beta$ -sheet. There is a 1% difference compared to the wild type enzyme which is within the 10% error of this technique.

Wavenumber (cm <sup>-1</sup> )	Secondary structure	% in the wild type	% in the NqrB G140A
1676	$\beta$ -turn	23	22
1652	$\alpha$ -helix	44	45
1634	$\beta$ -sheet	18	17
1620	$\beta$ -sheet	15	16

**Table 4.3.2: Secondary structure of the wild type protein and the NqrB G140A mutant enzyme determined by deconvolution of the amide I band.**

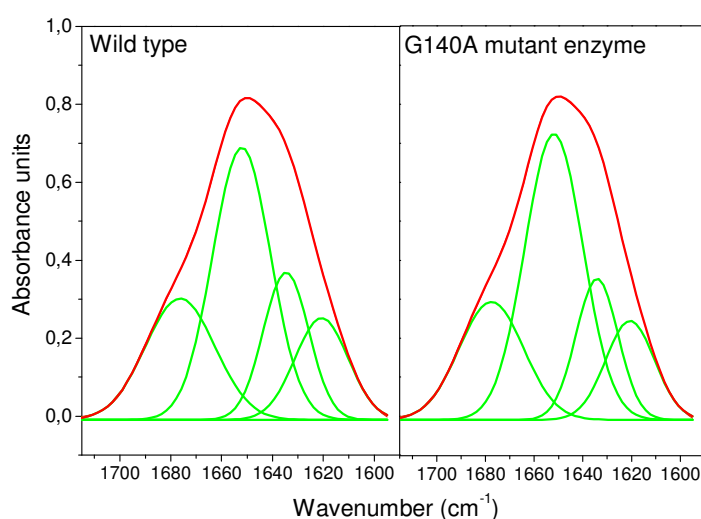


**Figure 4.3.8: Amide I deconvolution of the wild type protein and the NqrB G140A mutant enzyme.**

#### 4.3.7 Involvement of the NqrB G140 residue in quinone binding

Both korormicin and HQNO are quinone analogues (91). Hayashi et al. showed that these inhibitors are non-competitive for the binding of quinone (228). Moreover, the same authors identified enzymes carrying a single mutation on the G140 residue that were resistant to these inhibitors (92). Kinetic measurements showed that mutant enzymes of the G140 residue have non-saturating kinetics with ubiquinone (229). Reverse reduction

using ubiquinol also showed that the kinetics of reduction of the enzyme is altered (229). These results strongly suggest that G140 forms part of the quinone binding site. In the present work, redox induced FTIR difference spectroscopic studies show that NqrB G140A mutant enzyme has either less bound quinone or none. The signal attributed to the  $\nu(\text{C=O})$  vibrational mode of the quinone identified at  $1670\text{ cm}^{-1}$ , indicates a weak hydrogen bonding environment. Furthermore signals observed at  $1621$  and  $1530\text{ cm}^{-1}$  only in the redox induced difference spectra of the wild type enzyme suggest the involvement of ubiquinone oxidation is coupled with lysine protonation. These signals are not observed in the NqrB G140A mutant enzyme. Although the signals for deprotonation were not clearly identified, it can be suggested that deprotonation is coupled with reduction of ubiquinone.  $\nu(\text{C=O})$  mode of glutamine side chain was also identified at  $1680\text{ cm}^{-1}$  and may form a hydrogen bonding network with the head group of ubiquinol.

Redox induced difference spectra obtained in the presence of HQNO suggest that conformational changes are perturbed in the wild type enzyme. On the contrary no changes are observed in the difference spectrum of the G140A mutant enzyme.

It cannot be excluded that the peptide group of the glycine residue forms a hydrogen bonding network with oxygen from the quinone (230). NqrB G140 residue may not be directly involved in the quinone binding, mainly due to lack of essential functional groups required for electrostatic binding. The residue may be involved in packing of  $\alpha$ -helical structures. When mutated, the immediate environment of the quinone binding is perturbed. NqrB G140 may also form part of a pocket for quinone binding. When substituted with alanine, steric perturbation may explain the lack of ubiquinone in the NqrB G140A mutant enzyme and also its insensitivity to HQNO (231).

#### 4.4 The [cytochrome $c_{552}$ -Cu<sub>A</sub> fragment] complex

The hydrophobic nature of the interaction between cytochrome  $c_{552}$  and the Cu<sub>A</sub> fragment from the  $ba_3$  oxidase from the organism *Thermus thermophilus* gave us the opportunity to perform electrochemical measurements in the presence of salts.

First, the mid-point potential of the cofactors from two proteins were studied individually. Then equimolar samples were mixed for at least 4 hours prior to studies of the complex. To have an insight of what happens on a molecular level; redox-induced mid-IR difference spectroscopic studies were performed on the individual samples and on the complex. All the experiments were performed at pH 7 and pH 9.

##### 4.4.1 Redox titration

For cytochrome  $c_{552}$ , changes are observed at 400, 450, 520 and 552 nm upon redox reaction. To determine the redox potential, the difference in absorbance observed at 552 nm was plotted against the applied potential and a Nernst's equation was fitted on the data (figure 4.4.1). As a control, similar plots were performed at 420 nm in the Soret region.

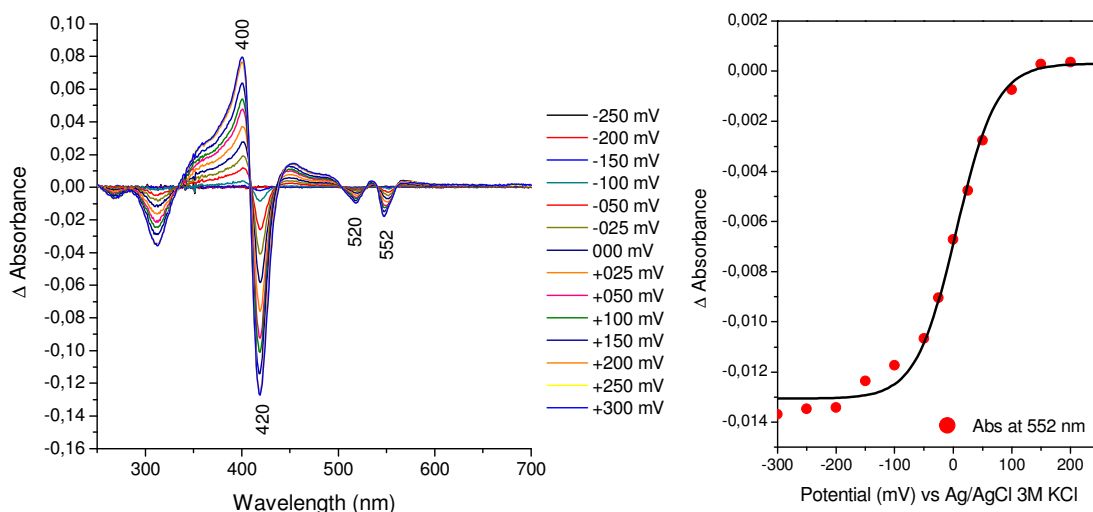


Figure 4.4.1: Redox titration of cytochrome  $c_{552}$  from -250 mV to +300mV (left). The difference in absorbance observed at 552 nm is plotted against the applied potential and presented together with a Nernst fit (right).

Oxidative and reductive titrations were performed. They were fully reversible. A mid-point potential of 212 mV vs SHE' (4 mV vs Ag/AgCl reference electrode) was observed after averaging from four experiments. In 1977, Hon-Nami and Ishima reported a mid-point potential of 232 mV determined by chemical titration with ferrous ammonium sulphate (136). The higher potential observed, may originate from the titration buffer ferrous/ferric ammonium sulfate interacting with the protein in the previous study. Direct electrochemistry with a three electrode setup performed by Fee et al. reported a mid-point potential of 202 mV for the native sample and 200 mV for the recombinant protein, in good correlation with our results (137).

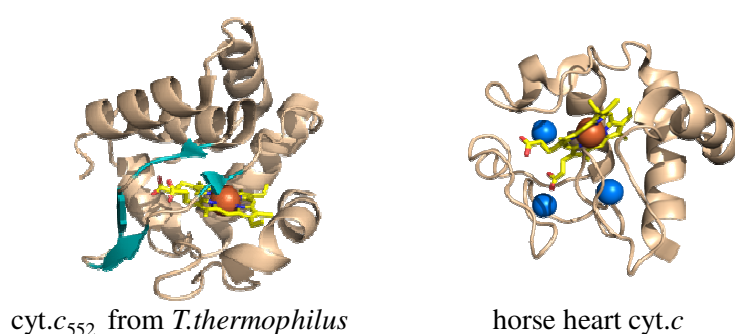
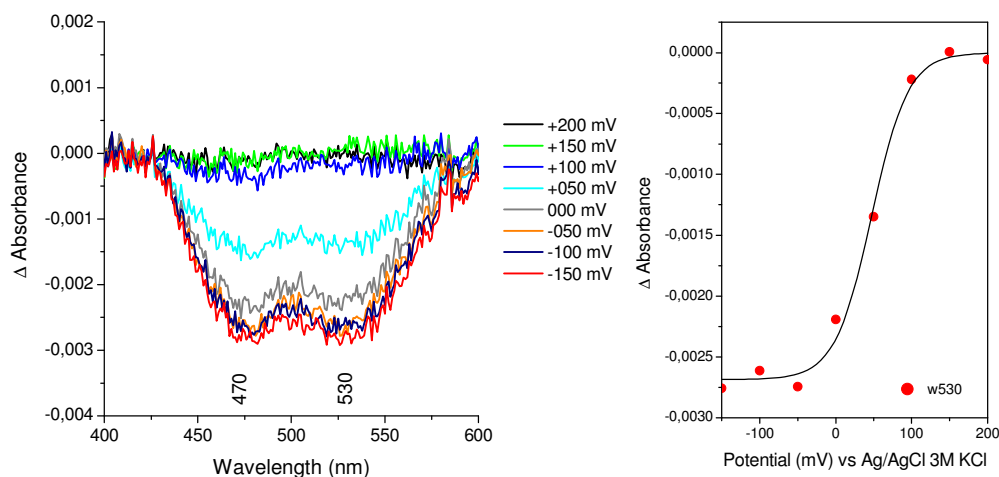


Figure 4.4.2: Crystallographic structure of cytochrome *c*<sub>552</sub> from *Thermus thermophilus* (PDB 1C52) shows the absence of water molecules in the inner core compared to horse heart cytochrome *c*, PDB 1HRC (17, 50).

Furthermore, no pH dependence of the redox potential was observed for cytochrome *c*<sub>552</sub> from *Thermus thermophilus*, compared to the analogue cytochrome *c* from horse heart (232). In the latter, crystallographic studies identified three water molecules in the inner structure on the enzyme suggesting that the interior of the molecule is accessible by the solvent (figure 4.4.2) (50). Varying the pH of the buffer, may modify the protonation state of the heme propionates and perturb the electronic structure of the heme (233). On the contrary, the structure of cytochrome *c*<sub>552</sub> from *Thermus thermophilus* has no inner solvent molecules. The heme propionates are protected from varying pH of the buffer. This property is suggested as being an adaptation of the organism to high temperatures as the increased hydrophobic core confers more thermo stability to the enzyme (17).

Similar measurements were performed on the Cu<sub>A</sub> fragment where metal ligand charge transfer gives two broad signals at 470 and 530 nm (figure 4.4.3).  $\Delta$  Absorbance was monitored at these two wavelength to determine the mid-point potential of the binuclear copper center. A value of 256 mV vs SHE' was obtained pH independent (48 mV vs Ag/AgCl). Previously, Immoos et al. reported a value of 240 mV for the Cu<sub>A</sub> fragment obtained by cyclic voltamperometry in solution, which is in good correlation with our results (135).



**Figure 4.4.3:** Redox titration monitored from +200 mV to -150 mV for the Cu<sub>A</sub> fragment (left). The difference in absorbance at 530 nm was plotted against the applied potential to determine the mid-point potential.

The UV-visible difference spectrum of the complex [cytochrome *c*<sub>552</sub>-Cu<sub>A</sub> fragment] is similar to that of cytochrome *c*<sub>552</sub> (figure 4.4.4). Signals arising from the Cu<sub>A</sub> fragment cannot be depicted, mainly due to the large absorption coefficients of the *c*-type heme ( $\epsilon_{\text{red-ox } 552 \text{ nm}} = 21.0 \text{ mM}^{-1} \cdot \text{cm}^{-1}$ ) compared to the binuclear copper center ( $\epsilon_{\text{ox-red } 530 \text{ nm}} = 3.1 \text{ mM}^{-1} \cdot \text{cm}^{-1}$ ) (138). With this constraint, in the complex, only the redox potential of cytochrome *c*<sub>552</sub> can be determined by this method.

Interestingly, the mid-point potential obtained was 125 mV vs SHE' (-83 mV vs Ag/AgCl). This corresponds to a shift of 90 mV to lower potential in the presence of the Cu<sub>A</sub> fragment (figure 3.2.5). Moreover, these potentials were not dependent on pH. To further investigate the complex, redox induced IR difference spectroscopic experiments were performed.

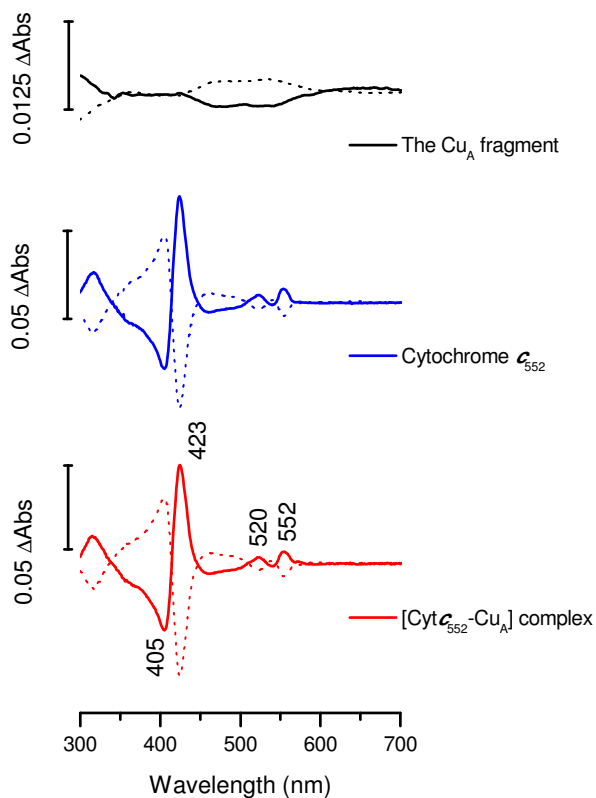


Figure 4.4.4: Reduced minus oxidized difference spectra (bold) in the UV-visible spectral domain for the potential range between -300 mV to +300 mV of the  $\text{Cu}_A$  fragment (black), cytochrome  $c_{552}$  (blue) and the complex  $[\text{cyt.}c_{552} - \text{Cu}_A \text{ fragment}]$  (red).

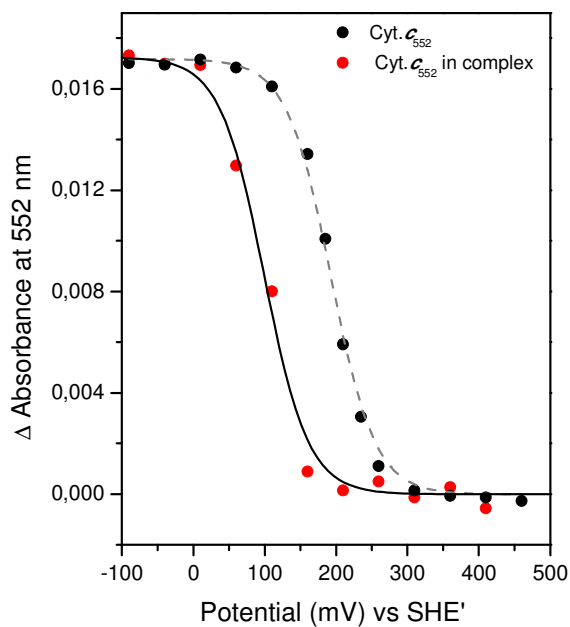


Figure 4.4.5: Comparison of the titration curve at 552 nm of the cytochrome  $c_{552}$  (black balls) and the complex cytochrome  $c_{552} - \text{Cu}_A$  fragment (red balls).

#### 4.4.2 Redox induced mid-IR difference spectroscopy

In the oxidized-reduced difference spectra of cytochrome  $c_{552}$  at pH 7 (figure 4.4.6), signals at 1666, 1652, 1631 and 1610  $\text{cm}^{-1}$  are attributed to the  $\nu(\text{C=O})$  of the polypeptide backbone showing small changes in conformation. The most intense signal observed at 1666  $\text{cm}^{-1}$  is typical of  $\beta$ -turn structures whereas the feature at 1652  $\text{cm}^{-1}$  is representative of  $\alpha$ -helical structures (181, 205). At 1555, 1546 and 1535  $\text{cm}^{-1}$  signals are attributed to the coupled  $\nu(\text{C=N})/\delta(\text{N-H})$  mode, the amide II.

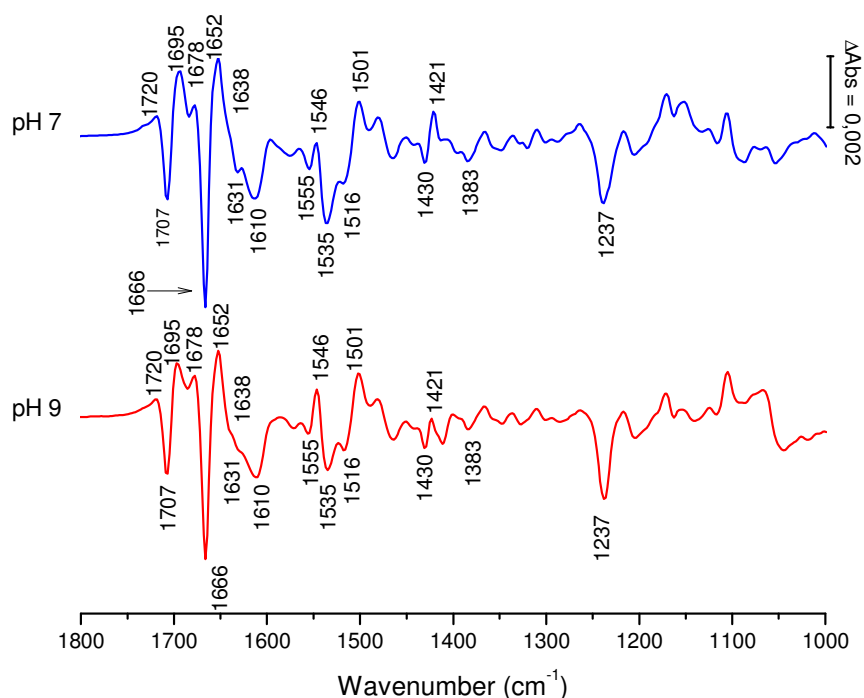
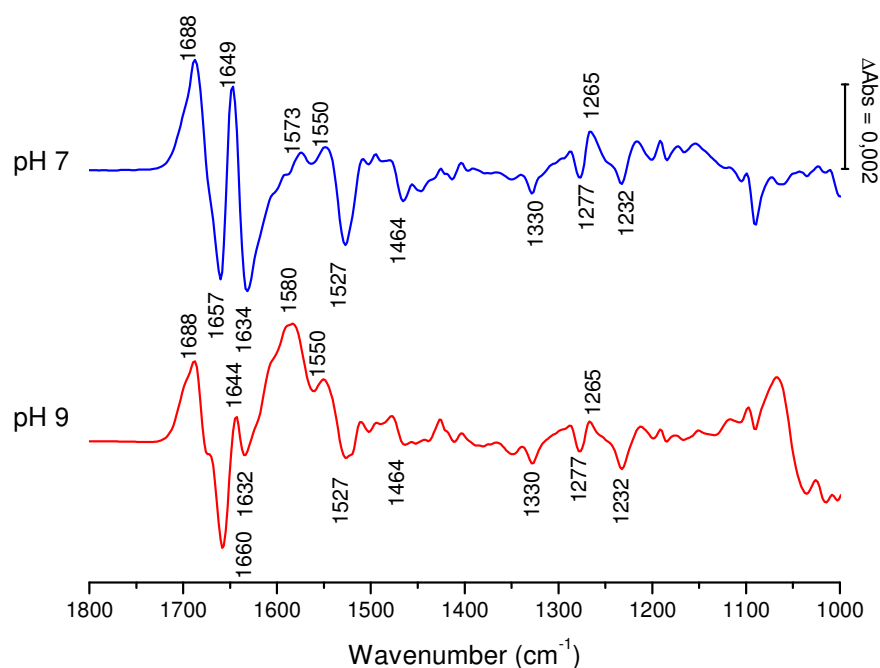


Figure 4.4.6: Oxidized minus reduced difference spectra of cytochrome  $c_{552}$  at pH 7 (bleu) and pH 9 (red) for the potential step between -300 mV to +300 mV.

The  $\nu(\text{C=O})$  mode from protonated Asp/Glu side chains gives rise to the feature at 1720  $\text{cm}^{-1}$  (63, 234). The signals observed at 1707 and 1695  $\text{cm}^{-1}$  are typical of  $\nu(\text{C=O})$  from protonated heme propionates. Contributions from deprotonated acidic side chains are expected in the region between 1580-1520  $\text{cm}^{-1}$  for the asymmetric  $\nu(\text{COO}^-)$  and in the region between 1480 and 1320  $\text{cm}^{-1}$  for the symmetric mode (235, 236). The feature observed at 1678  $\text{cm}^{-1}$  also include contributions from  $\nu_{\text{as}}(\text{CN}_3\text{H}_5)$  mode from arginine residues, the symmetric mode is expected in the region around 1631  $\text{cm}^{-1}$  (203, 237). Negative signal at 1516  $\text{cm}^{-1}$  and the positive signal at 1501  $\text{cm}^{-1}$  are typical of the coupled  $\nu(\text{C=C})/\delta(\text{C-H})$  mode of neutral form of Tyr and the deprotonated form respectively (203,

238). At 1430 and 1383  $\text{cm}^{-1}$ , contributions from  $\nu_s(\text{COO}^-)$  modes from acidic side chains are expected.  $\delta_s(\text{CH}_3)$  modes may be included at 1383  $\text{cm}^{-1}$ . Smaller contributions from tyrosine residues are included in the region between 1290 and 1270  $\text{cm}^{-1}$ . Similar contributions from tyrosine residues are observed in the difference spectra of cytochrome *c* from various species (238).

The *c*-type heme also contributes to the difference spectra. At 1631 and 1535  $\text{cm}^{-1}$ , the signals observed are attributed to  $\nu_{38}$  and  $\delta_{42}$  mode of the porphyrin ring system. The numbering was performed by Spiro and colleagues to simplify the nomenclature of these highly coupled vibrational modes (174, 175). An additional signal at 1237  $\text{cm}^{-1}$  is typical of contributions of pH 7 vibrations from the heme (176). At pH 9, no significant changes are observed. Differences observed between 1200 and 1000  $\text{cm}^{-1}$  arise from the buffer (KPi at pH 7 and Tris at pH 9). Tris buffer also contributes around 1630  $\text{cm}^{-1}$ . The tentative assignments are reported in [table 7.13](#) in the Appendix section.



**Figure 4.4.7:** Oxidized minus reduced difference spectra of the  $\text{Cu}_A$  fragment at pH 7 (blue) and 9 (red) for the potential range between -300 mV to +300 mV.

In the difference spectrum of the  $\text{Cu}_A$  fragment recorded at pH 7 presented in [figure 4.4.7](#), the most intense signals observed are in the amide I region at 1688, 1657, 1649 and 1634  $\text{cm}^{-1}$ , typical of  $\beta$ -sheets and loops (239). These conformational changes are also reflected in the amide II signature at 1573, 1550 and 1527  $\text{cm}^{-1}$ . Furthermore, the



features at 1688 and 1657  $\text{cm}^{-1}$  observed in the oxidized and the reduced form respectively may include contribution from sidechain  $\nu(\text{C}=\text{O})$  from Asn and Gln.  $\nu(\text{CN}_3\text{H}_5)^{\text{as}}$  mode from Arg is also not excluded in that region as the symmetric mode can be included in the large structure at 1634  $\text{cm}^{-1}$ . Between 1330-1230  $\text{cm}^{-1}$ , modes arising from the amide III,  $\delta(\text{N-H})$  and  $\omega(\text{S-CH}_2)$  from cysteine and methionine are observed. Contributions from the binuclear copper center is expected at lower wavenumbers in the far-IR around 500  $\text{cm}^{-1}$  (240). At pH 9, apart from contribution of the Tris buffer below 1100  $\text{cm}^{-1}$  and in the region around 1530  $\text{cm}^{-1}$ , large changes are observed in the amide I region, the signal observed at 1634  $\text{cm}^{-1}$  at pH 7 decreases intensity and a large structure is observed at 1580  $\text{cm}^{-1}$ . These changes may demonstrate the alteration of the conformational change that occurs during the redox reaction. Furthermore, these changes do not affect the redox potential obtained for the  $\text{Cu}_\text{A}$  center. The tentative attributions made on the difference spectra of the  $\text{Cu}_\text{A}$  fragment are reported in table 7.14 in the appendix section

In direct comparison of the difference spectra to that of the cytochrome  $c_{552}$  and the  $\text{Cu}_\text{A}$  fragment, identical signals are observed in the difference spectra of the complex (figure 4.4.8). The amide I region is dominated by an intense negative signal at 1666  $\text{cm}^{-1}$ . Contributions from the Tyr are also observed at 1516 and 1501  $\text{cm}^{-1}$ . The C-H vibration of the heme is also seen at 1237  $\text{cm}^{-1}$ . Further attribution is unrealistic as it is difficult to determine if the signal originates from the cytochrome  $c_{552}$  or the  $\text{Cu}_\text{A}$  fragment. The overlapping of the signals observed when the two samples were studied individually does not help.

The difference spectrum of the  $\text{Cu}_\text{A}$  fragment was interactively subtracted from the spectrum of the complex. In the resulting data, the double difference spectrum shows the contributions from the cytochrome  $c_{552}$  in the complex, but also changes that occur in the spectra of the  $\text{Cu}_\text{A}$  fragment.

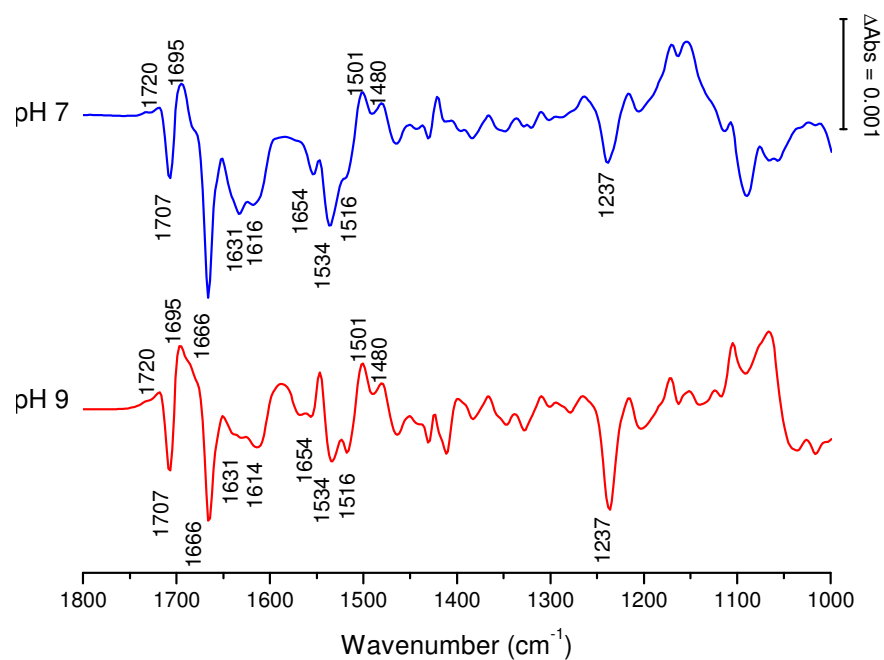


Figure 4.4.8: Oxidized minus reduced difference spectra of the complex [cytochrome  $c_{552}$ -Cu<sub>A</sub> fragment] at pH 7 (blue) and pH 9 (red) for the potential range between -300 mV to +300 mV.

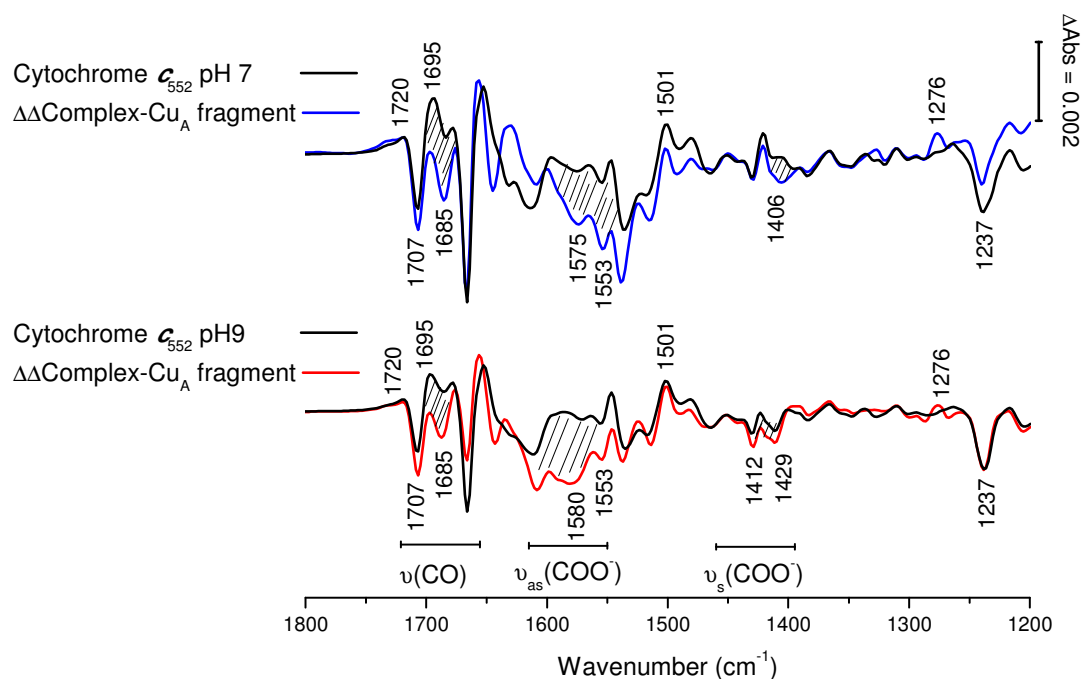


Figure 4.4.9: Double difference spectra obtained by interactive subtraction of the spectrum of the Cu<sub>A</sub> fragment from the spectrum of the complex, at pH 7 (blue) and pH 9 (red). Data in black are the corresponding difference spectra of cytochrome  $c_{552}$ .

Figure 4.4.9 shows the double difference spectra overlaid on the difference spectra obtained for the cytochrome  $c_{552}$ . Numerous changes can be observed. In the amide I region, the signal attributed to conformational changes involving  $\alpha$ -helical structures at  $1652\text{ cm}^{-1}$  for the cytochrome  $c_{552}$  is shifted to higher wavenumbers at  $1657\text{ cm}^{-1}$ . The most important alterations are observed between  $1710$  and  $1675\text{ cm}^{-1}$ , this region is typical of the  $\nu(\text{C=O})$  of protonated heme propionates. The decrease in the intensities of these signals suggests that at least one of the hemes propionates is deprotonated. Furthermore, in the region around  $1580\text{ cm}^{-1}$  is also perturbed and are attributed to the  $\nu(\text{COO}^-)$  asymmetric mode. The respective symmetric mode is observed around  $1410\text{ cm}^{-1}$ . Signals previously attributed to  $\nu(\text{CN}_3\text{H}_5)$  asymmetric and symmetric modes of arginine observed at  $1678$  and  $1630\text{ cm}^{-1}$  are also perturbed.

#### 4.4.3 Electron transfer complex

The electron transfer complex between cytochrome  $c_{552}$  and the  $\text{Cu}_A$  fragment was previously determined by a combined NMR spectroscopic and computational method (117). Both cytochrome  $c_{552}$  and the  $\text{Cu}_A$  fragment were expressed in  $^{15}\text{N}$  enriched medium. Reduced cytochrome  $c_{552}$  was added to fully oxidized  $^{15}\text{N}$  labeled  $\text{Cu}_A$  fragment, the chemical shift perturbation of residues that are the most perturbed were identified. Similarly,  $^{15}\text{N}$  labeled cytochrome  $c_{552}$  was added to  $\text{Cu}_A$  fragment. The results identified the residues that expressed the most important chemical shift perturbation as being those involved in formation of the complex and in electron transfer. In cytochrome  $c_{552}$ , the residues with the most pronounced chemical shift perturbation are those located around the heme cleft, the supposed contact surface.

Other residues that induced an important chemical shift are those located on the back side of the enzyme,  $\text{Ala}^{34}$  and  $\text{His}^{32}$ . Importantly these changes only occur in the reduced form of the protein. It was suggested that these perturbations resulted from the difference in electronic structure of the heme between the two redox states.  $\text{His}^{32}$  and  $\text{Arg}^{125}$  are suggested to form a hydrogen bonding network with the propionate A (figure 4.4.10). Since the electronic structure of hemes is propagated on the propionate, the latter can be used as a switch to control the redox properties of the heme. There is theoretical evidence that the redox potential of hemes can be modulated and differences of up to  $800\text{ mV}$  can be obtained (233). The perturbations of  $\text{Ala}^{34}$  and  $\text{His}^{32}$  may be relayed by the

conformational adjusted during inter-protein contact. Similar observations were obtained in *Paraccocus denitrificans* where Gly<sup>54</sup>, Gly<sup>55</sup> and Asp<sup>56</sup> also located on the back of the protein showed the largest chemical shift perturbation, and residues Trp<sup>57</sup> and Arg<sup>36</sup> were suggested to form a hydrogen network with the heme propionate A (128). Moreover fluorescence spectroscopic studies of the cytochrome *c*<sub>552</sub> from *Paraccocus denitrificans* revealed 20 nm shift of the tryptophane band (128). Due to the electrostatic nature of the interaction in *Paraccocus denitrificans*, there is no electrochemical evidence of potential shift.

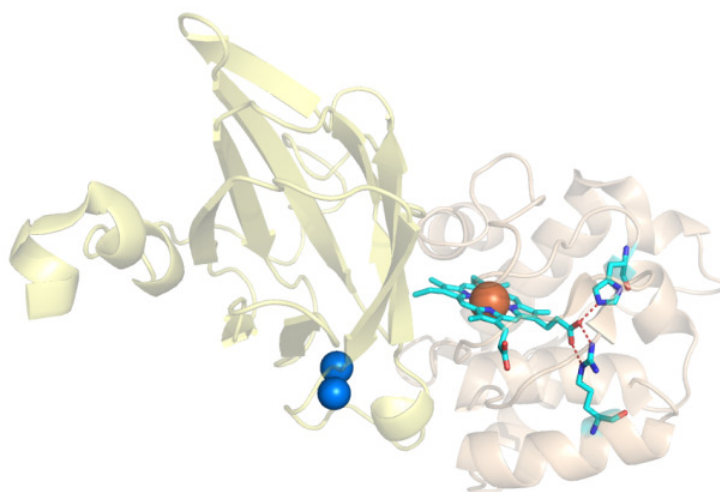


Figure 4.4.10: 3-dimensional structure of the complex (PDB 2FWL) depicting His<sup>32</sup> and Arg<sup>125</sup> which are suggested to form a hydrogen bonding network with the propionate A (117).

There are only few examples of electrochemical analysis of electron transfer partners forming stable complexes. Rusticyanin from *Thiobacillus ferrooxidans*, a blue copper protein was studied with its electron transfer partner, the di-heme cytochrome *c*<sub>4</sub>. In this system, the mid-point potential of cytochrome *c*<sub>4</sub> remained unchanged, but the potential of the mononuclear Cu center was downshifted by 100 mV (241). In our case, the experimental setup is not adapted to study the potential of the binuclear Cu<sub>A</sub> center in the complex. The strategy to have access to this information would be redox titration monitored by EPR spectroscopy (134).

In 1992, Pelletier et al. reported the crystal structure formed by cytochrome *c* peroxidase and cytochrome *c* from yeast (242). Crystals were obtained in solutions with 5-300 mM NaCl, although the crystals obtained at 150-200 mM salt were better. This study

identified acidic and basic residues which might be involved in the protein interaction surface, but it was suggested that these residues do not interact in the specific experimental salinity conditions. The complex was held together by hydrophobic interactions.

More recently, the crystal structure of yeast cytochrome *bc*<sub>1</sub> complex with its redox partner, the cytochrome *c* was reported by Lange and Hunte (243). The contact surface consisted of both polar and non polar interactions; the former included only two residues from each partner protein whereas the latter consisted of at least 4 residues from each. Nevertheless, the redox potential was not studied.

Evidence of potential shift of the heme in cytochrome *c* has been observed when cytochrome *c* interacts with lipids, a potential drop of 48 mV was reported (244). Cytochrome *c*<sub>552</sub> from *Thermus thermophilus* adsorbed on biomimetic electrode modified with thiol bound alkyl chains also revealed potential drop as the length of the alkyl chain increased (245). These results show that the potential of the heme of cytochrome *c* can be modulated by interaction with specific surfaces. In our study, the potential drop was observed in the presence of the Cu<sub>A</sub> fragment both in reductive and oxidative titration, suggesting that the redox state of the Cu<sub>A</sub> fragment does not affect the potential of cytochrome *c*<sub>552</sub>.

To have a better understanding of the system, it seems imperative to study the complex formed by cytochrome *c*<sub>552</sub> and the *ba*<sub>3</sub> oxidase. Although the presence of detergents may hinder the formation of the complex due to the hydrophobic nature of the interaction site, it may give valuable information in the comprehension of the system. As mentioned previously, the study of the redox potential of the Cu<sub>A</sub> center in the complex also seems crucial to understand the physiological meaning of the potential drop observed.

## 4.5 Characterisation of the mid-point potentials of the hemes in the

### *bc<sub>1</sub>-aa<sub>3</sub>* supercomplex from *Corynebacterium glutamicum*

The six hemes from the *bc<sub>1</sub>-aa<sub>3</sub>* supercomplex have been characterised by a spectroelectrochemical technique in the UV-visible domain. Plotting the difference in absorbance at a wavelength where a cofactor is observed against the applied potential, and fitting a Nernst curve gives the mid-point potential of the hemes. The redox induced UV-visible difference spectrum shows signals in the Soret region at 421, 407 and 435 nm. Smaller contributions from the  $\alpha$  bands can be observed at 552, 562 and 600 nm which are attributed to the *c*, *b* and *a* type hemes respectively (figure 4.5.1).

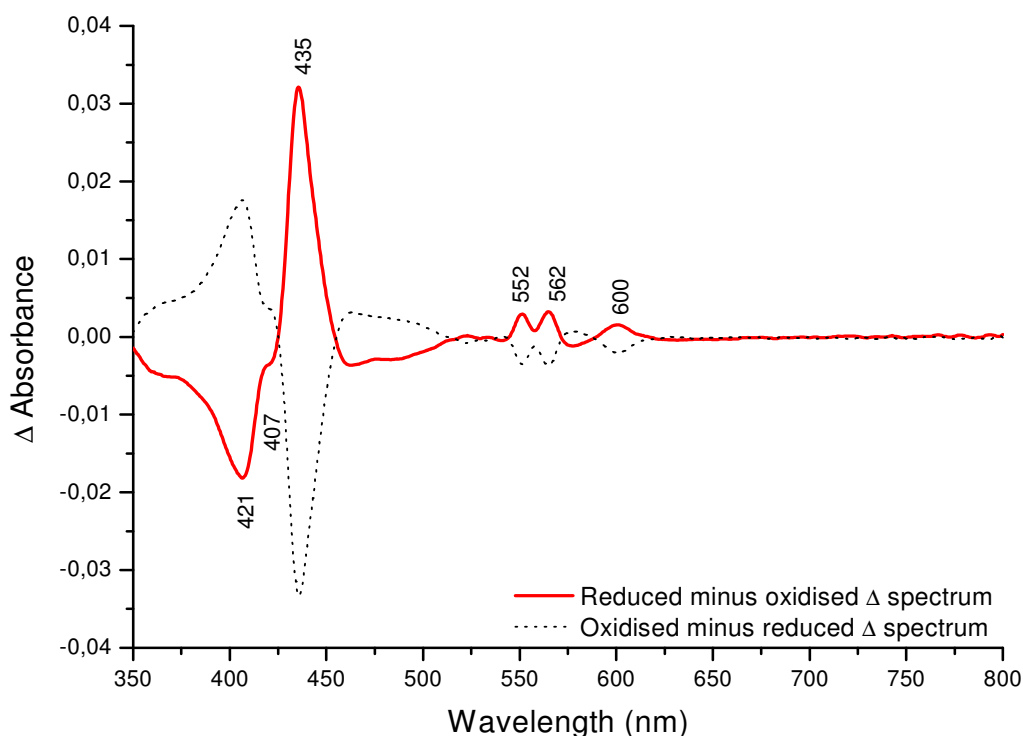


**Figure 4.5.1: Redox induced difference spectrum of the *bc<sub>1</sub>-aa<sub>3</sub>* supercomplex in the UV-visible domain for the potential range between -650 mV to +250 mV.**

Figure 4.5.2 shows the plot of the reductive titration of the sample for the spectral range between 200-800 nm. Oxidative titration was also performed, however since the sample seems less stable at lower potentials and the experiments lasted for more than 24 hours, a two step titration was done for oxidising the enzyme.

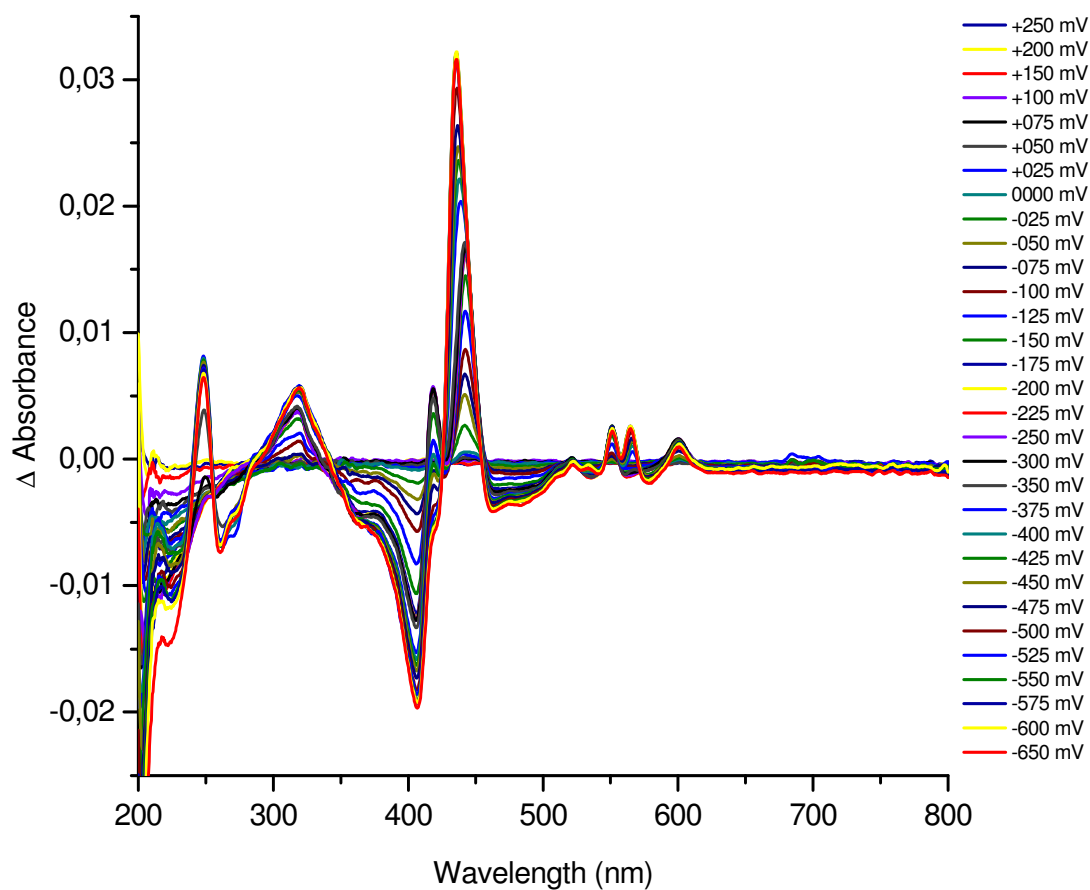


Figure 4.5.2: Reductive titration of the  $bc_1$ - $aa_3$  supercomplex from +250 mV to -650 mV.

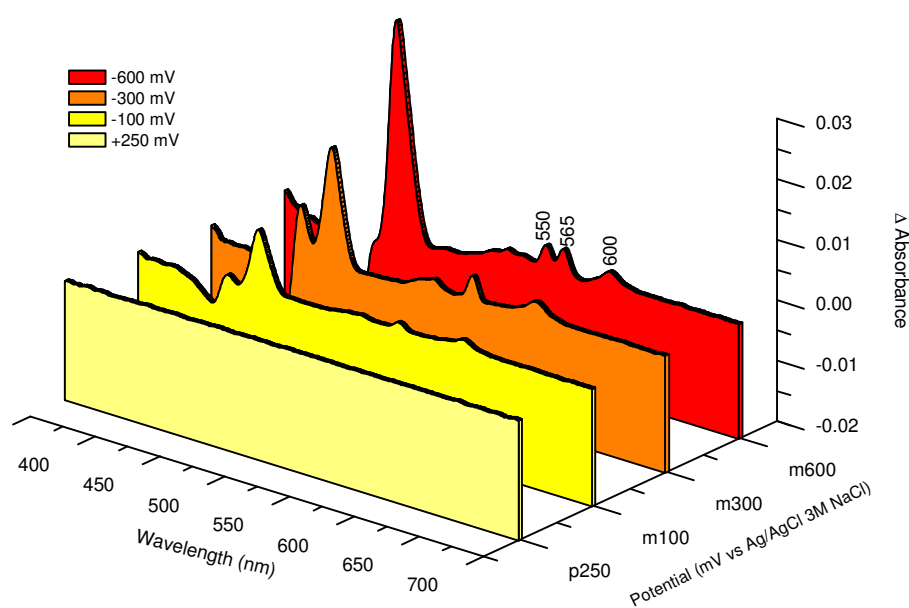
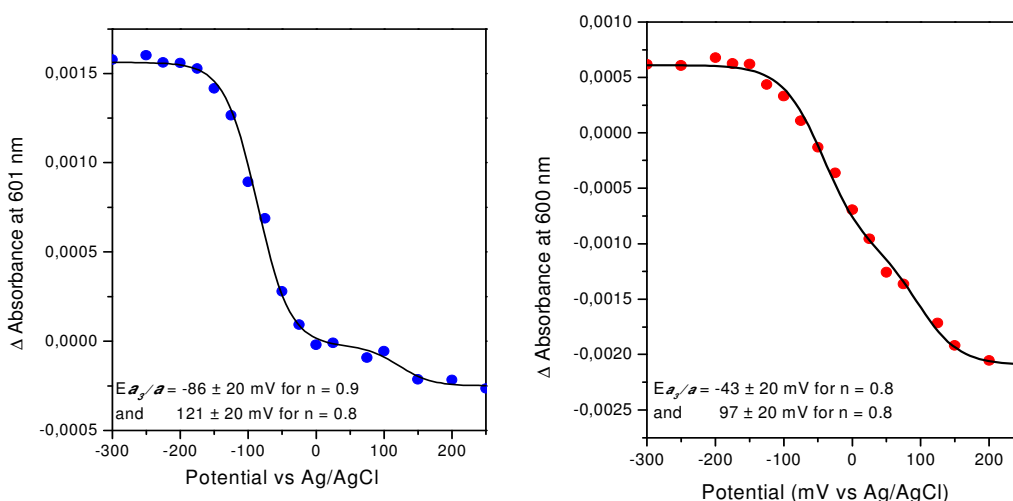


Figure 4.5.3: Evolution of the difference spectrum in the UV-visible depicting the appearance of signals attributed to the  $a$  (600 nm),  $b$  (565 nm) and  $c$  (550 nm) type hemes.

The evolution of the UV-visible difference spectrum while reduction shows the spectral changes of the *a*, *c* and *b* type hemes respectively (figure 4.5.3). Taking the spectrum at +250 mV as reference and plotting the difference spectrum at -100 mV shows the appearance of  $\alpha$  bands of the *a* type hemes at 600 nm. At -300 mV, the signals arising from the *c* type hemes are observed at 550 nm. Finally at -650 mV, the *b* type hemes are observed at 565 nm.

#### 4.5.1 Redox potentials of the *a* and *a*<sub>3</sub> hemes

The hemes in the cytochrome *c* oxidase are cooperative and cannot be completely separated (246, 247) as seen in figure 4.5.4. The two hemes are cooperative, for example if heme *a* accepts an electron, it will modify the electronic structure of heme *a*<sub>3</sub> which will accept the other electron. Here two *a*-type hemes are involved and the distinct midpoint potentials are obtained either by plotting the difference in absorbance in the Soret band or the  $\alpha$  band. Working with the  $\alpha$  band is more precise since the *c*-type hemes begin to modify the Soret signature when a reductive potential is applied. When reducing the enzyme, two potentials are observed at -86 mV and 121 mV with *n* = 0.9 and 0.8 respectively. When oxidising the enzyme, the values of the mid-point potential are -43 mV and 97 mV with *n* = 0.8 for both.



**Figure 4.5.4: Reductive (left) and oxidative (right) titration of the *a* hemes in the *bc*<sub>1</sub>-*aa*<sub>3</sub> supercomplex monitored at 600 nm.**



These results show a hysteresis effect between the oxidative and reductive titration, often found for cytochrome *c* oxidase. For the highest potential, an average gives a mid-point potential of +109 mV. For the lower potential, while reducing the best fit is obtained with  $n = 0.9$  and  $0.8$  while oxidising. The average gives a mid-point potential of -65 mV. To be able to distinguish the two hemes, the titration must be done in the presence of cyanide, since the heme redox potentials uncouple.

#### 4.5.2 Redox potentials of the *c* and *c*<sub>1</sub> hemes

Two *c*-type hemes are present in the protein, which are not clearly distinguished (figure 4.5.5). The mid-point potentials in the reductive titration are too close to each other ( $< 50$  mV) to be separated by this method. Working with the Soret band is not feasible because of the contribution of both the *a*-type and *b*-type hemes, therefore the plot is done only with the help of the  $\alpha$ -bands at 550 nm.

The best fit for the oxidative titration is obtained with two potentials but with  $n = 0.7$ . For the reduction of the sample, the best fit is obtained with one mid-point at -124 mV with  $n = 0.9$ . The low value for 'n' is an indication of a lack of equilibrium. The mid-point potential retained for the characterisation of both the *c* type hemes is -107 mV which is an average of the two lowest potentials (ie -124 and -89 mV)

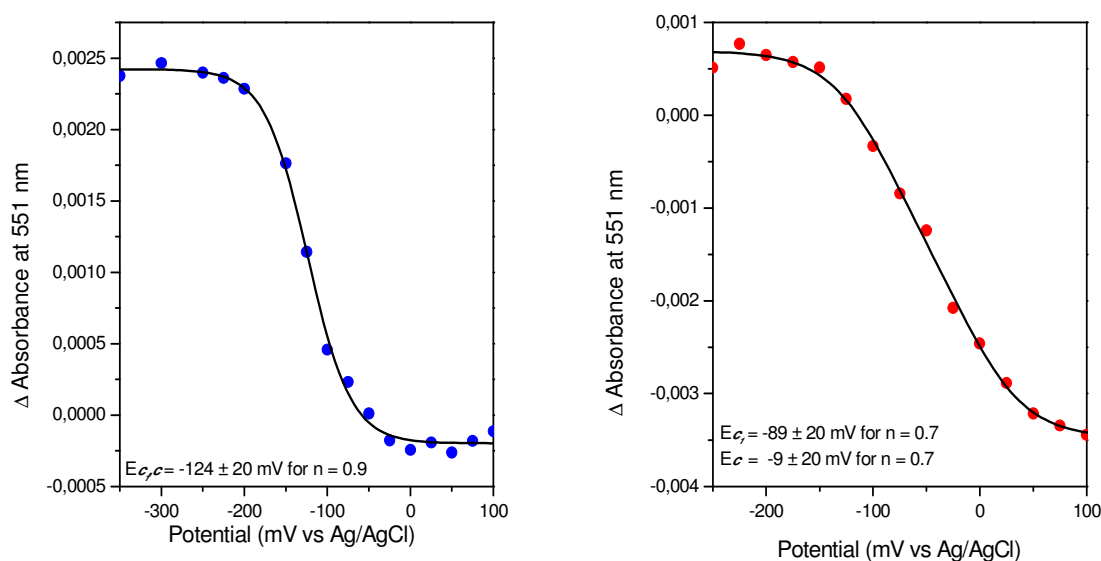


Figure 4.5.5: Reductive (left) and oxidative (right) titration of the *c* hemes in the *bc*<sub>1</sub>-*aa*<sub>3</sub> supercomplex monitored at 550 nm.

### 4.5.3 Redox potential of the $b_L$ and $b_H$ hemes

The midpoint potentials of the  $b$  type hemes were clearly observed. In this case, both the Soret band and the  $\alpha$ -bands gave the same result. No hysteresis was observed. -499 mV for heme  $b_L$  and -371 mV for heme  $b_H$  are retained (figure 4.5.6).

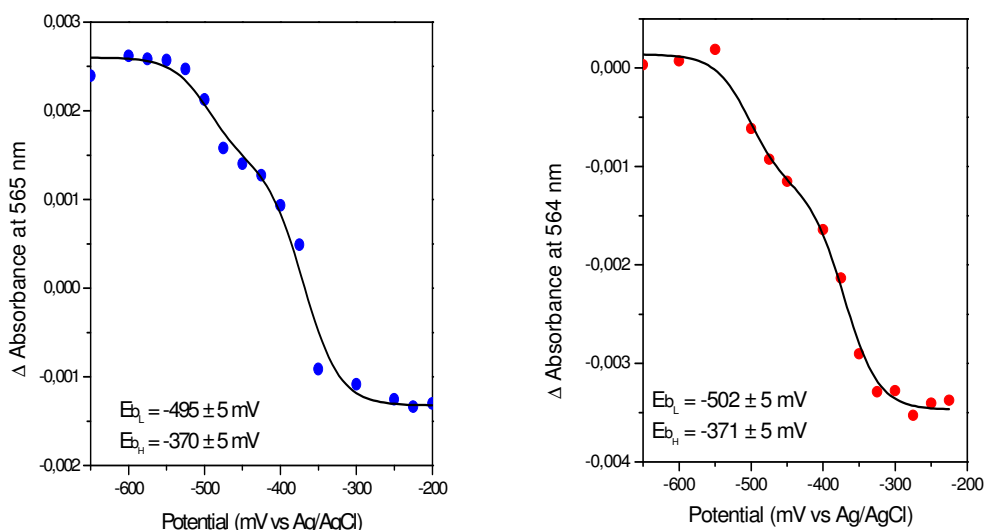


Figure 4.5.6: Reductive (left) and oxidative (right) titration of the  $b$  hemes in the  $bc_1$ - $aa_3$  supercomplex monitored at 565 nm.

Heme	Mid-point potential (mV)		
	vs Ag/AgCl	vs SHE'	error
$b_L$	-499	-291	$\pm 5$
$b_H$	-371	-163	$\pm 5$
$c_1/c$	-107	101	$\pm 20$
$a/a_3$	-65	143	$\pm 20$
	109	317	$\pm 20$

Table 4.5.1: The mid-point potentials of the hemes present in the  $bc_1$ - $aa_3$  supercomplex from *Corynebacterium glutamicum*.

The results are summarized in table 4.5.1. For the  $a$  and  $a_3$  hemes, even with an equilibration time of 1 hour between each point, a hysteresis effect is observed. To ameliorate the quality of the data, a longer equilibration time may help. The mid-point potentials of the  $c_1/c$  hemes could not be separated mainly due to their similar spectral

contributions. Further more if the redox potentials are separated by less than 50 mV, it is not possible to distinguish between the two hemes by our experimental setup. On the other hand, the redox potentials of the two *b* type hemes were clearly identified.

#### 4.5.4 Comparison with analogues from *Paracoccus denitrificans*

The potentials of the *b*-type hemes are lower in *Corynebacterium glutamicum* compared to their analogues from *Paracoccus denitrificans*, a downshift of 200 mV is observed (248). For the *c*<sub>1</sub> heme, the mid-point potential is lower in the isolated fragment and higher in the *bc*<sub>1</sub> complex (248). In *Corynebacterium glutamicum*, the potential for this heme is still approximately 200 mV lower. Cytochrome *c*<sub>552</sub> from *Paracoccus* has a redox mid-point potential of 270 mV, 170 mV higher than the *c*-type hemes present in the supercomplex (138). Cytochrome *c*<sub>552</sub> from *Paracoccus denitrificans* has an N-terminal membrane anchor and is suggested to form supramolecular complex with either the *bc*<sub>1</sub> complex, the terminal oxidase or both (249). The hemes *a* and *a*<sub>3</sub> on the contrary have higher potentials in the *aa*<sub>3</sub> oxidase from *Paracoccus denitrificans* than in the *bc*<sub>1</sub>-*aa*<sub>3</sub> supercomplex (250, 251). Initially, the redox potential of menaquinone is 150 mV lower than that of ubiquinone, the organism has adapted the functioning of the enzyme for respiration based on menaquinone.

Heme	Mid-point potential (mV)	Mid-point potential (mV)
	from <i>Corynebacterium glutamicum</i>	from <i>Paracoccus denitrificans</i>
<i>b<sub>L</sub></i>	-291	-92
<i>b<sub>H</sub></i>	-163	58
<i>c<sub>1</sub></i>	101	268-338
		-57 isolated <i>c</i> <sub>1</sub> fragment
<i>c</i>	101	270
<i>a/a<sub>3</sub></i>	143	178
	317	430

**Table 4.5.2 : Comparison of the redox potential of the hemes from the *bc*<sub>1</sub>-*aa*<sub>3</sub> supercomplex from *Corynebacterium glutamicum* with analogues from *Paracoccus denitrificans*.**

Just like in *Thermus thermophilus*, where fragments were used to study the complex formed by the different components, in this case, we have the complex as a whole. The next step would be the study of fragments of the complex individually. IR spectroscopic studies can also give clues in the mechanism of electron transfer in the complex as such a large complex has not been studied as a whole so far.

## **Chapter V: Conclusion and perspectives**

This thesis deals with different type of interactions of proteins from the respiratory chain. Firstly, the interaction of ions with the Na<sup>+</sup>-pumping NaDH:quinone oxidoreductase from *Vibrio cholerae* was investigated. Redox titration of the cofactors monitored in the UV-visible showed that the midpoint potential of the FMN<sub>C</sub> cofactor for the redox transition from Fl<sup>•+</sup> to Fl is -350 mV in the presence of Li<sup>+</sup> and Na<sup>+</sup> ions, a downshift to -460 mV was observed in the presence of K<sup>+</sup>, Rb<sup>+</sup> and NH<sub>4</sub><sup>+</sup> ions. Redox induced difference spectroscopic studies in the mid-IR spectral range were also performed to investigate the effect of the different types of ions on the Na<sup>+</sup>-NQR. Signals attributed to the (COO<sup>-</sup>Li<sup>+</sup>) and (COO<sup>-</sup>Na<sup>+</sup>) symmetric stretching modes of acid residues side chains were identified both in H<sub>2</sub>O and D<sub>2</sub>O buffer. These signals were observed both in the oxidized and reduced state of the enzyme. Furthermore, the inhibitory effects of Rb<sup>+</sup> ions were seen in the amide regions. Solvent accessibility of the enzyme monitored by hydrogen/deuterium exchange kinetics in the mid-IR spectral range has been used to monitor the conformation of the Na<sup>+</sup>-NQR in the presence of the different ions. The protein was found to be more accessible in the presence of Li<sup>+</sup> and Na<sup>+</sup> than in the presence of K<sup>+</sup> and Rb<sup>+</sup> ions. Further investigations are required to have a better understanding of the unique coupling mechanism in the Na<sup>+</sup>-NQR (218). FTIR redox induced difference spectroscopic measurement for crucial steps involved in Na<sup>+</sup>-uptake and Na<sup>+</sup>-release can be helpful. Hydrogen deuterium measurements with other reducing agents can also be performed. Furthermore the crystallographic structure of the enzyme may give important information to understand the mechanism. Recently a low resolution (16 Å) structure of the Na<sup>+</sup>-NQR showed that the enzyme has an overall asymmetric structure and a central region with low electron density spanning across the membrane (252).

The Na<sup>+</sup>-binding site was also investigated. Optimal Na<sup>+</sup>-binding involves six oxygen atoms forming an octahedral structure. Acid residues located on the cytoplasmic side of the protein were previously suggested to form the first Na<sup>+</sup>-binding site. NqrB D397E and NqrE E95Q mutant enzymes were studied thus to investigate the Na<sup>+</sup>-binding (89). Redox titrations of the cofactors present in both mutant proteins showed that the midpoint potentials of the cofactors are not dependent on the type of ions present. The mid-IR redox induced difference spectroscopic measurements performed, revealed important shift to higher wavenumbers in the (COO<sup>-</sup>Li<sup>+</sup>) and (COO<sup>-</sup>Na<sup>+</sup>) symmetric modes of acid residues

side chains. These findings suggest that Na<sup>+</sup>-binding network is perturbed in the D397E mutant enzyme. Evidence was found for a weaker Na<sup>+</sup>-binding. Hydrogen/deuterium exchange kinetics suggests that the enzyme is in different conformational states in the presence of the different ions. The NqrB D346 residue is suggested to be part of the Na<sup>+</sup>-release site in the periplasmic side of the enzyme. Study of this mutant enzyme seems to be crucial.

The quinone binding site of the Na<sup>+</sup>-NQR was also part of this study. Since enzymes resistant to HQNO and korormicin carry a single mutation on the NqrB G140 residue, the NqrB G140A mutant enzyme was studied. The redox midpoint potentials of the cofactors were similar to the wild type enzyme. Redox induced difference spectroscopic analysis in the mid-IR spectral range for the critical step involving the riboflavin and the attached quinone were performed for the wild type enzyme and the NqrB G140A mutant enzyme. Signals typical of vibrational modes of quinone were identified in the difference spectra of the wild type enzyme but not in the mutant protein. Furthermore, when HQNO was added to the wild type enzyme, large changes were revealed in the amide regions in the difference spectra. These changes were not observed in the difference spectra of the mutant enzyme. These results point to the crucial role of this glycine residue in the binding of quinone to the Na<sup>+</sup>-NQR.

The second part of this work deals with protein-protein interaction in the respiratory chain. Cytochrome *c*<sub>552</sub> and the Cu<sub>A</sub> fragment from the *ba*<sub>3</sub> terminal oxidase from the organism *Thermus thermophilus* provide a unique opportunity to investigate protein-protein interaction by electrochemistry. Indeed the association between the two enzymes is guided by hydrophobic interactions; addition of salts necessary for electrochemical analysis does not affect the formation of the complex. Primarily, the midpoint potentials of the cofactors from the two proteins were determined individually and in the complex. In the interaction complex, the midpoint potential of cytochrome *c*<sub>552</sub> was downshifted by 90 mV. Redox induced FTIR difference spectroscopy showed that the heme propionates participate to the interaction in the complex. Since they rule the redox properties of the hemes, it may explain the drop in the redox potential of the *c*-type heme.

To further investigate these observations, the study of the complex formed by cytochrome *c*<sub>552</sub> and the whole *ba*<sub>3</sub> oxidase seems to be the next step of this work.

Finally, protein-protein interaction within the *bc*<sub>1</sub>-*aa*<sub>3</sub> supercomplex from the respiratory chain of *Corynebacterium glutamicum* was studied. Supercomplexes seem to be formed to optimize electron transfer and minimize diffusion. The redox midpoint potential of the hemes have been determined and compared with analogous proteins from *Paraccocus denitrificans* to demonstrate the effect of the interaction. The study of the subunits separately can provide important information about the redox properties of the cofactors in the supercomplex. Furthermore, redox induced FTIR difference spectroscopic analysis can also provide insights on how the supercomplex works at a molecular level.

## Reference

1. Singer, S. J., and Nicolson, G. L. (1972) The fluid mosaic model of the structure of cell membranes, *Science* 175, 720-731.
2. Engelman, D. M. (2005) Membranes are more mosaic than fluid, *Nature* 438, 578-580.
3. Doyle, D. A., Cabral, J. M., Pfuetzner, R. A., Kuo, A., Gulbis, J. M., Cohen, S. L., Chait, B. T., and MacKinnon, R. (1998) The structure of the potassium channel: Molecular basis of K<sup>+</sup> conduction and selectivity, *Science* 280, 69-77.
4. Davis, J. T., Okunola, O., and Quesada, R. (2010) Recent advances in the transmembrane transport of anions, *Chemical Society Reviews* 39, 3843-3862.
5. Ganea, C., and Fendler, K. (2009) Bacterial transporters: Charge translocation and mechanism, *Biochimica et Biophysica Acta - Bioenergetics* 1787, 706-713.
6. Bernardi, P. (1999) Mitochondrial transport of cations: Channels, exchangers, and permeability transition, *Physiological Reviews* 79, 1127-1155.
7. Mueckler, M. (1994) Facilitative glucose transporters, *European Journal of Biochemistry* 219, 713-725.
8. Thurmond, D. C., Ceresa, B. P., Okada, S., Elmendorf, J. S., Coker, K., and Pessin, J. E. (1998) Regulation of insulin-stimulated GLUT4 translocation by Munc18c in 3T3L1 adipocytes, *Journal of Biological Chemistry* 273, 33876-33883.
9. Higgins, C. F. (2001) ABC transporters: Physiology, structure and mechanism - An overview, *Research in Microbiology* 152, 205-210.
10. Higgins, C. F. (1992) ABC Transporters: From microorganisms to man, *Annual Review of Cell Biology* 8, 67-113.
11. Bachmann, B. J. (1990) Linkage map of *Escherichia coli* K-12, Edition 8, *Microbiological Reviews* 54, 130-197.
12. Mitchell, P. (1961) Coupling of phosphorylation to electron and hydrogen transfer by a chemi-osmotic type of mechanism, *Nature*, 144-148.
13. Mitchell, P. (2011) Chemiosmotic coupling in oxidative and photosynthetic phosphorylation, *Biochimica et Biophysica Acta - Bioenergetics* 1807, 1507-1538.
14. Efremov, R. G., Baradaran, R., and Sazanov, L. A. (2010) The architecture of respiratory complex I, *Nature* 465, 441-445.
15. Yankovskaya, V., Horsefield, R., Törnroth, S., Luna-Chavez, C., Miyoshi, H., Léger, C., Byrne, B., Cecchini, G., and Iwata, S. (2003) Architecture of succinate dehydrogenase and reactive oxygen species generation, *Science* 299, 700-704.
16. Zhang, Z., Huang, L., Shulmeister, V. M., Chi, Y. I., Kim, K. K., Hung, L. W., Crofts, A. R., Berry, E. A., and Kim, S. H. (1998) Electron transfer by domain movement in cytochrome bc<sub>1</sub>, *Nature* 392, 677-684.
17. Than, M. E., Hof, P., Huber, R., Bourenkov, G. P., Bartunik, H. D., Buse, G., and Soulimane, T. (1997) *Thermus thermophilus* cytochrome-c<sub>552</sub>: A new highly thermostable cytochrome-c structure obtained by MAD phasing, *Journal of Molecular Biology* 271, 629-644.
18. Soulimane, T., Buse, G., Bourenkov, G. P., Bartunik, H. D., Huber, R., and Than, M. E. (2000) Structure and mechanism of the aberrant ba<sub>3</sub>-cytochrome c oxidase from *Thermus thermophilus*, *EMBO Journal* 19, 1766-1776.
19. Stock, D., Leslie, A. G. W., and Walker, J. E. (1999) Molecular architecture of the rotary motor in ATP synthase, *Science* 286, 1700-1705.
20. Kerscher, S., Dröse, S., Zickermann, V., and Brandt, U. (2008) The three families of respiratory NADH dehydrogenases, (Differ., R. P. C., Ed.), pp 185-222.
21. Brandt, U. (2006) Energy converting NADH:quinone oxidoreductase (complex I), pp 69-92.
22. Friedrich, T. (1998) The NADH:ubiquinone oxidoreductase (complex I) from *Escherichia coli*, *Biochimica et Biophysica Acta - Bioenergetics* 1364, 134-146.



23. Guénebaut, V., Schlitt, A., Weiss, H., Leonard, K., and Friedrich, T. (1998) Consistent structure between bacterial and mitochondrial NADH:ubiquinone oxidoreductase (complex I), *Journal of Molecular Biology* 276, 105-112.
24. Sazanov, L. A. (2007) Respiratory complex I: Mechanistic and structural insights provided by the crystal structure of the hydrophilic domain, *Biochemistry* 46, 2275-2288.
25. Mamedova, A. A., Holt, P. J., Carroll, J., and Sazanov, L. A. (2004) Substrate-induced conformational change in bacterial complex I, *Journal of Biological Chemistry* 279, 23830-23836.
26. Bandejas, T. M., Salgueiro, C. A., Huber, H., Gomes, C. M., and Teixeira, M. (2003) The respiratory chain of the thermophilic archaeon *Sulfolobus metallicus*: Studies on the type-II NADH dehydrogenase, *Biochimica et Biophysica Acta - Bioenergetics* 1557, 13-19.
27. Melo, A. M. P., Bandejas, T. M., and Teixeira, M. (2004) New insights into type II NAD(P)H:quinone oxidoreductases, *Microbiology and Molecular Biology Reviews* 68, 603-616.
28. Pereira, M. M., Bandejas, T. M., Fernandes, A. S., Lemos, R. S., Melo, A. M. P., and Teixeira, M. (2004) Respiratory Chains from Aerobic Thermophilic Prokaryotes, *Journal of Bioenergetics and Biomembranes* 36, 93-105.
29. Hägerhäll, C., and Hederstedt, L. (1996) A structural model for the membrane-integral domain of succinate:quinone oxidoreductases, *FEBS Letters* 389, 25-31.
30. Sun, F., Huo, X., Zhai, Y., Wang, A., Xu, J., Su, D., Bartlam, M., and Rao, Z. (2005) Crystal structure of mitochondrial respiratory membrane protein Complex II, *Cell* 121, 1043-1057.
31. Iverson, T. M., Luna-Chavez, C., Cecchini, G., and Rees, D. C. (1999) Structure of the *Escherichia coli* fumarate reductase respiratory complex, *Science* 284, 1961-1966.
32. Lancaster, C. R. D., Kröger, A., Auer, M., and Michel, H. (1999) Structure of fumarate reductase from *Wolinella succinogenes* at 2.2 Å resolution, *Nature* 402, 377-385.
33. Wolf, D. E., Hoffman, C. H., Trenner, N. R., Arison, B. H., Shunk, C. H., Linn, B. O., McPherson, J. F., and Folkers, K. (1958) Coenzyme Q. I. Structure studies on the coenzyme Q group, *Journal of the American Chemical Society* 80, 4752.
34. Ernster, L., and Dallner, G. (1995) Biochemical, physiological and medical aspects of ubiquinone function, *Biochimica et Biophysica Acta - Molecular Basis of Disease* 1271, 195-204.
35. Jeftic, L., and Manning, G. (1970) A survey on the electrochemical reduction of quinones, *Journal of Electroanalytical Chemistry* 26, 195-200.
36. Fisher, N., and Rich, P. R. (2000) A motif for quinone binding sites in respiratory and photosynthetic systems, *Journal of Molecular Biology* 296, 1153-1162.
37. Sato-Watanabe, M., Mogi, T., Ogura, T., Kitagawa, T., Miyoshi, H., Iwamura, H., and Anraku, Y. (1994) Identification of a novel quinone-binding site in the cytochrome bo complex from *Escherichia coli*, *Journal of Biological Chemistry* 269, 28908-28912.
38. Horsefield, R., Yankovskaya, V., Sexton, G., Whittingham, W., Shiomi, K., Omura, S., Byrne, B., Cecchini, G., and Iwata, S. (2006) Structural and computational analysis of the quinone-binding site of complex II (succinate-ubiquinone oxidoreductase): A mechanism of electron transfer and proton conduction during ubiquinone reduction, *Journal of Biological Chemistry* 281, 7309-7316.
39. Nyola, A., and Hunte, C. (2008) A structural analysis of the transient interaction between the cytochrome *bc*<sub>1</sub> complex and its substrate cytochrome *c*, *Biochemical Society Transactions* 36, 981-985.
40. Gao, X., Wen, X., Esser, L., Quinn, B., Yu, L., Yu, C. A., and Xia, D. (2003) Structural basis for the quinone reduction in the *bc*<sub>1</sub> complex: A comparative analysis of crystal structures of mitochondrial cytochrome *bc*<sub>1</sub> with bound substrate and inhibitors at the Q<sub>i</sub> site, *Biochemistry* 42, 9067-9080.

41. Lange, C., Nett, J. H., Trumpower, B. L., and Hunte, C. (2001) Specific roles of protein-phospholipid interactions in the yeast cytochrome *bc*<sub>1</sub> complex structure, *EMBO Journal* 20, 6591-6600.
42. Berry, E. A., Huang, L. S., Saechao, L. K., Pon, N. G., Valkova-Valchanova, M., and Daldal, F. (2004) X-ray structure of *Rhodobacter capsulatus* cytochrome *bc*<sub>1</sub>: Comparison with its mitochondrial and chloroplast counterparts, *Photosynthesis Research* 81, 251-275.
43. Kleinschroth, T., Anderka, O., Ritter, M., Stocker, A., Link, T. A., Ludwig, B., and Hellwig, P. (2008) Characterization of mutations in crucial residues around the Q(o) binding site of the cytochrome *bc* complex from *Paracoccus denitrificans*, *Febs J* 275, 4773-4785.
44. Xia, D., Yu, C. A., Kim, H., Xia, J. Z., Kachurin, A. M., Zhang, L., Yu, L., and Deisenhofer, J. (1997) Crystal structure of the cytochrome *bc*<sub>1</sub> complex from bovine heart mitochondria, *Science* 277, 60-66.
45. Ritter, M., Palsdottir, H., Abe, M., Mantele, W., Hunte, C., Miyoshi, H., and Hellwig, P. (2004) Direct evidence for the interaction of stigmatellin with a protonated acidic group in the *bc*<sub>1</sub> complex from *Saccharomyces cerevisiae* as monitored by FTIR difference spectroscopy and <sup>13</sup>C specific labeling, *Biochemistry* 43, 8439-8446.
46. Mitchell, P. (1975) Protonmotive redox mechanism of the cytochrome *b-c*<sub>1</sub> complex in the respiratory chain: protonmotive ubiquinone cycle, *FEBS Letters* 56, 1-6.
47. Cooley, J. W. (2010) A structural model for across membrane coupling between the Q<sub>o</sub> and Q<sub>i</sub> active sites of cytochrome *bc*<sub>1</sub>, *Biochimica et Biophysica Acta - Bioenergetics* 1797, 1842-1848.
48. Crofts, A. R. (2004) The cytochrome *bc*<sub>1</sub> complex: Function in the context of structure, pp 689-733.
49. Hunte, C., Palsdottir, H., and Trumpower, B. L. (2003) Protonmotive pathways and mechanisms in the cytochrome *bc*<sub>1</sub> complex, *FEBS Letters* 545, 39-46.
50. Bushnell, G. W., Louie, G. V., and Brayer, G. D. (1990) High-resolution three-dimensional structure of horse heart cytochrome *c*, *Journal of Molecular Biology* 214, 585-595.
51. Tezcan, F. A., Crane, B. R., Winkler, J. R., and Gray, H. B. (2001) Electron tunneling in protein crystals, *Proceedings of the National Academy of Sciences of the United States of America* 98, 5002-5006.
52. Green, D. R., and Reed, J. C. (1998) Mitochondria and apoptosis, *Science* 281, 1309-1312.
53. Kluck, R. M., Bossy-Wetzel, E., Green, D. R., and Newmeyer, D. D. (1997) The release of cytochrome *c* from mitochondria: A primary site for Bcl-2 regulation of apoptosis, *Science* 275, 1132-1136.
54. Garcia-Horsman, J. A., Barquera, B., Rumbley, J., Ma, J., and Gennis, R. B. (1994) The superfamily of heme-copper respiratory oxidases, *Journal of Bacteriology* 176, 5587-5600.
55. Iwata, S., Ostermeier, C., Ludwig, B., and Michel, H. (1995) Structure at 2.8 Å resolution of cytochrome *c* oxidase from *Paracoccus denitrificans*, *Nature* 376, 660-669.
56. Tsukihara, T., Aoyama, H., Yamashita, E., Tomizaki, T., Yamaguchi, H., Shinzawa-Itoh, K., Nakashima, R., Yaono, R., and Yoshikawa, S. (1996) The whole structure of the 13-subunit oxidized cytochrome *c* oxidase at 2.8 Å, *Science* 272, 1136-1144.
57. Abramson, J., Riistama, S., Larsson, G., Jasaitis, A., Svensson-Ek, M., Laakkonen, L., Puustinen, A., Iwata, S., and Wikström, M. (2000) The structure of the ubiquinol oxidase from *Escherichia coli* and its ubiquinone binding site, *Nature Structural Biology* 7, 910-917.
58. Svensson-Ek, M., Abramson, J., Larsson, G., Törnroth, S., Brzezinski, P., and Iwata, S. (2002) The X-ray crystal structures of wild-type and EQ(I-286) mutant cytochrome *c* oxidases from *Rhodobacter sphaeroides*, *Journal of Molecular Biology* 321, 329-339.
59. Brändén, G., Gennis, R. B., and Brzezinski, P. (2006) Transmembrane proton translocation by cytochrome *c* oxidase, *Biochimica et Biophysica Acta - Bioenergetics* 1757, 1052-1063.

60. Brunori, M., Giuffrè, A., and Sarti, P. (2005) Cytochrome c oxidase, ligands and electrons, *Journal of Inorganic Biochemistry* 99, 324-336.
61. Tsukihara, T., Aoyama, H., Yamashita, E., Tomizaki, T., Yamaguchi, H., Shinzawa-Itoh, K., Nakashima, R., Yaono, R., and Yoshikawa, S. (1995) Structures of metal sites of oxidized bovine heart cytochrome c oxidase at 2.8 Å, *Science* 269, 1069-1074.
62. Hellwig, P., Grzybek, S., Behr, J., Ludwig, B., Michel, H., and Mantele, W. (1999) Electrochemical and ultraviolet/visible/infrared spectroscopic analysis of heme *a* and *a*<sub>3</sub> redox reactions in the cytochrome c oxidase from *Paracoccus denitrificans*: separation of heme *a* and *a*<sub>3</sub> contributions and assignment of vibrational modes, *Biochemistry* 38, 1685-1694.
63. Hellwig, P., Behr, J., Ostermeier, C., Richter, O. M., Pfitzner, U., Odenwald, A., Ludwig, B., Michel, H., and Mantele, W. (1998) Involvement of glutamic acid 278 in the redox reaction of the cytochrome c oxidase from *Paracoccus denitrificans* investigated by FTIR spectroscopy, *Biochemistry* 37, 7390-7399.
64. Hellwig, P., Rost, B., Kaiser, U., Ostermeier, C., Michel, H., and Mantele, W. (1996) Carboxyl group protonation upon reduction of the *Paracoccus denitrificans* cytochrome c oxidase: direct evidence by FTIR spectroscopy, *FEBS Lett* 385, 53-57.
65. Abrahams, J. P., Leslie, A. G. W., Lutter, R., and Walker, J. E. (1994) Structure at 2.8 Å resolution of F<sub>1</sub>-ATPase from bovine heart mitochondria, *Nature* 370, 621-628.
66. Noji, H., Yasuda, R., Yoshida, M., and Kinosita Jr, K. (1997) Direct observation of the rotation of F<sub>1</sub>-ATPase, *Nature* 386, 299-302.
67. Tsunoda, S. P., Aggeler, R., Yoshida, M., and Capaldi, R. A. (2001) Rotation of the c subunit oligomer in fully functional F<sub>1</sub> F<sub>0</sub> ATP synthase, *Proceedings of the National Academy of Sciences of the United States of America* 98, 898-902.
68. Fillingame, R. H., Angevine, C. M., and Dmitriev, O. Y. (2003) Mechanics of coupling proton movements to c-ring rotation in ATP synthase, *FEBS Letters* 555, 29-34.
69. Häse, C. C., Fedorova, N. D., Galperin, M. Y., and Dibrov, P. A. (2001) Sodium ion cycle in bacterial pathogens: Evidence from cross-genome comparisons, *Microbiology and Molecular Biology Reviews* 65, 353-370.
70. Pollitzer, R., Swaroop, S., and Burrows, W. (1959) Cholera, *Monograph series. World Health Organization* 58, 1001-1019.
71. Kaper, J. B., Morris Jr, J. G., and Levine, M. M. (1995) Cholera, *Clinical Microbiology Reviews* 8, 48-86.
72. Häse, C. C., and Barquera, B. (2001) Role of sodium bioenergetics in *Vibrio cholerae*, *Biochimica et Biophysica Acta - Bioenergetics* 1505, 169-178.
73. Häse, C. C., and Mekalanos, J. J. (1999) Effects of changes in membrane sodium flux on virulence gene expression in *Vibrio cholerae*, *Proceedings of the National Academy of Sciences of the United States of America* 96, 3183-3187.
74. Murata, T., Yamato, I., and Kakinuma, Y. (2005) Structure and mechanism of vacuolar Na<sup>+</sup>-translocating ATPase from *Enterococcus hirae*, *Journal of Bioenergetics and Biomembranes* 37, 411-413.
75. Unemoto, T., and Hayashi, M. (1977) Na<sup>+</sup> dependent activation of NADH oxidase in membrane fractions from halophilic *Vibrio alginolyticus* and *Vibrio costicolus*, *Journal of Biochemistry* 82, 1389-1395.
76. Dimroth, P., and Thomer, A. (1989) A primary respiratory Na<sup>+</sup> pump of an anaerobic bacterium: the Na<sup>+</sup>-dependent NADH:quinone oxidoreductase of *Klebsiella pneumoniae*, *Archives of Microbiology* 151, 439-444.
77. Hayashi, M., Nakayama, Y., and Unemoto, T. (1996) Existence of Na<sup>+</sup>-translocating NADH-quinone reductase in *Haemophilus influenzae*, *FEBS Letters* 381, 174-176.
78. Hayashi, M., and Unemoto, T. (1984) Characterization of the Na<sup>+</sup>-dependent respiratory chain NADH:quinone oxidoreductase of the marine bacterium, *Vibrio alginolyticus*, in relation to the primary Na<sup>+</sup> pump, *BBA - Bioenergetics* 767, 470-478.

79. Tokuda, H., and Unemoto, T. (1984)  $\text{Na}^+$  is translocated at NADH:quinone oxidoreductase segment in the respiratory chain of *Vibrio alginolyticus*, *Journal of Biological Chemistry* 259, 7785-7790.
80. Zhou, W., Bertsova, Y. V., Feng, B., Tsatsos, P., Verkhovskaya, M. L., Gennis, R. B., Bogachev, A. V., and Barquera, B. (1999) Sequencing and preliminary characterization of the  $\text{Na}^+$ -translocating NADH:ubiquinone oxidoreductase from *Vibrio harveyi*, *Biochemistry* 38, 16246-16252.
81. Barquera, B., Hellwig, P., Zhou, W., Morgan, J. E., Hase, C. C., Gosink, K. K., Nilges, M., Bruesehoff, P. J., Roth, A., Lancaster, C. R., and Gennis, R. B. (2002) Purification and characterization of the recombinant  $\text{Na}^+$ -translocating NADH:quinone oxidoreductase from *Vibrio cholerae*, *Biochemistry* 41, 3781-3789.
82. Duffy, E. B., and Barquera, B. (2006) Membrane topology mapping of the  $\text{Na}^+$ -pumping NADH: Quinone oxidoreductase from *Vibrio cholerae* by PhoA-green fluorescent protein fusion analysis, *Journal of Bacteriology* 188, 8343-8351.
83. Hayashi, M., Nakayama, Y., Yasui, M., Maeda, M., Furuishi, K., and Unemoto, T. (2001) FMN is covalently attached to a threonine residue in the NqrB and NqrC subunits of  $\text{Na}^+$ -translocating NADH-quinone reductase from *Vibrio alginolyticus*, *FEBS Letters* 488, 5-8.
84. Barquera, B., Hase, C. C., and Gennis, R. B. (2001) Expression and mutagenesis of the NqrC subunit of the NQR respiratory  $\text{Na}^+$  pump from *Vibrio cholerae* with covalently attached FMN, *FEBS Lett* 492, 45-49.
85. Barquera, B., Ramirez-Silva, L., Morgan, J. E., and Nilges, M. J. (2006) A new flavin radical signal in the  $\text{Na}^+$ -pumping NADH:quinone oxidoreductase from *Vibrio cholerae*: An EPR/electron nuclear double resonance investigation of the role of the covalently bound flavins in subunits B and C, *Journal of Biological Chemistry* 281, 36482-36491.
86. Heuts, D. P. H. M., Scrutton, N. S., McIntire, W. S., and Fraaije, M. W. (2009) What's in a covalent bond?: On the role and formation of covalently bound flavin cofactors, *FEBS Journal* 276, 3405-3427.
87. Casutt, M. S., Huber, T., Brunisholz, R., Tao, M., Fritz, G., and Steuber, J. (2010) Localization and function of the membrane-bound riboflavin in the  $\text{Na}^+$ -translocating NADH:quinone oxidoreductase ( $\text{Na}^+$ -NQR) from *Vibrio cholerae*, *Journal of Biological Chemistry* 285, 27088-27099.
88. Juárez, O., Nilges, M. J., Gillespie, P., Cotton, J., and Barquera, B. (2008) Riboflavin is an active redox cofactor in the  $\text{Na}^+$ -pumping NADH: quinone oxidoreductase ( $\text{Na}^+$ -NQR) from *Vibrio cholerae*, *J Biol Chem* 283, 33162-33167.
89. Juárez, O., Athearn, K., Gillespie, P., and Barquera, B. (2009) Acid residues in the transmembrane helices of the  $\text{Na}^+$ -pumping NADH:quinone oxidoreductase from *Vibrio cholerae* involved in sodium translocation, *Biochemistry* 48, 9516-9524.
90. Yoshikawa, K., Takadera, T., Adachi, K., Nishijima, M., and Sano, H. (1997) Korormicin, a novel antibiotic specifically active against marine Gram-negative bacteria, produced by a marine bacterium, *Journal of Antibiotics* 50, 949-953.
91. Yoshikawa, K., Nakayama, Y., Hayashi, M., Unemoto, T., and Mochida, K. (1999) Korormicin, an antibiotic specific for gram-negative marine bacteria, strongly inhibits the respiratory chain-linked  $\text{Na}^+$ -translocating NADH: Quinone reductase from the marine *Vibrio alginolyticus*, *Journal of Antibiotics* 52, 182-185.
92. Hayashi, M., Shibata, N., Nakayama, Y., Yoshikawa, K., and Unemoto, T. (2002) Korormicin insensitivity in *Vibrio alginolyticus* is correlated with a single point mutation of Gly-140 in the NqrB subunit of the  $\text{Na}^+$ -translocating NADH-quinone reductase, *Archives of Biochemistry and Biophysics* 401, 173-177.
93. Casutt, M. S., Nedielkov, R., Wendelspiess, S., Vossler, S., Gerken, U., Murai, M., Miyoshi, H., Möller, H. M., and Steuber, J. (2011) Localization of ubiquinone-8 in the  $\text{Na}^+$ -pumping NADH: Quinone oxidoreductase from *Vibrio cholerae*, *Journal of Biological Chemistry* 286, 40075-40082.

94. Juárez, O., Morgan, J. E., and Barquera, B. (2009) The electron transfer pathway of the Na<sup>+</sup>-pumping NADH:Quinone oxidoreductase from *Vibrio cholerae*, *Journal of Biological Chemistry* 284, 8963-8972.
95. Backiel, J., Juárez, O., Zagorevski, D. V., Wang, Z., Nilges, M. J., and Barquera, B. (2008) Covalent binding of flavins to RnfG and RnfD in the Rnf complex from *Vibrio cholerae*, *Biochemistry* 47, 11273-11284.
96. Sääf, A., Johansson, M., Wallin, E., and Von Heijne, G. (1999) Divergent evolution of membrane protein topology: The *Escherichia coli* RnfA and RnfE homologues, *Proceedings of the National Academy of Sciences of the United States of America* 96, 8540-8544.
97. Rich, P. R., Meunier, B., and Ward, E. B. (1995) Predicted structure and possible ionmotive mechanism of the sodium-linked NADH-ubiquinone oxidoreductase of *Vibrio alginolyticus*, *FEBS Letters* 375, 5-10.
98. Barquera, B., Nilges, M. J., Morgan, J. E., Ramirez-Silva, L., Zhou, W., and Gennis, R. B. (2004) Mutagenesis study of the 2Fe-2S center and the FAD binding site of the Na<sup>+</sup>-translocating NADH:ubiquinone oxidoreductase from *Vibrio cholerae*, *Biochemistry* 43, 12322-12330.
99. Tao, M., Türk, K., Diez, J., Grütter, M. G., Fritz, G., and Steuber, J. (2006) Crystallization of the NADH-oxidizing domain of the Na<sup>+</sup>-translocating NADH:ubiquinone oxidoreductase from *Vibrio cholerae*, *Acta Crystallographica Section F: Structural Biology and Crystallization Communications* 62, 110-112.
100. Türk, K., Puhar, A., Neese, F., Bill, E., Fritz, G., and Steuber, J. (2004) NADH oxidation by the Na<sup>+</sup>-translocating NADH:quinone oxidoreductase from *Vibrio cholerae*: Functional role of the NqrF subunit, *Journal of Biological Chemistry* 279, 21349-21355.
101. MacHeroux, P., Kappes, B., and Ealick, S. E. (2011) Flavogenomics - A genomic and structural view of flavin-dependent proteins, *FEBS Journal* 278, 2625-2634.
102. Wyville Thomson, C. (1877) The "Challenger" collections, *Nature* 15, 254-256.
103. Macheroux, P., Ghisla, S., and Hastings, J. W. (1993) Spectral detection of an intermediate preceding the excited state in the bacterial luciferase reaction, *Biochemistry* 32, 14183-14186.
104. Blyth, A. W. (1879) LVI. - The composition of cows' milk in health and disease, *Journal of the Chemical Society* 35, 530-539.
105. Vetter, H. (1936) Lactoflavin, *Ergebnisse der Physiologie Biologischen Chemie und Experimentellen Pharmakologie* 38, 855-876.
106. Kuhn, R. (1935) Synthetic compound with vitamin B2 activity [5], *Nature* 135, 185.
107. Karrer, P. (1935) Vitamine A, C und B2 - Konstitution und Konstitutionsspezifität der Wirkung, *Monatshefte für Chemie* 66, 367-392.
108. Tan, S. L. J., and Webster, R. D. (2012) Electrochemically induced chemically reversible proton-coupled electron transfer reactions of riboflavin (Vitamin B 2), *Journal of the American Chemical Society* 134, 5954-5964.
109. Bogachev, A. V., Belevich, N. P., Bertsova, Y. V., and Verkhovsky, M. I. (2009) Primary steps of the Na<sup>+</sup>-translocating NADH:ubiquinone oxidoreductase catalytic cycle resolved by the ultrafast freeze-quench approach, *J Biol Chem* 284, 5533-5538.
110. Verkhovsky, M. I., and Bogachev, A. V. (2010) Sodium-translocating NADH:quinone oxidoreductase as a redox-driven ion pump, *Biochim Biophys Acta* 1797, 738-746.
111. Juárez, O., Morgan, J. E., Nilges, M. J., and Barquera, B. (2010) Energy transducing redox steps of the Na<sup>+</sup>-pumping NADH:quinone oxidoreductase from *Vibrio cholerae*, *Proc Natl Acad Sci U S A* 107, 12505-12510.
112. Juárez, O., Shea, M. E., Makhatadze, G. I., and Barquera, B. (2011) The role and specificity of the catalytic and regulatory cation-binding sites of the Na<sup>+</sup>-pumping NADH:quinone oxidoreductase from *Vibrio cholerae*, *Journal of Biological Chemistry* 286, 26383-26390.

113. Nayal, M., and Di Cera, E. (1996) Valence screening of water in protein crystals reveals potential Na<sup>+</sup> binding sites, *Journal of Molecular Biology* 256, 228-234.
114. Maneg, O., Malatesta, F., Ludwig, B., and Drosou, V. (2004) Interaction of cytochrome *c* with cytochrome oxidase: Two different docking scenarios, *Biochimica et Biophysica Acta - Bioenergetics* 1655, 274-281.
115. Vonck, J., and Schäfer, E. (2009) Supramolecular organization of protein complexes in the mitochondrial inner membrane, *Biochimica et Biophysica Acta - Molecular Cell Research* 1793, 117-124.
116. Ragan, C. I., and Heron, C. (1978) The interaction between mitochondrial NADH-ubiquinone oxidoreductase and ubiquinol-cytochrome *c* oxidoreductase. Evidence for stoichiometric association, *Biochemical Journal* 174, 783-790.
117. Muresanu, L., Pristovšek, P., Löhr, F., Maneg, O., Mukrasch, M. D., Rüterjans, H., Ludwig, B., and Lücke, C. (2006) The electron transfer complex between cytochrome *c*<sub>552</sub> and the Cu<sub>A</sub> domain of the *Thermus thermophilus* *ba*<sub>3</sub> oxidase: A combined NMR and computational approach, *Journal of Biological Chemistry* 281, 14503-14513.
118. Sujak, A., Sanghamitra, N. J. M., Maneg, O., Ludwig, B., and Mazumdar, S. (2007) Thermostability of proteins: Role of metal binding and pH on the stability of the dinuclear Cu<sub>A</sub> site of *Thermus thermophilus*, *Biophysical Journal* 93, 2845-2851.
119. Zhou, X. X., Wang, Y. B., Pan, Y. J., and Li, W. F. (2008) Differences in amino acids composition and coupling patterns between mesophilic and thermophilic proteins, *Amino Acids* 34, 25-33.
120. Petukhov, M., Kil, Y., Kuramitsu, S., and Lanzov, V. (1997) Insights into thermal resistance of proteins from the intrinsic stability of their  $\alpha$ -helices, *Proteins: Structure, Function and Genetics* 29, 309-320.
121. Vogt, G., Woell, S., and Argos, P. (1997) Protein thermal stability, hydrogen bonds, and ion pairs, *Journal of Molecular Biology* 269, 631-643.
122. Zimmermann, B. H., Nitsche, C. I., Fee, J. A., Rusnak, F., and Münck, E. (1988) Properties of a copper-containing cytochrome *ba*<sub>3</sub>: a second terminal oxidase from the extreme thermophile *Thermus thermophilus*, *Proceedings of the National Academy of Sciences of the United States of America* 85, 5779-5783.
123. Cava, F., Hidalgo, A., and Berenguer, J. (2009) *Thermus thermophilus* as biological model, *Extremophiles* 13, 213-231.
124. Janzon, J., Ludwig, B., and Malatesta, F. (2007) Electron transfer kinetics of soluble fragments indicate a direct interaction between complex III and the *caa*<sub>3</sub> oxidase in *Thermus thermophilus*, *IUBMB Life* 59, 563-569.
125. Hon-Nami, K., and Oshima, T. (1977) Purification and some properties of cytochrome *c*<sub>552</sub> from an extreme thermophile, *Thermus thermophilus* HB8, *Journal of Biochemistry* 82, 769-776.
126. Soulimane, T., Walter, M. V., Hof, P., Than, M. E., Huber, R., and Buse, G. (1997) Cytochrome-*c*<sub>552</sub> from *Thermus thermophilus*: A functional and crystallographic investigation, *Biochemical and Biophysical Research Communications* 237, 572-576.
127. Slutter, C. E., Langen, R., Sanders, D., Lawrence, S. M., Wittung, P., Di Bilio, A. J., Hill, M. G., Fee, J. A., Richards, J. H., Winkler, J. R., and Malmström, B. G. (1996) Electron-transfer studies with the Cu<sub>A</sub> domain of *Thermus thermophilus* cytochrome *ba*<sub>3</sub>, *Inorganica Chimica Acta* 243, 141-145.
128. Wienk, H., Maneg, O., Lücke, C., Pristovsek, P., Löhr, F., Ludwig, B., and Rüterjans, H. (2003) Interaction of cytochrome *c* with cytochrome *c* oxidase: An NMR study on two soluble fragments derived from *Paracoccus denitrificans*, *Biochemistry* 42, 6005-6012.
129. Smirnova, I. A., Zaslavsky, D., Fee, J. A., Gennis, R. B., and Brzezinski, P. (2008) Electron and proton transfer in the *ba*<sub>3</sub> oxidase from *Thermus thermophilus*, *Journal of Bioenergetics and Biomembranes* 40, 281-287.

130. Luna, V. M., Chen, Y., Fee, J. A., and Stout, C. D. (2008) Crystallographic studies of Xe and Kr binding within the large internal cavity of cytochrome *ba*<sub>3</sub> from *Thermus thermophilus*: Structural analysis and role of oxygen transport channels in the heme-Cu oxidases, *Biochemistry* 47, 4657-4665.
131. Tiefenbrunn, T., Liu, W., Chen, Y., Katritch, V., Stout, C. D., Fee, J. A., and Cherezov, V. (2011) High resolution structure of the *ba*<sub>3</sub> cytochrome *c* oxidase from *Thermus thermophilus* in a lipidic environment, *PLoS ONE* 6.
132. Slutter, C. E., Sanders, D., Wittung, P., Malmström, B. G., Aasa, R., Richards, J. H., Gray, H. B., and Fee, J. A. (1996) Water-soluble, recombinant Cu<sub>A</sub>-domain of the cytochrome *ba*<sub>3</sub> subunit II from *Thermus thermophilus*, *Biochemistry* 35, 3387-3395.
133. Williams, P. A., N. J. Blackburn, D. Sanders, H. Bellamy, E. A. Stura, J. A. Fee, and McRee, D. E. (1999) The Cu<sub>A</sub> domain of *Thermus thermophilus ba*<sub>3</sub>-type cytochrome *c* oxidase at 1.6 Å resolution, *Nature America Inc* 6, 509-516.
134. Karpefors, M., Slutter, C. E., Fee, J. A., Aasa, R., Källebring, B., Larsson, S., and Vänngård, T. (1996) Electron paramagnetic resonance studies of the soluble Cu<sub>A</sub> protein from the cytochrome *ba*<sub>3</sub> of *Thermus thermophilus*, *Biophysical Journal* 71, 2823-2829.
135. Immoos, C., Hill, M. G., Sanders, D., Fee, J. A., Slutter, C. E., Richards, J. H., and Gray, H. B. (1996) Electrochemistry of the Cu<sub>A</sub> domain of *Thermus thermophilus* cytochrome *ba*<sub>3</sub>, *Journal of Biological Inorganic Chemistry* 1, 529-531.
136. Hon-Nami, K., and Oshima, T. (1977) Purification and some properties of cytochrome *c*<sub>552</sub> from an extreme thermophile, *Thermus thermophilus* HB8, *Journal of Biochemistry* 82, 769-776.
137. Fee, J. A., Chen, Y., Todaro, T. R., Bren, K. L., Patel, K. M., Hill, M. G., Gomez-Moran, E., Loehr, T. M., Ai, J., Thony-Meyer, L., Williams, P. A., Stura, E., Sridhar, V., and McRee, D. E. (2000) Integrity of *Thermus thermophilus* cytochrome *c*<sub>552</sub> synthesized by *Escherichia coli* cells expressing the host-specific cytochrome *c* maturation genes, *ccmABCDEFGH*: Biochemical, spectral, and structural characterization of the recombinant protein, *Protein Science* 9, 2074-2084.
138. Maneg, O., Ludwig, B., and Malatesta, F. (2003) Different interaction modes of two cytochrome *c* oxidase soluble Cu<sub>A</sub> fragments with their substrates, *Journal of Biological Chemistry* 278, 46734-46740.
139. Drosou, V., Malatesta, F., and Ludwig, B. (2002) Mutations in the docking site for cytochrome *c* on the *Paracoccus* heme *aa*<sub>3</sub> oxidase: Electron entry and kinetic phases of the reaction, *European Journal of Biochemistry* 269, 2980-2988.
140. Kinoshita, S., Udaka, S., and Shimono, M. (1957) Studies on the amino acid fermentation. Part 1. Production of L-glutamic acid by various micro-organisms, *The Journal of General and Applied Microbiology* 3, 193-205.
141. Bott, M., and Niebisch, A. (2003) The respiratory chain of *Corynebacterium glutamicum*, *Journal of Biotechnology* 104, 129-153.
142. Bott, M. (2007) Corynebacteria: The good guys and the bad guys, *Microbiology Today* 34, 74-77.
143. Lee, S. Y., Kim, B. N., Han, J. H., Chang, S. T., Choi, Y. W., Kim, Y. H., and Min, J. (2010) Treatment of phenol-contaminated soil by *Corynebacterium glutamicum* and toxicity removal evaluation, *Journal of Hazardous Materials* 182, 937-940.
144. Bekker, M., Kramer, G., Hartog, A. F., Wagner, M. J., de Korster, C. G., Hellingwerf, K. J., and Teixeira de Mattos, M. J. (2007) Changes in the redox state and composition of the quinone pool of *Escherichia coli* during aerobic batch-culture growth, *Microbiology* 153, 1974-1980.
145. Prince, R. C., Leslie Dutton, P., and Malcolm Bruce, J. (1983) Electrochemistry of ubiquinones. Menaquinones and plastoquinones in aprotic solvents, *FEBS Letters* 160, 273-276.

146. Lawson, R. C., Ferrer, A., Flores, W., and Alegría, A. E. (1999) Sonochemistry of quinones in argon-saturated aqueous solutions: Enhanced cytochrome *c* reduction, *Chemical Research in Toxicology* 12, 850-854.
147. Buffinton, G. D., Ollinger, K., Brunmark, A., and Cadenas, E. (1989) DT-diaphorase-catalysed reduction of 1,4-naphthoquinone derivatives and glutathionyl-quinone conjugates. Effect of substituents on autoxidation rates, *Biochemical Journal* 257, 561-571.
148. Li, W. W., Hellwig, P., Ritter, M., and Haehnel, W. (2006) De novo design, synthesis, and characterization of quinoproteins, *Chemistry* 12, 7236-7245.
149. Sugiyama, Y., Kitano, K., and Kanzaki, T. (1973) Role of copper ions in the regulation of L glutamate biosynthesis, *Agricultural and Biological Chemistry* 37, 1837-1847.
150. Trutko, S. M., Kuznetsova, N. N., Balitskaya, R. M., and Akimenko, V. K. (1982) Effect of the glutamic acid oversynthesis on the development of cyanide-resistant respiration in the bacterium *Corynebacterium glutamicum*, *Biokhimiya* 47, 1608-1617.
151. Sugiyama, Y., Kitano, K., and Kanzaki, T. (1973) Purification of cytochrome *a* of an L glutamate producing microorganism, *Brevibacterium thiogenitalis*, *Agricultural and Biological Chemistry* 37, 1607-1612.
152. Sakamoto, J., Shibata, T., Mine, T., Miyahara, R., Torigoe, T., Noguchi, S., Matsushita, K., and Sone, N. (2001) Cytochrome *c* oxidase contains an extra charged amino acid cluster in a new type of respiratory chain in the amino-acid-producing Gram-positive bacterium *Corynebacterium glutamicum*, *Microbiology* 147, 2865-2871.
153. Hielscher, R. G. (2009) The role of lipids and nucleotides in the catalytic mechanism of proteins from the respiratory chain: an electrochemical and infrared spectroscopic approach, In *Chemistry*, Université Louis pasteur, Strasbourg.
154. Moss, D., Nabadryk, E., Breton, J., and Mäntele, W. (1990) Redox-linked conformational changes in proteins detected by a combination of infrared spectroscopy and protein electrochemistry. Evaluation of the technique with cytochrome *c*, *European Journal of Biochemistry* 187, 565-572.
155. Leif, H., Sled, V. D., Ohnishi, T., Weiss, H., and Friedrich, T. (1995) Isolation and characterization of the proton-translocating NADH:ubiquinone oxidoreductase from *Escherichia coli*, *European Journal of Biochemistry* 230, 538-548.
156. Darrouzet, E., Valkova-Valchanova, M., Ohnishi, T., and Daldal, F. (1999) Structure and function of the bacterial *bc<sub>1</sub>* complex: Domain movement, subunit interactions, and emerging rationale engineering attempts, *Journal of Bioenergetics and Biomembranes* 31, 275-288.
157. Kleinschroth, T., Anderka, O., Ritter, M., Stocker, A., Link, T. A., Ludwig, B., and Hellwig, P. (2008) Characterization of mutations in crucial residues around the Q<sub>o</sub> binding site of the cytochrome *bc<sub>1</sub>* complex from *Paracoccus denitrificans*, *FEBS Journal* 275, 4773-4785.
158. Hollas, J. M., (Ed.) (2004) *Modern Spectroscopy*, 4th ed., Wiley, West Sussex, England.
159. Goormaghtigh, E., Cabiaux, V., and Ruyschaert, J. M. (1994) Determination of soluble and membrane protein structure by Fourier transform infrared spectroscopy. I. Assignments and model compounds, *Sub-cellular biochemistry* 23, 329-362.
160. Goormaghtigh, E., Cabiaux, V., and Ruyschaert, J. M. (1994) Determination of soluble and membrane protein structure by Fourier transform infrared spectroscopy. II. Experimental aspects, side chain structure, and H/D exchange, *Sub-cellular biochemistry* 23, 363-403.
161. Goormaghtigh, E., Cabiaux, V., and Ruyschaert, J. M. (1994) Determination of soluble and membrane protein structure by Fourier transform infrared spectroscopy. III. Secondary structures, *Sub-cellular biochemistry* 23, 405-450.



162. Jackson, M., and Mantsch, H. H. (1995) The use and misuse of FTIR spectroscopy in the determination of protein structure, *Critical Reviews in Biochemistry and Molecular Biology* 30, 95-120.
163. Chittur, K. K. (1998) FTIR/ATR for protein adsorption to biomaterial surfaces, *Biomaterials* 19, 357-369.
164. Engen, J. R. (2009) Analysis of protein conformation and dynamics by hydrogen/deuterium exchange MS, *Analytical Chemistry* 81, 7870-7875.
165. Vigano, C., Smeyers, M., Raussens, V., Scheirlinckx, F., Ruyschaert, J. M., and Goormaghtigh, E. (2004) Hydrogen-deuterium exchange in membrane proteins monitored by IR spectroscopy: a new tool to resolve protein structure and dynamics, *Biopolymers* 74, 19-26.
166. Smith, J. R., Cicerone, M. T., and Meuseb, C. W. (2009) Measuring hydrogen-deuterium exchange in protein monolayers, *Surface and Interface Analysis* 41, 878-885.
167. Englander, S. W., Sosnick, T. R., Englander, J. J., and Mayne, L. (1996) Mechanisms and uses of hydrogen exchange, *Current Opinion in Structural Biology* 6, 18-23.
168. Vogel, R., and Siebert, F. (2000) Vibrational spectroscopy as a tool for probing protein function, *Current Opinion in Chemical Biology* 4, 518-523.
169. Džafić, E., Klein, O., Screpanti, E., Hunte, C., and Mäntele, W. (2009) Flexibility and dynamics of NhaA Na<sup>+</sup>/H<sup>+</sup>-antiporter of *Escherichia coli* studied by Fourier transform infrared spectroscopy, *Spectrochimica Acta - Part A: Molecular and Biomolecular Spectroscopy* 72, 102-109.
170. Džafić, E., Klein, O., Goswami, P., Kühlbrandt, W., and Mäntele, W. (2009) Infrared spectroscopic study of the structural and functional properties of the Na<sup>+</sup>/H<sup>+</sup> antiporter MjNhaP1 from *Methanococcus jannaschii*, *Biochimica et Biophysica Acta - Bioenergetics* 1787, 730-737.
171. Porter, M. D., Bright, T. B., Allara, D. L., and Chidsey, C. E. D. (1987) Spontaneously organized molecular assemblies. 4. Structural characterization of n-alkyl thiol monolayers on gold by optical ellipsometry, infrared spectroscopy, and electrochemistry, *Journal of the American Chemical Society* 109, 3559-3568.
172. Kötting, C., and Gerwert, K. (2005) Proteins in action monitored by time-resolved FTIR spectroscopy, *ChemPhysChem* 6, 881-888.
173. Lövy, J., Doskočilová, D., Schmidt, P., and Schneider, B. (1978) Conformational structure of N-methylpropionamide and N-methylisobutyramide. NMR shift reagent and IR study, *Journal of Molecular Structure* 50, 81-90.
174. Spiro, T. G. (1988) *Biological applications of Raman spectroscopy, Vol. 3: Resonance Raman spectra of heme proteins and other metalloproteins.*
175. Choi, S., and Spiro, T. G. (1983) Out-of-plane deformation modes in the resonance Raman spectra of metalloporphyrins and heme proteins, *Journal of the American Chemical Society* 105, 3683-3692.
176. Dörr, S., Wolpert, M., and Hellwig, P. (2006) Study on the redox state dependent  $\nu(\text{CH})$  vibrational modes of the c-type heme, *Biopolymers* 82, 349-352.
177. Hellwig, P., Mogi, T., Tomson, F. L., Gennis, R. B., Iwata, J., Miyoshi, H., and Mäntele, W. (1999) Vibrational modes of ubiquinone in cytochrome *bo*<sub>3</sub> from *Escherichia coli* identified by Fourier transform infrared difference spectroscopy and specific <sup>13</sup>C labeling, *Biochemistry* 38, 14683-14689.
178. Spexard, M., Immeln, D., Thöing, C., and Kottke, T. (2011) Infrared spectrum and absorption coefficient of the cofactor flavin in water, *Vibrational Spectroscopy* 57, 282-287.
179. Wille, G., Ritter, M., Friedemann, R., Mäntele, W., and Hübner, G. (2003) Redox-triggered FTIR difference spectra of FAD in aqueous solution and bound to flavoproteins, *Biochemistry* 42, 14814-14821.

180. Hellwig, P., Scheide, D., Bungert, S., Mantele, W., and Friedrich, T. (2000) FT-IR spectroscopic characterization of NADH:Ubiquinone oxidoreductase (complex I) from *Escherichia coli*: Oxidation of FeS cluster N2 is coupled with the protonation of an aspartate or glutamate side chain, *Biochemistry* 39, 10884-10891.
181. Barth, A. (2007) Infrared spectroscopy of proteins, *Biochimica et Biophysica Acta - Bioenergetics* 1767, 1073-1101.
182. Hellwig, P., Stolpe, S., and Friedrich, T. (2004) Fourier transform infrared spectroscopic study on the conformational reorganization in *Escherichia coli* complex I due to redox-driven proton translocation, *Biopolymers* 74, 69-72.
183. Bogachev, A. V., Bloch, D. A., Bertsova, Y. V., and Verkhovsky, M. I. (2009) Redox properties of the prosthetic groups of Na<sup>+</sup>-translocating NADH:Quinone oxidoreductase. 2. Study of the enzyme by optical spectroscopy, *Biochemistry* 48, 6299-6304.
184. Neehaul, Y., Juárez, O., Barquera, B., and Hellwig, P. (2012) Thermodynamic contribution to the regulation of electron transfer in the Na<sup>+</sup>-pumping NADH:quinone oxidoreductase from *Vibrio cholerae*, *Biochemistry* 51, 4072-4077.
185. Hielscher, R., Friedrich, T., and Hellwig, P. (2011) Far- and mid-infrared spectroscopic analysis of the substrate-induced structural dynamics of respiratory complex I, *ChemPhysChem* 12, 217-224.
186. Dong, A., Huang, P., and Caughey, W. S. (1990) Protein secondary structures in water from second-derivative amide i infrared spectra, *Biochemistry* 29, 3303-3308.
187. Lee, D. C., Haris, P. I., Chapman, D., and Mitchell, R. C. (1990) Determination of protein secondary structure using factor analysis of infrared spectra, *Biochemistry* 29, 9185-9193.
188. Whitmore, L., and Wallace, B. A. (2008) Protein secondary structure analyses from circular dichroism spectroscopy: Methods and reference databases, *Biopolymers* 89, 392-400.
189. Provencher, S. W., and Glöckner, J. (1981) Estimation of globular protein secondary structure from circular dichroism, *Biochemistry* 20, 33-37.
190. Sreerama, N., and Woody, R. W. (2000) Estimation of protein secondary structure from circular dichroism spectra: Comparison of CONTIN, SELCON, and CDSSTR methods with an expanded reference set, *Analytical Biochemistry* 287, 252-260.
191. Sreerama, N., and Woody, R. W. (2004) On the analysis of membrane protein circular dichroism spectra, *Protein Science* 13, 100-112.
192. Whitmore, L., and Wallace, B. A. (2004) DICHROWEB, an online server for protein secondary structure analyses from circular dichroism spectroscopic data, *Nucleic Acids Research* 32.
193. Lobley, A., Whitmore, L., and Wallace, B. A. (2002) DICHROWEB: An interactive website for the analysis of protein secondary structure from circular dichroism spectra, *Bioinformatics* 18, 211-212.
194. Hellwig, P., Soulimane, T., Buse, G., and Mantele, W. (1999) Electrochemical, FTIR, and UV/VIS spectroscopic properties of the ba3 oxidase from *Thermus thermophilus*, *Biochemistry* 38, 9648-9658.
195. Wyman, J. (1968) Regulation in macromolecules as illustrated by haemoglobin, *Quarterly Reviews of Biophysics* 1, 35-80.
196. Krab, K., and Wikström, M. (1979) On the stoichiometry and thermodynamics of proton-pumping cytochrome c oxidase in mitochondria, *BBA - Bioenergetics* 548, 1-15.
197. Ludwig, M. L., Pattridge, K. A., Metzger, A. L., Dixon, M. M., Eren, M., Feng, Y., and Swenson, R. P. (1997) Control of oxidation-reduction potentials in flavodoxin from *Clostridium beijerinckii*: The role of conformation changes, *Biochemistry* 36, 1259-1280.
198. Bogachev, A. V., Bertsova, Y. V., Bloch, D. A., and Verkhovsky, M. I. (2006) Thermodynamic properties of the redox centers of Na<sup>+</sup>-translocating NADH:quinone oxidoreductase, *Biochemistry* 45, 3421-3428.

199. Bogachev, A. V., Kulik, L. V., Bloch, D. A., Bertsova, Y. V., Fadeeva, M. S., and Verkhovsky, M. I. (2009) Redox properties of the prosthetic groups of Na<sup>+</sup>-translocating NADH:quinone oxidoreductase. 1. Electron paramagnetic resonance study of the enzyme, *Biochemistry* 48, 6291-6298.
200. Visser, A. J., Vervoort, J., O'Kane, D. J., Lee, J., and Carreira, L. A. (1983) Raman spectra of flavin bound in flavodoxins and in other flavoproteins. Evidence for structural variations in the flavin-binding region, *European Journal of Biochemistry* 131, 639-645.
201. Kitagawa, T., Nishina, Y., Kyogoku, Y., Yamano, T., Ohishi, N., Takai-Suzuki, A., and Yagi, K. (1979) Resonance Raman spectra of carbon-13 and nitrogen-15 labeled riboflavin bound to egg-white flavoprotein, *Biochemistry* 18, 1804-1808.
202. Lively, C. R., and McFarland, J. T. (1990) Assignment and the effect of hydrogen bonding on the vibrational normal modes of flavins and flavoproteins, *Journal of Physical Chemistry* 94, 3980-3994.
203. Wolpert, M., and Hellwig, P. (2006) Infrared spectra and molar absorption coefficients of the 20 alpha amino acids in aqueous solutions in the spectral range from 1800 to 500 cm<sup>-1</sup>, *Spectrochimica Acta - Part A: Molecular and Biomolecular Spectroscopy* 64, 987-1001.
204. Barth, A. (2000) The infrared absorption of amino acid side chains, *Progress in Biophysics and Molecular Biology* 74, 141-173.
205. KONG, J., and YU, S. (2007) Fourier Transform Infrared Spectroscopic Analysis of Protein Secondary Structures, *Acta Biochimica et Biophysica Sinica* 39, 549-559.
206. Nara, M., Torii, H., and Tasumi, M. (1996) Correlation between the vibrational frequencies of the carboxylate group and the types of its coordination to a metal ion: An ab initio molecular orbital study, *Journal of Physical Chemistry* 100, 19812-19817.
207. Nara, M., Tasumi, M., Tanokura, M., Hiraoki, T., Yazawa, M., and Tsutsumi, A. (1994) Infrared studies of interaction between metal ions and Ca<sup>2+</sup>-binding proteins. Marker bands for identifying the types of coordination of the side-chain COO<sup>-</sup> groups to metal ions in pike parvalbumin (pI = 4.10), *FEBS Letters* 349, 84-88.
208. Deacon, G. B., Huber, F., and Phillips, R. J. (1985) Diagnosis of the nature of carboxylate coordination from the direction of shifts of carbon-oxygen stretching frequencies, *Inorganica Chimica Acta* 104, 41-45.
209. Englander, S. W., Mayne, L., Bai, Y., and Sosnick, T. R. (1997) Hydrogen exchange: The modern legacy of Linderstrom-Lang, *Protein Science* 6, 1101-1109.
210. White, S. H., and Wimley, W. C. (1999) Membrane protein folding and stability: Physical principles, pp 319-365.
211. Popot, J. L., and Engelman, D. M. (2000) Helical membrane protein folding, stability, and evolution, pp 881-922.
212. Heimbürg, T., and Marsh, D. (1993) Investigation of secondary and tertiary structural changes of cytochrome c in complexes with anionic lipids using amide hydrogen exchange measurements: An FTIR study, *Biophysical Journal* 65, 2408-2417.
213. Pelton, J. T., and McLean, L. R. (2000) Spectroscopic methods for analysis of protein secondary structure, *Analytical Biochemistry* 277, 167-176.
214. Van Stokkum, I. H. M., Spoelder, H. J. W., Bloemendal, M., Van Grondelle, R., and Groen, F. C. A. (1990) Estimation of protein secondary structure and error analysis from circular dichroism spectra, *Analytical Biochemistry* 191, 110-118.
215. Venyaminov, S. Y., and Kalnin, N. N. (1990) Quantitative IR spectrophotometry of peptide compounds in water (H<sub>2</sub>O) solutions. II. Amide absorption bands of polypeptides and fibrous proteins in  $\alpha$ -,  $\beta$ -, and random coil conformations, *Biopolymers* 30, 1259-1271.
216. Dimroth, P. (1997) Primary sodium ion translocating enzymes, *Biochimica et Biophysica Acta - Bioenergetics* 1318, 11-51.
217. Verkhovsky, M. I., and Bogachev, A. V. (2010) Sodium-translocating NADH:quinone oxidoreductase as a redox-driven ion pump, *Biochimica et Biophysica Acta - Bioenergetics* 1797, 738-746.

218. Juárez, O., and Barquera, B. (2012) Insights into the mechanism of electron transfer and sodium translocation of the Na<sup>+</sup>-pumping NADH:quinone oxidoreductase, *Biochimica et Biophysica Acta - Bioenergetics*.
219. Venyaminov, S. Y., and Kalnin, N. N. (1990) Quantitative IR spectrophotometry of peptide compounds in water (H<sub>2</sub>O) solutions. I. Spectral parameters of amino acid residue absorption bands, *Biopolymers* 30, 1243-1257.
220. Chirgadze Yu, N., Fedorov, O. V., and Trushina, N. P. (1975) Estimation of amino acid residue side chain absorption in the infrared spectra of protein solutions in heavy water, *Biopolymers* 14, 679-694.
221. Celej, M. S., Montich, G. G., and Fidelio, G. D. (2004) Conformational flexibility of avidin: The influence of biotin binding, *Biochemical and Biophysical Research Communications* 325, 922-927.
222. Ishikita, H. (2008) Redox potential difference between *Desulfovibrio vulgaris* and *Clostridium beijerinckii* flavodoxins, *Biochemistry* 47, 4394-4402.
223. Hellwig, P., Barquera, B., and Gennis, R. B. (2001) Direct evidence for the protonation of aspartate-75, proposed to be at a quinol binding site, upon reduction of cytochrome bo3 from *Escherichia coli*, *Biochemistry* 40, 1077-1082.
224. Breton, J., Thibodeau, D. L., Berthomieu, C., Mantele, W., Vermeglio, A., and Navedryk, E. (1991) Probing the primary quinone environment in photosynthetic bacterial reaction centers by light-induced FTIR difference spectroscopy, *FEBS Letters* 278, 257-260.
225. Navedryk, E., Bagley, K. A., Thibodeau, D. L., Bauscher, M., Mantele, W., and Breton, J. (1990) A protein conformational change associated with the photoreduction of the primary and secondary quinones in the bacterial reaction center, *FEBS Letters* 266, 59-62.
226. Bauscher, M., and Mäntele, W. (1992) Electrochemical and infrared-spectroscopic characterization of redox reactions of p-quinones, *Journal of Physical Chemistry* 96, 11101-11108.
227. Takayama, Y., Castañeda, C. A., Chimenti, M., García-Moreno, B., and Iwahara, J. (2008) Direct evidence for deprotonation of a lysine side chain buried in the hydrophobic core of a protein, *Journal of the American Chemical Society* 130, 6714-6715.
228. Nakayama, Y., Hayashi, M., Yoshikawa, K., Mochida, K., and Unemoto, T. (1999) Inhibitor studies of a new antibiotic, korormicin, 2-n-heptyl-4- hydroxyquinoline N-oxide and Ag<sup>+</sup> toward the Na<sup>+</sup>-translocating NADH-quinone reductase from the marine *Vibrio alginolyticus*, *Biological and Pharmaceutical Bulletin* 22, 1064-1067.
229. Juárez, O., Neehaul, Y., Turk, E., Chahubon, N., DeMicco, J. M., Hellwig, P., and Barquera, B. (2012) The role of glycine residues 140 and 141 of subunit B in the functional ubiquinone binding site of the Na<sup>+</sup> pumping NADH:Quinone oxidoreductase from *Vibrio cholerae*, *Journal of Biological Chemistry*.
230. Derewenda, Z. S., Lee, L., and Derewenda, U. (1995) The occurrence of C - H... O hydrogen bonds in proteins, *Journal of Molecular Biology* 252, 248-262.
231. Han, M., Lin, S. W., Minkova, M., Smith, S. O., and Sakmar, T. P. (1996) Functional Interaction of Transmembrane Helices 3 and 6 in Rhodopsin, *Journal of Biological Chemistry* 271, 32337-32342.
232. Margalit, R., and Schejter, A. (1973) Cytochrome c: a thermodynamic study of the relationships among oxidation state, ion-binding and structural parameters. 1. The effects of temperature, pH and electrostatic media on the standard redox potential of cytochrome c, *European Journal of Biochemistry* 32, 492-499.
233. Zheng, Z., and Gunner, M. R. (2009) Analysis of the electrochemistry of hemes with Ems spanning 800 mV, *Proteins: Structure, Function and Bioinformatics* 75, 719-734.
234. Yang, K., Zhang, J., Vakkasoglu, A. S., Hielscher, R., Osborne, J. P., Hemp, J., Miyoshi, H., Hellwig, P., and Gennis, R. B. (2007) Glutamate 107 in subunit I of the cytochrome bd quinol oxidase from *Escherichia coli* is protonated and near the heme d/heme b<sub>595</sub> binuclear center, *Biochemistry* 46, 3270-3278.

235. Behr, J., Michel, H., Mantele, W., and Hellwig, P. (2000) Functional properties of the heme propionates in cytochrome *c* oxidase from *Paracoccus denitrificans*. Evidence from FTIR difference spectroscopy and site-directed mutagenesis, *Biochemistry* 39, 1356-1363.
236. Behr, J., Hellwig, P., Mantele, W., and Michel, H. (1998) Redox dependent changes at the heme propionates in cytochrome *c* oxidase from *Paracoccus denitrificans*: Direct evidence from FTIR difference spectroscopy in combination with heme propionate <sup>13</sup>C labeling, *Biochemistry* 37, 7400-7406.
237. Kannt, A., Pfitzner, U., Ruitenber, M., Hellwig, P., Ludwig, B., Mantele, W., Fendler, K., and Michel, H. (1999) Mutation of Arg-54 strongly influences heme composition and rate and directionality of electron transfer in *Paracoccus denitrificans* cytochrome *c* oxidase, *J Biol Chem* 274, 37974-37981.
238. Hellwig, P., Pfitzner, U., Behr, J., Rost, B., Pesavento, R. P., Donk, W. V., Gennis, R. B., Michel, H., Ludwig, B., and Mantele, W. (2002) Vibrational modes of tyrosines in cytochrome *c* oxidase from *Paracoccus denitrificans*: FTIR and electrochemical studies on Tyr-D<sup>4</sup>-labeled and on Tyr280His and Tyr35Phe mutant enzymes, *Biochemistry* 41, 9116-9125.
239. Wolpert, M., Maneg, O., Ludwig, B., and Hellwig, P. (2004) Characterization of the Cu<sub>A</sub> center in the cytochrome *c* oxidase from *Thermus thermophilus* for the Spectral Range 1800–500 cm<sup>-1</sup> with a combined electrochemical and Fourier transform Infrared spectroscopic setup, *Biopolymers Vol. 74*, 73-76.
240. El Khoury, Y., and Hellwig, P. (2009) Infrared spectroscopic characterization of copper-polyhistidine from 1800 to 50 cm<sup>-1</sup>: Model systems for copper coordination, *Journal of Biological Inorganic Chemistry* 14, 23-34.
241. Giudici-Orticoni, M. T., Guerlesquin, F., Bruschi, M., and Nitschke, W. (1999) Interaction-induced redox switch in the electron transfer complex rusticyanin-cytochrome *c*<sub>4</sub>, *Journal of Biological Chemistry* 274, 30365-30369.
242. Pelletier, H., and Kraut, J. (1992) Crystal structure of a complex between electron transfer partners, cytochrome *c* peroxidase and cytochrome *c*, *Science* 258, 1748-1755.
243. Lange, C., and Hunte, C. (2002) Crystal structure of the yeast cytochrome *bc*<sub>1</sub> complex with its bound substrate cytochrome *c*, *Proceedings of the National Academy of Sciences of the United States of America* 99, 2800-2805.
244. Kimelberg, H. K., and Lee, C. P. (1970) Interactions of cytochrome *c* with phospholipid membranes - Reactivity of cytochrome *c* bound to phospholipid liquid crystals, *The Journal of Membrane Biology* 2, 252-262.
245. Bernad, S., Leygue, N., Korri-Youssoufi, H., and Lecomte, S. (2007) Kinetics of the electron transfer reaction of cytochrome *c*<sub>552</sub> adsorbed on biomimetic electrode studied by time-resolved surface-enhanced resonance Raman spectroscopy and electrochemistry, *European Biophysics Journal* 36, 1039-1048.
246. Wikstrom, M. K. F. (1977) Proton pump coupled to cytochrome *c* oxidase in mitochondria, *Nature* 266, 271-273.
247. Wikström, M. (1988) How Does Cytochrome Oxidase Pump Protons?, *Annals of the New York Academy of Sciences* 550, 199-206.
248. Ritter, M., Anderka, O., Ludwig, B., Mantele, W., and Hellwig, P. (2003) Electrochemical and FTIR spectroscopic characterization of the cytochrome *bc*<sub>1</sub> complex from *Paracoccus denitrificans*: evidence for protonation reactions coupled to quinone binding, *Biochemistry* 42, 12391-12399.
249. Rajendran, C., Ermler, U., Ludwig, B., and Michel, H. (2010) Structure at 1.5 Å resolution of cytochrome *c*<sub>552</sub> with its flexible linker segment, a membrane-anchored protein from *Paracoccus denitrificans*, *Acta Crystallographica Section D: Biological Crystallography* 66, 850-854.
250. El Khoury, Y. (2010) Mid and far infrared spectroelectrochemical studies on the metal-ligand interactions in respiratory chain enzymes, *phd thesis, Université de Strasbourg*.

251. Hellwig, P., Grzybek, S., Behr, J., Ludwig, B., Michel, H., and Mäntele, W. (1999) Electrochemical and ultraviolet/visible/infrared spectroscopic analysis of heme *a* and *a*<sub>3</sub> redox reactions in the cytochrome *c* oxidase from *Paracoccus denitrificans*: Separation of heme *a* and *a*<sub>3</sub> contributions and assignment of vibrational modes, *Biochemistry* 38, 1685-1694.
252. Lunin, V. Y., Lunina, N. L., Casutt, M. S., Knoops, K., Schaffitzel, C., Steuber, J., Fritz, G., and Baumstark, M. W. (2012) Low-resolution structure determination of Na<sup>+</sup>-translocating NADH:ubiquinone oxidoreductase from *Vibrio cholerae* by ab initio phasing and electron microscopy, *Acta Crystallographica Section D: Biological Crystallography* 68, 724-731.

**Figure 7.1:** The first derivative of  $\Delta$ absorbance for a step of 5 nm from 300 to 600 nm upon redox titration, of samples of the  $\text{Na}^+$ -NQR in the presence of  $\text{Li}^+$ ,  $\text{Na}^+$ ,  $\text{K}^+$ ,  $\text{Rb}^+$  and  $\text{NH}_4^+$  ions.

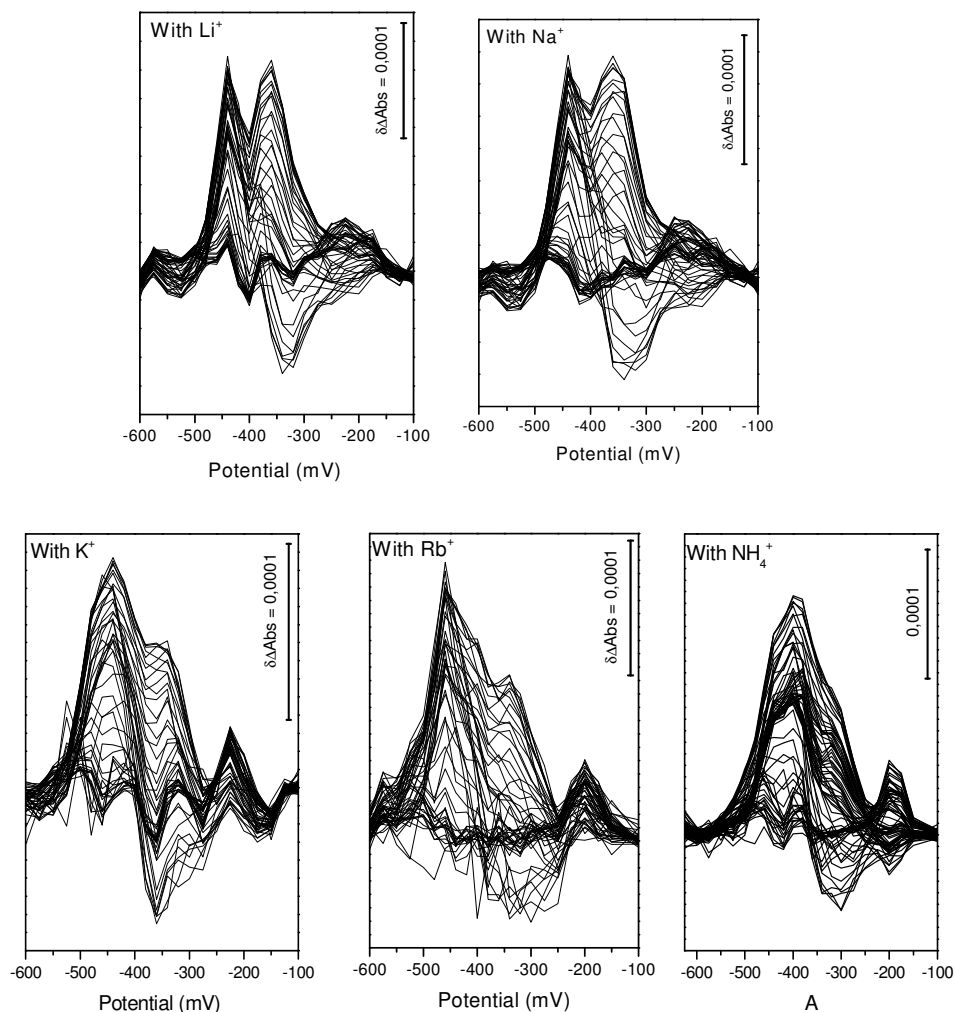


**Table 7.1:** Assignments of signals of signals observed in the redox induced FTIR difference spectra of FAD, FMN and riboflavin for the potential range between -620 to +200 mV. The positions are given in  $\text{cm}^{-1}$ .

FAD	FMN	Riboflavin	Assignment
1711 (+)	1713 (+)	1715 (+)	$\nu(\text{C}=\text{O})$
1673 (+)	1663 (+)	1660 (+)	$\nu(\text{C}=\text{O})$
1632 (-)	1630 (-)	1630 (-)	$\nu(\text{C}=\text{O})$
1599 (-)	1599 (-)	1595 (-)	$\nu(\text{C}=\text{N})$
1567 (-)	1568 (-)	1566 (-)	$\nu(\text{C}=\text{N})$
1548 (+)	1548 (+)	1548 (+)	$\nu(\text{C}=\text{C})$ of neutral flavins
1517 (-)	1516 (-)	1515 (-)	$\delta(\text{C}-\text{H})^{\text{in plane}}/\delta(\text{N}-\text{H})^{\text{in plane}}$
1410 (-)	1408 (-)	1407 (-)	isoalloxazine ring reorganization

**Table 7.2: Tentative attribution of signals observed in the redox induced FTIR difference spectra of the Na<sup>+</sup>-NQR in H<sub>2</sub>O buffer in the presence of Na<sup>+</sup> ions for the potential range between -620 to +200 mV.**

Position (cm <sup>-1</sup> )	Tentative attribution
1714	(+) $\nu(\text{C=O})$ from protonated side chains of Asp/Glu, $\nu(\text{C=O})$ of flavins
1705	(+) $\nu(\text{C=O})$ from protonated side chains of Asp/Glu, $\nu(\text{C=O})$ of flavins
1687	(+) Amide I; $\beta$ -turn , $\nu(\text{C=O})$ of flavins
1672	(+) Amide I; $\beta$ -turn , $\nu(\text{C=O})$ of flavins, $\nu(\text{C=O})$ quinone, $\nu(\text{C=O})$ Glutamine
1659	(+) Amide I; $\alpha$ -helix , $\nu(\text{C=O})$ of flavins
1645	(-) Amide I; random structures , $\nu(\text{C=N})$ of flavins
1633	(-) Amide I; $\beta$ -sheet , $\nu(\text{C=N})$ of flavins
1612	(-) Amide I; $\beta$ -sheet , $\nu(\text{C=N})$ of flavins
1593	(-) $\nu_{\text{as}}(\text{COO}^-)$ from deprotonated side chains of Asp/Glu, $\nu(\text{C=N})$ of flavins
1563	(-) Amide II, $\nu_{\text{as}}(\text{COO}^-)$ from deprotonated side chains of Asp/Glu, $\nu(\text{C=N})$ of flavins
1540	(+) Amide II, $\nu_{\text{as}}(\text{COO}^-)$ from deprotonated side chains of Asp/Glu, $\nu(\text{C=C})$ of neutral flavins
1517	(-) $\delta(\text{C-H})^{\text{in plane}}/\delta(\text{N-H})^{\text{in plane}}$ of flavins
1478	(-) $\delta_{\text{as}}(\text{C-H}_3)$
1463	(+) $\delta_{\text{as}}(\text{C-H}_3)$
1440	(+) $\delta(\text{C-H}_2)$
1404	(-) $\nu_{\text{s}}(\text{COO}^-)$ from deprotonated side chains of Asp/Glu , isoalloxazine ring reorganization
1372	(+) $\nu_{\text{s}}(\text{COO}^-)$ from deprotonated side chains of Asp/Glu
1350	(+) Amide III
1338	(-) Amide III, $\delta(\text{C-H})$ , ring reorganization of flavins
1322	(-) Amide III, $\delta(\text{C-H})$ , ring reorganization of flavins
1303	(-) Amide III, $\delta(\text{C-H})$ , ring reorganization of flavins
1288	(+) Amide III, ring reorganization of flavins
1270	(-) Amide III, ring reorganization of flavins
1259	(-) Amide III, ring reorganization of flavins
1250	(+) Amide III, ring reorganization of flavins, C-OCH <sub>3</sub> methoxy groups of quinone
1222	(+) Amide III, ring reorganization of flavins
1180	(+) ring reorganization of flavins
1085	(-) Phosphate buffer
1067	(-) Phosphate buffer



**Table 7.3: Tentative attribution of signals observed in the redox induced FTIR difference spectra of the Na<sup>+</sup>-NQR in D<sub>2</sub>O buffer in the presence of Na<sup>+</sup> ions for the potential range between -620 to +200 mV.**

Position (cm <sup>-1</sup> )	Tentative attribution
1704 (+)	$\nu(\text{C=O})$ from protonated side chains of Asp/Glu, $\nu(\text{C=O})$ of flavins
1687 (+)	Amide I, $\nu(\text{C=O})$ of flavins
1664 (+)	Amide I, $\nu(\text{C=O})$ of flavins
1637 (+)	Amide I, $\nu(\text{C=O})$ of flavins
1619 (+)	Amide I
1589 (-)	$\nu(\text{C=N})$ of flavins
1561 (-)	Amide II, $\nu(\text{C=N})$ of flavins Amide II, $\nu_{\text{as}}(\text{COO}^-)$ from deprotonated side chains of Asp/Glu, $\nu(\text{C=C})$ of neutral flavins
1539 (+)	
1512 (-)	$\delta(\text{C-H})^{\text{in plane}}/\delta(\text{N-H})^{\text{in plane}}$ of flavins
1463 (+)	$\delta_{\text{as}}(\text{C-H}_3)$
1445 (+)	$\delta_{\text{as}}(\text{C-H}_3)$
1402 (-)	$\nu_{\text{s}}(\text{COO}^-)$ from deprotonated side chains of Asp/Glu , isoalloxazine ring reorganization
1372 (+)	$\nu_{\text{s}}(\text{COO}^-)$ from deprotonated side chains of Asp/Glu
1351 (+)	Amide III, $\delta(\text{C-H})$ , ring reorganization of flavins
1335 (-)	Amide III, $\delta(\text{C-H})$ , ring reorganization of flavins
1297 (+)	Amide III, $\delta(\text{C-H})$ , ring reorganization of flavins
1255 (-)	Amide III, ring reorganization of flavins
1226 (+)	Amide III, ring reorganization of flavins
1213 (-)	Amide III, ring reorganization of flavins
1179 (+)	ring reorganization of flavins
1100 (-)	Phosphate buffer
1071 (-)	Phosphate buffer

**Table 7.4: Tentative attribution of signals observed in the double difference spectra of the  $\text{Na}^+$ -NQR with the different salts in  $\text{H}_2\text{O}$  buffer for the potential range between -620 to +200 mV.**

Position ( $\text{cm}^{-1}$ )		Tentative attribution
<b><math>\text{Na}^+</math>-<math>\text{Li}^+</math> double difference spectrum</b>		
1675	(+)	Amide I; $\beta$ -turn
1663	(-)	Amide I; $3_{10}$ -helix
1654	(+)	Amide I; $\alpha$ -helix and random structures
1634	(-)	Amide I; $\beta$ -sheet
1592	(+)	$\nu_{\text{as}}(\text{COO}^-)$ from deprotonated side chains of Asp/Glu
1549	(+)	Amide II, $\nu_{\text{as}}(\text{COO}^-)$ from deprotonated side chains of Asp/Glu
1415	(+)	$\nu_{\text{s}}(\text{COO}^-)$ from deprotonated side chains of Asp/Glu
1376	(-)	$\nu_{\text{s}}(\text{COO}^-)$ from deprotonated side chains of Asp/Glu
<b><math>\text{Na}^+</math>-<math>\text{K}^+</math> double difference spectrum</b>		
1665	(+)	Amide I; $\beta$ -turn
1643	(-)	Amide I; $\beta$ -sheet
1613	(+)	Amide I; $\beta$ -sheet
1580	(-)	$\nu_{\text{as}}(\text{COO}^-)$ from deprotonated side chains of Asp/Glu
1558	(-)	Amide II, $\nu_{\text{as}}(\text{COO}^-)$ from deprotonated side chains of Asp/Glu
1538	(+)	Amide II
1408	(-)	$\nu_{\text{s}}(\text{COO}^-\text{Na}^+)$ from deprotonated side chains of Asp/Glu
1367	(+)	$\nu_{\text{s}}(\text{COO}^-\text{Na}^+)$ from deprotonated side chains of Asp/Glu
<b><math>\text{Li}^+</math>-<math>\text{K}^+</math> double difference spectrum</b>		
1665	(+)	Amide I; $\beta$ -turn
1649	(-)	Amide I; random structures
1625	(+)	Amide I; $\beta$ -sheet
1580	(-)	$\nu_{\text{as}}(\text{COO}^-)$ from deprotonated side chains of Asp/Glu
1558	(-)	Amide II, $\nu_{\text{as}}(\text{COO}^-)$ from deprotonated side chains of Asp/Glu
1525	(+)	Amide II
1417	(-)	$\nu_{\text{s}}(\text{COO}^-\text{Li}^+)$ from deprotonated side chains of Asp/Glu
1376	(+)	$\nu_{\text{s}}(\text{COO}^-\text{Li}^+)$ from deprotonated side chains of Asp/Glu
<b><math>\text{Na}^+</math>-<math>\text{Rb}^+</math> double difference spectrum</b>		
1681	(-)	Amide I; $\beta$ -turn
1665	(-)	Amide I; $\beta$ -turn
1641	(+)	Amide I; $\beta$ -sheet
1610	(+)	Amide I; $\beta$ -sheet
1578	(-)	Amide II, $\nu_{\text{as}}(\text{COO}^-)$ from deprotonated side chains of Asp/Glu
1542	(-)	Amide II, $\nu_{\text{as}}(\text{COO}^-)$ from deprotonated side chains of Asp/Glu
1403	(-)	$\nu_{\text{s}}(\text{COO}^-\text{Rb}^+)$ from deprotonated side chains of Asp/Glu

<b>K<sup>+</sup>-Rb<sup>+</sup> double difference spectrum</b>		
1681	(-)	Amide I; $\beta$ -turn
1665	(-)	Amide I; $\beta$ -turn
1641	(+)	Amide I; $\beta$ -sheet
1610	(+)	Amide I; $\beta$ -sheet
1578	(-)	Amide II, $\nu_{\text{as}}(\text{COO}^-)$ from deprotonated side chains of Asp/Glu
1542	(-)	Amide II, $\nu_{\text{as}}(\text{COO}^-)$ from deprotonated side chains of Asp/Glu
1403	(-)	$\nu_{\text{s}}(\text{COO}^-\text{Rb}^+)$ from deprotonated side chains of Asp/Glu

---

**Table 7.5: Tentative attribution of signals observed in the double difference spectra of the Na<sup>+</sup>-NQR with the different salts in D<sub>2</sub>O buffer for the potential range between -620 to +200 mV.**

Position (cm <sup>-1</sup> )	Tentative attribution
<b>Na<sup>+</sup>-Li<sup>+</sup> double difference spectrum</b>	
1662 (+)	Amide I
1650 (-)	Amide I
1626 (-)	Amide I
1592 (+)	$\nu_{as}(\text{COO}^-)$ from deprotonated side chains of Asp/Glu
1416 (+)	$\nu_s(\text{COO}^-)$ from deprotonated side chains of Asp/Glu
1383 (-)	$\nu_s(\text{COO}^-)$ from deprotonated side chains of Asp/Glu
<b>Na<sup>+</sup>-K<sup>+</sup> double difference spectrum</b>	
1664 (+)	Amide I
1635 (+)	Amide I
1626 (+)	Amide I
1590 (-)	$\nu_{as}(\text{COO}^-)$ from deprotonated side chains of Asp/Glu
1538 (+)	Amide II, $\nu_{as}(\text{COO}^-)$ from deprotonated side chains of Asp/Glu
1530 (+)	Amide II, $\nu_{as}(\text{COO}^-)$ from deprotonated side chains of Asp/Glu
1403 (-)	$\nu_s(\text{COO}^-\text{Na}^+)$ from deprotonated side chains of Asp/Glu
1372 (+)	$\nu_s(\text{COO}^-\text{Na}^+)$ from deprotonated side chains of Asp/Glu
<b>Li<sup>+</sup>-K<sup>+</sup> double difference spectrum</b>	
1664 (+)	Amide I
1626 (+)	Amide I
1590 (+)	Amide I
1530 (-)	Amide II, $\nu_{as}(\text{COO}^-)$ from deprotonated side chains of Asp/Glu
1414 (-)	$\nu_s(\text{COO}^-\text{Li}^+)$ from deprotonated side chains of Asp/Glu
1380 (+)	$\nu_s(\text{COO}^-\text{Li}^+)$ from deprotonated side chains of Asp/Glu
<b>Na<sup>+</sup>-Rb<sup>+</sup> double difference spectrum</b>	
1707 (-)	$\nu(\text{C=O})$ from protonated side chains of Asp/Glu
1683 (-)	Amide I
1664 (+)	Amide I
1624 (-)	Amide I
1590 (-)	$\nu_{as}(\text{COO}^-)$ from deprotonated side chains of Asp/Glu
1537 (+)	Amide II, $\nu_{as}(\text{COO}^-)$ from deprotonated side chains of Asp/Glu
1414 (-)	$\nu_s(\text{COO}^-\text{Na}^+)$ from deprotonated side chains of Asp/Glu
1383 (+)	$\nu_s(\text{COO}^-\text{Na}^+)$ from deprotonated side chains of Asp/Glu
<b>K<sup>+</sup>-Rb<sup>+</sup> double difference spectrum</b>	
1707 (-)	$\nu(\text{C=O})$ from protonated side chains of Asp/Glu
1683 (-)	Amide I

## Appendix

---

1664	(+)	Amide I
1624	(-)	Amide I
1590	(-)	$\nu_{\text{as}}(\text{COO}^-)$ from deprotonated side chains of Asp/Glu
1537	(+)	Amide II, $\nu_{\text{as}}(\text{COO}^-)$ from deprotonated side chains of Asp/Glu
1414	(-)	$\nu_{\text{s}}(\text{COO}^-)$ from deprotonated side chains of Asp/Glu
1383	(+)	$\nu_{\text{s}}(\text{COO}^-)$ from deprotonated side chains of Asp/Glu

---

**Table 7.6: Tentative attribution of signals observed in the redox induced FTIR difference spectra of the NqrB D397E mutant enzyme in H<sub>2</sub>O buffer in the presence of Na<sup>+</sup> ions for the potential range between -620 to +200 mV**

Position (cm <sup>-1</sup> )		Tentative attribution
1715	(+)	$\nu(\text{C=O})$ from protonated side chains of Asp/Glu, $\nu(\text{C=O})$ of flavins
1705	(+)	$\nu(\text{C=O})$ from protonated side chains of Asp/Glu, $\nu(\text{C=O})$ of flavins
1687	(+)	Amide I; $\beta$ -turn , $\nu(\text{C=O})$ of flavins
1675	(+)	Amide I; $\beta$ -turn , $\nu(\text{C=O})$ of flavins, $\nu(\text{C=O})$ quinone, $\nu(\text{C=O})$ Glutamine
1659	(+)	Amide I; $\alpha$ -helix , $\nu(\text{C=O})$ of flavins
1647	(-)	Amide I; random structures , $\nu(\text{C=N})$ of flavins
1631	(-)	Amide I; $\beta$ -sheet , $\nu(\text{C=N})$ of flavins
1595	(-)	$\nu_{\text{as}}(\text{COO}^-)$ from deprotonated side chains of Asp/Glu, $\nu(\text{C=N})$ of flavins
1566	(-)	Amide II, $\nu_{\text{as}}(\text{COO}^-)$ from deprotonated side chains of Asp/Glu, $\nu(\text{C=N})$ of flavins Amide II, $\nu_{\text{as}}(\text{COO}^-)$ from deprotonated side chains of Asp/Glu, $\nu(\text{C=C})$ of neutral
1541	(+)	flavins
1517	(-)	$\delta(\text{C-H})^{\text{in plane}}/\delta(\text{N-H})^{\text{in plane}}$ of flavins
1405	(-)	$\nu_{\text{s}}(\text{COO}^-)$ from deprotonated side chains of Asp/Glu , isoalloxazine ring reorganization
1351	(+)	$\nu_{\text{s}}(\text{COO}^-)$ from deprotonated side chains of Asp/Glu
1322	(-)	Amide III, $\delta(\text{C-H})$ , ring reorganization of flavins
1288	(+)	Amide III, $\delta(\text{C-H})$ , ring reorganization of flavins
1250	(+)	Amide III, ring reorganization of flavins, C-OCH <sub>3</sub> methoxy groups of quinone
1222	(+)	Amide III, ring reorganization of flavins
1196	(-)	ring reorganization of flavins
1180	(+)	ring reorganization of flavins
1085	(-)	Phosphate buffer
1067	(-)	Phosphate buffer

**Table 7.7: Tentative attribution of signals observed in the double difference spectra of the NqrB D397E mutant enzyme with the different salts for the potential range between -620 to +200 mV.**

Position (cm <sup>-1</sup> )		Tentative attribution
<b>Na<sup>+</sup>-Li<sup>+</sup> double difference spectrum</b>		
1713	(-)	$\nu(\text{C=O})$ from protonated side chains of Asp/Glu
1705	(+)	$\nu(\text{C=O})$ from protonated side chains of Asp/Glu
1675	(+)	Amide I; $\beta$ -turn
1660	(+)	Amide I; $\alpha$ -helix
1643	(-)	Amide I; random structures
1613	(-)	Amide I; $\beta$ -sheet
1547	(+)	Amide II, $\nu_{\text{as}}(\text{COO}^-)$ from deprotonated side chains of Asp/Glu
1536	(-)	Amide II, $\nu_{\text{as}}(\text{COO}^-)$ from deprotonated side chains of Asp/Glu
1518	(+)	$\nu_{\text{as}}(\text{COO}^-)$ from deprotonated side chains of Asp/Glu
1419	(-)	$\nu_{\text{s}}(\text{COO}^-)$ from deprotonated side chains of Asp/Glu
1400	(+)	$\nu_{\text{s}}(\text{COO}^-)$ from deprotonated side chains of Asp/Glu
<b>Na<sup>+</sup>-K<sup>+</sup> double difference spectrum</b>		
1673	(+)	Amide I; $\beta$ -turn
1635	(-)	Amide I; $\beta$ -sheet
1586	(+)	Amide II, $\nu_{\text{as}}(\text{COO}^-)$ from deprotonated side chains of Asp/Glu
1408	(+)	$\nu_{\text{s}}(\text{COO}^-\text{Na}^+)$ from deprotonated side chains of Asp/Glu
1372	(-)	$\nu_{\text{s}}(\text{COO}^-\text{Na}^+)$ from deprotonated side chains of Asp/Glu
<b>Li<sup>+</sup>-K<sup>+</sup> double difference spectrum</b>		
1713	(+)	$\nu(\text{C=O})$ from protonated side chains of Asp/Glu
1676	(-)	Amide I; $\beta$ -turn
1635	(-)	Amide I; $\beta$ -sheet
1586	(+)	Amide II, $\nu_{\text{as}}(\text{COO}^-)$ from deprotonated side chains of Asp/Glu
1540	(+)	Amide II, $\nu_{\text{as}}(\text{COO}^-)$ from deprotonated side chains of Asp/Glu
1519	(-)	$\nu_{\text{as}}(\text{COO}^-)$ from deprotonated side chains of Asp/Glu
1414	(+)	$\nu_{\text{s}}(\text{COO}^-\text{Li}^+)$ from deprotonated side chains of Asp/Glu
1387	(-)	$\nu_{\text{s}}(\text{COO}^-\text{Li}^+)$ from deprotonated side chains of Asp/Glu
<b>Na<sup>+</sup>-Rb<sup>+</sup> double difference spectrum</b>		
1687	(+)	Amide I; $\beta$ -turn
1671	(+)	Amide I; $\beta$ -turn
1657	(+)	Amide I; $\alpha$ -helix
1641	(+)	Amide I; random structures
1608	(+)	Amide I; $\beta$ -sheet
1595	(+)	$\nu_{\text{as}}(\text{COO}^-)$ from deprotonated side chains of Asp/Glu
1538	(+)	Amide II, $\nu_{\text{as}}(\text{COO}^-)$ from deprotonated side chains of Asp/Glu
1403	(-)	$\nu_{\text{s}}(\text{COO}^-\text{Rb}^+)$ from deprotonated side chains of Asp/Glu

1378    (-)     $\nu_s(\text{COO}^-)$  from deprotonated side chains of Asp/Glu

**K<sup>+</sup>-Rb<sup>+</sup> double difference spectrum**

1641    (+)    Amide I; random structures

1608    (+)    Amide I;  $\beta$ -sheet

1538    (+)    Amide II,  $\nu_{\text{as}}(\text{COO}^-)$  from deprotonated side chains of Asp/Glu

1403    (-)     $\nu_s(\text{COO}^-\text{Rb}^+)$  from deprotonated side chains of Asp/Glu

---



**Table 7.8: Tentative attribution of signals observed in the D397E-wild type double difference spectra for the potential range between -620 to +200 mV in the presence of the different ions.**

Position (cm <sup>-1</sup> )	Tentative attribution
<b>D397E-wild type double difference spectra, presence of Na<sup>+</sup> ions</b>	
1714 (+)	$\nu(\text{C=O})$ from protonated side chains of Asp/Glu
1670 (-)	Amide I; $\beta$ -turn
1644 (+)	Amide I; random structures
1615 (+)	Amide I; $\beta$ -sheet
1544 (+)	Amide II, $\nu_{\text{as}}(\text{COO}^-)$ from deprotonated side chains of Asp/Glu
1403 (-)	$\nu_{\text{s}}(\text{COO}^-)$ from deprotonated side chains of Asp/Glu
<b>D397E-wild type double difference spectra, presence of Li<sup>+</sup> ions</b>	
1714 (+)	$\nu(\text{C=O})$ from protonated side chains of Asp/Glu
1670 (-)	Amide I; $\beta$ -turn
1644 (+)	Amide I; random structures
1612 (+)	Amide I; $\beta$ -sheet
1554 (+)	Amide II, $\nu_{\text{as}}(\text{COO}^-)$ from deprotonated side chains of Asp/Glu
1523 (-)	$\nu_{\text{as}}(\text{COO}^-)$ from deprotonated side chains of Asp/Glu
1415 (+)	$\nu_{\text{s}}(\text{COO}^-)$ from deprotonated side chains of Asp/Glu
<b>D397E-wild type double difference spectra, presence of K<sup>+</sup> ions</b>	
1670 (-)	Amide I; $\beta$ -turn
1644 (+)	Amide I; random structures
1615 (+)	Amide I; $\beta$ -sheet
1580 (-)	Amide II, $\nu_{\text{as}}(\text{COO}^-)$ from deprotonated side chains of Asp/Glu
1538 (-)	$\nu_{\text{as}}(\text{COO}^-)$ from deprotonated side chains of Asp/Glu
<b>D397E-wild type double difference spectra, presence of Rb<sup>+</sup> ions</b>	
1714 (+)	$\nu(\text{C=O})$ from protonated side chains of Asp/Glu
1666 (-)	Amide I; $\beta$ -turn
1615 (+)	Amide I; $\beta$ -sheet
1584 (-)	Amide II, $\nu_{\text{as}}(\text{COO}^-)$ from deprotonated side chains of Asp/Glu
1541 (+)	Amide II, $\nu_{\text{as}}(\text{COO}^-)$ from deprotonated side chains of Asp/Glu
1408 (-)	$\nu_{\text{as}}(\text{COO}^-)$ from deprotonated side chains of Asp/Glu
1374 (+)	$\nu_{\text{as}}(\text{COO}^-)$ from deprotonated side chains of Asp/Glu

**Table 7.9: Tentative attribution of signals observed in the wild type-NqrB G140A double difference spectra for the potential range between -620 to +200 mV.**

Position (cm <sup>-1</sup> )		Tentative attribution
1688	(+)	Amide I; $\beta$ -turn, $\nu(\text{C=O})$ of glutamine.
1674	(+)	Amide I; $\beta$ -turn, $\nu(\text{C=O})$ of quinone, $\nu_{\text{as}}(\text{CN}_3\text{H}_5^+)$ from arginine
1658	(+)	Amide I; $\alpha$ -helix, $\nu(\text{C=O})$ of quinone, $\nu_{\text{s}}(\text{CN}_3\text{H}_5^+)$ from arginine, $\delta_{\text{as}}(\text{NH}_3^+)$ of lysine
1531	(+)	Amide II, $\delta_{\text{s}}(\text{NH}_3^+)$ of lysine
1485	(-)	quinol ring rearrangement
1410	(-)	quinol ring rearrangement
1286	(+)	C-OCH <sub>3</sub> methoxy group
1268	(-)	quinol ring rearrangement
1250	(+)	C-OCH <sub>3</sub> methoxy group

**Table 7.10: Tentative attribution of signals observed in the difference spectra of the wild type protein and the mutant enzyme, in H<sub>2</sub>O and D<sub>2</sub>O buffer, for the potential range between -280 to +200 mV.**

Position (cm <sup>-1</sup> )		Tentative attribution
<b>Wild type enzyme in H<sub>2</sub>O</b>		
1688	(+)	Amide I; $\beta$ -turn, $\nu(\text{C=O})$ from riboflavin, $\nu(\text{C=O})$ from glutamine
1670	(+)	Amide I; $\beta$ -turn, $\nu(\text{C=O})$ of quinone, $\nu_{\text{as}}(\text{CN}_3\text{H}_5^+)$ from arginine, $\nu(\text{C=O})$ from riboflavin
1660	(+)	Amide I; $\beta$ -turn
1623	(+)	Amide I; $\alpha$ -helix, $\nu(\text{C=C})$ of quinone, $\nu_{\text{s}}(\text{CN}_3\text{H}_5^+)$ from arginine, $\delta_{\text{as}}(\text{NH}_3^+)$ of lysine
1586	(-)	Amide II, $\nu(\text{C=N})$ from riboflavin, $\nu_{\text{as}}(\text{COO}^-)$ from deprotonated side chains of Asp/Glu
1530	(+)	Amide II, $\delta_{\text{s}}(\text{NH}_3^+)$ of lysine
1413	(-)	--
1375	(+)	--
1266	(+)	C-OCH <sub>3</sub> methoxy group
1227	(+)	Quinol ring reorganization
1086	(-)	Phosphate buffer
<b>Wild type enzyme in D<sub>2</sub>O</b>		
1690	(+)	Amide I, $\nu(\text{C=O})$ from riboflavin
1670	(+)	Amide I, $\nu(\text{C=O})$ of quinone, $\nu_{\text{as}}(\text{CN}_3\text{H}_5^+)$ from arginine, $\nu(\text{C=O})$ from riboflavin
1640	(-)	Amide I
1618	(+)	Amide I; $\alpha$ -helix, $\nu(\text{C=C})$ of quinone, $\nu_{\text{s}}(\text{CN}_3\text{H}_5^+)$ from arginine, $\delta_{\text{as}}(\text{NH}_3^+)$ of lysine
1570	(-)	Amide II, $\nu(\text{C=N})$ from riboflavin
1542	(+)	Amide II, $\nu(\text{C=C})$ from riboflavin
1527	(+)	Amide II, $\delta_{\text{s}}(\text{NH}_3^+)$ of lysine
1417	(-)	Quinol ring reorganization
1400	(-)	Quinol ring reorganization
1269	(+)	C-OCH <sub>3</sub> methoxy group
1226	(+)	Quinol ring reorganization
1097	(-)	Phosphate buffer
1071	(-)	Phosphate buffer
<b>NqrB G140A mutant enzyme in H<sub>2</sub>O</b>		
1660	(+)	Amide I; $\beta$ -turn, $\nu(\text{C=O})$ from riboflavin
1623	(+)	Amide I; $\alpha$ -helix, $\nu(\text{C=O})$ from riboflavin
1584	(-)	Amide II, $\nu(\text{C=N})$ from riboflavin
1413	(-)	--
1375	(+)	--
1086	(-)	Phosphate buffer
<b>NqrB G140A mutant enzyme in D<sub>2</sub>O</b>		
1670	(+)	Amide I, $\nu_{\text{as}}(\text{CN}_3\text{H}_5^+)$ from arginine, $\nu(\text{C=O})$ from riboflavin

## Appendix

---

1635	(-)	Amide I
1622	(+)	Amide I, $\nu_s(\text{CN}_3\text{H}_5^+)$ from arginine
1604	(-)	Amide II, $\nu(\text{C}=\text{N})$ from riboflavin
1575	(-)	Amide II, $\nu(\text{C}=\text{N})$ from riboflavin
1540	(+)	Amide II, $\nu(\text{C}=\text{C})$ from riboflavin
1097	(-)	Phosphate buffer
1071	(-)	Phosphate buffer

---

**Table 7.11: Tentative attribution of signals observed in the wild type – G140A double difference spectra measured in H<sub>2</sub>O and D<sub>2</sub>O buffer, for the potential range between -280 to +200 mV.**

Position (cm <sup>-1</sup> )	Tentative attribution
<b>Wild type-G140A double difference spectrum in H<sub>2</sub>O</b>	
1680 (-)	Amide I; $\beta$ -turns, $\nu(\text{C=O})$ of glutamine
1670 (+)	Amide I, $\nu(\text{C=O})$ of quinone, $\nu_{\text{as}}(\text{CN}_3\text{H}_5^+)$ from arginine
1640 (-)	Amide I
1621 (+)	Amide I, $\nu(\text{C=C})$ of quinone, $\nu_{\text{s}}(\text{CN}_3\text{H}_5^+)$ from arginine, $\delta_{\text{s}}(\text{NH}_3^+)$ of lysine
1580 (+)	Amide II
1563 (+)	Amide II
1530 (+)	Amide II, $\delta_{\text{s}}(\text{NH}_3^+)$ of lysine
1398 (-)	Quinol ring reorganization
1353 (-)	Quinol ring reorganization
1336 (-)	Quinol ring reorganization
1268 (+)	C-OCH <sub>3</sub> methoxy group
1224 (+)	Quinol ring reorganization
<b>Wild type-G140A double difference spectrum in D<sub>2</sub>O</b>	
1680 (-)	Amide I, $\nu(\text{C=O})$ of glutamine
1670 (+)	Amide I, $\nu(\text{C=O})$ of quinone, $\nu_{\text{as}}(\text{CN}_3\text{H}_5^+)$ from arginine
1645 (-)	Amide I
1620 (+)	Amide I, $\nu(\text{C=C})$ of quinone, $\nu_{\text{s}}(\text{CN}_3\text{H}_5^+)$ from arginine, $\delta_{\text{s}}(\text{NH}_3^+)$ of lysine
1559 (+)	Amide II
1528 (+)	Amide II, $\delta_{\text{s}}(\text{NH}_3^+)$ of lysine
1399 (-)	Quinol ring reorganization
1353 (-)	Quinol ring reorganization
1336 (-)	Quinol ring reorganization
1268 (+)	C-OCH <sub>3</sub> methoxy group
1224 (+)	Quinol ring reorganization

**Table 7.12: Tentative attribution of signals observed in the difference spectrum of the wild type enzyme in the presence of HQNO for the potential range between -280 to +200 mV.**

Position (cm <sup>-1</sup> )	Tentative attribution
1690 (+)	Amide I, $\nu(\text{C=O})$ of riboflavin
1670 (+)	Amide I, $\nu(\text{C=O})$ of riboflavin, $\nu_{\text{as}}(\text{CN}_3\text{H}_5^+)$ from arginine
1648 (-)	Amide I
1622 (+)	Amide I, $\nu_{\text{as}}(\text{CN}_3\text{H}_5^+)$ from arginine, $\delta_{\text{s}}(\text{NH}_3^+)$ of lysine
1590 (-)	$\nu(\text{C=N})$ from riboflavin
1531 (+)	Amide II, $\delta_{\text{s}}(\text{NH}_3^+)$ of lysine

**Table 7.13: Tentative attribution of signals observed in the difference spectra of cytochrome  $c_{552}$  (pH 7 and 9) for the potential range between -300 to +300 mV.**

pH 7		pH 9		Tentative attribution
Position ( $\text{cm}^{-1}$ )		Position ( $\text{cm}^{-1}$ )		
1720	(+)	1720	(+)	$\nu(\text{C=O})$ of protonated propionates, $\nu(\text{C=O})$ from protonated Glu/Asp
1707	(-)	1707	(-)	$\nu(\text{C=O})$ of protonated propionates
1695	(+)	1695	(+)	$\nu(\text{C=O})$ of protonated propionates
1678	(+)	1678	(+)	Amide I; $\beta$ -turn, $\nu(\text{C=O})$ of quinone, $\nu_{\text{as}}(\text{CN}_3\text{H}_5^+)$ from arginine
1666	(-)	1666	(-)	Amide I; $\beta$ -turn
1652	(+)	1652	(+)	Amide I; $\alpha$ -helix
1638	(+)	1638	(+)	Amide I; $\beta$ -sheet
1631	(-)	1631	(-)	Amide I; $\beta$ -sheet, $\nu_{38}$ of <i>c</i> -type heme
1610	(-)	1610	(-)	Amide I; $\beta$ -sheet
1555	(-)	1555	(-)	Amide II, $\nu_{\text{as}}(\text{COO}^-)$ from deprotonated side chains of Asp/Glu
1546	(+)	1546	(+)	Amide II, $\nu_{\text{as}}(\text{COO}^-)$ from deprotonated side chains of Asp/Glu
1535	(-)	1535	(-)	Amide II, $\nu_{\text{as}}(\text{COO}^-)$ from deprotonated side chains of Asp/Glu, $\delta_{42}$ of <i>c</i> -type heme
1516	(-)	1516	(-)	$\nu_{\text{as}}(\text{COO}^-)$ from deprotonated side chains of Asp/Glu, $\nu(\text{C=C})/\delta(\text{C-H})$ of neutral Tyr
1501	(+)	1501	(+)	$\nu(\text{C=C})/\delta(\text{C-H})$ of deprotonated Tyr
1430	(-)	1430	(-)	$\nu_{\text{s}}(\text{COO}^-)$ from deprotonated side chains of Asp/Glu
1421	(+)	1421	(+)	$\nu_{\text{s}}(\text{COO}^-)$ from deprotonated side chains of Asp/Glu
1383	(-)	1383	(-)	$\delta_{\text{s}}(\text{CH}_3)$
1237	(-)	1237	(-)	$\gamma(\text{C-H})$ of heme

**Table 7.14: Tentative attribution of signals observed in the difference spectra of the Cu<sub>A</sub> fragment (pH 7 and 9) for the potential range between -300 to +300 mV.**

pH 7		pH 9		Tentative attribution
Position (cm <sup>-1</sup> )		Position (cm <sup>-1</sup> )		
1688	(+)	1688	(+)	Amide I; $\beta$ -turn, $\nu(\text{C=O})$ from Gln and Asn
1657	(-)	1660	(-)	Amide I; $\beta$ -turn, $\nu(\text{C=O})$ from Gln and Asn
1649	(+)	1644	(+)	Amide I; $\beta$ -sheet
1634	(-)	1632	(-)	Amide I; $\beta$ -sheet, $\nu(\text{CN}_3\text{H}_5)$ as of Arg
1573	(+)	1580	(+)	Amide II
1550	(+)	1550	(+)	Amide II
1527	(-)	1527	(-)	Amide II
1330	(-)	1330	(-)	Amide III, $\delta(\text{N-H})$ and $\omega(\text{S-CH}_2)$ from cys and met
1277	(-)	1277	(-)	Amide III, $\delta(\text{N-H})$ and $\omega(\text{S-CH}_2)$ from cys and met
1265	(+)	1265	(+)	Amide III, $\delta(\text{N-H})$ and $\omega(\text{S-CH}_2)$ from cys and met
1232	(-)	1232	(-)	Amide III, $\delta(\text{N-H})$ and $\omega(\text{S-CH}_2)$ from cys and met

# Study of protein interactions in the respiratory chain by IR spectroscopy and electrochemistry

## Résumé

Le domaine de la bioénergie moléculaire concerne le transfert et le stockage d'énergie dans les cellules biologique. Ce projet s'articule autour de la respiration et plus précisément le mécanisme de pompage de sodium et de protons, et son couplage au transfert d'électrons. Premièrement, nous nous sommes intéressés au pompage d'ions sodium par la NADH:quinone oxidoreductase de la bactérie *Vibrio cholerae*. L'importance de flavines spécifiques et des résidus acides dans le transfert de sodium ont été démontrée. Par la suite, l'interaction entre protéines, notamment le cytochrome  $c_{552}$  et le fragment  $Cu_A$  de l'oxidase de type  $ba_3$  de l'organisme *Thermus thermophilus* a été étudié. Une réorganisation structurale induit par le transfert d'électron a été démontrée par la spectroscopie IRTF différentielle. Enfin, dans la dernière partie de ce travail, l'interaction au sein du supercomplexe  $bc_1-aa_3$  de la chaîne respiratoire du *Corynebacterium glutamicum* a été analysée.

Bioénergétique, Respiration, Spectroscopie IRTF, Electrochimie, Cinétique d'échange H/D, Transport de sodium, NADH:quinone oxidoreductase, interaction protéine-protéine, cytochrome  $c_{552}$ ,  $Cu_A$ , supercomplexe

## Résumé en anglais

The field of molecular bioenergetics deals with the energy transduction in biological cells. In this project, respiration and more specifically proton and sodium pumping enzymes and their coupling to electron transfer have been in focus. First we have been interested in the  $Na^+$ -pumping NADH:quinone reductase from *Vibrio cholerae* which is the entry site of electrons in the respiratory chain of several pathogens. The role of specific flavin cofactors and amino acids involved in  $Na^+$  transfer has been shown in a combined IR spectroscopic and electrochemical approach. The interaction between proteins, namely the cytochrome  $c_{552}$  and the  $Cu_A$  fragment from the terminal  $ba_3$  oxidase from the organism *Thermus thermophilus* was then investigated. Structural reorganization during electron transfer was revealed by IR spectroscopy. Finally, in the third part of the project the interaction within the  $bc_1-aa_3$  supercomplex from the respiratory chain from *Corynebacterium glutamicum* was analyzed.

Bioenergetics, Respiration, FTIR spectroscopy, Electrochemistry, H/D exchange kinetics,  $Na^+$  transport,  $Na^+$ -pumping NADH:quinone oxidoreductase, Protein-protein interaction, cytochrome  $c_{552}$ ,  $Cu_A$ , supercomplex.